Cover Page

The handle http://hdl.handle.net/1887/24911 holds various files of this Leiden University dissertation.

Author: Venderbos, Jörn Willem Friedrich
Title: Integer and fractional quantum hall effects in lattice magnets
Issue Date: 2014-03-25

Integer and Fractional Quantum Hall effects in Lattice Magnets

J.W.F. Venderbos

Integer and Fractional Quantum Hall effects in Lattice Magnets

PROEFSCHRIFT

ter verkrijging van
de graad van Doctor aan de universiteit Leiden,
op gezag van Rector Magnificus prof. mr. C. J. J. M. Stolker,
volgens het besluit van het College voor Promoties
te verdedigen op dinsdag 25 maart 2014
te klokke 15:00 uur

door

Jörn Willem Friedrich Venderbos
geboren te Kleve, Duitsland, in 1984

Promotiecommissie

Promotoren:	Prof.dr.ir. J.W.M. Hilgenkamp (Universiteiten Twente en Leiden)
	Prof.dr. J. van den Brink (TU Dresden en IFW Dresden)
Overige leden:	Prof.dr. E.R. Eliel (Universiteit Leiden)
	Prof.dr. C.W.J. Beenakker (Universiteit Leiden)
	Prof.dr. C. Chamon (Boston University)
	Dr. C.D. Batista (Los Alamos National Laboratory)

CONTENTS

CHAPTER 1

INTRODUCTION

The subject of this thesis is unconventional phases of matter in strongly correlated materials.

1.1 Strong correlations and topological states of matter

In the course of the past decade or so, a new and exciting field of condensed matter physics has opened up and expanded rapidly. It is the field of topological states of matter, which is centered around a material class called the topological insulators. The birth and subsequent development of this field was precipitated by a simple yet profound question: does the existance of an energy gap uniquely define the insulating state? It was believed that in a way, the atomic insulator (where electrons are uniquely associated to an atomic site and do not move), the band insulator (where an integer number of Bloch bands are filled and separated from empty bands by an energy gap) and, for instance, the vacuum essentially define the same insulating state in the sense that it takes a finite amount of energy to create an excitation in the ground state. However, as was shown in a series of seminal papers [1–5], the mere existance of an energy gap does not uniquely define the insulating state. It turns out that insulating states may be classified according to a global poperty, that for a given Hamiltonian

describing the insulating system, is obtained from the mapping from the Brillouin zone to the space of occupied energy bands corresponding to the Hamiltonian.

This classification is rather different from the way in which we are used to think about distinguishing phases of matter. The traditional way to distinguish phases of matter is due to Landau and assumes the presence of a *local* order parameter which represents the breaking of a symmetry. For instance, the crystalline solid breaks the translational symmetry of the underlying quantum Hamiltonian, while the longe-range magnetic order breaks rotational symmetry. The broken symmetry in a superconductor is related to the more subtle concept of gauge invariance. Hence, distinct phases break different symmetries. In contrast, the additional quantum numbers insulators may acquire in their ground state are given by a topological invariant, a *global* quantity. This invariant does not change when the system is smoothly deformed. The qualification smooth here pertains to the energy gap, which has to remain finite during deformation.

As such, the quantum numbers connected to the topological invariant of the system are insensitive to microscopic details, and the physical properties associated to these quantum numbers are uniquely robust. The fundamental property of a topological insulator material is the presence of gapless boundary or edge excitations at interfaces with topologically distinct systems, such as the vacuum itself. As the topological character cannot change without closing the energy gap, there must be gapless states precisely at the interface between electronic systems with different topology. Examples of this bulk-edge correspondence, which have been famously confirmed in experiment, include the spin-filtered one-dimensional edge states of the Quantum Spin Hall effect [6, 7] and the Dirac cone surface states of three dimensional time-reversal invariant topological insulators [8, 9]. While these two examples, and many others, can be understood from the theory of non-interacting electron band structure, topological states of matter are by no means restricted to non-interacting or weakly interacting systems. An increasing amount of attention is given to material systems where interactions are important. Even more, topology and strong interaction have a long and rich history. Indeed, the fractional quantum Hall effect [10] is a consequence of electron-electron interaction and the quantum Hall liquids hosting this effect are said to be topologically ordered [11]. The work reflected in this thesis is part of the general effort to study and understand the role and consequence of topology in (strongly) correlated materials.

In what follows, the very basis physics of topological states of matter is introduced with a focus on aspects that are relevant to the remainder of this thesis.

1.1.1   Integer and Fractional Quantum Hall effects

In this part of the introduction we review the basics of electrons in a (strong) magnetic field with two purposes in mind. As the second part of this thesis deals explicitly with lattice versions of both integer and fractional quantum Hall effects, some details of the continuum versions will be helpful. In subsequent chapters an understanding will then be developed of how they may be realized in a crystalline solid without external fields. In addition, the quantum Hall effects, in particular the Integer one, are a good starting point to uncover and explain the key role played by topology in electronic structure theory [12].

Previously in this introductory chapter, we have noted that lattice fermion model will be employed to describe electrons in solids. Here we briefly depart from that and consider free electrons subject to a magnetic field without any reference to a periodic crystal lattice. In fact, one of the questions addressed in this thesis is how and in what form do the Integer and in particular the Fractional Quantum Hall effects of the continuum description carry over to the crystal lattice description.

The Hamiltonian for free fermions in two dimensions is simply given by the kinetic energy term as

$$\hat{H} = \frac{1}{2m} \sum_{\alpha} \hat{p}_{\alpha}^2, \tag{1.1}$$

where $\hat{p}_{\alpha}$ is the momentum operator canonically conjugate to the position operator $\hat{r}_{\alpha}$, $\alpha = x, y$. In a magnetic field given by the vector potential $A_{\alpha}(\hat{r})$ we make the Peierls substitution, which amounts to

$$\hat{\Pi}_{\alpha} = \hat{p}_{\alpha} - eA_{\alpha}(\hat{r}) = -i\hbar\partial_{\alpha} + |e|A_{\alpha}(\hat{r}). \tag{1.2}$$

This changes the Hamiltonian to simply to $\hat{H} = \sum_{\alpha} \hat{\Pi}_{\alpha}^2/2m$. Due to the presence of the vector potential, the operators $\hat{\Pi}_j$ do not commute between themselves but instead are found to obey the canonical commutation relation

$$\begin{aligned} [\hat{\Pi}_{\alpha}, \hat{\Pi}_{\beta}] &= [\hat{p}_{\alpha} + |e|A_{\alpha}(\hat{r}), \hat{p}_{\beta} + |e|A_{\beta}(\hat{r})] \\ &= -i\hbar|e|F_{\alpha\beta} \end{aligned} \tag{1.3}$$

where $F_{\alpha\beta} = \partial_{\alpha}A_{\beta} - \partial_{\beta}A_{\alpha}$ is the field strength. We are interested in the situation of a uniform magnetic field B perpendicular to the plane in which the electrons live, i.e. the $\hat{z}$ direction. In general the magnetic field is given by $B_{\lambda} = \epsilon_{\lambda\mu\nu}F_{\mu\nu}/2$, meaning that $F_{\mu\nu} = \epsilon_{\mu\nu\lambda}B_{\lambda}$. In particular this implies for a uniform field $B_z \equiv B$ in the $\hat{z}$ direction that $[\hat{\Pi}_{\alpha}, \hat{\Pi}_{\beta}] = -i\hbar|e|B\epsilon_{\alpha\beta z}$. Defining the fundamental characteristic length scale in the system, the magnetic length, as $l = \sqrt{\hbar/(|e|B)}$, we can write

$$[\hat{\Pi}_{\alpha}, \hat{\Pi}_{\beta}] = -i\hbar^2\epsilon_{\alpha\beta z}/l^2. \tag{1.4}$$
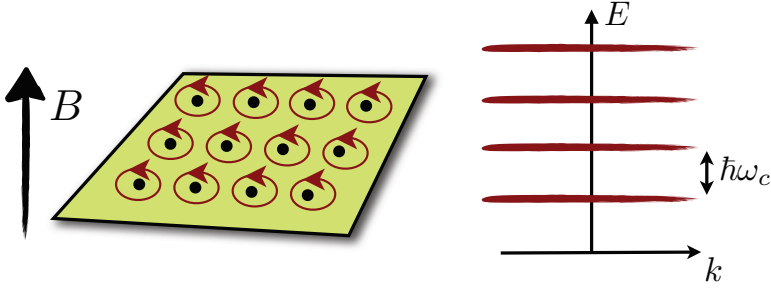
Figure 1.1: (left) Schematic illustration of the (classical) electronic cyclotron orbits in the presence of a magnetic field pointing in the z-direction. (right) Schematic illustration of the electronic Landau levels, i.e. the equidistant quantized energy levels, in the presence of a magnetic field.

Since Hamiltonian consists of the quadrature of operators obeying a canonical commutation relation one can diagonlize the Hamiltonian in the same way as the harmonic oscillator. We define the raising and lowering operators as

$$\hat{a}^\dagger = \frac{l}{\sqrt{2}\hbar}(\hat{\Pi}_x + i\hat{\Pi}_y), \qquad \hat{a} = \frac{l}{\sqrt{2}\hbar}(\hat{\Pi}_x - i\hat{\Pi}_y), \tag{1.5}$$

which obey $[\hat{a}, \hat{a}^\dagger] = 1$, we simple derive that the Hamiltonian takes the form $\hat{H} = \hbar\omega_c(\hat{a}^\dagger\hat{a} + \frac{1}{2})$ with $\omega_c = |e|B/m$ the corresponding frequency. We have thus achieved the diagonalization of the single-particle Hamiltonian, yielding energies $E_n = \hbar\omega_c(n + \frac{1}{2})$. Here n labels the energy levels, which are generally referred to as Landau levels, $n = 0$ corresponding to the lowest Landau level (LLL).

However, to fully characterize the quantum problem and account for all degeneracies, it is helpful to quickly revisit the classical cyclotron orbits. Classicaly, the position of a particle and its velocity in a circular orbit are given by

$$\begin{aligned}
\vec{r} &= \vec{R} + r_0(\cos(\omega_c t), \sin(\omega_c t), 0), \\
\vec{v} &= r_0\omega_c(-\sin(\omega_c t), \cos(\omega_c t), 0)
\end{aligned} \tag{1.6}$$

where $\vec{R}$ denotes the coordinates of the center of the orbit and r_0 is the radius of the orbit. Here ω_c is the cyclotron frequency of the orbit, which is equal to one used above. Classically momentum and velocity are related by $m_e\vec{v} = \vec{p}$. Using

equation (1.6) we may identify

$$\frac{p_x}{m_e\omega_c} = -r_0\sin(\omega_c t) = \frac{l_B^2 p_x}{\hbar},$$

$$\frac{p_y}{m_e\omega_c} = r_0\cos(\omega_c t) = \frac{l_B^2 p_y}{\hbar} \tag{1.7}$$

which has the consequence of Eq. (1.6) taking the simply form

$$\vec{R} = \vec{r} - \frac{l^2}{\hbar}(\vec{p}\times\hat{z}). \tag{1.8}$$

This relation between classical variables leads to the definition of the so-called guiding center operators $\hat{R}_x$ and $\hat{R}_y$ in the quantum case as

$$\hat{R}_\alpha = \hat{r}_\alpha - \frac{l^2}{\hbar}(\vec{\Pi}\times\hat{z})_\alpha = \hat{r}_\alpha - \frac{l_B^2}{\hbar}\epsilon^{\alpha\beta z}\hat{\Pi}_\beta. \tag{1.9}$$

These guiding center operators obey the commutation relation

$$[\hat{R}_\alpha, \hat{R}_\beta] = il^2\epsilon^{\alpha\beta z} \tag{1.10}$$

In addition, it is a simple matter to demonstrate that the dynamical momentum operators and guiding center operators commute with one another

$$[\hat{R}_\alpha, \hat{\Pi}_\beta] = [\hat{r}_\alpha - \frac{l^2}{\hbar}\epsilon^{\alpha\mu z}\hat{\Pi}_\mu, \hat{\Pi}_\beta] = i\hbar\delta_{\alpha\beta} + i\hbar\epsilon^{\alpha\mu z}\epsilon^{\mu\beta z} = 0 \tag{1.11}$$

This has the consequence that the guiding center operators commute with the Hamiltonian. One can construct momentum operators canonically conjugate to the guiding center operators, which are defined as

$$\hat{K}_\alpha = \hat{\Pi}_\alpha - \frac{\hbar}{l^2}(\hat{z}\times\hat{\vec{r}})_\alpha = \hat{\Pi}_\alpha - \frac{\hbar}{l^2}\epsilon^{\alpha z\beta}\hat{r}_\beta. \tag{1.12}$$

which are easily found to satisfy $[\hat{R}_\alpha, \hat{K}_\beta] = i\hbar\delta_{\alpha\beta}$. In addition, in the same way as above, the commutator with the dynamical momentum vanishes, $[\hat{\Pi}_\alpha, \hat{K}_\beta] = 0$.

To summarize this brief exposition, the single-particle Hamiltonian may be diagonalized by constructing raising and lowering operators frmo the dynamical momenta and both the guiding center operators and their canonically conjugate momenta commute with the Hamiltonian. For electrons in a uniform magnetic field we expect translational invariance to hold. When constructing operators that implement these translations we cannot use the dynamical momenta as generators, since they do not

commute with the Hamiltonian, i.e. $[\hat{\Pi}_\alpha, \hat{\Pi}_\beta] = -i\hbar^2 \epsilon_{\alpha\beta z}/l^2$. The momenta $\hat{K}_\alpha$ do however commute with the Hamiltonian and the operator that implements a translation of a single particle by $\vec{a}$ is

$$\hat{T}(\vec{a}) = e^{ia_\alpha \hat{K}_\alpha/\hbar}. \tag{1.13}$$

The momenta $\hat{K}_\alpha$ do not commute between themselves, which has the profound consequence that different translations do not commute with each other

$$[\hat{T}(\vec{a}), \hat{T}(\vec{b})] = -2\sin\left(\frac{1}{2l^2}\hat{z}\cdot(\vec{a}\times\vec{b})\right)\hat{T}(\vec{a}+\vec{b}). \tag{1.14}$$

This commutation relation is known as the magnetic translation algebra or Girvin-MacDonald-Platzman (GMP) algebra [13] and lies as the heart of Quantum Hall and Fractional Quantum Hall physics [14]. In particular, it is precisely this relation that is responsible for the Aharonov-Bohm phase electrons pick up when encircling magnetic flux.

The GMP algebra can be recast in a different form by first defining a density operator based on the guiding center operators

$$\hat{\rho}(\vec{q}) = e^{iq_\alpha \hat{R}_\alpha}, \tag{1.15}$$

and since the guiding center operators are related to their conjugate momenta by the relation

$$\hat{R}_\alpha = \frac{l^2}{\hbar}\epsilon^{\alpha z\beta}\hat{K}_\beta \tag{1.16}$$

one may easily verify that the density operators thus defined satisfy an algebra equivalent to the one for the translation operators, given specifically by

$$[\hat{\rho}(\vec{q}), \hat{\rho}(\vec{q}')] = -2\sin\left(\frac{1}{2l^2}\hat{z}\cdot(\vec{q}\times\vec{q}')\right)\hat{\rho}(\vec{q}+\vec{q}'). \tag{1.17}$$

Hence, the GMP algebra is also satisfied by density operators constructed from the guiding center operators. Why these play a crucial role in particular for the fractional quantum Hall physics in the presence of interactions may be seen by considering the electron density operators $\bar{\rho}(\vec{p}) = \exp(ip_\alpha \hat{r}_\alpha)$ projected into the lowest Landau level. If $\hat{P}$ is the projector into the LLL, it is a simple matter to verify that

$$\hat{P}e^{ip_\alpha \hat{r}_\alpha}\hat{P} = e^{-q^2l^2/4}\hat{\rho}(\vec{q}). \tag{1.18}$$

We thus draw the consequential conclusion that the GMP algebra is obeyed by density operators when they are projected to the lowest Landau level. It may be argued in a

similar way that this holds for any Landau level labeled by n, however the LLL is the most prominent one, in which the fractional quantum Hall effect is observed.

The GMP algebra is of great importance for the physics of both the integer and the fractional Quantum Hall effect. Neglecting the interactions between electrons we may express the contribution of Landau level n to off-diagonal Hall conductivity in the form of the Kubo formula as [15]

$$\sigma_{xy}^n = \frac{e^2\hbar}{im_e^2} \frac{1}{2\pi l^2 N_\phi} \sum_{n'\neq n} \sum_{m,m'} \frac{\langle n,m|\hat{\Pi}_x|n',m'\rangle\langle n',m'|\hat{\Pi}_y|n,m\rangle - (x \leftrightarrow y)}{(E_n - E_{n'})^2},$$

(1.19)

and using the relation $\hat{\Pi}_\alpha = im_e[\hat{H},\hat{r}_\alpha]/\hbar$ together with $P\hat{r}_\alpha P = \hat{R}_\alpha$ for any Landau level, one can derive

$$\sigma_{xy}^n = -\frac{ie^2}{2\pi l^2 N_\phi \hbar} \sum_m \langle n,m|[\hat{R}_x,\hat{R}_y]|n,m\rangle = \frac{e^2}{h}.$$

(1.20)

We conclude that each *filled* Landau level contributes one quantum of e^2/h to the Hall conductivity [16]. This is a direct consequence of the underlying noncommutative GMP algebra.

There is another way in which the GMP algebra is of crucial importance, which concerns the physics of the fractional quantum Hall effect, i.e. the explicit inclusion of Coulomb interactions. An electron-electron interaction of the form $V(\vec{r}_i - \vec{r}_j)$ translates into a Hamiltonian term

$$\sum_{i\neq j} V(\vec{r}_i - \vec{r}_j) \sim \sum_{\vec{q}} V(\vec{q}) \sum_{i<j} e^{i\vec{q}\cdot(\vec{r}_i - \vec{r}_j)}$$

(1.21)

where we have taken the system to live on torus geometry, the reciprocal lattice vectors $\vec{q}$ being related to the generators of the torus. The fractional quantum Hall effect is most clearly observed for rather large magnetic fields, in which case the degeneracy of a single Landau level is huge and one may restrict the Hilbert space to the lowest Landau level. The interaction takes the form

$$\sum_{\vec{q}} \sum_{i<j} V(\vec{q})\hat{\rho}_i(\vec{q})\hat{\rho}_j(-\vec{q})e^{-q^2 l^2/2},$$

(1.22)

with $\hat{\rho}_i(\vec{q})$ the aforementioned projected density operators. As the Hamiltonian is purely expressed in terms of these density operators, it is certainly not surprising that their algebraic properties and the organization of Hilbert space following from them are fundamental to the physics of the fractional quantum Hall effect. The algebra expressed in equation (1.17) is therefore at the heart of bringing the fractional Quantum

Hall effect from the continuum (electrons in a strong magnetic field) to the lattice (electrons in a periodic crystal with a band structure), which is the subject of part II of this thesis.

1.1.2 Chern Insulators and their generalizations

A key feature of Landau levels that was highlighted above is their contribution to the quantized Hall conductivity $\sigma_{xy} = e^2/h$, when a Landau level is completely filled [16]. Focusing on a single Landau level for the moment, we may express this property in a response equation given by

$$J_i = \sigma_H \epsilon^{ij} E_j, \tag{1.23}$$

where J_i is the current in the i-direction and E_i the i-th electric field component. This can actually be generalized to include the time t component, which gives the response equation

$$J_\mu = \sigma_H \epsilon^{\mu\nu\lambda} \partial_\nu A_\lambda. \tag{1.24}$$

One may functionally integrate this to obtain an effective action of the form

$$S[A_\mu] = \frac{\sigma_H}{2\pi} \int d^2\vec{r}dt \; \epsilon^{\mu\nu\lambda} A_\mu \partial_\nu A_\lambda. \tag{1.25}$$

This action describes the fundamental low-energy electromagnetic field theory of the quantum Hall state [17].

One way – perhaps an unsual way – to make a connection to general topological states of matter is to ask the question: are there more states of matter that have an action of this form as their low-energy effective theory? Or, to reformulate this question, are there other insulators that have the same electromagnetic response equation? The answer to this question is "yes", and this affirmative answer is the first step towards a much broader class of distinct insulating states that cannot be adiabatically connected to the trivial atomic insulator.

Imagine we are given a material system governed by the Hamiltonian $\hat{H} = \sum_k \hat{\Psi}^\dagger(\vec{k})\mathcal{H}(\vec{k})\hat{\Psi}(\vec{k})$ (suppressing orbital and spin indices for convenience), and we are told that this defines an insulator. Then we may first obtain its Green's function $\mathcal{G}$, given by

$$\mathcal{G}(\omega, \vec{k}) = [\omega + i\delta - \mathcal{H}(\vec{k})]^{-1}, \tag{1.26}$$

and proceed to calculate the following quantity [18]

$$C = \frac{1}{4\pi} \int_{BZ} d^2k d\omega \; \epsilon^{\mu\nu\lambda} \text{Tr} \, [\mathcal{G}\partial_\mu \mathcal{G}^{-1} \mathcal{G}\partial_\nu \mathcal{G}^{-1} \mathcal{G}\partial_\lambda \mathcal{G}^{-1}], \tag{1.27}$$

where $\partial_\mu \equiv \partial/\partial k_\mu$. It can be proven that C is necessarily an integer [16, 18] and in addition is it clearly a "global" object, as it involves integration over the whole Brillouin zone (BZ). What does C have to do with equation (1.25)? The answer to that question can be expressed in a simple yet profound equation (setting $\hbar = e = 1$ for the moment),

$$\sigma_H = \frac{C}{2\pi}, \tag{1.28}$$

or in words, the integer C is the constant coefficient that multiplies the action and consquently determines the physical response, i.e. the Hall conductivity. As C is restricted to be integer, the Hall conductivity is quantized. For the Quantum Hall state induced by an external magnetic we have $\sigma_H = C = 1$, while in general it may be any number. For ordinary insulators one has $C = 0$.

For the sake of clarity and definiteness we may particularize to the situation of a two-band Hamiltonian, which can be expanded in the space Pauli matrices $\vec{\tau}$ as

$$\mathcal{H}(\vec{k}) = \varepsilon(\vec{k})I_2 + \vec{d}(\vec{k}) \cdot \vec{\tau}. \tag{1.29}$$

This Hamiltonian has energies $E_\pm(\vec{k}) = \varepsilon(\vec{k}) \pm |\vec{d}(\vec{k})|$, which we assume to correspond to an insulator (min $E_+(\vec{k}) > $ max $E_-(\vec{k})$, $\vec{k} \in$ BZ), and since $\varepsilon(\vec{k})$ multiplies the (2×2) identity matrix I_2, the eigenstate structure only depends on $\vec{d}$. Indeed, $\vec{d}(\vec{k})$ contains the information on the topological character of the electronic ground state of the system. Taking the Hamiltonian of equation (1.29) and substituting it into equation (1.27) yields an expression of C in terms of $\vec{d}(\vec{k})$

$$C = \frac{1}{4\pi} \int d^2k \; \epsilon^{\alpha\beta\gamma} \tilde{d}^\alpha \partial_x \tilde{d}^\beta \partial_y \tilde{d}^\gamma. \tag{1.30}$$

Here $\tilde{d}^\alpha(\vec{k}) = d^\alpha(\vec{k})/|\vec{d}(\vec{k})|$ is the normalized $\vec{d}$ vector. The normalized vector $\tilde{d}^\alpha(\vec{k})$ has unit length and thus lives on a sphere, which means we may interpret it as a mapping from the Brillouin zone, a 2-torus T^2, to the sphere S^2. The integrand in equation (1.30) is nothing but the Jacobian of this mapping, which implies that C counts the number of times the image of the mapping wraps around the sphere, which is clearly an integer and cannot change under smooth deformation of the mapping given by $\vec{\tilde{d}}(\vec{k})$. This establishes C as a topological invariant [18]. The integer invariant C is generally referred to as the Chern number, a term borrowed from mathematics. It has become customary to refer to insulators with nonzero C as *Chern insulators*. Chern insulators are systems in the same universality class as the quantum Hall state, and thus fundamentally distinct from "ordinary", or atomic insulators.

As a spoiler for chapter 7, an example of a Chern insulator having $C \neq 0$ is

$$\mathcal{H}(\vec{k}) = \cos k_1 \tau^x + \cos k_2 \tau^y + \cos k_3 \tau^z. \tag{1.31}$$
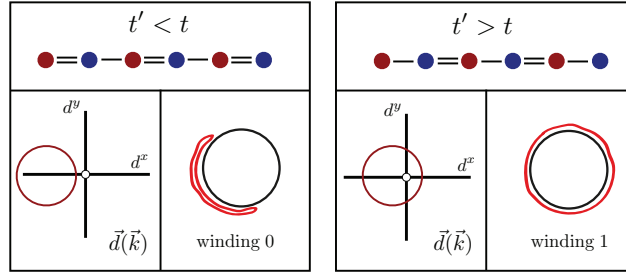
Figure 1.2: The two different topological sectors of the $1D$ Peierls chain discussed in the text. Left, the situation $t' < t$ in which case the d-vector does not wrap around the circle as one traces the $1D$ Brillouin zone (equivalent to a circle). Right, on the other hand, the situation $t' > t$, in which case the d-vector wraps around the circle once.

Here $k_i = \vec{k} \cdot \vec{x}_i$ ($i = 1, 2, 3$) and $\vec{x}_i$ are lattice vectors of length a making an angle $2\pi/3$ with each other. It corresponds to electrons hopping on the triangular lattice with a flux of $\phi = \pi/2$ threading each triangle. Using equation (1.30) one finds that for this Hamiltonian the insulating round state is characterized by $C = 1$.

At this point a few comments with regard to equation (1.25) are in order. First, by looking at the integrations we notice that this action applies to a two-dimensional ($2D$) system. Consequently, all considerations above apply to $2D$ systems. Second, it can be checked by looking at the transformation of the electromagnetic field A_μ under time-reversal, that the actions represents a time-reversal symmetry broken state. These observations are a manifestation of the crucial importance of both symmetry and dimensionality in classifying topological phases. The class of systems defined by nonzero C must live in $2D$ and do not require any symmetry. Other topological phases, which can exist in for instance one or three dimensions and have distinct physical properties, often require the presence of a symmetry. To illustrate this we briefly review a famous example in $1D$, the Peierls chain realized in polyacetylene [19].

Imagine a $1D$ chain of atoms with alternating hopping integral t and t', where one is weaker and one is stronger $t > t'$ (or $t < t'$). This is graphically shown in Fig. 1.2, where the two different cases are shown on the right (left) side. The alternation of stronger and weaker bonds mandates a two-site unit cell, with atoms A and B, and the Hamiltonian describing this system can again be expanded in Pauli matrices, now representing the sublattice degree of freedom,

$$\mathcal{H}(k) = \vec{d}(k) \cdot \vec{\tau}, \quad \vec{d}(k) = (t + t'\cos k, \sin k, 0) \tag{1.32}$$

Crucially, since hopping takes place only between A and B atoms, we have $d^z(k) = 0$. This forces the $\vec{d}$ vector to be in the $x - y$ plane and it defines a mapping from the $1D$ Brillouin zone, i.e. the circle, to the $2D$ plane. It is easy to check that for $t \neq t'$ the system is insulating. The topological nature of this insulating state is revealed by taking a closer look that the mapping from the circle to the $x - y$ plane defined by $\vec{d}$. The loop mapped out in the $x - y$ plane either encircles the origin or it does not. In Fig. 1.2, for both $t < t'$ and $t > t'$, the lower left square shows the red loop traced out by the $\vec{d}$-vector as function of $\vec{k}$. The origin is special because there $\vec{d} = 0$ and the insulating gap would vanish. If the loop does not enclose the origin, such as in the left of Fig. 1.2, we can smoothly deform it to a single point, representing the atomic insulator, without closing the energy gap. However, if $\vec{d}(k)$ does enclose the origin, see right side of Fig. 1.2, we cannot do so, and this situation defines a topologically distinct state. In essence, since we must exclude the origin from the plane; we are classifying mappings from the circle to the circle, which are known to come with an integer index: the number of times the image wraps around the target circle. This is schematically depicted in the lower right boxes of Fig. 1.2, where the red "circles" are mapped to the black circles and either wrap around the black circle once (right) or not at all (left). For the Peierls Hamiltonian expressed in equation (1.32) the topological winding number is therefore 1.

How do symmetry and dimensionality manifest themselves? A symmetry constrains the Hamiltonian so that the $\vec{d}$-vector cannot have a z-component. The symmetry is a chiral symmetry and expressed as an anti-commutation relation

$$\{\mathcal{H}, \tau^z\} = 0. \tag{1.33}$$

This relations forces $d^z(k) = 0$ and it furthermore ensures that every state $|\psi\rangle$ of energy E has a partner τ^z at energy $-E$. If $d^z(k)$ was not forced to be zero, but allowed to take arbitrary values, then our argument for distinguishing loops would not hold anymore. Any loop could be smoothly contracted to a point by using the z-component of the $\vec{d}$-vector. In other words, instead of classifying mappings from a circle to a circle, we would be classifying mappings from the circle to the sphere. Mappings of the latter kind are all trivial, as they can always be continuously deformed to a single point on the sphere [20].

Symmetry and dimensionality are fundamental. One of most prominent symmetries permitting a topological classification of insulators in $2D$ and in $3D$ is time-reversal symmetry [1–5, 21, 22]. Up until now, we have discussed topological classifications based on integers. The Chern number C can take any integer value, and the $[d^x(k), d^y(k)]$ vector may in principle encircle the origin any number of times, depending on the form of the Hamiltonian.

Time-reversal symmetry, however, leads to a $\mathbb{Z}_2$ classification, which is to say that there are only two flavors, trivial and nontrivial – topological and non-topological [1–

5]. Real materials belonging to the class of nontrivial systems are then generally refered to as time-reversal invariant topological insulators. Dimensionality is again important. In two dimensions a time-reversal invariant topological state is referred to as the Quantum Spin Hall state [1, 23]. The physical manifestation of the topological nature of the electronic state is the existance of an odd number of spin-filtered counterpropagating edge state pairs. The locking of propagation direction and spin polarization implies the requirement of spin-rotation symmetry breaking, at least partially. Not surprisingly, strong spin-orbit coupling plays a key role in the field of topological insulators. In chapter 10 we will see examples of precisely such two-dimensional Quantum Spin Hall states, where the spin-rotation symmetry breaking comes from electronic interactions. In three dimensions spin-rotation symmetry must be completely broken in order for an insulator to be a topological insulator. The physical consequence of non-trivial topology in three dimensions is the presence of an odd number of two-dimensional Dirac fermions at a sample surface. This is forbidden in a genuinely two-dimensional electronic system [24]. In both two and three dimensions we see that odd and even (edge or surface states) are clearly distinguished when it comes to the physical manifestation of non-trivial topology, which essentially defines the $\mathbb{Z}_2$ classification of time-reversal invariant topological insulators.

Other symmetries giving rise to topologically insulating systems with robust physical properties mandated by their topological character are particle-hole symmetry and the product of time-reversal and particle-hole symmetry, often called sublattice symmetry or chiral symmetry. The robustness follows from the fact that disorder may respect these symmetries and therefore cannot harm the physical consequences of the topological nature of a quantum state. A complete classification based on these three symmetries has been achieved and has resulted in the "periodic table" of topological insulators [21, 22].

1.2 Strongly correlated electrons and electronic degrees of freedom

Generally speaking there are two points of departure for describing electrons in solids. One is to start from the free electron gas and subject the electrons to a weak periodic potential originating from the crystal lattice. Wave functions obtained by solving Schrödinger's equation are perturbed and modified by the periodic potential, which results in the typical band structure of crystalline solids. The other is to picture the electrons as still associated to the atoms of the crystal and construct the electron wave function from corresponding atomic orbital functions. Due to the periodic array of atoms, the atomic wave functions overlap and electrons may tunnel, or "hop", from

atom to atom. The latter approach is referred to as the tight-binding description of electrons, as they are considered to be tightly bound to the atomic sites of the lattice.

Which perspective to adopt depends to a large extent on what objective one has set out to achieve. In this thesis we will work with the tight-binding description, or alternatively called lattice fermion model, as it is the method of preference for addressing materials with strong correlations between electrons from a model Hamiltonian perspective. The prototype of such a model Hamiltonian, designed to capture the essential physics of strongly correlated electrons, is the famous Hubbard model. The Hubbard model is given by the following equation

$$\hat{H}_{\text{HM}} = \sum_{ij} t_{ij} \hat{\psi}_{i\sigma}^{\dagger} \hat{\psi}_{j\sigma} - \mu \sum_i \hat{n}_i + U \sum_i \hat{n}_{i\uparrow} \hat{n}_{i\downarrow} \qquad \textbf{Hubbard Model} \qquad (1.34)$$

and here $\hat{\psi}_{i\sigma}^{\dagger}$ ($\hat{\psi}_{j\sigma}$) are second-quantized operators which create (annihilate) an electron at lattice site i with spin σ, where σ can take the values "↑" and "↓". The matrix t_{ij} represents the overlap integral of atomic wave functions on site i and site j. In the most simple cases one only considers finite overlap between nearest neighbor sites which is taken to be uniform, i.e. $t_{ij} \to t$. In general however the most important assumption is translational invariance $t_{ij} = t_{-i+j}$. The chemical potential μ controls the particle number, as $\hat{n}_i = \sum_\sigma \hat{\psi}_{i\sigma}^{\dagger} \hat{\psi}_{i\sigma}$ is the number operator.

The third term represents the repulsive Coulomb interaction between electrons and assigns an energy penalty of U to two electrons sitting on the same atomic site. Fermi statistics require these electrons to have opposite spin. This form of the interaction term is a substantial simplification as it only takes into account the Coulomb interaction of electrons at the same site. In general, for electrons in close proximity yet different atomic sites there is a repulsive Coulomb force as well, however the screening effect causes the longe-range part of the Coulomb interaction to be weak, which justifies the retaining of only on-site repulsion.

Despite its apparent simplicity, the above Hamiltonian is notoriously hard to solve. Nevertheless, advanced and often involved numerical as well as analytical techniques have achieved considerable progress in applying the Hubbard model to the physical phenomena in real materials. One general approach is to focus on the regime of very strong interaction, i.e. $U \gg t$. In this strong coupling regime doubly occupancy of the same site is very strongly disfavored. In particular at half filling Hilbert space is most conveniently organized by the number of doubly occupancies. The lowest energy sector is the one with no doubly occupied sites. As charge excitations are very expensive in terms of energy, the proper picture of this sector of Hilbert space is that of localized spins. The effective interaction between these localized

$$\vec{Q} = (\pi, \pi) \qquad\qquad \vec{Q} = (4\pi/3, 0)$$
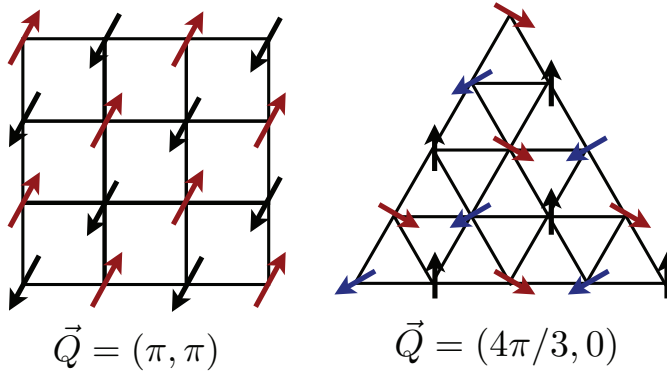
Figure 1.3: Illustration of spin configurations that represent the classical ground state of the Heisenberg spin model on the square lattice (left) and the triangular lattice (right). On the square lattice spins are anti-parallel on neighboring sites, realizing the collinear anti-ferromagnet. Due to frustration of the triangular lattice the spins do not order in a anti-parallel collinear pattern, but make an angle of $2\pi/3$ with one another.

spins is captured by the Heisenberg Hamiltonian which takes the form

$$\hat{H}_{\text{HB}} = \sum_{ij} J_{ij} \vec{s}_i \cdot \vec{s}_j \qquad \textbf{Heisenberg Hamiltonian} \qquad (1.35)$$

where the spin operators $\vec{s}_i$ are given in terms of fermions as

$$\vec{s}_i = \hat{\psi}^\dagger_{i\sigma} \vec{\sigma}_{\sigma\sigma'} \hat{\psi}_{i\sigma'}, \qquad (1.36)$$

where the the vector $\vec{\sigma}$ represents the spin Pauli matrices, i.e. $\vec{\sigma} = (\sigma^x, \sigma^y, \sigma^z)$. That the effective interaction between spins should have this form may be understood by considering virtual processes out of and back into the singly occupied subspace. If electrons on neighboring sites occupy opposite spin states, virtual processes with amplitude $\sim t^2/U \simeq J$ are allowed by the Pauli principle and electrons can lower their energy in this way. Hence, in the general case one has $J_{ij} = J = +|J|$ and the effective interaction is anti-ferromagnetic. A virtual process of this kind is also referred to as a superexchange process, and the Heisenberg Hamiltonian is alternatively named superexchange Hamiltonian. In strong coupling and at half filling the system is an insulator, as there are no charge excitations, and the Heisenberg Hamiltonian pertains solely to the magnetic state of the system. The canonical approach that leads

to an understanding of the magnetic ground state is to consider the electron spin $\vec{s}_i$ as a very large spin, i.e. $|\vec{s}_i| \gg 1$, and treat it a classical spin. The latter means that we disregard for the moment that it actually represents an operator acting on a finite dimensional Hilbert space, but instead picture it as a classical $O(3)$ vector pointing in any direction in space. Particularizing to the simple square crystal lattice, and keeping only nearest neighbor magnetic interactions ($J \sum \vec{S}_i \cdot \vec{S}_j$), it is straightforward to deduce that the (classical) energy on each bond is minimized by anti-parallel spin, i.e. $J\vec{S}_i \cdot \vec{S}_j = -JS^2$ if $\vec{S}_i = -\vec{S}_j$, S being the magnitude of the spin. On the square this leads to the anti-ferromagnetic spin state, as depicted in Fig. 1.3.

The situation is different for a different crystal lattice, the triangular lattice (see Fig. 1.3). Due to lattice connectedness it is not possible to have spins on all neighboring sites aligned anti-parallel consistently. This is an example of frustration: the energy cannot be simultaneously minimized on each and every bond. The solution to this problem is for the spins to arrange so as to optimally relieve the frustration, in this particular case by making angles of $2\pi/3$ with each other. This noncollinear but coplanar order is thus a consequence of frustration.

The example of the triangular lattice already hints at the key role the crystal structure plays in the manifestation of magnetism in real materials. Even more complicated behaviour is expected and observed for kagome lattice compounds, or compounds which approximately realize a kagome structure. The kagome lattice consists of corner sharing triangles, which directly results in a macroscopic degeneracy of (classical) magnetic ground states. From the triangular lattice we learned that on each triangle the spins are coplanar but make an angle of $2\pi/3$. For corner sharing triangles this does not fix all spins and a huge number of configurations satisfying the energetic constraints exist. This is reflected in thermodynamic quantities and leads to exotic phenomena such as spin-liquid behaviour.

Even though the pictorial representation of spins as classical arrows such as in Fig. 3.3 provides an intuitive understanding of the magnetism observed in materials, one should not forget that the electron spin is a quintessentially quantum mechanical object. The assumption of large spin, $|\vec{s}_i| \gg 1$, is not at all justified for the electron spin, which has length $1/2$. Quantum corrections need to be taken into account and the general recepy to do that is spin-wave analysis. Spin-waves are collective excitations on top of the ordered classical state, in the same way as lattice distortions (*phonons*) are collective modes corresponding to the ordered crystal. Depending on the lattice structure, quantum fluctuations may either give corrections to the classical state, or completely invalidate the classical description and necessitate new physical concepts. Away from half filling, when one cannot think of all sites as being occupied by precisely a single electron, hopping processes become possible again, as their will be empty sites (for either electrons or holes). In this case the Heisenberg Hamiltonian

needs to be supplemented with a hopping term

$$\hat{H}_{\text{DLU}} = \sum_{ij} t_{ij} \hat{P} \hat{\psi}_{i\sigma}^{\dagger} \hat{\psi}_{j\sigma} \hat{P} + \hat{H}_{\text{HB}}, \qquad \textbf{D}\text{oped } \textbf{L}\text{arge } \textbf{U} \text{ Model} \qquad (1.37)$$

and the projection operators $\hat{P}$ make sure that doubly occupied sites are excluded.

The most drastic simplification of the Hubbard model given in equation 1.34 is its single-band nature. Orbital degeneracy is however ubiquitous in real materials and neglecting the orbital degree of freedom of electron wave-functions can be a major distortion of reality. In some cases that may be legitimate and sufficient to capture the essential features, as for instance in many cuprates, where only the $d_{x^2-y^2}$ orbital is close to the Fermi level. In many cases however, in particular widely studied d-electron systems, orbital degeneracy is an unavoidable source of complicated behaviour.

A prime example of the relevance of orbital physics are the Mn and Co ions. The Mn may exist in a Mn^{4+} or Mn^{3+} valence state. In the latter case the t_{2g} orbital manifold contains three electrons and is separated from the the e_g orbitals by a cubic crystal field originating from the local octahedral oxygen environment. Hund's rule coupling aligns the three spins in the t_{2g} sector, effectively creating a larger $S = 3/2$ localized "core" spin, and putting the remaining electron in an e_g orbital. The splitting between e_g and t_{2g} is generally large, justifying the assumption of localized t_{2g} spins. This particular physical picture will reappear many times in the remainder of this thesis. Figure 1.4 schematically summarizes these considerations for d-electrons in a cubic environment.

A simple model Hamtiltonian that captures the essentials of an e_g electron interacting with a large localized spin is given by the Kondo-Lattice or Double-Exchange Hamiltonian,

$$\hat{H}_{\text{KLM}} = \sum_{ij} t_{ij} \hat{\psi}_{i\sigma}^{\dagger} \hat{\psi}_{j\sigma} + J_{\text{Kondo}} \sum_{i} \vec{S}_i \cdot \vec{s}_i, \qquad \textbf{K}\text{ondo } \textbf{L}\text{attice } \textbf{M}\text{odel} \qquad (1.38)$$

which explicitly couples an electron spin $\vec{s}_i$ to a "core" spin $\vec{S}_i$ on every site i. Even though this simplified version does not even take into account the orbital flavor of itinerant electron, it certainly derives from orbtal physics. This double-exchange model has proven very successful in particular in describing Mn based materials, where large J_{Kondo} leads to wide range of ferromagnetic metal in the phase diagram. The ferromagnetic tendency build into this model, as opposed to the anti-ferromagnetic interaction of the Heisenberg model, and the corresponding transition to a ferromagnetic metal is intimately related to the observed colossal negative magnetoresistance in these materials. The Kondo-Lattice model of equation (1.38) is at the heart of Part I of thesis. In Chapter 2 the Kondo-Lattice model will be discussed in more details
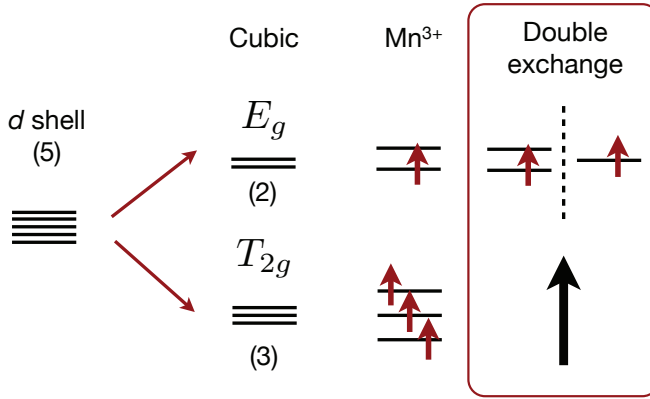
Figure 1.4: Illustration of the significance of electronic orbital degrees of freedom. The five-fold degenerate d-levels are split by the crystal field with cubic symmetry into an E_g and a T_{2g} manifold, two-fold and three-fold degenerate, respectively. In a manganese ion, three electrons occupy the T_{2g} manifold, with their spins aligned by Hund's coupling. The itinerant electron(s) in the E_g manifold effectively "see" a spin of length $3/2$, as is shown on the right in the red box. Depending on the strength of the coupling to this localized spin, the itinerant electrons can be either both aligned and anti-aligned, the latter costing energy, or can only be aligned (very strong coupling).

and different approaches to apply and study it in specific cases will be presented. Then, in Chapters 3 and 4 the Kondo-Lattice model and its derivative version, the Double-Exchange model will be the starting point for addressing the physics of interacting local moments and itinerant electons on the honeycomb and checkerboard lattice, respectively. It will be demonstrated how lattice topology and competing ordering tendencies (ferromagnetic vs. antiferromagntic) lead to a rich magnetic and electronic phase diagram.

Increasing the degree of complexity and taking full account of orbital degeneracy leads to an involved Hamiltonian with a number of distinct interaction terms. It is precisely such a Hamiltonian that will be the object of study in Part II of this thesis. Due to the spatial anisotropy of p- and d-orbitals, the overlap integrals between them depend both on the orbital and the *direction* of hopping, contrary to the s-orbitals. Hopping between a d_{xz} and a d_{xy} orbital is different in the x-direction than it is in the z-direction. Even more, electrons may also hop from one d_{xz} state to a d_{xy} state via ligand oxygen orbitals. Hence, the kinetic part of the Hamiltonian is now given

by

$$\hat{H}_{\text{MOK}} = \sum_{ij} t_{ij}^{\gamma\gamma'} \hat{\psi}_{i\gamma\sigma}^{\dagger} \hat{\psi}_{j\gamma'\sigma}, \qquad \textbf{M}\text{ulti } \textbf{O}\text{ribtal } \textbf{K}\text{inetic Hamiltonian} \qquad (1.39)$$

(summation of Greek indices implied), where γ (γ') denote the orbital degree of freedom. Taking the simple cubic lattice as an example, and assuming only nearest neighbor hopping, we must distinguish three different matrices, $t_{\hat{x}}^{\gamma\gamma'}$, $t_{\hat{y}}^{\gamma\gamma'}$ and $t_{\hat{z}}^{\gamma\gamma'}$. They represent hopping in the x, y and z directions, respectively, and are generally all different yet related by symmetry.

The repulsive on-site Coulomb interactions can be expressed by the following Hamiltonian

$$\hat{H}_{\text{C}} = U \sum_{i} \hat{n}_{i\gamma\uparrow} \hat{n}_{i\gamma\downarrow} + (U' - J/2) \sum_{i,\gamma<\gamma'} \hat{n}_{i\gamma} \hat{n}_{i\gamma'} - 2J \sum_{i,\gamma<\gamma'} \vec{s}_{i\gamma} \cdot \vec{s}_{i\gamma'}$$

$$+ J' \sum_{i,\gamma<\gamma'} \left(\hat{\psi}_{i\gamma\uparrow}^{\dagger} \hat{\psi}_{i\gamma\downarrow}^{\dagger} \hat{\psi}_{i\gamma'\downarrow} \hat{\psi}_{i\gamma'\uparrow} + \text{hc} \right) \qquad \textbf{C}\text{oulomb Hamiltonian} \qquad (1.40)$$

The various terms represent (i) the intra-orbital Coulomb repulsion, given by a Hubbard U, energetically penalizing two electrons occupying the same orbital with opposite spin quantum numbers, (ii) the inter-orbital Coulomb repulsion, given by $U' - J/2$, energetically penalizing two electrons on the same site but in different orbitals, (iii) Hund's rule coulpling, given by J, favoring alignment of electron spins occupying different orbitals, and (iv) the pair hopping term, given by J', changing the orbital flavor of a doubly occupied orbital.

Together with the kinetic term this interaction Hamiltonian constitutes a rather involved model of interacting electrons in solids. One may again assume very strong coupling and diagonalize the interaction Hamiltonian first, after which perturbatively including the hopping Hamiltonian generally yields a spin-orbital superexchange Hamiltonian. The latter will be $SU(2)$ invariant in the spin sector, but will depend in a non-symmetric way in the orbital degree of freedom, which is consequence of the intrinsic spatial anisotropy of the orbitals. An alternative approach is to employ a mean-field decoupling of the Coulomb Hamiltonian. This is the method of choice used in Part II of this thesis.

1.3 This thesis

Based on this general introduction to two important concepts, i.e. strong electron correlations and topology, we give a brief overview of the content of this thesis.

Part I of this thesis reports on a study of the Kondo-Lattice model, i.e. the model that describes interacting spins and electrons, on the honeycomb (chapter 3) and checkerboard (chapter 4) lattices. The honeycomb lattice is a two-dimensional bi-partite lattice, while the checkerboard lattice is two-dimensional spin-ice lattice and hence frustrated.

Part II deals with the question whether coupling between localized magnetic moments and itinerant electrons can lead to lattice Quantum Hall effects. The specific focus will be on looking into model systems which can exhibit Fractional Quantum Hall effects and the importance of electronic orbital degrees of freedom will be addressed.

Part III provides a symmetry classification of density wave orders emerging from electronic interactions, with the aim of obtaining insight into the possibilities of realizing interaction-induced topological states of matter. Chapter 8 will introduce the subject and will summarize the main results and conclusions of chapters 9 and 10. Chapter 11 summarizes once again from a slightly different perspective.

Part I

Magnetism and the Double-Exchange Model

CHAPTER 2

INTRODUCTION

2.1 Interacting electrons and spins

The Kondo lattice model (KLM) is probably the most celebrated starting point for the investigation of the interplay between localized spins and itinerant electrons [25]. It provides the canonical explanation for the Kondo effect and for the heavy-fermion behaviour observed in many materials [26]. Furthermore, the KLM and its cousin, the double-exchange (DE) model, have proven very powerful in understanding and explaining the properties of manganese-based oxides. The abundance of relevant literature on this subject is nicely summarized in [27,28]. The manganese ion Mn^{3+} provides perhaps the best example of a (large) local spin interacting with an itinerant conduction electron, which is a consquence of the orbital degeneracy present in $3d$ systems and the particular valence of Mn^{3+}.

Motivated by the search for topologically non-trivial states of matter, several groups have studied the itinerant KLM on frustrated lattices, such as the triangular or the pyrochlore one, and have shown that due to the strong geometrical frustration scalar-chiral types of magnetic ordering emerge [29–33]. In addition, the KLM has rather recently come into focus as a good framework to address unusual transport phenomena in spin ice pyrochlores [34–37].

All these distinct examples highlight the broad relevance and applicability of the KLM to a wide range of material classes.

2.2 Kondo Lattice and Double Exchange models

As already briefly introduced in chapter 1, the simplest Hamiltonian that captures the interaction of itinerant electrons and spins is given by

$$\hat{H} = \sum_{ij} t_{ij} \hat{\psi}_{i\sigma}^{\dagger} \hat{\psi}_{j\sigma} + J_{\text{Kondo}} \sum_{i} \vec{\mathcal{S}}_i \cdot \vec{s}_i, \qquad (2.1)$$

where $\vec{s}_i$ is the spin of the itinerant electron and $\vec{\mathcal{S}}_i$ represents the localized spin. The coupling may be anti-ferromagnetic (AFM) if $J_{\text{Kondo}} > 0$ or ferromagnetic (FM) if $J_{\text{Kondo}} < 0$. Writing the electron spin in terms of the creation and annihilation operators we arrive at the Hamiltonian

$$\hat{H} = \sum_{ij} t_{ij} \hat{\psi}_{i\sigma}^{\dagger} \hat{\psi}_{j\sigma} + J_{\text{Kondo}} \sum_{i} \hat{\psi}_{i\sigma}^{\dagger} \, \vec{\mathcal{S}}_i \cdot \vec{\sigma}_{\sigma\sigma'} \, \hat{\psi}_{i\sigma'}, \qquad (2.2)$$

which we may call the quantum Kondo Lattice model. In some cases it is important to include an explicit AFM coupling of the localized spins , i.e. $J_{\text{AFM}} \sum_{ij} \vec{\mathcal{S}}_i \cdot \vec{\mathcal{S}}_j$, in order to capture a strong AFM tendency caused by superexchange processes.

Generally, the electron spin will be coupled to a localized spin of arbitrary length S. In case S becomes large, it makes sense to approximate the local spin degree of freedom by a classical spin variable. The assumption of classical spins is justified in Mn based compounds, for instance, where the electron spin is coupled to a local spin of length $S = 3/2$, consisting of three t_{2g} spins perfectly aligned. In the rest of this chapter we will work from this assumption as well, but just for the moment we keep the theory general and write the combined action of electrons and spins as

$$S[\vec{\mathcal{S}}, \hat{\psi}^{\dagger}, \hat{\psi}] = S_{\text{s}}[\vec{\mathcal{S}}] + S_{\text{e}}[\vec{\mathcal{S}}, \hat{\psi}^{\dagger}, \hat{\psi}]. \qquad (2.3)$$

In this expression, the variables $\vec{\mathcal{S}}, \hat{\psi}^{\dagger}$ and $\hat{\psi}$ should be understood as spin and fermion coherent states. $S_{\text{s}}[\vec{\mathcal{S}}]$ is the Berry phase term of the spin coherent state path integral, encoding its quantum nature. Its specific form is irrelevant for our purposes as we will proceed to neglect quantum effects of the local spins. The electronic action is simply given by $S_{\text{e}} = \int_0^{\beta} d\tau [\sum \hat{\psi}^{\dagger} (\partial_{\tau} - \mu) \hat{\psi} + \hat{H}]$, with β the inverse temperature. With this action the partition function reads

$$Z = \int \mathcal{D}[\vec{\mathcal{S}}] \int \mathcal{D}[\hat{\psi}^{\dagger}, \hat{\psi}] \, e^{-S_{\text{s}} - S_{\text{e}}} \qquad (2.4)$$

Indeed, for large spins S it is justified to neglect the time depedence of the spin field and the Berry phase term S_{s}, and one is left with a bilinear fermionic action coupled

to a classical time-independent field. Such an action is similar in its structure to a Hubbard-Stratonovich decoupled Hubbard model with space-time dependent spin quantization axis [38, 39], and as a result may be used to describe a very broad class of phenomena. In the present case, where we model the interaction of electrons and spins, we can use the bilinearity of the action to calculate the fermionic trace exactly,

$$Z_{\text{e}} = \int \mathcal{D}[\hat{\psi}^{\dagger}, \hat{\psi}]e^{-\sum_{x,x'} \bar{\psi}(x)\hat{G}^{-1}(x,x')\psi(x')} = \text{Det}\left[\hat{G}^{-1}\right]. \qquad (2.5)$$

The determinant still depends on the spin fields and the full partition function requires an integration over the spin variables. For brevity we have collected all indices in the variable x. The full fermionic Green's function can be decomposed as

$$\hat{G}^{-1}(x, x') = \hat{G}_0^{-1}(x, x') + \hat{K}(x, x'), \qquad (2.6)$$

where $\hat{G}_0^{-1}(x, x')$ denotes the free electron Green's function (when they are not interacting with the classical spins), and $\hat{K}(x, x')$ denotes the Kondo coupling controlled by J_{Kondo}.

Calculating the full partition function is still a difficult problem, even though we can evaluate the fermionic trace in principle. In order to extract information from the partition function and calcualte observables it is necessary to employ approximation schemes. In the following we discuss two limits that will play a key role in the next two chapters. The first is the limit of weak-coupling, where we suppose that $J_{\text{Kondo}}/t \ll 1$. In this limit we may expand the fermionic determinant in the Kondo coupling and obtain an effective free energy for the spins. In the other limit, $t/J_{\text{Kondo}} \ll 1$, allows for a perturbative expansion in the inverse of the Kondo coupling, yielding an effectively spinless Hamiltonian, which depends on the classical spin variables. The latter can be studied by numerical Monto Carlo simulations. We note here that in the case of classical spins the sign of the Kondo coupling is immaterial.

2.2.1   Perturbation in J_{Kondo}/t

In case of weakly coupled conduction electrons and spins, $J_{\text{Kondo}}/t \ll 1$, we can expand the determinant $\text{Det}\left[\hat{G}^{-1}\right]$ in powers of the small parameter J_{Kondo}/t. An effective action, or free energy F, for the spins can be defined as $e^{-\beta F} = \text{Det}\left[\hat{G}^{-1}\right]$, from which it easily follows that

$$F = -\frac{1}{\beta} \ln \text{Det}\left[\hat{G}^{-1}\right] = -\frac{1}{\beta}\text{Tr}\left[\ln \hat{G}^{-1}\right]. \qquad (2.7)$$

Expanding this in the Kondo coupling strength and subtracting the bare electronic part one obtains the general expression

$$F - F_0 = F^{(2)} + F^{(4)} + \mathcal{O}(J_H^6).$$

(2.8)

The second order term represents the conduction electron mediated spin-spin interaction and is generally refered to as the Ruderman-Kittel-Kasuya-Yosida (RKKY) interaction. Its explicit form is given by

$$F^{(2)} = -\frac{1}{\beta}\text{Tr}\left[\hat{G}_0\hat{K}\hat{G}_0\hat{K}\right] = -J_{\text{Kondo}}^2 \sum_{\vec{p}} \chi_0(\vec{p})\vec{\mathcal{S}}(\vec{p}) \cdot \vec{\mathcal{S}}(-\vec{p})$$

(2.9)

where the sum is over all momenta and

$$\chi_0(\vec{p}) = \sum_{k,i\omega} \hat{G}_0(i\omega, \vec{k}+\vec{p})\hat{G}_0(i\omega, \vec{k})/(\beta N)$$

(2.10)

is the susceptibility, with N the number of lattice sites. Since we are dealing with classical spins at this stage, the saddle-point of the spin effective action is simply given by the maximum (or degenerate maxima) of the susceptibility.

In case the non-interacting electronic Fermi surface exhibits special structure, such as nesting at a particular wave-vector $\vec{Q}$, then this will be reflected in the susceptibility. A very illustrative example is the triangular lattice at filling $n = 3/4$, where the bare Fermi surface is hexagon inscribed in the Brillouin zone hexagon [30]. The Fermi surface is nested by three inequivalent momentum vectors which lead to logarithmically diverging susceptibility as function of temperature. The system gains the most energy by using all three degenerate order parameter components equally, as this fully gaps out the Fermi surface. In fact, the divergent susceptibility suggests that electrons will self-organize spontaneously into a spin-density wave composed of the three ordering vectors as a consequence of interactions. A mean-field decoupling of an interacting Hubbard model, where the mean field takes the place of the local moments, can be employed to test this hypothesis, which has indeed been confirmed in case of the triangular and hexagonal lattices [30, 40].

2.2.2 Perturbation in t/J_{Kondo}

If the coupling between conduction electrons and spins is very strong then it makes sense to focus on this Kondo coupling first and then proceed to ask how the itineracy of the electrons alters the picture. It is straightforward to convince oneself that the Kondo term mandates all electronic spins to be perfectly aligned with the local spins. As the sign of the Kondo coupling does not matter for classical spins, we focus on perfect alignment only without loss of generality.

The assumption of perfect alignment of spins is accounted for in a convenient way by defining the spin quantization axis locally on every site. For each site we then has the spin states $|\uparrow, (\theta_i, \phi_i)\rangle$ and $|\downarrow, (\theta_i, \phi_i)\rangle$, where θ_i and ϕ_i are the polar and azimuthal angles representing the spin $\vec{S}_i$. Transforming to the local quantization is achieved by the $SU(2)$ representation of a rotation of the z axis to $\vec{n} = (\cos\phi_i \sin\theta_i, \sin\phi_i \sin\theta_i, \cos\theta_i)$, which takes the form

$$U(\theta_i, \phi_i) = e^{-i\phi_i \sigma^z/2} e^{-i\theta_i \sigma^y/2}. \tag{2.11}$$

By construction this rotation operator diagonalizes the spin-conduction electron interactions,

$$U(\theta, \phi)\sigma^z U^\dagger(\theta, \phi) = \vec{S}(\theta, \phi) \cdot \vec{\sigma}, \tag{2.12}$$

at the cost of making the hopping processes spin-dependent in terms of the local quantization. Explicit expressions of the matrix U and the spin-conduction electron interaction $\vec{S}(\theta, \phi) \cdot \vec{\sigma}$ in terms of the angles (θ_i, ϕ_i) are

$$\vec{S}(\theta, \phi) \cdot \vec{\sigma} = \begin{bmatrix} \cos\theta & e^{-i\varphi}\sin\theta \\ e^{i\varphi}\sin\theta & -\cos\theta \end{bmatrix},$$
$$U(\theta, \phi) = \begin{bmatrix} \cos\frac{\theta}{2} & e^{-i\varphi}\sin\frac{\theta}{2} \\ e^{i\varphi}\sin\frac{\theta}{2} & -\cos\frac{\theta}{2} \end{bmatrix}. \tag{2.13}$$

With these explicit expression we can evaluate the hopping term in terms of the angles $\{\theta_i, \phi_i\}$. The spin-dependent hopping matrix $t_{ij}^{\sigma\sigma'}$, where σ and σ' label spin-up and spin-down in the local basis, becomes

$$t_{ij}^{\sigma\sigma'} = t_{ij} u_{ij}^{\sigma\sigma'} = t_{ij}\left(U^\dagger(\theta_i, \phi_i) U(\theta_j, \phi_j)\right), \tag{2.14}$$

where the angle-dependence is contained in the $u_{ij}^{\sigma\sigma'}$ functions, which can be read off from the matrix product as

$$u_{ij}^{\sigma\sigma} = \cos\frac{\theta_i}{2}\cos\frac{\theta_j}{2} + \sin\frac{\theta_i}{2}\sin\frac{\theta_i}{2}e^{i\sigma(\phi_j - \phi_i)}$$
$$u_{ij}^{\sigma\overline{\sigma}} = \sigma\left(\cos\frac{\theta_i}{2}\sin\frac{\theta_j}{2}e^{-i\sigma\phi_j} - \sin\frac{\theta_i}{2}\cos\frac{\theta_i}{2}e^{-i\sigma\phi_i}\right). \tag{2.15}$$

So far we have not made any approximations but just rewritten the problem in terms of basis states obtained from diagonalizing the spin-conduction electron interaction. Under the assumption that J_{Kondo}/t is very large, we can integrate out the spin-down states, as excitations into the spin-down sector of Hilbert space will be

heavily penalized energetically. Integrating out the spin-down or anti-aligned states yields an effectively spinless Hamtiltonian which reads

$$\hat{H} = \sum_{ij} t_{ij}(\theta_{ij}, \phi_{ij})\hat{\psi}_i^\dagger \hat{\psi}_j + J_{\text{AFM}} \sum_{i,j} \vec{\mathcal{S}}_i \cdot \vec{\mathcal{S}}_j, \qquad (2.16)$$

where

$$t_{ij}(\theta_{ij}, \phi_{ij}) \equiv t_{ij} u_{ij}^{\uparrow\uparrow} = t_{ij}(\cos\frac{\theta_i}{2}\cos\frac{\theta_j}{2} + \sin\frac{\theta_i}{2}\sin\frac{\theta_i}{2}e^{i(\phi_j - \phi_i)}). \qquad (2.17)$$

An AFM interaction between the localized spins is perturbatively generated at order $\sim t^2/J_{\text{Kondo}}$. This Hamiltonian, given in equation 2.16 is generally refered to as the Double-Exchange (DE) model. It describes electrons strongly interacting with localized spins in such a way that their spin is always tied to the local spin. The kinetic part favors FM alignment of the local spins, as the electrons gain kinetic energy, in such spin configuration. The AFM interaction, which generically models a perturbatively generated interactions between spins, or an intrinsic AFM interaction driven by superexchange, obviously favors anti-ferromagnetism. It is the competition between these two tendencies that is at the heart of the rich and sometimes unexpected physics observed and predicted for systems with spin-electron interactions.

The DE Hamiltonian still depends parametrically on the spins and in order to determine the spin-electron ground state or calcualte correlation functions, one must still integrate over all spin configurations in the partition function. For classical spins the path integral measure is simply an integration over the spin variables $\{\theta_i, \phi_i\}$, i.e.

$$\int \mathcal{D}[\vec{\mathcal{S}}] = \prod_i^N \left(\int_0^\pi d\theta_i \sin\theta_i \int_0^{2\pi} d\phi_i \right) \qquad (2.18)$$

Calculating the partition function or correlation functions exactly or even analytically is impossible and one must resort to numerical routines to extract information from the system. The method of choice is classical Monte Carlo where the spin configuration space is sampled according to standard Monte Carlo techniques [27, 28]. In these Monte Carlo simulations, the fermionic problem is diagolized exactly on a finite cluster, which amounts to calculating the fermionic trace in the path integral exactly. The fermionic trace then enters as a weight factor for the sampling of classical spin configurations.

CHAPTER 3

THE HONEYCOMB LATTICE MAGNET

3.1 Introduction

The physics of the KLM on non-frustrated lattices, such as the square and cubic one, has been studied extensively. In particular the limit of strong coupling and large localized moments, where the KLM goes over into the double-exchange (DE) model, is directly relevant to the colossal magnetoresistance effect in perovskite manganites [28,41–45]. In such cases, the competition between DE and antiferromagnetic (AFM) superexchange can lead to canted spin states or phase separation [28]. Although the honeycomb lattice is also bi-partite, it has the smallest possible coordination number for proper 2D lattices. That the honeycomb lattice can support physical phenomena fundamentally different from square lattices, is illustrated by recent Quantum Monte Carlo calculations [46], which identify a novel spin-liquid phase for the Hubbard model on the honeycomb lattice, a finding supported by analytical studies [47–49].

In this chapter, we investigate the consequences of the competition between AFM superexchange and ferromagnetic (FM) DE on the honeycomb lattice. We find that two exotic ground states exist between the trivial, fully FM and AFM phases. In the first, nearer to the FM state, the spins self-organize into FM hexagons that are coupled antiferromagnetically. Since the hexagonal rings form a *frustrated* triangular lattice, their order is reminiscent of the Yafet-Kittel state [50]. The competition between

isotropic magnetic interactions thus causes geometric frustration to emerge in a non-frustrated lattice.

For slightly stronger AFM interactions, we find the *exact* groundstate to consist of independent FM dimers containing one electron each. Apart from the requirement that the alignment of adjacent dimers be AFM, they are independent. The groundstate of this N-spin system therefore has a high degeneracy $\propto 2^{\sqrt{N}}$. While the macroscopic degeneracy $\propto e^{\alpha N}$ in (spin) ice is caused by the local symmetry of the frustrated tetrahedra [51, 52], our $\sqrt{N}$ exponent indicates the presence of an 'intermediate' symmetry – a symmetry between local and global [53]. It is remarkable that this highly degenerate groundstate manifold arises as an *emergent* effect in a Hamiltonian that itself does not have such a symmetry.

In many materials, the essence of the electronic structure is captured by interacting spins and electrons on a honeycomb lattice. Interactions between impurity magnetic moments on the honeycomb lattice of graphene have been intensely studied in a Ruderman-Kittel-Kasuya-Yosida (RKKY) framework [54–56] and using the KLM [57]. Going beyond RKKY is even more important in transition metal oxides, e.g., $Bi_3Mn_4O_{12}(NO_3)$ [58–62] or Li_2MnO_3 [63], with Mn ions on a honeycomb lattice.

3.2 Model and method

The Hamiltonian corresponding to the one-band DE model in the presence of competing AFM superexchange interactions on a honeycomb lattice is

$$H = -\sum_{\langle ij \rangle} t_{ij}(\hat{\psi}_i^\dagger \hat{\psi}_j + H.c.) + J_{\mathrm{AF}} \sum_{\langle ij \rangle} \vec{S}_i \cdot \vec{S}_j, \tag{3.1}$$

where $\hat{\psi}_i^\dagger$ and $\hat{\psi}_i$ are the fermionic creation and annihilation operators, respectively. In accordance with the DE scheme these fermions have their spin aligned with the on-site spins $\vec{S}_i$. The on-site core spins are treated as classical spins with $|\vec{S}_i| = 1$ and thus can be specified by their polar and azimuthal angles (θ_i, ϕ_i). Both sums are over nearest neighbors. Due to the alignment of electron spin to the core spins, the hopping amplitude depends on the direction of the core spins, $t_{ij} = t_0[\cos(\theta_i/2)\cos(\theta_j/2) + \sin(\theta_i/2)\sin(\theta_j/2)e^{-i(\phi_i-\phi_j)}]$ [28]. The strength of the AFM super-exchange is given by J_{AF} and all energies are in units of the hopping amplitude t_0. To guarantee an unbiased search for groundstate candidates, we employ a well-established hybrid method of exact diagonalization (ED) for the bilinear fermionic part of the Hamiltonian and Monte Carlo (MC) for the classical spins [28]. Each MC configuration is defined by a given core spin texture and Markov chains are generated by
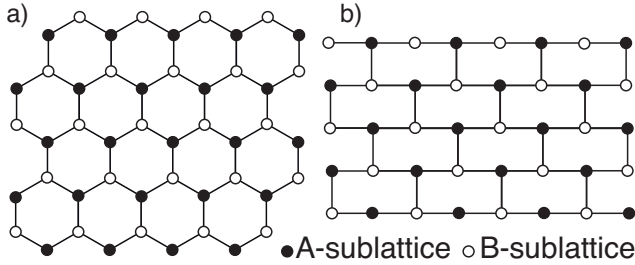
Figure 3.1: Schematic view of (a) the honeycomb lattice and (b) the brick-wall lattice having the same topology.

diagonalizing the fermionic problem for each configuration update. We also make use of the travelling cluster approximation (TCA), which has proven its validity and success in earlier studies on a similar class of models [43–45], to go to larger lattice sizes. We report here results based on calculations on an $N = 12^2$ honeycomb lattice, using a cluster of size $N_c = 6^2$. In the MC routine we use $\sim 10^4$ steps for equilibration and the same number of steps for thermal averaging. We focus on the case of a half-filled band, which refers to 1/2 an electron per site, equivalent to quarter-filling in the spinful problem. For selected parameter values, the MC procedure was further refined by an optimization routine that diminishes thermal fluctuations [64].

To identify the magnetically ordered states, we calculate the spin structure factor

$$S(\vec{q}) = \frac{1}{4N^2} \sum_{i,j} \langle \vec{S}_i \cdot \vec{S}_j \rangle e^{i\vec{q}\cdot(\vec{r}_i - \vec{r}_j)}, \tag{3.2}$$

where $\langle \ldots \rangle$ is a thermal average and $\vec{r}_i$ is the position space vector of site i. For a clear understanding of the real-space structure of the magnetic states it is helpful to look at $S(\vec{q})$ on a square geometry [see Fig. 3.1(b)]. A specific long-range ordering is expressed as the point in the Brillouin zone where the structure factor shows a peak. To analyze the electronic properties we compute the density of states (DOS) as $D(\omega) = \langle \frac{1}{N} \sum_k \delta(\omega - \epsilon_k) \rangle$ and approximate the delta-function by a Lorentzian with broadening γ.

3.3   Results

In the absence of super-exchange interaction ($J_{\mathrm{AF}} = 0$), the spins order ferromagnetically, as expected from the DE mechanism. The fermionic problem is then equivalent

to non-interacting spinless electrons on a honeycomb lattice, giving rise to a dispersion and DOS that is well-known from graphene [see Fig. 4.2(a)]. Introducing a small J_{AF} still leads to a FM ground state. At $J_{AF} \approx 0.14$, the FM state becomes unstable and gives way to a state with $S(\vec{q})$ peaked at $\frac{2}{3}(\pi, 0)$ (and the points related to it by symmetry). and with the peculiar four-peak DOS shown in Fig. 4.2(b). Real-space snapshots show that a superlattice formed of hexagons emerges at low temperatures T, as depicted in Fig. 3.3(a). This result was corroborated by zero-temperature optimization of the spin pattern. Spins within one hexagon are almost FM, the allowed energies for electrons moving on a six-site ring are $-2t_0 \cos 0 = -2t_0$ and $-2t_0 \cos \pi/3 = -t_0$, with twice as many states at $-t_0$, which gives precisely the DOS seen in Fig. 4.2(b). Coupling between the hexagons is AF, but since they occupy a frustrated triangular lattice, see Fig. 3.3(a), perfect AFM order is not possible. The hexagons instead are at an angle of $\approx 2\pi/3$, corresponding to the Yafet-Kittel state [50] well known for the triangular lattice, leading to the signals at $\frac{2}{3}(\pi, 0)$ in $S(\vec{q})$. Thus a geometrically frustrated triangular lattice emerges spontaneously from isotropic, competing interactions on the non-frustrated honeycomb lattice.

For $0.18 \leq J_{AF} \lesssim 0.25$, we find a state consisting of classical dimers. The dimers each consist of two spins aligned in parallel, they cover the lattice in such a way that the neighboring dimers are anti-parallel with respect to each other. In Fig. 3.3(b) and 3.3(c) we show two possible dimer configurations. In this spin texture, the electron kinetic energy reduces to that of uncoupled two-level problems, having only two eigenenergies $\pm t_0$. The DOS is therefore given by $D(\omega) = \delta(\omega - t_0)/2 + \delta(\omega + t_0)/2$, in excellent agreement with MC calculations [see Fig. 4.2(c)]. The dimer state can be understood as a trade-off between the FM ordering and the AFM ordering: the electrons are allowed to populate all the $-t_0$ levels (which is more favorable compared to AFM) and the spins are anti-parallel with respect to two of their nearest neighbors (which is more favorable compared to FM).

Interestingly, the dimer ground state of this quantum system has a macroscopic degeneracy, i.e., there is a macroscopically large number of ways to cover the lattice by dimers such that the neighboring dimers are anti-parallel. One way to see the degeneracy is to start covering lattice rows in Fig. 3.1(b) by dimers. It is easy to see that having fixed the dimer pattern in the 1st row, there are two independent ways of covering each subsequent row, giving $2^{\sqrt{N}-1}$ states for a N-site lattice. The fact that there is thus no long-range order along the y direction of the brick-wall is reflected in $S(\vec{q})$, which becomes finite along *lines* in momentum space, as in compass models [65–68]. In the 2D compass model, different degenerate configurations can be reached by flipping a row of spins. The corresponding $\sqrt{N}$ operators commute with the compass Hamiltonian and thus define an *intermediate* symmetry, i.e., between a local, gauge-like ($\propto e^N$) symmetry and global one (independent of N) [53]. The
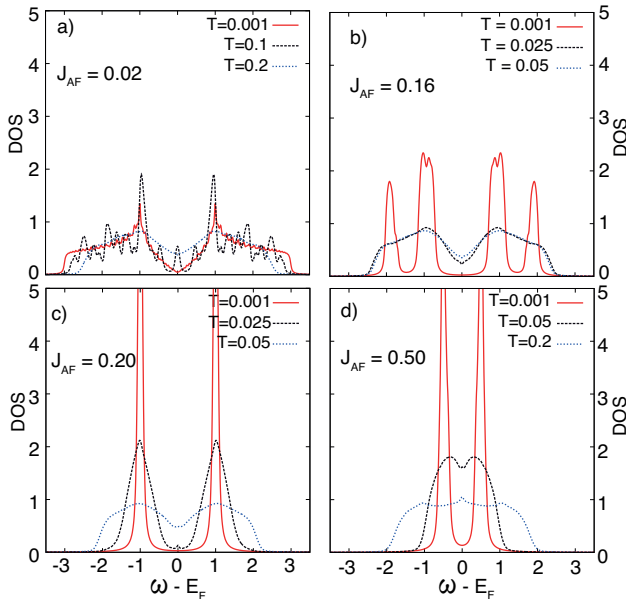
Figure 3.2: (a)-(d) DOS at low, intermediate and high temperatures for different values of J_{AF} ($\gamma = 0.04$). In (a) the $T = 0.001$ curve shows the DOS of free fermions on a honeycomb lattice in the thermodynamic limit. In (d) the $T = 0.001$ curve represents a gapped insulating phase, the seemingly finite DOS at E_F being a broadening effect. Except for the FM phase, all ground states are gapped.

magnetic order parameter that obeys the intermediate symmetry is consequently of nematic type. In the dimer state, the minimal symmetry operations involves translation of all spins in two adjacent zig-zag rows by one lattice spacing, $\sigma_{ij} \mapsto \sigma_{ij+1}$ [σ_{ij} is the spin at site (i,j)]. An example for two dimer configurations connected by such an operation is given in Figs. 3.3(b) and 3.3(c), where the second and third rows were shifted. However, this operator does *not commute with the Hamiltonian* Eq. (4.1), and the intermediate symmetry is thus rather a property that *emerges* in the system's ground state, similar to the case of striped phases at fractional filling in the regime of narrow bandwidth and small Jahn-Teller coupling in a model used for manganites [69]. This intermediate macroscopic degeneracy should lead to a large specific heat at low temperature.

For strong super-exchange coupling, there is a continuous way in which the dimer state can approach the AFM ordered state, captured by a canting angle θ [see Fig.
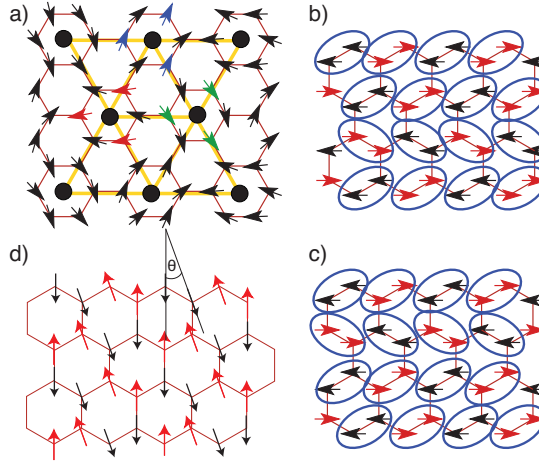
Figure 3.3: (a) Snapshot from MC simulations supplemented by optimization routines showing an emergent triangular lattice (black circles) formed by FM hexagons at $J_{AF} = 0.14$. Spins within each hexagon are almost FM, a small canting angle between groups of three is illustrated by shading. The colored spins illustrate the $2\pi/3$-angle order of the Yafet-Kittel state. Schematic view of, (b)-(c) two dimer states related by a translational symmetry (see text), and (d) a canted dimer state.

3.3(d)], which is the angle between the two spins forming a dimer in the pure dimer phase. The spins remain antiparallel to those of the neighboring canted dimers. In this way, the two-level dimer systems remain uncoupled. The hopping amplitude between the two spins in the dimer is renormalized by the DE mechanism to $t_0 \cos(\theta/2)$. The DOS for a canted dimer state is consequently given by $D(\omega) = \delta(\omega - t_0 \cos(\theta/2))/2 + \delta(\omega + t_0 \cos(\theta/2))/2$, as can indeed be observed in the DOS for $J_{AF} = 0.50$ shown in Fig. 4.2(d). The canted-dimer groundstate has a gap $\propto \cos(\theta/2)$ at the chemical potential, which shrinks as θ approaches π for $J_{AF} \to \infty$. At finite T, the two peaks widen and merge due to thermal spin fluctuations, leading to a metal with reduced band width, see Fig. 4.2(d). This canted state retains the macroscopic degeneracy inherent to the AFM dimer state discussed above – also this ordering is therefore of nematic type.
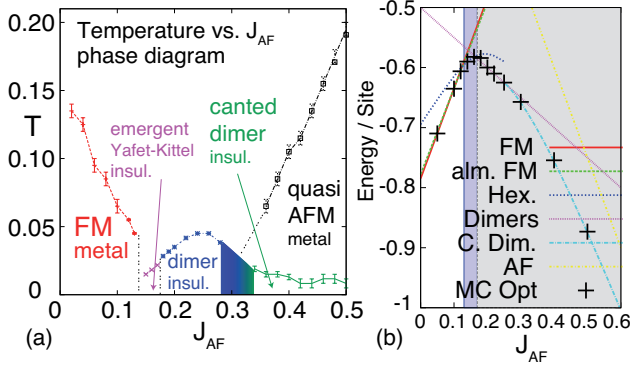
Figure 3.4: (a) T-J_{AF} phase diagram at half-filling obtained by MC for a 12×12 lattice. (b) The energy of the various states: "alm. FM" refers to a spiral with the longest wavelength supported by the lattice, converging to FM in the thermodynamic limit. Similar finite-size effects are reported in doped 1D and 2D lattices [70]. "Hex" denotes the emergent Yafet-Kittel order between hexagons depicted in Fig. 3.3(a), the energy was optimized with respect to the canting angle within the hexagons. "Dimers" and "C. Dim" are the highly degenerate FM and canted dimer states, and "AFM" denotes perfectly AFM order. The black crosses are energies obtained by unbiased MC and a subsequent energy optimization.

3.4 Discussion

Our results are in good agreement with elementary energy considerations. The energy per site varies as $3J_{AF}/2$ and $-J_{AF}/2$ for the FM and the dimer states, respectively. This would imply a phase transition at $J_{AF} \approx 0.15$, the FM state is indeed stable for $J_{AF} \lesssim 0.14$ and the dimers for $J_{AF} \gtrsim 0.18$. In between, the emergent Yafet-Kittel state, with a more complex energy dependence, is favorable, see Fig. 3.4(b). The energy per site for the canted dimer state is $-(2J_{AF} - \cos(\theta)J_{AF} + t_0 \cos(\theta/2))/2$. By differentiating with respect to the canting angle θ, one easily obtains that canting becomes favorable for $J_{AF} \geq 0.25$ and that the optimal energy is then given by $-3J_{AF}/2 - t_0^2/(16J_{AF})$. This is reflected in the behavior of the ordering temperature for the dimer state, which starts decreasing at $J_{AF} = 0.25$ [see Fig. 3.4(a)].

The results are summarized in Fig. 3.4. In the finite-T phase diagram Fig. 3.4(a), phase boundaries for the FM and quasi-AFM regions are obtained by determining the inflection point in the $\langle M \rangle(T)$ and $\langle \overline{M} \rangle(T)$ ($\overline{M}$ denotes staggered magnetization) curves. The onset of dimer and other phases is determined by tracking the temperature

dependence of the spin structure factor and the characteristic features in the DOS. Figure 3.4(b) compares the ground-state energies of the various phases and perfectly agrees with the unbiased numerical data, indicating that we have identified the ground states correctly.

In a full quantum treatment of the spin system additional quantum fluctuations can affect the stability of these ordered phases. Here one anticipates the FM building blocks (hexagons and dimers) to be robust as they are stabilized by a substantial DE energy, and the FM state remains an eigenstate of the hexagon (dimer) for quantum spins. The Yafet-Kittel ordering between the large total spins of the hexagons is expected to be more classical, and thus robust, than for $S = 1/2$, where it is found for $T \to 0$ [71]. If one can describe the magnetism of a dimer state by an effective NN AFM Heisenberg model, then this model remains the same if one performs the operation illustrated in Fig. 3.3. The emergent symmetry would thus commute with the effective low-energy Hamiltonian so that the corresponding degeneracies are preserved.

3.5 Conclusions

We conclude that the isotropic double-exchange model with competing super-exchange interactions on the *non-frustrated* honeycomb lattice has an unexpectedly rich phase diagram with exotic magnetic phases. In one of these, FM rings become the essential building blocks, which form a frustrated triangular lattice and are antiferromagnetically coupled. The stabilization of such frustrated spin states on a bipartite honeycomb lattice, without explicit frustration, is so far unique and an example of geometrical frustration emerging from competing interactions. Another novel phase consists of FM dimers ordered antiferromagnetically and has a $2^{\sqrt{N}}$ degeneracy. This is reminiscent of compass models, but in the present case the corresponding symmetry is not a property of the Hamiltonian given a priori, but rather a property that emerges in the systems ground state [65–69]. These phenomena are not only relevant in a theoretical context, immediately raising the question which other models share such features and how further residual interactions might affect the degeneracy, but pertains in particular to honeycomb manganese oxides, which form a promising class of materials to realize these novel types of highly frustrated states harboring macroscopic degeneracies.

CHAPTER 4

THE CHECKERBOARD LATTICE MAGNET

4.1 Introduction

The study of topologically non-trivial states of matter is one of the hottest topics in present-day condensed-matter physics. Topological states require a theoretical paradigm that goes beyond the concept of global symmetry breaking as laid out by Landau. It is remarkable that the theoretical predictions on the existence of various topologically ordered states have rather swiftly led to the discovery of an entirely new class of materials, the topological insulators [1, 3, 4, 72]. Recent pioneering experiments have confirmed the key signatures of non-trivial topology in certain materials, e.g. spin-momentum-locked undoubled Dirac fermions [9, 73, 74] and the Quantum Spin Hall (QSH) effect [7]. These topological insulators are time-reversal (TR) invariant generalizations of the first, much older, topological state of matter, the famous Integer Quantum Hall (IQH) states [16,75] that are induced by a magnetic field, which obviously breaks TR symmetry.

In a seminal work in 1988, Haldane established that a magnetic field is not required to induce states with the same topology as IQH states [76]. It was shown that adding complex hopping to a graphene-like Hamiltonian for electrons on a honeycomb lattice opens up topologically nontrivial gaps at the Dirac points, which yields

a topologically ordered, insulating state, referred to as a Quantum Anomalous Hall (QAH) state. An important feature of QAH states are edge channels, in which current can run only in one direction. This is in contrast to QSH states, where each edge has two channels carrying currents in opposite directions, one for each spin [77]. QAH states would thus allow very robust, dissipationless charge transport along edge channels, as backscattering would be completely suppressed. However, while signatures of QAH behavior have been reported in some compounds [78–80], the only QAH state so far reported has very recently been realized in 'molecular graphene', a nanostructure tailored to this purpose [81]. Other approaches suggested so far are spin-orbit coupled magnetic semi-conductors [82], spin-orbit coupled ad-atoms on graphene [83], or spin-polarized QSH states [77].

The experimental difficulty is mirrored by the frailty of theoretical mass-generating mechanisms for a graphene-like kinetic energy with a linear dispersion at the Fermi level. TR-symmetry breaking via (magnetic) order requires rather specific and strong longer-range Coulomb interactions [84], because the Dirac cones' vanishing density of states at the Fermi level renders interaction-driven ordered states energetically less favorable. QAH states can more readily be induced in models with a finite density of states [30, 32, 85], especially in cases of quadratic band crossings [86], as for instance found in the checkerboard lattice, which exhibit a weak-coupling instability [86–88].

We will show here that the ground state of itinerant electrons strongly coupled to localized spins on a checkerboard lattice is given by massless Dirac fermions or by a chiral QAH state, depending on parameters. The spin texture underlying the QAH state has a net ferromagnetic (FM) moment, flipping the FM polarization therefore allows both to induce the QAH state from Dirac fermions and to switch between ground-states of opposite chirality. This possibility to control an edge current by an external magnetic field is an attractive feature in the context of spintronics.

4.2   The itinerant checkerboard lattice magnet

We model the itinerant electrons coupled to localized core spins by a one-band double-exchange (DE) model with a competing antiferromagnetic (AFM) super-exchange interaction,

$$\hat{H} = -\sum_{\langle ij \rangle} t_{ij}(\hat{\psi}_i^\dagger \hat{\psi}_j + H.c.) + J_{\text{AFM}} \sum_{\langle ij \rangle} \vec{S}_i \cdot \vec{S}_j, \qquad (4.1)$$

where $\hat{\psi}_i^\dagger$ ($\hat{\psi}_i$) creates (annihilates) a fermion on site i. Our discussion will for simplicity first focus on infinite Hund's rule perfectly aligning the fermion spin to the localized spins $\vec{S}_i$, but the main results remain valid for finite and even weak coupling, as discussed later. We investigate here the checkerboard lattice, shown in Fig. 4.1(b),
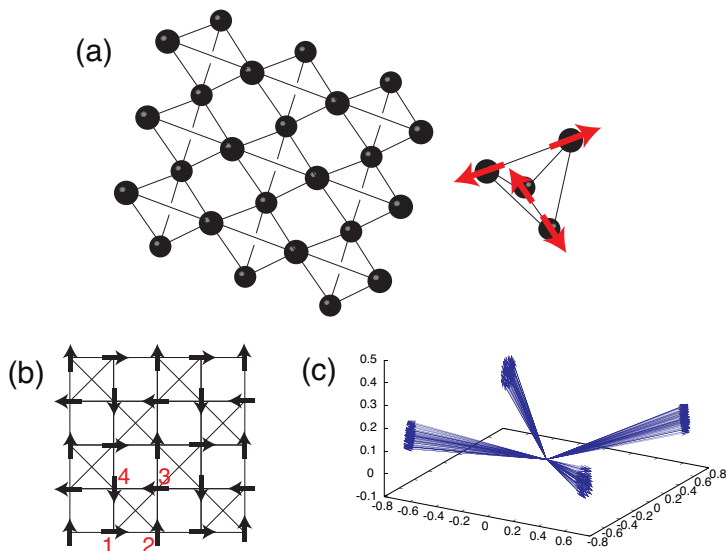
Figure 4.1: (a) Shows the arrangement of tetrahedra that gives rises to the hopping topology of the checkerboard lattice. Spins of the flux phase in the tetrahedral unit cell are also shown (b) Ordered pattern of spins in the coplanar flux phase represented on the projected checkerboard lattice. (c) Representation of the spins in the "umbrella" spin-chiral state, as obtained with MCMC+optimization for a 16x16 lattice with $J_{AFM} = 0.105$, where $\delta = 0.148$ compared to 0.141 as would be expected analytically; all spins have been translated to a single site.

whose first Brillouin zone (BZ) is given by $(k_x, k_y) \in \{|k_x + k_y| \leq \pi\} \cap \{|k_x - k_y| \leq \pi\}$. Both "straight" and "diagonal" edges are here included in the sum over $\langle ij \rangle$. This equivalence of the bonds arises when the chequerboard lattice is seen as reflecting the hopping topology of connected tetrahedra, see Fig. 4.1(a). Since such tetrahedra are building blocks in various frustrated structures, e.g. the pyrochlore lattice of quasi one-dimensional compounds [89], understanding their frustration is of high interest. We have verified that the results remain intact for weaker "diagonal" hoppings. Stronger diagonal hopping favors a Néel-type ordering, where the electron-spin system decouples into one-dimensional diagonal chains with van Hove singularities at the band edges.

In the absence of charge carriers or for strong AFM coupling $J_{AFM} \to \infty$, the Heisenberg term dominates. We may define a plaquette spin $\vec{S}_{\mathcal{P}}$ as the sum over all spins of a crossed plaquette

$$\vec{S}_{\mathcal{P}} = \vec{S}_1 + \vec{S}_2 + \vec{S}_3 + \vec{S}_4. \tag{4.2}$$

Then the Heisenberg term in the Hamiltonian can be expressed in terms of plaquette spins only, which gives

$$J_{\text{AFM}} \sum_{\langle ij \rangle} \vec{S}_i \cdot \vec{S}_j = \frac{J_{\text{AFM}}}{2} \sum_{\mathcal{P}} \vec{S}_{\mathcal{P}} \cdot \vec{S}_{\mathcal{P}} - J_{\text{AFM}} N \tag{4.3}$$

where N is the number of sites and the sum is over all crossed plaquettes $\mathcal{P}$. Clearly, the lowest energy is obtained whenever $\vec{S}_{\mathcal{P}} = 0$ for all crossed plaquettes. Since a macroscopic number of configurations fulfill these *local* constraints, the ground state manifold (GSM) is highly degenerate. For Ising spins, these local constraints, $\vec{S}_{\mathcal{P}} = 0$, are equivalent to the requirement of "two up-two down" spins on each crossed plaquette [90]. This is akin to the "two in-two-out" rule, the ice rule, that governs the magnetic energetics in three-dimensional spin-ice systems, which remain disordered down to the lowest temperatures. The spin-ice rule $\vec{S}_{\mathcal{P}} = 0$ on the checkerboard leads to an even larger class of ground states, if Heisenberg spins instead of Ising spins are considered, as is the case in the present work.

Doping with itinerant charge carriers can (partly) lift the macroscopic degeneracy of the GSM [91] because the kinetic energy competes with the ice-rule constraints due to the double-exchange mechanism: For classical on-site spins (with $|\vec{S}_i| = 1$), which are specified by polar and azimuthal angles (θ_i, ϕ_i), the effective hopping amplitude is modified by the relative spin orientation as $t_{ij} = t[\cos(\theta_i/2)\cos(\theta_j/2) + \sin(\theta_i/2)\sin(\theta_j/2)e^{-i(\phi_i - \phi_j)}]$ [27], where the bare hopping amplitude t is our unit of energy. For the uniform ferromagnet, the electronic bands correspond to those of

spinless free fermions on the checkerboard, given by the expressions

$$
\begin{aligned}
E_+(\vec{k}) &= 2t \\
E_-(\vec{k}) &= -2t(1 + \cos k_1 + \cos k_2)
\end{aligned}
\tag{4.4}
$$

where $k_i = \vec{k} \cdot \vec{x}_i$ ($i = 1, 2$) with $\vec{x}_i$ the Bravais lattice vectors. The density of states (DOS), $D(\omega) = \langle \frac{1}{N} \sum_k \delta(\omega - \epsilon_k) \rangle$, is shown in Fig. 4.2(a). In this work we consider here the average density of one electron per two sites, where the kinetic energy has the strongest impact. We use Markov Chain Monte Carlo (MCMC) simulations to anneal the classical spins, where the probability of a spin configuration is given by the free energy of the effective fermionic Hamiltonian, as obtained by exact diagonalization [27]. We have performed calculations on lattices with $N = 8^2$, 12^2, 16^2, and 20^2 sites. MCMC calculations were supplemented with an energy optimization in order to suppress thermal fluctuations [64] and complemented by an analytic weak-coupling analysis.

4.3 Results for half-filling

4.3.1 Massless Dirac fermions through lifting of the spin-ice degeneracy.

For large super-exchange coupling $J_{AFM} \gg 1$, the magnetic order is expected to belong to the highly degenerate GSM fulfilling $\vec{S}_{\mathcal{P}} = 0$. Our MCMC calculations show that the kinetic energy lifts this degeneracy completely and picks out the particular coplanar, but non-collinear, state that is schematically depicted in Fig. 4.1(b). Non-diagonal bonds connect orthogonal spins, while diagonal bonds connect AFM spins, effectively excluding them from the hopping term. Going around a square plaquette, the electrons pick up a phase $e^{i\pi}$, corresponding to a TR invariant flux of π, and this special "flux" phase has been shown to arise in models for high-Tc superconductors [92,93] and in the double-exchange models on the square lattice [94–97]. On the unfrustrated square lattice, it competes with the Néel state for strong J_{AFM} [94–96], but since it fulfills the ice-rules, it remains stable for $J_{AFM} > 0.12$ on the checkerboard lattice.

The DOS of the flux phase shows semi-metallic behaviour [see Fig. 4.2(b)] that originates from two Dirac points in the spectrum. Low-energy excitations are described by a relativistic Dirac equation, in full analogy with graphene [98]. The core-spin texture $\Lambda_i = (\theta_i, \phi_i)$ of the flux phase can be written as $\Lambda_i = (\pi/2, (i - 1)\pi/2)$ with $i = 1, 2, 3, 4$ [see Fig. 4.1(a)]. Even though the magnetic texture has a 4-site unit cell, the two-site electronic unit cell need not be enlarged as the system is electronically equivalent to a π-flux state. The electronic Hamiltonian, in the $(\psi_A^\dagger, \psi_B^\dagger)$ basis
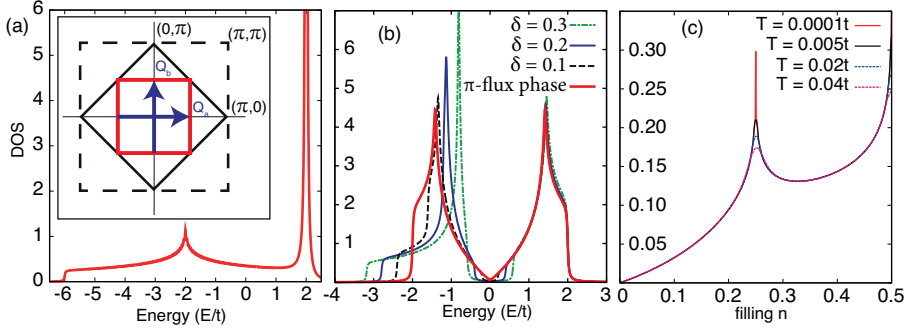
Figure 4.2: Electronic density of states of (a) the FM (spinless) phase, (b) the "flux" phase (in red) and spin-chiral umbrella phase for various δ (see text). The inset of (a) shows the BZ (black solid line) and the Fermi surface (red solid) of the non-interacting checkerboard lattice at quarter filling. The two vectors $\vec{Q}_a = (\pi, 0)$ and $\vec{Q}_b = (0, \pi)$ perfectly nest the Fermi surface. (c) Spin susceptibility $\chi_0(\vec{Q}_a) = \chi_0(\vec{Q}_b)$ for various temperatures.

may then simply be represented by a momentum dependent vector function $\vec{d}(\vec{k})$ and the three Pauli matrices $\vec{\tau} = (\tau^x, \tau^y, \tau^z)$ as

$$\mathcal{H}(\vec{k}) = \vec{d}(\vec{k}) \cdot \vec{\tau}. \tag{4.5}$$

where the compontents of the $\vec{d}$-vector are given by

$$
\begin{aligned}
d_x(\vec{k}) &= -\frac{t}{\sqrt{2}}(\cos(k_1 + k_2) + \cos k_1 + \cos k_2 - 1) \\
d_y(\vec{k}) &= -\frac{t}{\sqrt{2}}(\sin(k_1 + k_2) + \sin k_1 + \sin k_2) \\
d_z(\vec{k}) &= 0
\end{aligned}
\tag{4.6}
$$

Note that the explicit specification of the $\vec{d}$ required a gauge convention for the fictitious flux threaded through the square. Here we choose the convention of putting the phase $e^{i\pi} = -1$ on one single bond of each square. The electronic energy bands corresponding to this Hamiltonian are shown in Fig. 4.3(a). The two inequivalent Dirac points, or valleys, are located at $\vec{M}_\pm = (\pm\pi/2, 0)$.

Expanding around the Dirac points yields an effective low-energy Hamiltonian.

Defining the spinor $\Psi(\vec{q})$ as

$$\Psi(\vec{q}) = \begin{bmatrix} \psi_A(\vec{M}_+ + \vec{q}) \\ \psi_B(\vec{M}_+ + \vec{q}) \\ \psi_A(\vec{M}_- + \vec{q}) \\ \psi_B(\vec{M}_- + \vec{q}) \end{bmatrix} \tag{4.7}$$

we may write the Dirac Hamiltonian as

$$\mathcal{H}(\vec{q}) = \hbar v_F(-q_x \nu^z \tau^x + q_y \tau^y), \tag{4.8}$$

having chosen the set of Pauli matrices ν to operate on the valley degree of freedom and $v_F = \sqrt{2}t$. This is equivalent to graphene, with two valleys around which the electrons are described by the Dirac equation. In fact, one may define a set of Hamiltonians which connect the square lattice to both the π-flux phase and graphene [99]. If instead of the d_x-component specified above, we would have $d_x(\vec{k})[f] = -t(\cos(k_1 + k_2) + \cos k_1 + \cos k_2 - f)$, with $-1 \leq f \leq 1$, then $f = 1$ corresponds to a simple square lattice dispersion, while $f = 0$ corresponds to graphene. Obviously $f = -1$ gives the π-flux phase. For any value of f except $f = 1$ the electronic dispersion exhibits Dirac points. One important difference to graphene is that we have here no spin degeneracy, as the spin degree of freedom was integrated out by tying the fermion spin to the core spins.

4.3.2 Massive QAH Dirac fermions.

Having established that electronic kinetic energy selects a unique non-collinear pattern for the checkerboard double-exchange magnet, which has a graphene-like Dirac spectrum, we consider next what happens upon an increase of the itinerancy. Lowering J_{AFM}, we find that the magnetic interactions enforcing the tetrahedron rules are overcome by the electronic kinetic energy for $J_{\text{AFM}} \lesssim 0.12$. The transition is continuous and can be understood as a tilting of the flux-pattern out of the plane, forming an "umbrella". An example is shown in Fig. 4.1(c): the spins fall along four directions, whose projections onto the x-y plane mirror the "π-flux"-phase pattern, but there is an additional FM component along the z axis. The spins can be described using an Ising variable $s = \pm 1$ (which will turn out to correspond to a scalar spin chirality) and a continuous parameter δ giving the tilting along $\mp z$: $\{\Lambda_i^s(\delta)\} = (\pi/2 + \delta, s(i-1)\pi/2)$, where $i = 1, 2, 3, 4$ again runs around a crossed plaquette. A similar scenario, but with an 8-site unit cell and Chern numbers ± 2, arises on a square lattice with longer-range couplings when nearest-neighbor hoppings are strongly modulated [97].

The scalar spin chirality of the state is defined as

$$\chi = \sum_{\mathcal{T}} \vec{S}_i \cdot \vec{S}_j \times \vec{S}_k, \tag{4.9}$$

where the sum is over all triangles $\mathcal{T}$ of the checkerboard lattice, and $\vec{S}_i \cdot \vec{S}_j \times \vec{S}_k$ is taken in the counter-clockwise direction. The chirality as function of δ is plotted in the inset of Fig.4.3(b) for umbrella states $\Lambda^\pm$, it is $\chi \approx -s\delta$ for small δ. The label $\pm s$ decides the sign of the chirality for $\delta > 0$ and is related to a (counter-)clockwise rotation of the spin projection onto the x-y plane. The umbrella states, in addition to a continuous spin rotation symmetry, thus also break a discrete $\mathbb{Z}_2$ symmetry. As a discrete symmetry can also be broken at finite temperature in $2D$, chiral ordering may be possible even without long-range magnetic ordering [100].

Tilting the spins breaks TR symmetry for the electronic degrees of freedom, as fluxes through elementary plaquettes are related to the solid angle subtended by the spins surrounding the plaquette. Calculating the hoppings in the umbrella states, we find that hopping on the straight bonds is given by $t_1^s = e^{-si\pi/4}(1 - si \sin \delta)/\sqrt{2}$, with

$$\begin{aligned} |t_1^s| &= \sqrt{(1 + \sin^2 \delta)/2} \equiv t_1 \\ \phi_1^s &= \arctan(-s \sin \delta) - s\pi/4 \equiv \phi^s \end{aligned} \tag{4.10}$$

[see Fig. 4.1(c)]. In addition, hopping along the diagonal bonds is no longer vanishing but $t_2 = -\sin \delta$, independent of chirality. This leads us to the effective electronic Hamiltonian of general structure

$$\mathcal{H}^s(\vec{k}) = \epsilon(\vec{k})\tau^0 + \vec{d}(\vec{k}) \cdot \vec{\tau} \tag{4.11}$$

where τ^0 is the unit matrix and with the functions $\epsilon(\vec{k})$ and $\vec{d}(\vec{k})$ given by

$$\begin{aligned} d^0(\vec{k}) &= -t_2(\cos k_1 + \cos k_2), \\ d^3(\vec{k}) &= -t_2(\cos k_1 - \cos k_2) \\ d^1(\vec{k}) &= -t_1 [\cos \phi^s (1 + \cos(k_1 + k_2) + \cos k_1 + \cos k_2) \\ &\qquad \sin \phi^s (-\sin(k_1 + k_2) + \sin k_1 + \sin k_2)] \\ d^2(\vec{k}) &= -t_1 [\cos \phi^s (\sin(k_1 + k_2) + \sin k_1 + \sin k_2) \\ &\qquad \sin \phi^s (1 + \cos(k_1 + k_2) - \cos k_1 - \cos k_2)] \end{aligned} \tag{4.12}$$

The Hamiltonian above for the π-flux is recovered for $\delta = 0$, implying $\phi^s = \pi/4$ and $t_2 = 0$. This amount to a different gauge choice than the one leading to the expression

in equation (4.6). From the DOS [Fig. 4.2(b)] and the band structure [Fig. 4.3(a)], it is clear that finite $\delta \neq 0$ opens a gap for the Dirac cones. Since the hoppings are complex and the diagonal bonds have been activated, both TR and parity symmetries are broken, allowing a QAH state [101]. To establish that the gapped state is indeed topologically non-trivial, we calculate the Chern number of the occupied band (for a generalband n $C_n = \frac{1}{2\pi i} \oint_{\partial BZ} d\vec{k} \cdot \vec{A}(\vec{k})$, where $\vec{A}(\vec{k}) = \langle n\vec{k}|\nabla_{\vec{k}}|n\vec{k}\rangle$ is the Berry connection) and find $C = \text{sgn}(t_2)\text{sgn}(\sin 2\phi^s)$. Chirality and Chern number hence perfectly correlate and we observe that inverting the magnetic polarization $\delta \to -\delta$ flips both the spin chirality and the Chern number. The off-diagonal Hall conductivity as a function of chemical potential, obtained from Eq. (4.12) for $\delta = 0.3$, is shown in Fig. 4.3(b). Figure 4.3(c-e) shows the effect of non-trivial topology on the edge of the system: chiral edge states connect valence and conduction band. As can be seen by comparing Figs. 4.3(d) and 4.3(e), the direction of the edge currents can be reversed by inverting the spin chirality. Particularly appealing would be a system with a ground state still in the "massless" flux phase, but close to the transition to the QAH state, where a topological gap could be opened by a small magnetic field, and the direction of the edge currents could be manipulated by its orientation.

The observation that spin configurations of the umbrella states are continuously connected to the coplanar flux phase suggests that the electronic QAH state can be understood from the low-energy physics of the electrons at the Dirac points. In general, when the low-energy electronic theory is described by two inequivalent Dirac fermions there are four possible mass terms that may gap out the spectrum [102]. Three of those are compatible and correspond to a one-component charge density wave instability (sublattice potential) parameter and a two-component bond-density wave instability. The fourth possibility to open a gap is a time-reversal symmetry breaking perturbation. The latter case applies to the present situation, in full correspondence with the original proposal for the graphene lattice [76]. We will demonstrate this by analyzing, in the spirit of Ref. [76], the system in a presence of an external magnetic field B and then take the limit of $B \to 0$. Focusing on the low-energy theory of the spinless model, $\vec{q} = \vec{k} - \vec{M}_\gamma$ ($\gamma = \pm$), we introduce the magnetic field by way of a Peierls substitution $\hbar q_\alpha \to \hat{\Pi}_\alpha$ ($\alpha = x, y$), where $\hat{\Pi}_\alpha$ is the dynamical momentum whose components satisfy the commutation relation $[\hat{\Pi}_x, \hat{\Pi}_y] = ieB\hbar$. We obtain two independent Hamiltonians for the two Dirac points,

$$\hat{H}_\gamma = v_F(\hat{\Pi}_{1\gamma}\tau^x + \hat{\Pi}_{2\gamma}\tau^y) + m_\gamma\tau^z \qquad (4.13)$$

, which indeed has the structure of the relativistic Dirac equation in a magnetic field. As can be seen by comparing to Eq. (4.12), our mass term $m_\gamma = 2\gamma t_2$ is a direct consequence of finite $t_2 = -\sin\delta$, and thus of finite chirality $\delta \neq 0$. Operators $\hat{\Pi}_{1\gamma}$
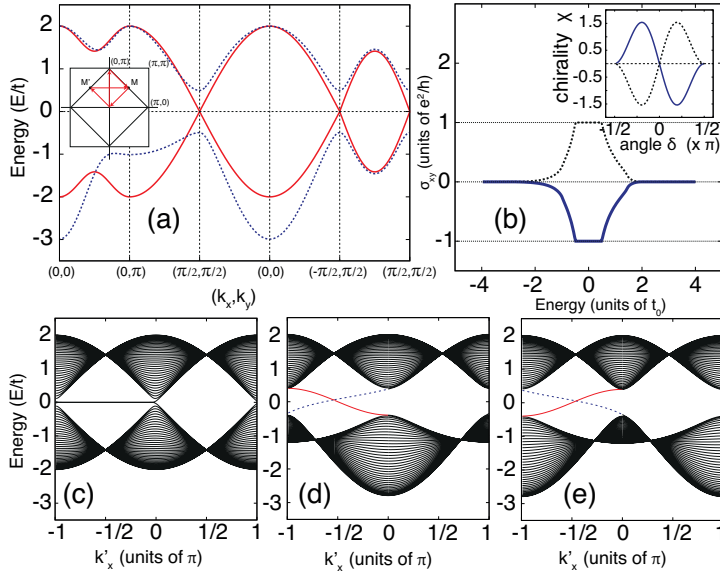
Figure 4.3: (a) The band structure of the gapless flux phase (red) and the insulating chiral phase (blue, $\delta = 0.3$) along a path in the Brillouin zone specified in the inset. (b) Quantized Hall conductivity in the chiral state ($\delta = 0.3$), when the Fermi level is in the gap, the quantized value depends on the chirality of the spin state. The inset shows the calculated chirality of the states $\Lambda^{\pm}$, where dashed (solid) corresponds to $+$ ($-$). (c-e) Spectrum of the flux phase calculated for a strip geometry, which explicitly shows the edge states at the open boundary. (c) π-flux phase ($\delta = 0.0$) exhibits edge states similar to graphene. (d,e) Chiral gapped phase ($\delta = 0.2$); chiral edge states connect valence and conduction bands. The states drawn with solid (dashed) lines lives on the top (bottom) edge. The chirality in (e) is reversed with respect to (d), the right- and left-moving states are consequently exchanged.

and $\hat{\Pi}_{2\gamma}$ are derived from $\hat{\Pi}_\alpha$ and satisfy the commutation relation

$$[\hat{\Pi}_{1\gamma}, \hat{\Pi}_{2\gamma}] = -i\gamma \sin(2\phi^s)eB\hbar \tag{4.14}$$

Relativistic Dirac fermions in a magnetic field are known to exhibit zero modes in their spectrum [103], which cause the charge density imbalance in the ground state, potentially leading to an integer QAH effect. Here, the zero modes have energy

$$E_{0,\gamma} = -\gamma m_\gamma \mathrm{sgn}(\sin 2\phi^s)\mathrm{sgn}(eB), \tag{4.15}$$

and the spectrum is asymmetric when m_+ and m_- have opposite sign. Following Haldane, we obtain the off-diagonal conductivity in the limit $B \to 0$, $\sigma_{xy} = \nu e^2/h$, where

$$\nu = \frac{1}{2}\mathrm{sgn}(\sin 2\phi^s)[\mathrm{sgn}(m_+) - \mathrm{sgn}(m_-)] = \mathrm{sgn}(t_2)\mathrm{sgn}(\sin 2\phi^s). \tag{4.16}$$

Hence, the gapped QAH umbrella state can be interpreted as Dirac fermions becoming massive, with masses of *opposite* sign, indeed, the $d^z(\vec{k})$ component of Eq. (4.12) has opposite sign at the two Dirac points $(\pm\pi/2, \pi/2)$. A sublattice potential, which also gaps out the Dirac fermions, would in contrast lead to equal masses, and the edge states would not cross the chemical potential.

4.3.3 Weak Hund's rule coupling.

Up to this point we have studied Hamiltonian in Eq. (4.1), which assumes a very strong coupling between localized and itinerant electronic spins.Here we discuss in more detail the case when the coupling between localized and itinerant spins, Hund's rule coupling, is finite. The Kondo Lattice Hamiltonian then reads

$$\hat{H} = -t \sum_{\langle ij \rangle, \alpha} (\hat{\psi}_{i\alpha}^\dagger \hat{\psi}_{j\alpha} + H.c.) - J_\mathrm{H} \sum_i \vec{S}_i \cdot \hat{\psi}_{i\alpha}^\dagger \vec{\sigma}_{\alpha\beta} \hat{\psi}_{i\beta}, \tag{4.17}$$

where the vector of Pauli matrices $\vec{\sigma}_{\alpha\beta}$ refers the spin of the itinerant electrons and i, j label the sites of the lattice. Half filling in the spinless case corresponds to quarter filling in the spinful case, where the the Fermi surface of free fermions on the checkerboard lattice is a square, as shown in the inset of Fig. 4.2, and where the DOS shows a van Hove singularity, see main panel of Fig. 4.2. We still consider classical spins ($\mathbf{S}_i \gg 1$), so that we can fix the magnitude S and absorb that into J_H. As was shown in the main text, in the infinite J_H limit the flux phase is stable over a very large range of parameter space. We now consider this phase from the finite J_H perspective. The spin configuration of the flux phase corresponds to two ordering vectors $\vec{Q}_a = (\pi, 0)$

and $\vec{Q}_b = (0, \pi)$ [95] and the magnetic state is hence generally referred to as $2q$ or double-Q ordering. As is shown in Fig. 4.2 of the main text, these ordering vectors perfectly nest the Fermi surface of the free-fermion checkerboard bands at quarter filling. When considering finite J_H the unit cell is quadrupled in the double-Q phase and we can write the order parameter as

$$\vec{S}(\vec{r}_i) = [\mathcal{S}_a \cos(\vec{Q}_a \cdot \vec{r}_i), \mathcal{S}_b \cos(\vec{Q}_b \cdot \vec{r}_i), 0]. \tag{4.18}$$

Since the double-Q phase is essentially a coplanar phase, we choose the z-component of the order parameter zero, wihtout loss of generality. $\mathcal{S}_a$ and $\mathcal{S}_b$ are equal in magnitude but can differ in sign. The vector $\vec{r}_i$ is the real space position of lattice site i. Observe that the collection of lattice positions $\{\vec{r}_i\}$ define a square grid that is spanned by elementary vectors $\vec{a}_1 = (1, 0)$ and $\vec{a}_2 = (0, 1)$ which necessitates the use of both ordering momenta $\vec{Q}_a$ and $\vec{Q}_b$. Due to the checkerboard topology of the hopping pattern the lattice has a basis and hence acquires sublattice structure. The Bravais lattice is spanned by $\vec{x}_1 = (1, 1)$ and $\vec{x}_2 = (-1, 1)$ and the momenta $\vec{Q}_a$ and $\vec{Q}_b$ are equivalent in the checkerboard lattice Brillouin zone, as may be seen in Fig. 4.2(a) (inset), i.e. the sum of ordering vectors is equal to a reciprocal lattice vectors, $\vec{Q}_a + \vec{Q}_b = \vec{G} \cong \vec{0}$, and same holds for all combinations of additions and subtrations. In particular it means that $\vec{Q}_a \cong \vec{Q}_b$ which inspires to simplify notation by setting $\vec{Q}_a = \vec{Q}_b \equiv \vec{Q}$.

In order to study the electronic Hamiltonian in the background of spin configuration in momentum space, the most convenient approach, we need to take into account the two-sublattice structure properly. In particular, the spin configuration may be specified by

$$\vec{S}_i = \begin{bmatrix} \vec{S}_{iA} \\ \vec{S}_{iB} \end{bmatrix} = \begin{bmatrix} \mathcal{S}_a \vec{u}_x \\ \mathcal{S}_b \vec{u}_y \end{bmatrix} e^{i\vec{Q} \cdot \vec{r}_i}, \tag{4.19}$$

where here i labels the unit cell, $\vec{r}_i$ denotes the corresponding lattice vector, and spin fields that live on each sublattice $\vec{S}_{i\xi}$, $\xi = A, B$ have been defined. The vectors $\vec{u}_{x,y}$ are unit vectors in the x- and y-direction respectively. For the electronic operators we write the two-component operators $\hat{\psi}_i^\dagger = (\hat{\psi}_{iA}^\dagger, \hat{\psi}_{iB}^\dagger)$, again i labeling the unit cell. The Hamiltonian, as compared to Eq. (4.17), then reads

$$\hat{H} = -t \sum_{\langle ij \rangle, \alpha} (\hat{\psi}_{i\xi\alpha}^\dagger \mathcal{H}_{ij}^{\xi\eta} \hat{\psi}_{j\eta\alpha} - J_\text{H} \sum_{i\xi} \vec{S}_{i\xi} \cdot \hat{\psi}_{i\mathcal{A}\alpha}^\dagger \vec{\sigma}_{\alpha\beta} \hat{\psi}_{i\xi} \tag{4.20}$$

where ξ and η both label sublattice indices. Substituting the spin configuration given

in Eq. 4.19 into the Hamtiltonian it takes the form

$$\hat{H} = \sum_{\vec{k},\alpha} \hat{\psi}_\alpha^\dagger(\vec{k})\mathcal{H}(\vec{k})\hat{\psi}_\alpha(\vec{k}) - J_H\mathcal{S}_a \sum_{\vec{k}} \hat{\psi}_{A\alpha}^\dagger(\vec{k})\sigma_{\alpha\beta}^x\hat{\psi}_{A\beta}(\vec{k}+\vec{Q})$$

$$- J_H\mathcal{S}_b \sum_{\vec{k}} \hat{\psi}_{B\alpha}^\dagger(\vec{k})\sigma_{\alpha\beta}^y\hat{\psi}_{B\beta}(\vec{k}+\vec{Q}). \tag{4.21}$$

As a consequence of translational symmetry breaking the unit cell is doubled and the dimension of the Hamiltonian and momentum dependent fermion operators is eight, due to sublattice and spin degrees of freedom and translational symmetry breaking. We may however use symmetry arguments to block diagonalize the Hamiltonian into 4×4 blocks. We can decompose the Hamiltonian as

$$\hat{H}(\vec{k}) = \hat{\Phi}_\mathrm{I}^\dagger\mathcal{H}(\vec{k})\hat{\Phi}_\mathrm{I} + \hat{\Phi}_\mathrm{II}^\dagger\mathcal{H}(\vec{k})\hat{\Phi}_\mathrm{II} \tag{4.22}$$

where the fermion operators $\hat{\Phi}_\mathrm{I}$ and $\hat{\Phi}_\mathrm{II}$ are given by

$$\hat{\Phi}_\mathrm{I} = \begin{bmatrix} \hat{\psi}_{A\uparrow}(\vec{k}) \\ \hat{\psi}_{A\downarrow}(\vec{k}+\vec{Q}) \\ \hat{\psi}_{B\uparrow}(\vec{k}) \\ \hat{\psi}_{B\downarrow}(\vec{k}+\vec{Q}) \end{bmatrix}, \quad \hat{\Phi}_\mathrm{II}^\dagger = \begin{bmatrix} \hat{\psi}_{A\downarrow}(\vec{k}) \\ \hat{\psi}_{A\uparrow}(\vec{k}+\vec{Q}) \\ \hat{\psi}_{B\downarrow}(\vec{k}) \\ -\hat{\psi}_{B\uparrow}(\vec{k}+\vec{Q}) \end{bmatrix}. \tag{4.23}$$

The reason for this is that we may rotate the spin state by an angle π about the x axis and have that followed by a rotation by π on the B-spins only about the z axis. These transformations exchange the two states while leaving the Hamiltonian invariant. In order to wrote down the Hamiltonian $\mathcal{H}(\vec{k})$ we need the hopping Hamiltonian on the checkerboard, which we write here as

$$\mathcal{M}(\vec{k}) = -t \begin{bmatrix} 2\cos(k_x+k_y) & 1+T_x^*T_y^*+T_y^*T_x+(T_y^*)^2 \\ 1+T_xT_y+T_yT_x^*+(T_y)^2 & 2\cos(k_x-k_y) \end{bmatrix}, \tag{4.24}$$

where we define for convenience $T_x = e^{ik_x}$ and $T_y = e^{ik_y}$. We will also need $\mathcal{M}(\vec{k}+\vec{Q})$, which reads

$$\mathcal{M}(\vec{k}+\vec{Q}) = -t \begin{bmatrix} -2\cos(k_x+k_y) & 1-T_x^*T_y^*-T_y^*T_x+(T_y^*)^2 \\ 1-T_xT_y-T_yT_x^*+(T_y)^2 & -2\cos(k_x-k_y) \end{bmatrix}. \tag{4.25}$$

The Hamiltonian $\mathcal{H}(\vec{k})$ is then specified by

$$\mathcal{M}(\vec{k}) = \begin{bmatrix} \mathcal{M}^{AA}(\vec{k}) & -J_{\mathrm{H}}\mathcal{S}_a & \mathcal{M}^{AB}(\vec{k}) & 0 \\ -J_{\mathrm{H}}\mathcal{S}_a & \mathcal{M}^{AA}(\vec{k}+\vec{Q}) & 0 & \mathcal{M}^{AB}(\vec{k}+\vec{Q}) \\ \mathcal{M}^{BA}(\vec{k}) & 0 & \mathcal{M}^{BB}(\vec{k}) & iJ_{\mathrm{H}}\mathcal{S}_b \\ 0 & \mathcal{M}^{BA}(\vec{k}+\vec{Q}) & -iJ_{\mathrm{H}}\mathcal{S}_b & \mathcal{M}^{BB}(\vec{k}+\vec{Q}) \end{bmatrix}, \qquad (4.26)$$

This Hamiltonian can be diagonlized and we obtain bands as shown in Fig. 4.4. The bands structure shows the Dirac points at quarter filling of the spinful system. We find the Dirac points emerging for infinitesimal J_{H}, indicating that the formation of this spin configuration will be due to a weak-coupling instability. Indeed, at quarter filling, the Fermi surface of fermions on the checkerboard lattice is nested by precisely the $\vec{Q}$ vector. In order to see whether the susceptibility indeed diverges we calculate the RKKY interaction between the classical spins mediated by the electrons. The RKKY interaction mediated by the electrons between the spins is given by $\Omega^{(2)} = -J_H^2 \sum_{\vec{p}} \chi_0(\vec{p}) S^\alpha(-\vec{p}) S^\alpha(\vec{p})$ and is thus determined by the spin susceptibility $\chi_0(\vec{p}) = -\sum_n \sum_{\vec{k}} \mathrm{Tr}[\hat{G}_0(\vec{k}, i\omega_n)\hat{G}_0(\vec{k}+\vec{p}, i\omega_n)]/(2N)$, where $\hat{G}_0(\vec{k}, i\omega_n)$ is the non-interacting electronic Green's function. The temperature dependence of $\chi_0(\pi, 0)$ and $\chi_0(0, \pi)$ is shown in Fig. 4.2, clearly showing divergent behaviour at quarter filling.

In the same way as above we can write down the order parameter for the umbrella magnetic ordering. We add a uniform magnetization in the z-direction and the order parameter becomes

$$\vec{\mathcal{S}}(\vec{r}_i) = \left[\mathcal{S}_a \cos(\vec{Q}_a \cdot \vec{r}_i), \mathcal{S}_b \cos(\vec{Q}_b \cdot \vec{r}_i), \mathcal{S}_c \right]. \qquad (4.27)$$

Here once again $\mathcal{S}_a$ and $\mathcal{S}_b$ are equal in absolute value but may differ in sign. The additional constraint now is $\mathcal{S}_a^2 + \mathcal{S}_b^2 + \mathcal{S}_c^2 = 1$. It is straightforward to write down the modification of the momentum space Hamiltonian

$$\delta H = \begin{bmatrix} -J_H \mathcal{S}_c & & & \\ & J_H \mathcal{S}_c & & \\ & & -J_H \mathcal{S}_c & \\ & & & J_H \mathcal{S}_c \end{bmatrix}, \qquad (4.28)$$

With this modification the Dirac points in the band structure become massive.

Our model is appropriate to describe a lattice of connected tetrahedra, see Fig. 4.1(a), e.g. as a two-dimensional projection of the three-dimensional pyrochlore lattice. This implies equivalent couplings on both "straight" and "diagonal" bonds. We find that weaker hopping on the diagonal bonds does not alter the physics qualitatively, while
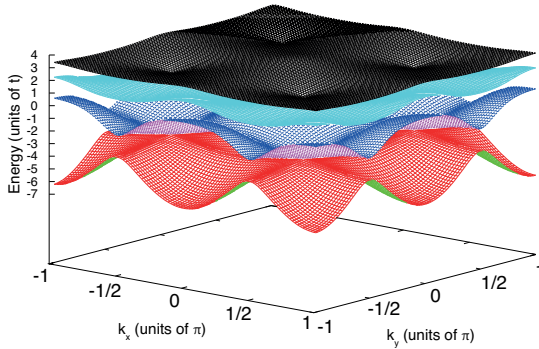
Figure 4.4: Spectrum corresponding to the finite Hund's rule coupling Hamiltonian 4.26, where the coupling constant is $J_H/t = 2$.

stronger diagonal hopping favors a Neel-type ordering, where the electron-spin system decouples into one-dimensional diagonal chains with van Hove singularities at the band edges.

4.3.4 Discussion and conclusions.

In conclusion, we investigated the interplay of itinerant electrons with a frustrated AFM spin background on the checkerboard lattice using Monte-Carlo methods and analytic approaches. The electron kinetic energy selects a unique magnetic ground state, the π-flux phase, from the macroscopically degenerate *spin-ice* manifold optimizing the AFM interactions. Its electronic states feature massless Dirac fermions. Both a magnetic field and slightly stronger kinetic energy can induce a spin chirality, from which the Dirac fermions inherit a topologically nontrivial mass.

The Kondo-lattice model on the checkerboard model thus provides a direct realization of Haldane's proposal for obtaining a QAH state [76]. QAH states on the checkerboard lattice have also been proposed as candidates for hosting an anomalous *fractional* quantum-Hall–like state [87, 104, 105]. This require nearly dispersionless bands; in the present scenario, additional longer-range hopping $-2t_3(\cos 2k_x + \cos 2k_y)$ can give a ratio of band gap vs. band width of ≈ 5 for $\delta = 0.3$. While this is considerably less than ratios achievable by tuning all parameters [87] or in t_{2g}-orbital systems [106, 107], it is comparable to e_g [106] systems or a square-lattice model [108].

Interestingly, the QAH state's chirality is coupled to a FM spin polarization and

the direction of the edge currents can thus be switched by a magnetic field, an alluring property for quantum spintronics applications. Such a magnetic field would also tend to suppress magnetic domains with opposite FM moment and chirality. However, magnetic domains with opposite uniform ferromagnetic component would also be very interesting, because the domain walls separating them are expected to provide one-dimensional chiral transport channels. In addition, recent work has shown that topological defects of the spin texture, e.g. $\mathbb{Z}_2$ vortices, carry electronic midgap states representing fractionally charged excitations [109].

4.4 Results for general filling

4.4.1 Introduction

In the previous section we have focused exclusively on a specific density of itinerant charge carriers, i.e. one electron per two sites. As advertised in the introduction, results we also obtained for more general, mostly commensurate, electron fillings and in this section we report and discuss these results.

As in the analysis so far, we assume that the localized spins are Heisenberg spins with fixed length and can therefore point in any direction. It is worth considering the case of Ising spins for the moment in order to get a feeling for the effect of doping charge carriers into the Coulomb phase. In particular, we will demonstrate that within our framework of finite cluster MCMC, the magnetism induced by electrons in the Coulomb phase is purely collinear. When the classical spins are restricted to be collinear and are subjected to the ice-rule constraint by assuming J_{AF} to be by far the largest energy scale, each spin configuration can be regarded as consisting of one-dimensional loops. This is a property of the Coulomb phase. As Ising spins may point either up or down, the loops emerge as a collection of spins pointing in the same direction and connected by bonds. Hence, a given spin configuration satisfying the spin-ice rules may be equivalently specified by a loop covering of the lattice [90]. These loops may be thought of as the extended degrees of freedom of the Coulomb phase. In the absence of electrons, properties of the peculiar magnetic Coulomb phase can be elucidated by studying statistical characteristics of loop coverings [90]. Electrons added to the systems of spins are constrained to move within these loops only, as hopping between anti-parallel spins is not possible. Consequently, the electronic energetics reduce to an effective one dimensional band dispersion. Specifically, a loop of length N has energy levels

$$E(k) = -2t\cos(ak), \quad k = j \times 2\pi/N, \quad \text{with } j = 0, \ldots, N-1 \qquad (4.29)$$

which implies that short loops have a very discrete set of energy levels. The energy

level $E = -2t$ always exists indepedent of loop length N and for a very low electron density it is expected that each loop only hosts one electron in precisely this level.

The problem of Ising spins coupled to itinerant electons has been addressed by Jaubert *et. al.* [91] who identified certain limiting cases where analytical arguments can be employed to predict properties of itinerant electrons in the Coulomb phase. Spins were explicitly taken to be Ising variables and the energy scales were chosen such that the electron kinetic energy was much smaller than the Hund's rule coupling between electrons and localized spins, which in turn was assumed to be much smaller than the anti-ferromagntic coupling between the spins. The ice-rule $\vec{S}_{\mathcal{P}} = 0$ was therefore a priori enforced. Building on the approach outlined so far in this chapter we investigate the question of what spin-electron ground states are stabilized as function of the anti-ferromagnetic coupling J_{AFM} and electron doping n. Employing the hybrid scheme of MCMC and exact diagonalization (ED) of the fermions allows for an unbiased test of the assertions and predictions that are based analytical arguments. Whereas the latter are valid for general system sizes but do not always take into account constraints imposed by the periodic lattice, the ED+MCMC approach is limited to finite clusters and manifestly respects lattice constraints.

To clearly distinguish this work from the previous preliminary studies, we briefly comment on the various parameters of the model. In this section we consider electron fillings $n = p/q$, by which we mean p electrons per q sites, and we study the DE model on the checkerboard lattice as function of the anti-ferromagnetic coupling J_{AFM}. We define two general regimes, the "Coulomb phase regime" for which $J_{\mathrm{AFM}} \gg t$, and the "itinerant regime", for wich $J_{\mathrm{AFM}} \ll t$. In the itinerant regime J_{AFM} may not be strong enough to enforce the ice-rules and resulting spin state may not be part of the set of loop coverings. As we have consistently done in this chapter so far, we consider Heisenberg spins $\vec{S}_i$, as opposed to Ising spins. Consequently we do not a priori restrict the spin states to consitute a collinear loop covering of the lattice even in the Coulomb phase regime. Any state (or degenerate collection of states), collinear or not, satisfying the ice-rules may be singled out by the electrons as the ground state (manifold). We have already observed in the previous section that at $n = 1/2$ electrons single out a non-collinear state as the ground state, which nevertheless respects the ice-rules. As is reflected in the DE model, we continue to assume a large energetic coupling between localized classical spins and itinerant electron spins.

In what follows we present results for commensurate fillings $n = 1/4$ and $n = 3/4$, as well as $n = 3/8$ and $n = 5/8$. The dispersion of the checkerboard lattice magnet is not particle-hole symmetric and hence n and $1 - n$ need to be treated separately. After having discussed these commensurate fillings we discuss the interesting intermediate fillings.
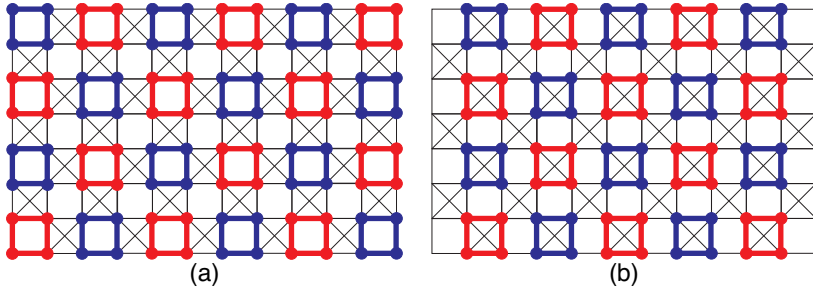
Figure 4.5: The 2 different collinear spin arrangements for the case of $n = 1/4$ and $n = 3/4$ (colours indicate up and down) ; (a) spins around a non-crossed square plaquette are FM, in such a way that the FM squares are decoupled from one another; (b) spin state found for $n = 1/4$ at small J_{AF}, FM squares are now crossed squares and hence the "up" (and "down") squares are no longer decoupled.

4.4.2   The $n = 1/4$ and $n = 3/4$ fillings

The most obvious filling to be considered beyond one electron per two sites is one electron per four sites. For large J_{AF}, the Coulomb phase regime, the spin state must obey the ice-rule constraint $\vec{S}_{\mathcal{P}} = 0$ and contribute an energy per site of $-J_{AF}$. This is confirmed by the numerical calculations, which consistently show a robust "loop-crystal" phase consisting of an ordered arrangement of loops of length 4 only. The term "loop crystal" is defined as a covering of the lattice of loops of equal length. The two flavors of loops, i.e. up and down loops, are arrangemed in an Neel type pattern, which is schematically shown in Fig. 4.5(a) The reason for the stability of this state is the discreteness of the electronic spectrum in case of a 4-loop. Applying the elementary formula (4.29), he eigenvalues are simply $\epsilon = \{-2t, 0, 0, 2t\}$ and with one electron per chain it can occupy the $E = -2t$ level. The density of states of this state is shown on Fig. 4.2(e). This turns out to be the energetically most favorable ground state even (and especially) for the case of $n = 3/4$, since the two additional electrons can occupy the zero energy levels and the total energy is not raised. For both fillings $n = 1/4$ and $n = 3/4$ we conclude from the numerical simulations that 4-loop crystal is the unique ground state in the Coulomb phase regime. This is consistent with the analytical result that at these fillings the lowest energy loop-crystal is the one with loop length 4.

When J_{AF} is lowered and we approach the itinerant phase, we find that the 4-loop state is very robust for $n = 3/4$ and only gives way to the fully FM state very close to $J_{AF} = 0$. The situation is very different for electron filling $n = 1/4$, due to the inher-

ent particle-hole asymmetry. At this electron filling, for small J_{AF}, ($J_{AF} \lesssim 0.13$), we find a spin state similar to the 4-loop crystal, but with the loops residing on the crossed plaquettes, see Fig. 4.5(b). One observes that in this way the loops of the same flavor (up or down) are no longer decoupled but form a true $2D$ extended structure which resembles the so-called square-octagon lattice. The spin configuration is therefore not a Coulomb phase loop covering of the lattice and explicitly breaks the ice-rule. Note that this configuration corresponds to two disconnected $2D$ lattices on which electrons can hop, one for up spins and one for down spins. Each. Each energy level is therefore (at least) twofold degenerate. The density of states of this state is shown in Fig. 4.2(e) and the energies are given by

$$
\begin{aligned}
E_1(\vec{k}) &= -1 - \sqrt{5 + 4\cos k_x \cos k_y} \\
E_2(\vec{k}) &= 0 \\
E_3(\vec{k}) &= -1 + \sqrt{5 + 4\cos k_x \cos k_y} \\
E_4(\vec{k}) &= 2.
\end{aligned}
\tag{4.30}
$$

A simple observation suffices to conclude that electronically this state is more favorable than the 4-loop crystal state, in which the electronic energy per site is $E/N = -t/2$ (energy per loop is $-2t$). By filling the lowest energy band $E_1(\vec{k})$ the energy per site $E/N = \int d\omega\, \omega D(\omega)$ ($D(\omega) = \sum_k \delta(\omega - E_1(\vec{k}))/N$) is strictly lower than $-t/2$ as $E_1(\vec{k})/4 \leq -t/2$, where the equality holds for $\vec{k} = (\pi, 0)$. This however comes at a magnetic cost, as the spin state is not a loop covering satisfying the ice-rules. A simple calculations shows that the magnetic energy per site is $+J_{AF}$, which is why this state is only stable for small J_{AF}. We can obtain the value of J_{AF} where the transition should occur by equating the two expression for the energy per site

$$
-\frac{1}{2}t - J_{AF} = J_{AF} + 2 \cdot \int_{-4t}^{-2t} d\omega\, \omega D(\omega)
$$

$$
\rightarrow J_{AF} = -\frac{1}{4}t - \int_{-4t}^{-2t} d\omega\, \omega D(\omega)
\tag{4.31}
$$

and from this we get $J_{AF} = 0.148$, which is close to the value obtained from numerical simulations. Elementary energetics are equally sufficient to conclude that the state depicted in Fig. 4.5(b) does not show up at $n = 3/4$. Electrons would fill the first three bands, leading to an electronic energy per site of $-t/4$, while the 4-loop crystal is already more favorable electronically and in addition satisfies the ice-rules. Our numerical simulations confirm that the extended spin state is absent from the ground state phase diagram at $n = 3/4$. In fact, we find no other intermediate state that interpolates between the Coulomb phase 4-loop covering and the fully developed
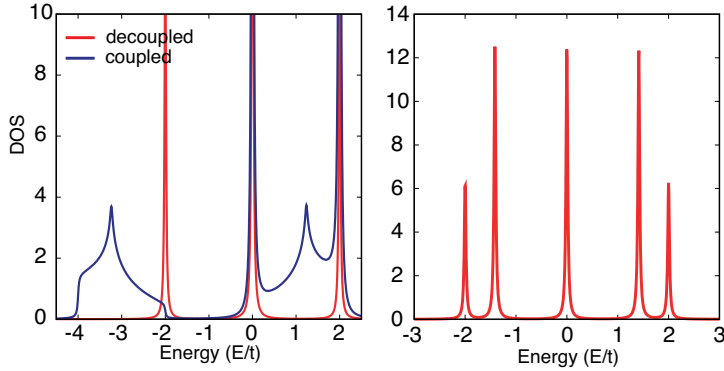
Figure 4.6: Density of states corresponding to the $l = 4$ and $l = 8$ loop states. (left) Plot of the densities of states of the two distinct spin configurations at filling $n = 1/4$. In red: the decoupled $l = 4$ loops with discrete energy levels shown in Fig. 4.5(a). In blue: extended $2D$ states originating from 4-loops on crossed plaquettes as shown in Fig. 4.5(b). (right) Density of states corresponding to all states made up of $l = 8$ loops presented in Fig. 4.8

ferromagnetic state at $J_{AF} = 0$. Evidence suggests that for any finite J_{AF} the 4-loop covering emerges as the ground state.

Before we continue to discuss the commensurate fillings $n = 3/8$ and $n = 5/8$, we explicitly state the observation that in the Coulomb phase regime ($J_{AF} \gg t$) the ground state is in fact a (collinear) loop covering over the lattice. Even though we started with Heisenberg spins, which for $n = 1/2$ arrange themselves non-collinearly in the presence of electrons, the ground state for $n = 1/4$ and $n = 3/4$ is collinear and since it satisfies the ice-rule it must be loop covering. Hence we see the first example of the itinerant electron-induced emergence of new degrees of freedom, the $1D$ loops with flavor index, out of a collection of Heisenberg spins.

4.4.3 The $n = p/8$ fillings

The next commensurate fillings we consider are part of the series $n = p/8$, where p is integer. The cases $p = 2, 4, 6$ we have already treated and hence we focus on $p = 3, 5$ here. We first consider $p = 3, 5$. In the Coulomb phase regime where $J_{AF} \gg t$ we find the ground state configuration, both for $n = 3/8$ and $n = 5/8$, to be an $l = 8$ loop crystal, i.e. a covering of the lattice by loops of length $l = 8$. Hence, similar to the fillings $n = 1/4$ and $3/4$ numerical evidence shows that the electrons induce a spin
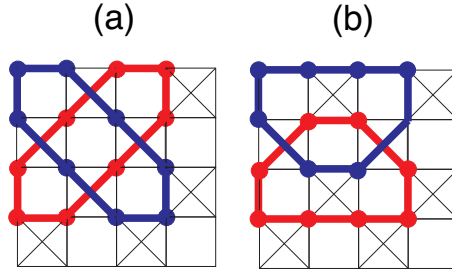
Figure 4.7: Two different realizations of $l = 8$ loops at fillings $n = 3/8$ and $n = 5/8$; (a) loop structure that we refer as type I, (b) loop structure of type II

configuration from loop covering manifold. On a perdiodic lattice the loop covering must be compatible with the lattice geometry, which leads to a loop crystal. A loop of length $l = 8$ has discrete energies $\epsilon = \{-2t, -\sqrt{2}t, -\sqrt{2}t, 0, 0, \sqrt{2}t, \sqrt{2}t, 2t\}$ causing the electronic energy per site to be $E/N = -t(1 + \sqrt{2})/4$ both for $n = 3/8$ and $n = 5/8$. Note that for these fillings the $l = 8$ loop crystal is energetically more favorable than the $l = 4$ loop crystal. From the numerical simulations we find two different realizations of the $l = 8$ loops, which are schematically depicted in Fig. 4.7. In both cases, Fig. 4.7(a) and Fig. 4.7(b), we oberve that two loops of different flavor necessarily come together and cannot be separated. The lattice is then covered by pairs of $l = 8$ loops with opposite flavor. These two realization of $l = 8$ loops on the checkerboard lattice differ from each other in the following way that is relevant to the question of degeneracy of ground states. Taking the pair of loops depicted in Fig. 4.7(a) we see that both a relfection in the x-axis and a relfection in the y-axis changes the flavor of the loops. The spin-down loop is converted into spin-up and vice versa. To fix nomenclature we refer to this pair of loop as type I. Instead, the pair of loops in Fig. 4.7(b) is mirror symmetric with respect to reflection in the y-axis. We comment on this disctinction in more detail below, when discussing the degeneracies of the $l = 8$ loop crystal ground state manifold.

The electron fillings $n = 1/8$ and $n = 7/8$ are special in the sense that at these fillings the $l = 4$ and $l = 8$ loops crystals are degenerate electronically. In case of the $l = 4$ loops the two out of every four loops have the electronic state at energy $\epsilon = -2t$ occupied, while for the $l = 8$ loops each loop has the $\epsilon = -2t$ level occupied. Even more, precisely at these fillings is possible for the system to choose two loops of length $l = 6$ and $l = 10$ instead of a pair of length $l = 8$. The number of loops is conserved, which means that electronically the energy does not change. In addition, such an arrangement is compatible with constraints imposed by the periodic lattice.

The question of ground state degeneracy becomes relevant for the fillings $n = 3/8$

and $n = 5/8$, as there is an emergent symmetry of the ground state manifold associated to the covering of the lattice with $l = 8$ loops. This emergent symmetry is related to the fact that for a pair of intrinsically connected $l = 8$ loops, one may invert the flavor index. How that works is best demonstrated by making use of Fig. 4.8(a,b). Fig. 4.8(a) shows a piece of an $l = 8$ loop crystal where the pairs of $l = 8$ have been arranged in a highly regular fashion. If one thinks of the loop covering as a covering of entire rows, then one realizes that once the first row is fixed (i.e. covered), there are two distinct choices for covering the second row. The choice which is alternative to Fig. 4.8(a) is depicted in Fig. 4.8(b). In Fig. 4.8(b) the flavor of the loops in the second row has been inverted, i.e. up and down loops have been flipped, and shifted so as to satisfy the ice-rule constraint. We can define the process of going fro Fig. 4.8(a) to Fig. 4.8(b) as *flipping* of one row of $l = 8$ loops. We observe that one may equivalently have flipped a column instead of a row. It is however crucial to realize that once a row (or column) has been flipped a sense of direction has been introduced and even though one can still flip individual other rows (columns), it is not possible to flip columns (rows) as they are no longer unambiguously defined. Consequently, the emergent symmetry is defined as the arrangement of rows (or columns) with respect to each other, i.e. the flipping, and connects two distinct states of the $l = 8$ loop ground state manifold. As it involves one entire row (or column) this is a symmetry operation intermediate between local and global in the same way as was observed in case of the honeycomb lattice (see earlier this chapter). This emergent intermediate symmetry hence causes degeneracy of the ground state manifold to scale exponentially with linear dimensions of system size. If N is the number of atomic sites, the degeneracy scales as $\sim 2^{\sqrt{N}}$.

We have already commented on the two distinct ways of forming pairs of inseparable $l = 8$ loops, which we labeled type I and type II for convenience. In the previous paragraph it was implicitly assumed that only loop pairs of type I cover the lattice (the focus on Fig. 4.8[a,b]). The observation remain valid however when allowing for both types to occur in a loop configuration. It is nevertheless important to make the distinction between the two, as $l = 8$ loops of type II immediately imply a sense of direction. This is most easily understood from Fig. 4.8(c,d). In both these schematic represenations of loop coverings both types of $l = 8$ loops occur. It is straightforward to convince oneself that once loops of type II occur, as in the second column of Fig. 4.8(c), the entire column must be of type II as it is impossible to connect loops of type I and type II in one column without violating the ice-rule constraint. Hence the orientation of loops of type II fixes a sense of direction. Consequently, only columns can be flipped with respect to Fig. 4.8(c), as demonstrated in Fig. 4.8(d) where the third column is flipped. In addition Fig. 4.8(c) shows that the number of columns (or altnatively rows) of type II $l = 8$ loops must be even for a

periodic lattice and the same is true for type I $l = 8$ loops. This follows from the fact that in the third column of Fig. 4.8(c), the $l = 8$ loop pair has changed flavor, without however the necessary translation by two lattice sites required for true flip. This implies that for a loop crystal that is consistent with the ice-rule to exist, the linear dimension of the system in one of the two orthogonal directions must be a multiple of 8, while in the other direction it must be a multiple of 4. In other words, if L_x and L_y are the number of atomic sites in the x, y directions, respectively, then $L_x = 8\tilde{l}_x$ and $L_y = 4\tilde{l}_y$ or vice versa.

The numerical calculations at filling $n = 3/8$ and $n = 5/8$ provide clear evidence for ground states that fall outside the class of Ising loop coverings of the lattice. While in case of Ising loops of fixed length, $l = 8$ in case of the filling presently under consideration, the loops are purely local objects and hence force electrons to be locally confined, we find a spin configuration that is fully extended in one linear dimension of the lattice, but nevertheless strictly degenerate with a local loop of length $l = 8$. The spin configuration is depicted in Fig. 4.8(e), where again red (blue) indicates spin up (down), i.e. pointing into the plane or out of the plane, but the black arrows are in plane spins which are orthogonal to the up and down spins, instead of (anti-)parallel. As a consequence of the orthogonality electrons can hop along the full one-dimensional chain, here extended along the y-direction. It is quite remarkable that the dispersion of electrons hopping along this particular one-dimensional chain does not have any momentum dependence and leads to flat bands, which are located precisely at the energies $\epsilon = \{-2t, -\sqrt{2}t, -\sqrt{2}t, 0, 0, \sqrt{2}t, \sqrt{2}t, 2t\}$. We thus conclude that even though this spin configuration is a departure from collinearity, it is nevertheless degenerate with it. We further observe that we may also define a "flip" for this extended $1D$ structure, which corresponds to inverting the in plane spins, as represented in Fig. 4.8(f).

To conclude the exposition of the results for $n = 3/8$ and $n = 5/8$, we focus on the itinerant regime where $J_{\text{AFM}} \ll t$. As was the case for $n = 1/4$ and $n = 3/4$ there is a clear difference between $n = 3/8$ and $n = 5/8$. For filling $n = 5/8$ we find no transition to a spin state that does not respect the ice-rule as $J_{\text{AFM}} \to 0$, except for the fully spin polarized FM state at $J_{\text{AFM}} \sim 0$. Instead, and in line with results for $n = 1/4$, we find that a spiral state is stabilized with spiral angle $\delta\phi = 2\pi/8 = \pi/4$. The spiral state is fully coplanar and breaks the ice-rule constraint. Due to the coplanar nature we may specify the state by setting all $\{\theta_i\}$ angles $\pi/2$ and write the
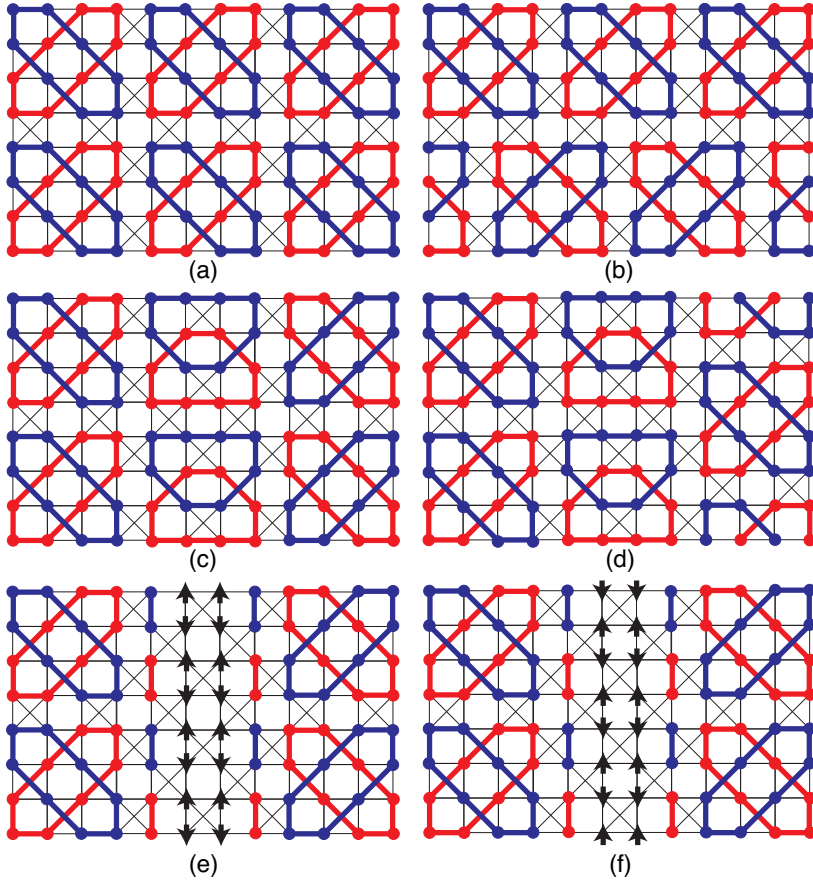
Figure 4.8: Different spin states found for $n = 3/8$ and $n = 5/8$; (a) shows a spin texture of $l = 8$ loops constructed by using only building blocks of type I; (b) spin texture of type I $l = 8$ loops where we have "flipped" the lower row with respect to (a); (c) spin texture of $l = 8$ loops that is built out of type I and type II chains, the latter are shown in column 2; (d) same as in (b) but here we flipped the 3rd column; (e) a spin state built out of type I and type III building blocks, the type III building blocks is a infinite $1D$ loop consisting of up and down spins (blue and red) and spins in the plane plane orthogonal to the up and down direction as shown in the 2nd column; (f) same as in (e) but where the black planar spin pairs have been flipped.

$\{\phi_i\}$ as

$$
\begin{aligned}
\phi_{(2i,2j)} &= \delta\phi(i+j) \\
\phi_{(2i+1,2j)} &= \delta\phi(i+j-1) \\
\phi_{(2i,2j+1)} &= \delta\phi(i+j-1) \\
\phi_{(2i+1,2j+1)} &= \delta\phi(i+j+1)
\end{aligned}
\tag{4.32}
$$

where (i,j) label the sites in the x and y direction respectively.

4.4.4 The intermediate fillings

Until now we have focused on the commensurate fillings $n = p/8$, whith $p = 1, 2, 3, 5, 6, 7$ and found from numerical calculations that in the Coulomb phase regime the spin ground states belong to the set of loop coverings of the lattice. It is intriguing to depart from commensurability and look at electron densities which interpolate between the commensurate densities. Here we will present numerical results obtained for a specific density region, which is $\frac{1}{4} \leq n < \frac{3}{8}$, and comment on densities $\frac{1}{4} \leq n < \frac{3}{8}$. As we have observed the ground states to be loop coverings of the lattice at commensurate fillings, it is natural to first consider the question which of the loop crystals would be favored at intermediate fillings if the choice was only between them. It is a simple matter to work out the energy per site $\epsilon_i(n)$ for loops of length $l = i$ $(i = 4, 8)$ as function of filling. The two loop crystals are degenerate up to filling $n = 1/8$, where the $l = 4$ loop crystal becomes lower in energy. At filling $n = 1/4$ all $-2t$ levels are filled for the $l = 4$ loops, while for $l = 8$ loops we may keep filling the $\epsilon = -\sqrt{2}t$ levels up until filling $n = 3/8$, after which the energy per site can not be further decreased by adding electrons. This can be more precisely summarized as

$$
\begin{aligned}
0 \leq n < \frac{1}{8} \qquad & \epsilon_4(n) = \epsilon_8(n) = -2tn \\
\frac{1}{8} \leq n < \frac{1}{4} \qquad & \epsilon_4(n) = -2tn, \quad \epsilon_8(n) = -\frac{1}{4}tn - \sqrt{2}t\left(n - \frac{1}{8}\right) \\
\frac{1}{4} \leq n < \frac{3}{8} \qquad & \epsilon_4(n) = -\frac{1}{2}t, \quad \epsilon_8(n) = -\frac{1}{4}tn - \sqrt{2}t\left(n - \frac{1}{8}\right) \\
\frac{3}{8} \leq n < \frac{1}{2} \qquad & \epsilon_4(n) = -\frac{1}{2}t, \quad \epsilon_8(n) = -\frac{1}{4}t(1 + \sqrt{2}),
\end{aligned}
\tag{4.33}
$$

and these density dependencies are graphically represented in Fig. 4.10(a) by the green and blue solid lines. We stress that in the Coulomb phase regime, when spin configurations are loop coverings, all these relations are particle-hole symmetric in the sense that filling n yields the same results as $1 - n$. With respect to the range

$\frac{1}{4} \leq n < \frac{3}{8}$ Fig. 4.10(a) shows that energies per site of the $l = 4$ loops and the $l = 8$ loops may be connected by a straight line which lowers the energy with respect to both single loop length crystals. This Maxwell construction indicated that it is more favorable to mix loops of length $l = 4$ and $l = 8$ in the intermediate region. A mixture of loops of length $l = 4$ and $l = 8$ respects all lattice constraints, as two $l = 8$ loops may be locally converted into four $l = 4$ loops. This was also noted in Ref. [91]. Schematically the coexistance of both loop lengths is represented in Fig. 4.9(a,b). The local conversion of loops may be understood from energetics by starting from two $l = 8$ loops and removing one electron. Keeping the two $l = 8$ loops and depopulating one $\epsilon = -\sqrt{2}t$ level is then more favorable than creating four $l = 4$ loops and populating the $\epsilon = -2t$ levels and one $\epsilon = 0$ level. Removing another electron shifts the balance towards the conversion into $l = 4$ loops. Consqently, the conversion process is connected to the removal or addition of two electrons and hence a total charge of $2e^-$.

It is interesting to observe that the ground states found from unbiased MC simulations are indeed mixtures of loops of length $l = 4$ and loops of length $l = 8$. Fig. 4.10(a) shows that the energy per site obtained from numerical calculations is precisely on the line interpolating between the two loop crystals. Monte Carlo snapshots confirm that spins states are mixtures of both loop states. Below we will discuss this "phase separation" and ground state degeneracies related to it in more detail. Due to the observed symmetry around half filling the conclusions hold for $\frac{5}{8} \leq n < \frac{3}{4}$.

We have already mentioned that for $n = 1/8$ the spin states consisting of loops of length $l = 8$ and $l = 4$ are degenerate. Even more, we observed that in principle two $l = 8$ loops may be converted into loops of length $l = 6$ and $l = 10$, for which there exists a consistent embedding into the periodic lattice. For the fillings below $n = 1/8$ the $l = 8$ and $l = 4$ loop coverings remain degenerate as decreasing the amount of electrons amounts to depopulating the $\epsilon = -2t$ energy levels. In principle any loop configuration that is compatible with the lattice constraints and has the property that there are more loops than electrons is energetically equivalent.

4.4.5 Summary of results

We now summarize some of our key results.

A first key result is the fact in the Coulomb phase regime, where the magnetic energy of the localized spins enforces the ice-rule constraint in the spins, we find the spin states at general filling n to be loop coverings of the lattice. The loops are $1D$ collinear chains of spins as up and down spins are disconnected from each other in the sense that electrons cannot hop between them. This is different from the specific filling $n = 1/2$, where spins organize in a coplanar orthogonal state leading to an intrinsically $2D$ electronic state [110]. We thus observe that classical Heisenberg
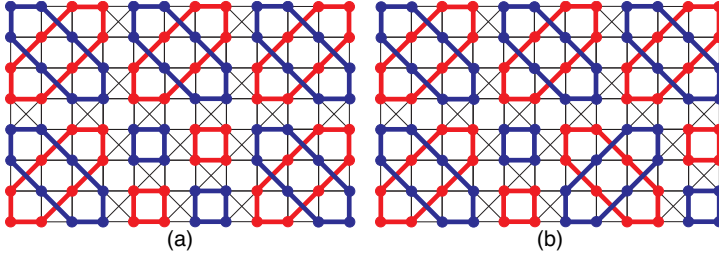
Figure 4.9: Examples of patches of the collinear spin arrangements found for fillings in between $n = 1/4$ and $n = 3/8$ (and also $n = 5/8$ and $n = 3/4$), (a) two 8-loops have been converted into 4 4-loops, (b) a local flip has been performed to switch the positions of the adjacent 4-loops and 8-loops: one example of the freedom to distribute the 4-loops.

spins behave effectively as Ising spins on a checkerboard lattice when coupled to electrons. Fig. 4.10(a) corroborates this observation graphically by showing that the energy per site obtained from MC simulations indeed matches the energies per site of the $l = 4$ and $l = 8$ loop crystal states. For pure AFM (classical) spin models on the checkerboard lattice, the ground state manifold is infinitely degenerate. All states that satisfy the ice-rule are energetically equivalent. In case of Ising spins the set of ground states is given by all loop coverings of the lattice, and for Heisenberg spins such as considered here the degeneracy is even larger. When coupling the spins to electrons we observe that this degeneracy is lifted, to an extent which depends on filling. It was already reported that for $n = 1/2$ a unique spin configuration is selected which minimizes the electronic energy while respected the magnetic ice-rule. The same degree of degeneracy lifting is found at $n = 1/4$ (and $n = 3/4$), where the $l = 4$ loop state is formed. This constitutes a unique state in the same way as the Neels state is the unique ground state of the AFM nearest-neighbor Heisenberg model on the square lattice. The situation is different for the commensurate filling $n = 3/8$ (and $n = 5/8$) which leads to $l = 8$ loop states. Here we found the degeneracy to be proportional to linear system size (square root of number of atomic sites), as there exists an emergent "symmetry" operation indermediate between local and global. For electron densities between $n = 1/4$ and $n = 3/8$ where the mixture of $l = 4$ and $l = 8$ loops was found the degeneracy is even larger as the loop conversion is a purely local process. This restores an extensive degeneracy of ground states for these fillings which comment on more specifically below. For electron densities $n = 1/8$ and smaller, where the $l = 4$ and $l = 8$ loops are fully degenerate, the ground state degeneracy is bounded from below by the degeneracy of the $l = 8$
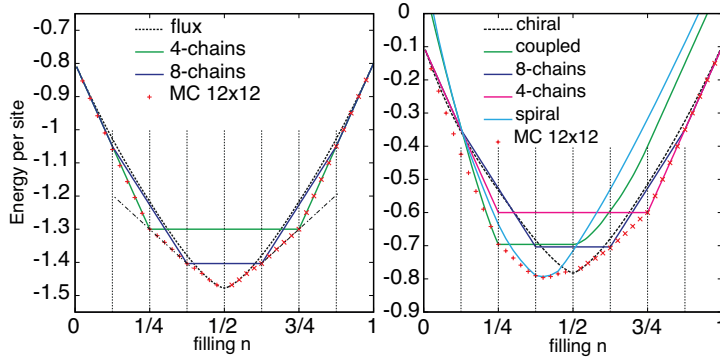
Figure 4.10: Energy per site for two different values of J_{AF}, (a) $J_{AF} = 0.8$; (b) $J_{AF} = 0.1$. (a) Here the magnetic phases are dominated by the super-exchange interaction and we find the 4-chains, 8-chains and the flux phase (the latter at $n = 1/2$), (b) for small J_{AF} new phases show up only for $n < 1/2$ that do not have magnetic energy $-J_{AF}$ per site; the electronic spectra have genuine $2D$ character. MC results are shown for 12x12 lattice.

loop crystal. Ground states which are arbitrary mixtures of $l = 4$ and $l = 8$ loops are energetically equivalent, the ratio between the two types of loops is however not density controlled. In addition, for very low densities, other configurations become accessible, as long as the number of loops exceeds the number of electrons and the spin configurations respects constraints imposed by the lattice structure. A third key result is the identification of spin states that are stabilized in the itinerant regime. We have found that when the AFM superexchange between spin is decreased the ground state spin configurations lead to an extended $2D$ electronic state. For filling $n = 1/4$ this is collinear state depicted in Fig. 4.5(b) and for $n = 3/8$ it is a coplanar spiral state with spiral angle $\delta\phi = \pi/4$.

A fourth key result is the observation that while in the Coulomb phase regime where spin configurations are loop coverings and consequently n and $1 - n$ are equivalent, in the itinerant phase densities n and $1 - n$ are not equivalent and the particle-hole asymmetry of the checkerboard lattice manifests itself. It is remarkable and surprising that for $n > 1/2$ no spin states that interpolate between the Coulomb phase loops states and the fully polarized FM state occur. For $n > 1/2$ we find no J_{AFM} dependence on the ground states and conclusions valid in the Coulomb phase remain valid down to $J_{\text{AFM}} \sim 0$.

Part II

Lattice Fractional Quantum Hall Effects

CHAPTER 5

TOPOLOGICAL BANDS AND ORBITAL DEGREES OF FREEDOM

5.1 Introduction

Investigating the repercussions of topology on the electronic states in condensed matter systems has a long and rich history. The Integer Quantum Hall (IQH) effect, discovered [75] in 1980, was soon understood to be a profound manifestation of the topological properties of the Landau levels. The quantized Hall conductance was shown to be a topological invariant that classifies the ground state [16]. Later that decade, Haldane [76] showed that the IQH state is not restricted to two-dimensional (2D) electron gases in a strong magnetic field. It can also be realized in lattice systems without Landau levels, by introducing electrons on a lattice with complex hoppings that break time-reversal symmetry. In recent years, topologically nontrivial electronic phases were moreover discovered in time-reversal invariant insulators [1, 3, 4, 72], leading to the Quantum Spin Hall effect in 2D [6, 7] and to the existence of protected 2D Dirac fermions on the surface of 3D topological insulators [12, 111] and a related quantum Hall effect [112].

These presently much studied 2D and 3D topological insulators are time-reversal invariant lattice systems that can therefore be perceived as a further generalization of the Quantum Hall states. The generalization of Fractional Quantum Hall (FQH)

states, the fractional counterpart of the IQH states, was considered only very recently [87, 108, 113]. Such a lattice FQH effect will be quite different from the ordinary FQH in 2D electron gases, for instance requiring a variational wavefunction distinct from the Laughlin wave function [114–116], and it can occur without magnetic field and potentially at high temperature [87, 108, 113]. Its realization in a material system would offer an exciting prospect for quantum computation, since the presence of non-Abelian FQH states allows for the creation of topologically protected qbits [117]. Creating the analogue of the FQH effect in a lattice system requires the fractional filling of topologically nontrivial bands, which should be very narrow [87, 108, 113], so that the electron-electron interactions can dominate over the kinetic energy and induce FQH states [104].

The theoretical approach used to progress toward this goal so far relies on the fine-tuning of the electron kinetic energy in model Hamiltonians containing bands with the correct topological properties [87, 108, 113]. Such a flattening procedure of the bands usually requires tuning (very) long-range hopping parameters to a set of quite peculiar strengths, which in real materials represents a rather formidable challenge from an experimental point of view.

We consider orbital degrees of freedom as an alternative agent for band flattening. Orbitals naturally occur in many transition metal (TM) compounds, which at the same time feature strong electron-electron interactions [118]. We concentrate on manganites, where Mn^{3+} ions are in a high-spin $3d^4$ configuration, with three electrons in the more localized t_{2g} states forming a spin of 3/2 and one electron in either of the two more itinerant e_g orbitals ferromagnetically coupled to this spin. Apart from other $3d$ systems besides Mn, the versatile class of TM oxides also contains $4d$ and $5d$ materials with orbital degrees of freedom, of which ruthenates [119] and iridates [120, 121] are important examples.

We will show that in the presence of a chiral spin texture, such an orbital make-up leads to nearly flat topologically nontrivial bands. It is well established that geometric frustration may stabilize non-coplanar spin-chiral magnetic textures when itinerant electrons couple to localized spins [29–33]. The Berry phase acquired by the electrons then leads to topologically nontrivial bands [30, 31, 78, 85, 97]. The pronounced spatial anisotropy of the e_g and t_{2g} orbitals strongly affects the symmetry of hopping integrals, even suppressing hopping completely along some directions.This can result in very flat bands like the dispersionless bands found in several multi-orbital TM compounds – a number of antiferromagnetic phases in cubic manganites are stabilized by such a mechanism [122, 123]. Here, we report a strong orbital-induced flattening of topological bands in spin-chiral phases on frustrated kagome and triangular lattices, demonstrating that orbital degrees of freedom of transition-metal ions generically provide a route to realizing a lattice version of the FQH effect. We also present indications that residual interactions can then induce a FQH state.
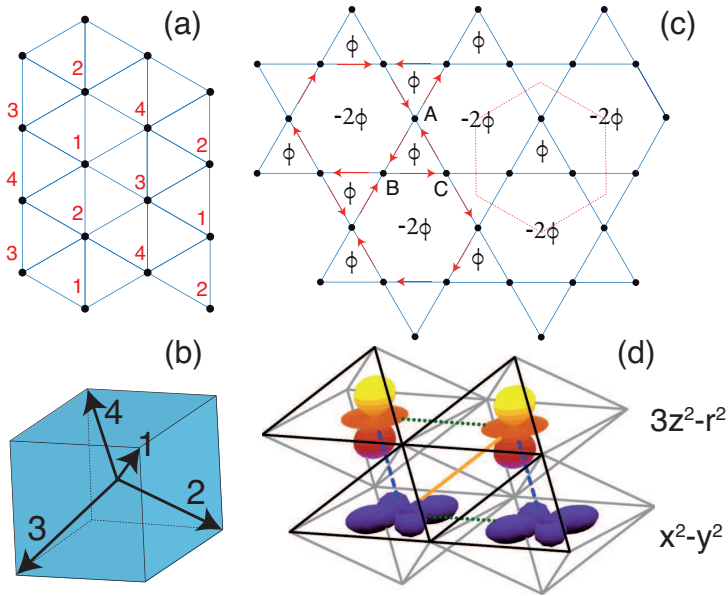
Figure 5.1: (a) Chiral spin ordering on the triangular lattice. (b) Spins forming a regular tetrahedron, numbers refer to sites in (a). (c) Flux-phase state on the kagome lattice. The unit cell is indicated by the dashed hexagon and the gauge choice by arrows; a flux ϕ threads each triangle. (d) Nearest-neighbor hopping geometry in lattices with triangular symmetry. Grey lines illustrate the oxygen octahedra, black front facets illustrate the triangular geometry. Thick dotted, dashed and solid lines indicate the bonds corresponding to the hopping matrices $\hat{T}_1$, $\hat{T}_2$, and $\hat{T}_3$. Two $d_{3z^2-r^2}$ (top) and $d_{x^2-y^2}$ (bottom) orbitals are also shown.

5.2 Chiral spin ordering

We first summarize the situation on the triangular and kagome lattices for mobile charge carriers without orbital degrees of freedom in presence of a nontrivial spin-texture. The Kondo Lattice Model, which describes the interaction between localized (t_{2g}) spins and itinerant (e_g) electrons, exhibits a topologically nontrivial chiral spin state on the triangular lattice [30–32]. This state has a four–sub-lattice ordering, illustrated in Fig. 5.1(a) and a finite scalar spin chirality $\langle \vec{S}_1 \cdot \vec{S}_2 \times \vec{S}_3 \rangle \neq 0$ for spins on the corners of triangles. The situation then becomes equivalent to electrons hopping on a triangular lattice with a fictitious gauge flux of $\phi = \pi/2$ threading each triangle, see Fig. 5.1. The effective electronic Hamiltonian has a two-site unit cell [30] and two bands, with Chern numbers ± 1, are separated by a gap. On the kagome lattice, a staggered flux pattern, shown in Fig. 5.1, can result from topologically nontrivial spin states, where a flux ϕ threads each triangle and a flux -2ϕ each hexagon [85]. Time-reversal symmetry is broken for $\phi \neq 0, \pi$ and two gaps open, leading to three bands. The middle band has zero Chern number, but the lowest and highest are topologically nontrivial with $C = \mp \text{sgn}(\sin \phi)$ [85]. However, all topologically nontrivial bands have a considerable dispersion on both lattices, which we will now show to be substantially reduced by the presence of an orbital degree of freedom.

5.3 Orbital degrees of freedom

In many TM oxides, the TM ions are inside oxygen octahedra, which are edge-sharing in a triangular lattice, see Fig. 5.1. The cubic symmetry splits the TM d levels into three t_{2g} and two e_g orbitals. We focus mainly on the latter, but later also demonstrate an analogous effect for the former. Collecting the e_g orbital degree of freedom in a pseudo-spin $\tau^z = \pm 1$ object we write

$$|e_g\rangle = \begin{bmatrix} |3z^2 - r^2\rangle \\ |x^2 - y^2\rangle \end{bmatrix} \equiv \begin{bmatrix} |z\rangle \\ |x\rangle \end{bmatrix}. \tag{5.1}$$

Along the $\vec{a}_1 = (0, 1)$ direction, indicated by a dotted line in Fig. 5.1, hopping for e_g orbitals conserves orbital flavor and is given by t (t') for the $|x^2 - y^2\rangle$ ($|3z^2 - r^2\rangle$) orbital. This is captured by the hopping matrix acting on the orbital pseudospin

$$\hat{T}_1 = \begin{bmatrix} t' & 0 \\ 0 & t \end{bmatrix}. \tag{5.2}$$

Hoppings along the other two bonds are obtained by a rotation in orbital space, which are representations of real space rotations in pseudospin space. As the pseudospin
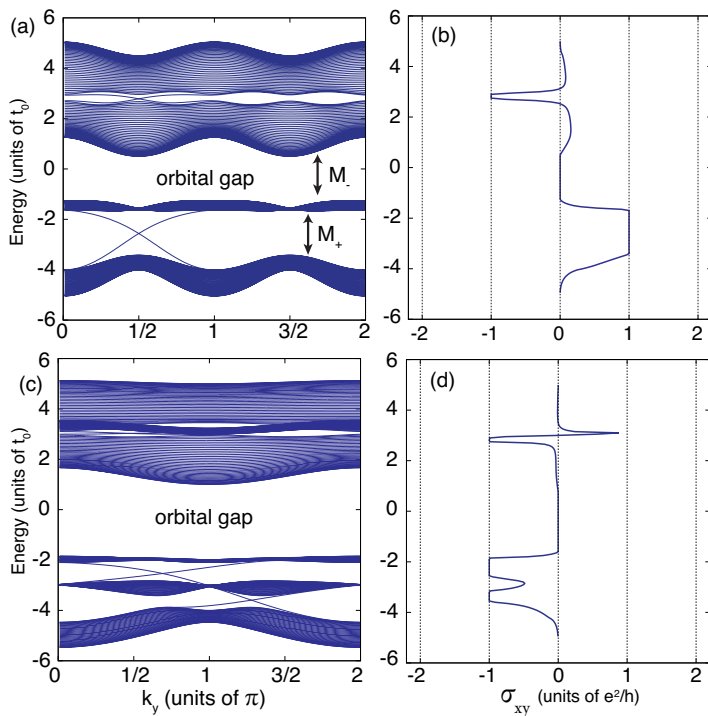
Figure 5.2: Top: kagome lattice, bottom: triangular lattice. Left: bands of a strip geometry, clearly showing the chiral edge states of the flattened bands. Right: off-diagonal Hall conductivity as function of chemical potential, providing the Chern numbers for the flat bands. For the Kagome lattice $t' = -0.46$, $\Delta = 2.75$, $\phi = \pi/4$ and for the triangular case $t' = -0.46$, $\Delta = 2.5$.

must transform as a real representation rotations over an angle θ are implemented by the matrix $e^{-i\theta\tau^y}$. Using this one may obtain for the other directions $\vec{a}_2$ and $\vec{a}_3$

$$\hat{T}_2 = \frac{1}{4}\begin{pmatrix} t' + 3t & \sqrt{3}(t' - t) \\ \sqrt{3}(t' - t) & 3t' + t \end{pmatrix},$$

$$\hat{T}_3 = \frac{1}{4}\begin{pmatrix} t' + 3t & -\sqrt{3}(t' - t) \\ -\sqrt{3}(t' - t) & 3t' + t \end{pmatrix}, \tag{5.3}$$

We use t as unit of energy and vary the material-dependent ratio t'/t between -1 and 1, concentrating on $t'/t < 0$ inferred from direct overlaps of the orbitals. For our fillings of approximately one electron per site, the Jahn-Teller effect is important and can induce a uniform crystal field

$$\hat{H}_{\text{JT}} = \Delta(\hat{n}_x - \hat{n}_z) \tag{5.4}$$

lifting orbital degeneracy.

Even though the spin pattern underlying the chiral spin state on the triangular lattice has a four-site unit cell, the electronic Hamiltonian has only a two-site unit cell and can thus be described by a 2×2 matrix if the original model is a one-band model. [30] With an underlying multi-orbital Hamiltonian, this becomes a Hamiltonian matrix consisting of four blocks ($\mathcal{H}_{11}(\vec{k})$, $\mathcal{H}_{12}(\vec{k})$, $\mathcal{H}_{21}(\vec{k})$ and $\mathcal{H}_{22}(\vec{k})$), where the blocks refer to the lattice sites of the spatial unit cell and are matrices in orbital space, leading to

$$\mathcal{H}(\vec{k}) = \begin{bmatrix} \mathcal{H}_{\text{JT}} + \mathcal{H}_{11}(\vec{k}) & \mathcal{H}_{12}(\vec{k}) \\ \mathcal{H}_{21}(\vec{k}) & \mathcal{H}_{\text{JT}} + \mathcal{H}_{22}(\vec{k}) \end{bmatrix} \tag{5.5}$$

where the blocks are given by

$$\mathcal{H}_{11} = -\mathcal{H}_{22} = -2\hat{T}_1 \cos(\vec{k} \cdot \vec{a}_3), \tag{5.6}$$

$$\mathcal{H}_{12} = \mathcal{H}_{21}^{\dagger} = -2\hat{T}_2 \cos(\vec{k} \cdot \vec{a}_1) - 2i\hat{T}_3 \cos(\vec{k} \cdot \vec{a}_2)$$

The hopping matrices T_i are the 2×2 matrices Eq. (5.3) for e_g electrons defined above. The matrices H_{JT} given by the crystal field refer to Eqs. (5.4). Figure 5.2 shows the energy bands calculated for a strip geometry, with periodic boundary conditions in one direction and two edges in the orthogonal direction. For a large enough crystal-field splitting $\Delta > t, t'$, a gap separates bands with different orbital character. Within each subsystem, chiral magnetic order induces a further splitting into two topologically nontrivial bands with Chern numbers $C = \pm 1$. This is unambiguously indicated by the topological edge states connecting the bands with $C > 0$ and

$C < 0$ in Fig. 5.2(a). The transverse Hall conductivity σ_{xy}^n is shown in Fig. 5.2(b) and directly reflects the topological character of the bands. The Hall conductivity is calculated as

$$\sigma_{xy}^n = -i \sum_{\vec{k}, m \neq n} \frac{\langle m\vec{k}|J_x|n\vec{k}\rangle\langle n\vec{k}|J_y|m\vec{k}\rangle - \text{h.c.}}{(E_n(\vec{k}) - E_m(\vec{k}))^2} f(E_n(\vec{k})) \tag{5.7}$$

where $|n\vec{k}\rangle$ are the eigenstates of the Hamiltonian (n being the band index) and $E_n(\vec{k})$ are the corresponding eigenvalues. The current operators J_i are obtained from

$$\hat{J}_i = \sum_{\vec{k}} \hat{\psi}^\dagger(\vec{k}) \frac{\partial \mathcal{H}(\vec{k})}{\partial k_i} \hat{\psi}(\vec{k}). \tag{5.8}$$

The topological character of the bands is related to the Hall conductivity by the identity

$$\sigma_{xy}^n = \frac{e^2}{h} C_n = \frac{-ie^2}{2\pi h} \int_{BZ} d^2k \, \text{Tr}\,[\mathcal{F}_{xy}]$$

$$= \frac{-ie^2}{2\pi h} \int_{BZ} d^2k \sum_{n \in \text{occ}} \partial_x \mathcal{A}_y^{nn} - \partial_y \mathcal{A}_x^{nn} \tag{5.9}$$

where C_n is the Chern number of the n-th band. The non-Abelian Berry connection $\mathcal{A}_i^{mn}$ is defined as

$$\mathcal{A}_i^{mn} = -i\langle m\vec{k}|\partial_i|n\vec{k}\rangle, \tag{5.10}$$

from which the field strength $\mathcal{F}_{ij}^{mn}$ is derived as

$$\mathcal{F}_{ij} = \partial_i \mathcal{A}_j - \partial_j \mathcal{A}_i + i[\mathcal{A}_i, \mathcal{A}_j]. \tag{5.11}$$

The gap between the topological bands is smaller in the upper ($x^2 - y^2$) sector, but robust between the two $3z^2 - r^2$ bands below the crystal-field gap. The upper band of the $3z^2 - r^2$ sector with $C = -1$, has a weak dispersion, becoming nearly flat for $t' \approx -t/2$, see Fig. 5.2(a). The figure of merit quantifying the flatness is the ratio of the gaps M separating it from other bands to its band width W. Here we monitor both the 'topological' gap (M_+), which is induced by chiral order and the 'trivial' crystal-field gap (M_{-1}), which separates it from the $x^2 - y^2$ sector above. Figure 5.3(a) shows these ratios depending on t' and Δ, the relevant figure of merit is the smaller of the two ratios M_+/W and M_{-1}/W. It is appreciable in a broad range of Δ and t', reaching a maximum of ~ 4.25 for $\Delta = 2.5$ and $t' = -0.45$.
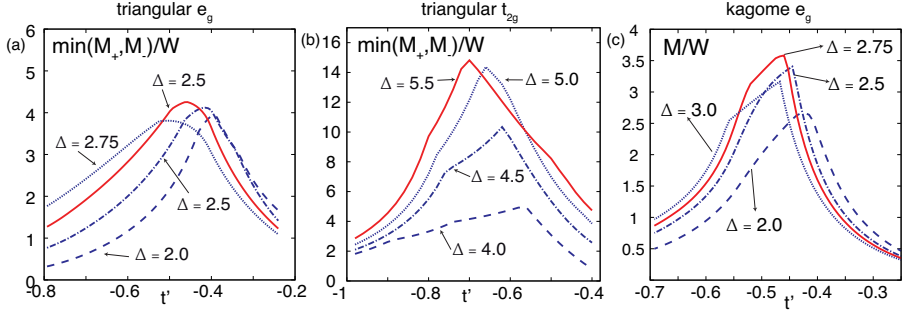
Figure 5.3: (a) The smallest band gap over bandwidth ratios for e_g electrons the triangular lattice, for the gaps M_+ and M_- indicated in Fig. 5.2(a). (b) The same for t_{2g} electrons on a triangular lattice and (c) for e_g on the kagome lattice. Orbital splittings are indicated by Δ.

In addition to e_g orbitals we may also consider t_{2g} orbitals. Collecting them in a vector again we write

$$|t_{2g}\rangle = \begin{bmatrix} |xy\rangle \\ |xz\rangle \\ |yz\rangle \end{bmatrix} \equiv \begin{bmatrix} |a\rangle \\ |b\rangle \\ |c\rangle \end{bmatrix}. \tag{5.12}$$

The t_{2g}-hopping matrices are given by the expressions

$$\hat{T}_1 = \begin{pmatrix} t' & 0 & 0 \\ 0 & 0 & t \\ 0 & t & 0 \end{pmatrix}, \quad \hat{T}_2 = \begin{pmatrix} 0 & 0 & t \\ 0 & t' & 0 \\ t & 0 & 0 \end{pmatrix}, \quad \hat{T}_3 = \begin{pmatrix} 0 & t & 0 \\ t & 0 & 0 \\ 0 & 0 & t' \end{pmatrix}, \tag{5.13}$$

and consist of inter-orbital hopping t (primarily via ligand oxygen ions [124]) and orbital-conserving hopping t' due to direct overlap [125]. In a three-fold symmetry, the t_{2g} manifold is further split into one a_{1g} and two e'_g states separated by a crystal field $\hat{H}_{\text{JT}}$. The crystal field related to elongating or shortening the octahedra is naturally expressed in the $\{a_{1g}, e'_{g+}, e'_{g-}\}$ basis reflecting the triangular symmetry. It is then explicitly given by $\hat{H}_{\text{JT}} = \Delta(\hat{n}_{e_{g+}} + \hat{n}_{e_{g-}} - 2\hat{n}_{a_{1g}})/3$, which can be expressed in the original $\{xy, xz, yz\}$ basis via the basis transformation defined in Ref. [125] and becomes

$$\mathcal{H}_{\text{JT}} = -\frac{\Delta}{3} \begin{pmatrix} 0 & 1 & 1 \\ 1 & 0 & 1 \\ 1 & 1 & 0 \end{pmatrix} \tag{5.14}$$

Qualitatively, we find similar behavior as for e_g orbitals, but the figure of merit reaches $M/W \approx 14$, see Fig. 5.3(b). This extraordinarily large M/W reflects the very large spatial anisotropy of t_{2g} hopping integrals, well-known in triangular vanadates [124] and cobaltates [125].

After discussing the triangular lattice, we now come to e_g orbitals on the kagome lattice illustrated in Fig. 5.1(b). The lattice has a three-site unit cell, and one proceeds with an approach analogous to the two-site unit cell discussed above. The sublattices of the kagome lattice are labeled as A, B and C, and taking the orbital degree of freedom into account the fermion operator becomes

$$\hat{\psi}^\dagger(\vec{k}) = (\hat{\psi}^\dagger_{Az}(\vec{k}), \hat{\psi}^\dagger_{Ax}(\vec{k}), \hat{\psi}^\dagger_{Bz}(\vec{k}), \hat{\psi}^\dagger_{Bx}(\vec{k}), \hat{\psi}^\dagger_{Cz}(\vec{k}), \hat{\psi}^\dagger_{Cx}(\vec{k}))$$

and the Hamiltonian is given by

$$\mathcal{H}(\vec{k}) = \begin{bmatrix} \mathcal{M}_0 & \mathcal{M}_1 & \mathcal{M}_3^\dagger \\ \mathcal{M}_1^\dagger & \mathcal{M}_0 & \mathcal{M}_2 \\ \mathcal{M}_3 & \mathcal{M}_2^\dagger & \mathcal{M}_0 \end{bmatrix} \tag{5.15}$$

where the orbital matrices $\mathcal{M}$ take the form

$$\begin{aligned} \mathcal{M}_0 &= \mathcal{H}_{\text{JT}} \\ \mathcal{M}_i(\vec{k}) &= 2\hat{T}_i \cos(\vec{k} \cdot \vec{a}_i) e^{-i\phi/3}. \end{aligned} \tag{5.16}$$

Bands are again separated by the crystal field into two parts with a different orbital character, see Fig. 5.2. While the $x^2 - y^2$ sector is hardly gapped, the $3z^2 - r^3$ sector shows three sub-bands with $C = 0, \pm 1$ similar to the one-band model [85]. Again, the topological character can be inferred from edge states and is confirmed by the Hall conductivity shown in Fig. 5.2(d) and as for the triangular lattice, the top band of the $3z^2 - r^3$ sector (with $C = +1$) is very flat for $t' \approx -t/2$. The figure of merit M/W is plotted in Fig. 5.3(c); it reaches values up to ~ 3.5 for $\Delta = 2.75$ and $t' = -0.45$, compared to $W/M \lesssim 1$ in the one-band model without orbital degrees of freedom.

5.4   FQH state induced by residual interactions

After showing that orbital degrees of freedom can lead to flat bands with Chern number $C \neq 0$, we analyze the impact of Coulomb repulsion on the triangular-lattice e_g system. We include electron-electron interactions

$$\hat{H}_{\text{int}} = U \sum_i \hat{n}_{ix} \hat{n}_{iz} + V \sum_{\langle i,j \rangle, \alpha\beta} \hat{n}_{i\alpha} \hat{n}_{j\beta} \, , \tag{5.17}$$
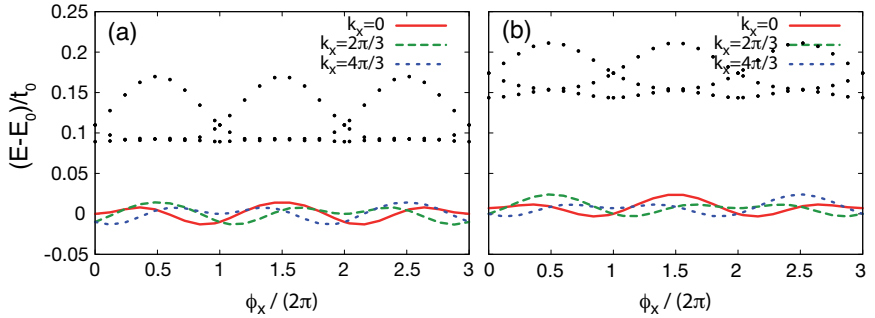
Figure 5.4: Lowest energies of the interacting e_g system on the triangular lattice, depending on flux inserted for (a) $U = 2$, $V = 1$, and (b) $U = 4$, $V = 2$. The ED results presented here were obtained for a 2×6 system with $t'/t = -0.46$ and $\Delta = 1.5$.

where $\hat{n}_{i\alpha}$ is the electron density in orbital α on site i, U acts on electrons occupying two orbitals on the same site, and V gives the nearest-neighbor (NN) interaction. It should be noted that the nearest-neighbor interaction V is defined on the original underlying triangular lattice, i.e., the same interaction V acts both between the two real-space sites of the same unit cell and between sites in different unit cells, if these sites are nearest-neighbors on the triangular lattice. Following Refs. [104, 108], we use Exact Diagonalization (ED) to study signatures of FQH-like states for a filling $1/3$ of the topologically nontrivial flat band. When adding these interactions to the Hamiltonian, we have to take into account that U implies an additional energy cost for electrons in the energetically higher $x^2 - y^2$ orbitals, thus changing the crystal field splitting Δ. In our ED calculations, we therefore reduce Δ from the value $\Delta = 2.5$ that would give the flattest band.

Exact diagonalization studies were only performed for the e_g triangular lattice model, because this case has the smallest unit cell of the models considered here. Even so, only very small systems are accessible. We use $N_x \times N_y$ real-space sites, giving $N_c = N_s/2 = N_x \times N_y/2$ unit cells of the chiral phase, but $N_{sp} = 2N_s$ "generalized" orbitals determining the size of the Hilbert space. There is no spin degree of freedom, i.e., we study spinless fermions. The filling is the one expected to correspond to the simplest FQH state, i.e., $\nu = 1/3$ filling of the nearly flat band. Since this band is close to half filling, this also implies a total filling of $1/3$, i.e., an electron number of $N_e = N_{sp}/3$.

Due to the large number of "generalized" orbitals per unit cell and due to the fact that our total electron filling is closer to half filling (which additionally increases
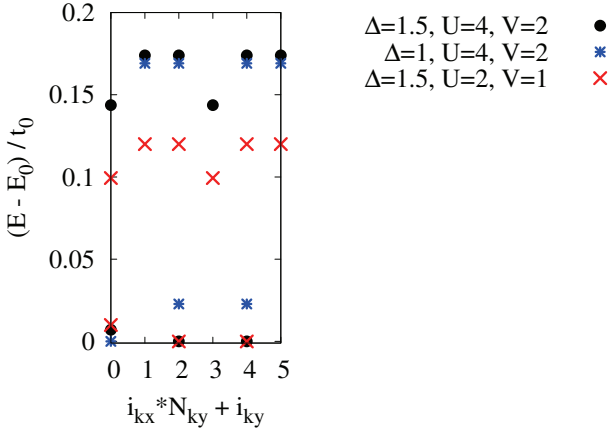
Figure 5.5: Lowest energies of the interacting e_g system on the triangular lattice for the various total momenta of the 6×2 lattice for a few parameter sets, $t'/t = -0.46$

the size of the Hilbert space), the lattice sizes accessible are considerably smaller than for models considered previously. [104, 108] Since we need the total number of sites to be divisible by 3 in order to obtain $1/3$ filling and since we also want bot N_x and N_y to be even, we consider a 2×6 "ladder" ($N_c = 6$, $N_{sp} = 24$). For simplicity, we "distort" the triangular lattice and assume the x direction to lie along $\vec{a}_1$ and the y direction along $\vec{a}_2$ to be orthogonal, the third nearest-neighbor bond is still determined by $\vec{a}_3 = \vec{a}_1 - \vec{a}_2$.

The Hamiltonian is invariant under translations, hence total momentum constitutes a good quantum number. Figure 5.5 shows the lowest two eigenvalues within the sectors corresponding to the total momenta possible on a 6×1 chain (the two sites in y-direction define the two-site unit cell in real space), and one clearly sees three low-energy states separated from the remaining spectrum by a gap. We find an approximate threefold ground-state manifold, which is an indication for the topological degeneracy of a FQH state. The three "ground states" cross each other upon inserting a magnetic flux [126], see Fig. 5.4. Adiabatic flux insertion is implemented by dividing the total flux ϕ in smaller phases ϕ/N_x added to each hopping process, which is equivalent to using twisted boundary conditions and preserves translational invariance. This replaces the two hopping matrices whose corresponding lattice vectors have a component along $\vec{a}_1$, i.e., T_1 and T_3 by $T_1 e^{i\phi/N_x}$ and $T_3 e^{i\phi/N_x}$. Figure 4 in the main text shows the evolution of the ground state manifold as function of

the inserted flux. The system assumes an equivalent, yet not identical, state after one unit $\phi = 2\pi$ of flux is threaded through the system, meaning that states in the ground state manifold have switched places. After 3 periods of flux insertion, where 3 corresponds to the inverse of the filling fraction, ν^{-1}, with $\nu = 1/3$, we recover an identical situation as zero flux. This is in agreement with results for other models [105, 108]. Figure 5.6 shows the same for various other parameter sets, indicating that the behavior is stable. This level crossing of the degenerate many body ground state manifold reveals the existence of the FQH ground state, provided that the spectral gap persists in the thermodynamic limit, in order to unambiguously exclude a charge density wave [105].

5.5   Discussion

The flattening due to the orbital degrees of freedom presented here can be further enhanced by introducing and fine-tuning longer-range hopping integrals, as in one-band models. Perfectly flat and topologically nontrivial bands ($M/W \to \infty$) can in principle be obtained by allowing for arbitrarily long-range hoppings [87]. We do not explore this here, as we aim to show that the anisotropy inherent in d-orbital degrees of freedom can robustly flatten topological bands even with purely NN hopping, and obtain flattening ratios up to $M/W \approx 4$ ($M/W \approx 14$) for e_g (t_{2g}) systems.

Orbital degrees of freedom are directly relevant to numerous well-known TM systems. Manganese compounds alone, which closely correspond to the e_g model studied here, occur in a variety of crystal structures: in simple cubic or square lattices in $La_{1-x}Sr_xMnO_3$ and $LaSrMnO_4$, honeycomb in e.g. Li_2MnO_3 or $(Bi_3Mn_4O_{12})NO_3$ but also in strongly frustrated pyrochlore lattices as in e.g. $Ti_2Mn_2O_7$ and in triangular lattices as in $YMnO_3$. The pyrochlore lattice, in particular, is realized by the B-site TM ions in the very common spinel crystal structure, and can be thought of as consisting of kagome and triangular layers stacked along the $(1, 1, 1)$ direction. Singling out the triangular or kagome layers, possibly via chemical substitution or controlled monolayer growth, may thus lead to systems similar to the ones studied here.

A FQH ground state needs an interaction V that exceeds the bandwidth ($V > W$), but remains smaller than the gap ($V < M$) so that bands are not mixed. Fortunately, TM oxides have substantial Coulomb interactions and NN repulsion V can become as large as or larger than the hoppings. On the other hand, is is almost always smaller than onsite repulsion, which increases one of the two gaps delimiting the flat band. The remaining challenge is thus to keep the effective interaction small compared to the gap separating the bands with $C = \pm 1$. A large figure of merit M/W provides a large window for this separation of energy scales $W < V < M$ and our ED results
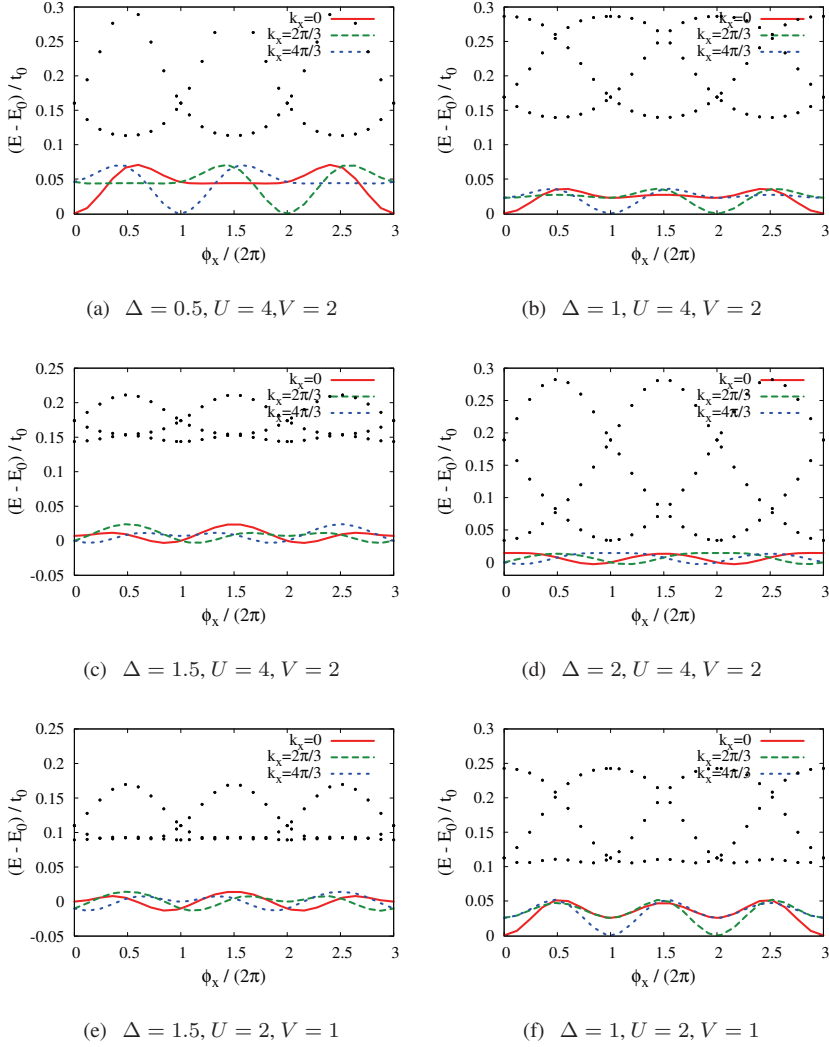
Figure 5.6: Lowest energies of the interacting e_g system on the triangular lattice, depending on flux inserted for various parameter sets. (c) and (e) are given in the main text as Fig. 4(a,b). The ED results presented here were obtained for a 2×6 system with $t'/t = -0.46$.

in Fig. 5.4 suggest that one indeed has some flexibility in this regard, as interactions differing by a factor of two lead to similar results. The crystal field splitting needed to obtain the desired flattening can be varied by applying (chemical) pressure. Finally, many of these materials, manganites in particular, are easy to dope which allows control of the (fractional) band filling.

Theoretically, there is no fundamental objection to the realization of lattice FQH states, but it remains an intriguing challenge from an experimental and practical point of view. We have demonstrated here that d-orbital degrees of freedom, ubiquitous in TM compounds, substantially narrow the topologically nontrivial bands of electrons moving in a background of non-coplanar spins. The separation of energy scales is comparable to that achievable by long-range hopping, and we find signatures of a FQH-like ground state. In the search for the lattice FQH effect, geometrically frustrated TM compounds with an orbital degree of freedom thus come to the fore as a promising class of candidate systems.

CHAPTER 6

---

t_{2g} TRIANGULAR LATTICE SYSTEMS

6.1 Introduction

The Integer Quantum Hall (IQH) effect [75] is a prime example of an electronic state that cannot be classified within the traditional framework of symmetry breaking, but is instead characterized by a topological invariant [16]. It is by now theoretically well established that an external magnetic field is in principle not needed and that states within the same topological class as IQH states can be realized in lattice models, if time-reversal symmetry is broken by other mechanisms, e.g., by complex electron hoppings [76]. Related topologically nontrivial Quantum Spin-Hall (QSH) states even occur in systems where time-reversal symmetry is not broken at all [1, 3, 4, 72, 127], see Refs. [12, 111] for reviews. At present, many intriguing features intrinsic to topologically non-trivial states have been observed in the absence of magnetic fields, such as the metallic Dirac cones at the surface of a topological insulator [74, 128], or the QSH effect in quantum wells [6, 112].

Fractional Quantum Hall (FQH) states [10] are topological states that can be seen as composed of quasi-particles carrying an exact fraction of the elementary electronic charge [114]. Apart from the fundamental interest in observing a quasi-particle that behaves in many ways like a fraction of an electron, some FQH states also have properties relevant to fault-tolerant quantum computation [129]. Very recently [87,
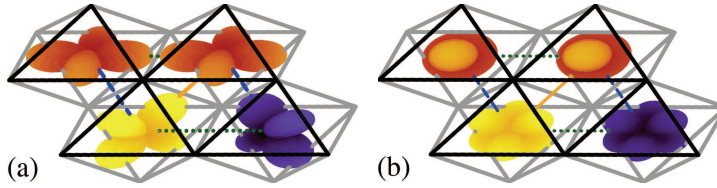
Figure 6.1: Triangular perovskite lattice and t_{2g} orbitals. Oxygen octahedra are indicated by lines, with black lines illustrating the front facets. Thick dotted (dashed, solid) lines indicate nearest-neighbor bonds along lattice vector $\mathbf{a}_1$ ($\mathbf{a}_2$, $\mathbf{a}_3$). (a) Shows two d_{xy} orbitals (top) and one d_{xz} and d_{yz} orbital (bottom). In (b), the orbitals reflecting the three-fold lattice symmetry are shown: The two e'_g orbitals (bottom), which differ by their complex phases, will turn out to be half filled, while the a_{1g} orbital (pointing out of the plane, see top) forms nearly flat bands with non-trivial topological character that can support spontaneous FQH states.

108, 113], it was suggested that lattice-FQH states [115] may similarly arise without a magnetic field, in fractionally filled topologically nontrivial bands.

In contrast to the IQH and QSH effects, which can be fully understood in terms of non-(or weakly-)interacting electrons, interactions are an essential requirement for FQH states, which places demanding restrictions on candidate systems: One needs a topologically nontrivial band that must be nearly flat – similar to the highly degenerate Landau levels – so that the electron-electron interaction can at the same time be large compared to the band width and small compared to the gap separating it from other bands [87, 108, 113]. If the requirements can be fulfilled, however, the temperature scale of the FQH state is set by the energy scale of the interaction. This can allow temperatures considerably higher than the sub-Kelvin range of the conventional FQH effect, which would be extremely desirable in view of potential quantum-computing applications.

In all recently proposed model Hamiltonians [87, 106, 108, 113, 130, 131], the topological nature of the bands was introduced by hand and model parameters were carefully tuned to obtain very flat bands. On the other hand, topologically nontrivial bands can in principle emerge spontaneously in interacting electron systems [84], e.g., for charge-ordered systems [132] or for electrons coupling to spins in a non-coplanar magnetic order [78, 133]. We demonstrate here that such a scenario indeed arises in a Hubbard model describing electrons with a t_{2g} orbital degree of freedom on a triangular lattice: a ground state with topologically nontrivial and nearly flat bands is stabilized by onsite Coulomb interactions, and upon doping the flat bands, longer-range Coulomb repulsion induces a FQH state.

6.2 t_{2g} orbitals on the triangular lattice

The building blocks of our system are oxygen octahedra with a transition-metal (TM) ion in the center, the most common building block in the large and versatile material class of TM oxides. In this case the local symmetry around a TM ion is cubic, with ligand oxygens forming an octahedron, as depicted in Fig. 6.2(a). This splits the degeneracy between the d levels, because the two e_g orbitals point toward the negatively charged oxygens, while the three t_{2g} levels have their lobes in between. Consequently, the energy of e_g levels is higher. Depending on the total electron filling, the valence states may be found in either manifold. We are here discussing the situation where the three t_{2g} levels share 2.5 to 3 electrons and the e_g levels are empty. Furthermore, we consider the case of a layered triangular lattice, as can be realized in compounds of the form ABO_2.

In this geometry, the octahedra are edge sharing and electrons (or holes) can hop from one TM ion to its neighbor either through direct overlap or via the ligand oxygens. The hopping symmetries can be most easily worked out using the usual basis functions for the t_{2g} states, $|xz\rangle$, $|yz\rangle$, and $|xy\rangle$ [124, 125] and following Refs. [134, 135]. Considering hopping for bonds along the $\vec{a}_1$ direction and choosing the local coordinate system such that this corresponds to the $(1,1)$ direction in the x-y plane, one finds that direct hopping t_d is only relevant for the xy orbital and conserves orbital flavor. Due to the $90°$ angle of the TM-O-TM bond, oxygen-mediated hopping t_0 is, on the other hand, mostly via the oxygen-p_z orbital and mediates processes between xz and yz states, thereby always *changing* orbital flavor. Hoppings along the other two, symmetry-related, directions $\vec{a}_2$ and $\vec{a}_3$ are obtained by symmetry transformations.

These hoppings can then be expressed in orbital- and direction- dependent matrix elements $t_{\vec{a}_j}^{\alpha, \beta}$, where α and β denote orbitals (xz, yz, and xy) and $\vec{a}_j$ the direction. They are given by

$$\hat{T}_{\vec{a}_1} = \begin{pmatrix} t_{dd} & 0 & 0 \\ 0 & 0 & t_0 \\ 0 & t_0 & 0 \end{pmatrix}, \; \hat{T}_{\vec{a}_2} = \begin{pmatrix} 0 & 0 & t_0 \\ 0 & t_{dd} & 0 \\ t_0 & 0 & 0 \end{pmatrix},$$

$$\hat{T}_{\vec{a}_3} = \begin{pmatrix} 0 & t_0 & 0 \\ t_0 & 0 & 0 \\ 0 & 0 & t_{dd} \end{pmatrix} \tag{6.1}$$

for NN bonds along the three directions $\vec{a}_1$, $\vec{a}_2$, $\vec{a}_3$. The two hopping processes are expected to be of comparable strength, but with $|t_d| \lesssim |t_0|$ for $3d$ elements, and will typically have opposite sign. [125]

If the width of a triangular layer made of octahedra is compressed (extended), the energy of the highly symmetric orbital state $|a_{1g}\rangle = (|xz\rangle + |yz\rangle + |xy\rangle)/\sqrt{3}$ is

raised (lowered) with respect to the remaining orbital doublet (e'_g), see Fig. 6.2(b) for illustration. This energy shift can be written as

$$\hat{H}_{\text{JT}} = -\Delta_{\text{JT}}(\hat{n}_{e_{g+}} + \hat{n}_{e_{g-}} - 2\hat{n}_{a_{1g}})/3 \tag{6.2}$$

and depends on the Jahn-Teller effect as well as on the lattice. [125] Especially for large splitting between a_{1g} and e'_g states, which may also be enhanced through on-site Coulomb interactions, see Section 6.3 and also 7.2, it is more appropriate to use a basis that reflects the triangular lattice symmetry. We thus go over into the $(a_{1g}, e'_{g,1}, e'_{g,2})$ basis, which is done via [125]

$$\begin{pmatrix} a_{1g} \\ e'_{g,1} \\ e'_{g,2} \end{pmatrix} = \hat{U} \begin{pmatrix} xz \\ yz \\ xy \end{pmatrix} = \frac{1}{\sqrt{3}} \begin{pmatrix} 1 & 1 & 1 \\ 1 & e^{i2\pi/3} & e^{-i2\pi/3} \\ 1 & e^{i4\pi/3} & e^{-i4\pi/3} \end{pmatrix} \begin{pmatrix} xz \\ yz \\ xy \end{pmatrix}. \tag{6.3}$$

The transformed hopping matrices $\widetilde{T}_{\vec{a}_i}$ are then obtained from Eq. (6.1) as

$$\widetilde{T}_{\vec{a}_1} = \hat{U}^\dagger \hat{T}_{\vec{a}_1} \hat{U} = \frac{1}{3} \begin{pmatrix} 3t_0 + \delta t & \delta t & \delta t \\ \delta t & \delta t & 3t_0 + \delta t \\ \delta t & 3t_0 + \delta t & \delta t \end{pmatrix},$$

$$\widetilde{T}_{\vec{a}_2} = \hat{U}^\dagger \hat{T}_{\vec{a}_2} \hat{U} = \frac{1}{3} \begin{pmatrix} 3t_0 + \delta t & \delta t\,\omega & \delta t\,\omega^{-1} \\ \delta t\,\omega^{-1} & \delta t & (3t_0 + \delta t)\omega \\ \delta t\,\omega & (3t_0 + \delta t)\omega^{-1} & \delta t \end{pmatrix},$$

$$\widetilde{T}_{\vec{a}_3} = \hat{U}^\dagger \hat{T}_{\vec{a}_3} \hat{U} = \frac{1}{3} \begin{pmatrix} 3t_0 + \delta t & \delta t\,\omega^{-1} & \delta t\,\omega \\ \delta t\,\omega & \delta t & (3t_0 + \delta t)\omega^{-1} \\ \delta t\,\omega^{-1} & (3t_0 + \delta t)\omega & \delta t \end{pmatrix}, \tag{6.4}$$

where $\delta t = t_{dd} - t_0$ and $\omega = e^{i2\pi/3}$. Observe that the intra-orbital hopping of the a_{1g} state is the same in all three lattice directions, as expected for a_{1g} symmetry. However, we also see that hopping elements mix all three orbitals. We set here $n < 3$ and choose $t > 0$ [125] as unit of energy, but analogous results hold for $n > 3$, $t < 0$, and $t_{dd} \to -t_{dd}$, $\Delta_{\text{JT}} \to -\Delta_{\text{JT}}$ due to particle-hole symmetry.

6.3 Multi-orbital interacting model

In TM oxides, Coulomb interaction is substantial compared to the kinetic energy of t_{2g} orbitals and spin-orbital physics induced by correlations are known to be rich in t_{2g} systems on triangular lattices [124, 136]. We take into account the onsite inter-action including Coulomb repulsion U (intra-orbital) and U' (interorbital) as well as
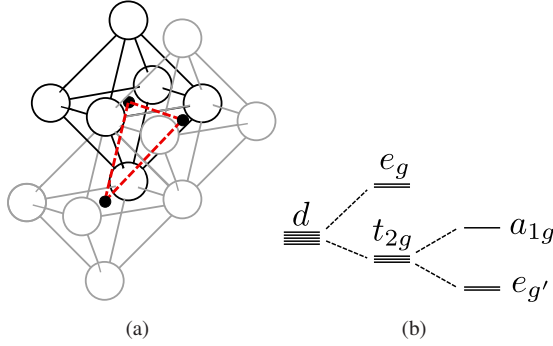
Figure 6.2: (a) Illustration of a triangular-lattice plane built of edge-sharing oxygen octahedra. (b) The five d orbitals of the transition-metal ion in the center are split into an e_g doublet and a t_{2g} triplet due to the local cubic symmetry; the latter is further split into one a_{1g} state and an e_g' doublet. (The splitting between the latter is exaggerated here for visibility.)

Hund's-rule coupling J. The Hamiltonian corresponding to the kinetic energy of the t_{2g} electrons is given by

$$\hat{H}_{\text{int}} = \sum_{ij,\alpha\beta} t_{ij}^{\alpha\beta} \hat{\psi}_{i\alpha\sigma}^\dagger \hat{\psi}_{j\beta\sigma} + \text{hc} \tag{6.5}$$

where the matrix $t_{ij}^{\alpha\beta}$ depends on the direction and orbital flavor and is constructed from the previously explicitly defined $\widetilde{T}_{\vec{a}_i}$. The full Coulomb interaction interaction for equivalent t_{2g} orbitals reads

$$\hat{H}_{\text{int}} = U \sum_{i,\alpha} \hat{n}_{i\alpha\uparrow}\hat{n}_{i\alpha\downarrow} + (U' - J/2) \sum_{i,\alpha<\beta} \hat{n}_{i\alpha}\hat{n}_{i\beta} - 2J \sum_{i,\alpha<\beta} \vec{s}_{i\alpha} \cdot \vec{s}_{i\beta}$$

$$+ J' \sum_{i,\alpha<\beta} \left(\hat{\psi}_{i\alpha\uparrow}^\dagger \hat{\psi}_{i\alpha\downarrow}^\dagger \hat{\psi}_{i\beta\downarrow} \hat{\psi}_{i\beta\uparrow} + \text{hc} \right) \tag{6.6}$$

where $U = U' + 2J$ and $J' = J$ holds in the case of equivalent t_{2g} orbitals. The spin operators $\vec{s}_{i\alpha}$ are defined as

$$\vec{s}_{i\alpha} = \hat{\psi}_{i\alpha\sigma}^\dagger \vec{\sigma}_{\sigma\sigma'} \hat{\psi}_{i\alpha\sigma'}. \tag{6.7}$$

We concentrate on the regime of interest, where the a_{1g} orbital is separated from the e_g doublet by a sizable Δ_{JT} and does not have to be equivalent. As long as intraor-

bital interaction (controlled by U) and Hund's rule coupling (controlled by J) dominate over interorbital interaction ($U' - J/2$) and crystal-field splitting (Δ), doubly occupied orbitals will be suppressed and the last term in Eq. (6.3) will consequently not be important and hence neglected.

To study the magnetic and ordbital ordering of these t_{2g} orbitals on the triangular lattice we employ a mean-field approximation with a decoupling into expectation values of densities $\langle \hat{n}_{i\alpha\sigma} \rangle = \langle \hat{\psi}_{i\alpha\sigma}^{\dagger} \hat{\psi}_{i\alpha\sigma} \rangle$ for site i, orbital α, and spin σ [30,137]. For the interacting term $\vec{s}_{i\alpha} \cdot \vec{s}_{i\beta}$ the fact that we only keep densities has the consequence that

$$-2J \sum_{i,\alpha<\beta} \vec{s}_{i\alpha} \cdot \vec{s}_{i\beta} \ \rightarrow \ -2J \sum_{i,\alpha<\beta} \hat{s}_{i\alpha}^{z} \hat{s}_{i\beta}^{z}. \tag{6.8}$$

This apparent breaking of $SU(2)$ invariance can be restored by defining the spin quantization axis locally. The fact that the spin-quantization axis is not the same at all sites implies that the hopping no longer conserves the new spin. Instead, hopping acquires as spin-dependent factor $t_{ij}^{\alpha\beta} \rightarrow t_{ij}^{\alpha\beta\sigma\sigma'} = t_{ij}^{\alpha\beta} u_{ij}^{\sigma\sigma'}$, [28] with

$$u_{ij}^{\uparrow\uparrow} = c_i c_j + s_i s_j e^{-i(\phi_i - \phi_j)}, \tag{6.9}$$

$$u_{ij}^{\downarrow\downarrow} = c_i c_j + s_i s_j e^{i(\phi_i - \phi_j)}, \tag{6.10}$$

$$u_{ij}^{\sigma\bar{\sigma}} = \sigma(c_i s_j e^{-i\sigma\phi_j} - c_j s_i e^{-i\sigma\phi_i}),$$

where $\bar{\sigma} = -\sigma$ and $c_i = \cos\theta_i/2$, $s_i = \sin\theta_i/2$ and the set of angles $\{\theta_i\}$ and $\{\phi_i\}$ are the polar and azimuthal angles corresponding to $\{\vec{s}_i\}$, respectively. As one can see, these effective hoppings can become complex, and it has been shown that non-coplanar spin configurations can endow the electronic bands with a nontrivial topology. [30,85] Additionally, the itinerant electrons mediate an interaction between the localized spins, which typically competes with antiferromagnetic spin-spin interactions; on frustrated lattices, this competition can resolve itself in non-coplanar – and thus topologically nontrivial – phases [30–32,100]. There is no reason for spins in different orbitals, but on the same site, to point in different directions, as the only interactions between spins are FM, i.e., we can use the same local quantization axis for all orbitals, which is why we decomposed $t_{ij}^{\alpha\beta} \rightarrow t_{ij}^{\alpha\beta} u_{ij}^{\sigma\sigma'}$. In the case of doubly occupied orbitals, one spin can be seen as lying antiparallel and from now on "↑" ("↓") denotes a spin parallel (antiparallel) to the local quantization axis.

The mean-field decoupling then takes the specific form

$$U \sum_{i,\alpha} \hat{n}_{i\alpha\uparrow}\hat{n}_{i\alpha\downarrow} \rightarrow U \sum_{i,\alpha} \langle \hat{n}_{i\alpha\uparrow}\rangle \hat{n}_{i\alpha\downarrow} + \hat{n}_{i\alpha\uparrow}\langle \hat{n}_{i\alpha\downarrow}\rangle - \langle \hat{n}_{i\alpha\uparrow}\rangle \langle \hat{n}_{i\alpha\downarrow}\rangle$$

$$(U' - \frac{J}{2}) \sum_{i,\alpha<\beta} \hat{n}_{i\alpha}\hat{n}_{i\beta} \rightarrow (U' - \frac{J}{2}) \sum_{i,\alpha<\beta} \langle \hat{n}_{i\alpha}\rangle \hat{n}_{i\beta} + \hat{n}_{i\alpha}\langle \hat{n}_{i\beta}\rangle - \langle \hat{n}_{i\alpha}\rangle \langle \hat{n}_{i\beta}\rangle$$

$$-2J \sum_{i,\alpha<\beta} \hat{s}_{i\alpha}^z \hat{s}_{i\beta}^z \rightarrow -2J \sum_{i,\alpha<\beta} \langle \hat{s}_{i\alpha}^z\rangle \hat{s}_{i\beta}^s + \hat{s}_{i\alpha}^z\langle \hat{s}_{i\beta}^z\rangle - \langle \hat{s}_{i\alpha}^z\rangle \langle \hat{s}_{i\beta}^z\rangle \quad (6.11)$$

Due to the last term Eq. (6.3), an electron in orbital β feels a FM coupling to a "classical localized spin" with length $\sum_{\alpha\neq\beta}\langle \hat{s}_{i\alpha}\rangle$ that points along the local quantization axis.

6.4 Mean field phase diagram

We use numerical optimization routines to find the spin pattern with the lowest energy among all orderings with unit cells of up to four sites, including all patterns considered in Ref. [31] of the main text. We search for mean-field solutions which break translational symmetry such that the unit cell is either tripled or quadrupled. In each step, the mean-field energy is calculated self-consistently for a lattice of 16×16 (four-site unit cell) or 24×16 (three-site unit cell). (For selected points in parameter space, we also used larger lattices and did not find a significant difference.) In order to minimize the impact of our approximations on the symmetries of the orbital degrees of freedom, we perform the mean-field decoupling in the $\{a_{1g}, e'_{g+}, e'_{g-}\}$ basis, where the symmetry between the half-filled e'_{g+} and the quarter-filled a_{1g} orbitals (for the fillings discussed here) is already broken by the crystal field. We verified that decoupling directly in the $\{xy, xz, yz\}$ basis, where all three orbitals have the same electronic density, leads to qualitatively identical and quantitatively very similar results.

For simplicity, we present here results for $J/U = 1/4$ and the relation $U' = U - 2J$ between the Kanamori parameters was used, but we have verified that the results presented remain robust for other choices.

For wide parameter ranges (see below), the ground state is the non-coplanar spin-chiral phase illustrated in Fig. 6.4(a,b). As demonstrated in the context of the Kondo-lattice model [30, 31], this magnetic order leads to topologically nontrivial bands, which can also be seen in the one-particle bands shown in Fig. 6.4(c). The chemical potential lies within the a_{1g} states of the lower Hubbard band, where the electron spin is mostly parallel (labelled by $\uparrow$) to the direction defined by the spin-chiral pattern.

(a)

(b)
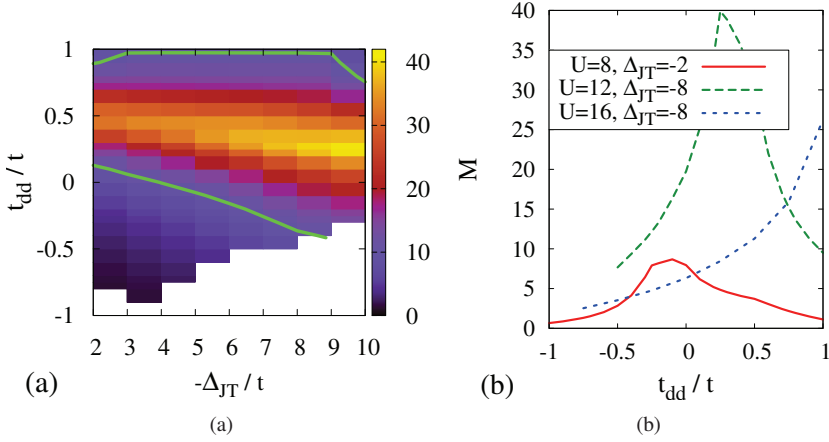
Figure 6.3: Stability of the spin-chiral phase and flatness of the topological bands depending on parameters of the Hamiltonian. In (a), shaded areas in the t_{dd}-Δ_{JT} plane indicate a spin-chiral ground state Fig. 6.4(a,b) for $U/t = 12$, white areas have a different ground state. Shading indicates the figure of merit M for the flatness of the upper chiral subband, bright thick lines bound the region with $M \geq 10$. (b) shows M depending on t_{dd} for selected sets of U and Δ_{JT}. Where the "Mott gap", which separates the flat topologically non-trivial band from the upper Hubbard band, becomes very small, M is determined by the minimal gap separating the band of interest from other bands. $J = U/4$ and $t = 1$ were used in all cases.

Dashed and dotted lines decorate states living on the top and bottom edges of a cylinder, they cross the chiral gap exactly once as one left- and one right-moving edge mode, indicating the different Chern numbers associated with the two bands directly above and below the chemical potential.

Figure 6.4(c) also indicates that the upper chiral subband has a very small width, ~ 14 times smaller than the chiral gap. One can quantify the band flatness by a figure of merit M given by the ratio of the gap to the band width. Its dependence on various parameters of the Hamiltonian is shown in Fig. 6.3. It peaks at $M > 40$, but the more striking observation is that it is above 5 or even 10 for wide ranges of U, Δ_{JT} and t_{dd}, in contrast to many other proposals that require carefully fine-tuned parameters [87, 104, 106, 108, 113, 130, 131]. Nearly flat chiral bands are thus very robust in this system and both their topological character and their flat dispersion emerge spontaneously with purely onsite interaction and short-range hopping, without spin-orbit
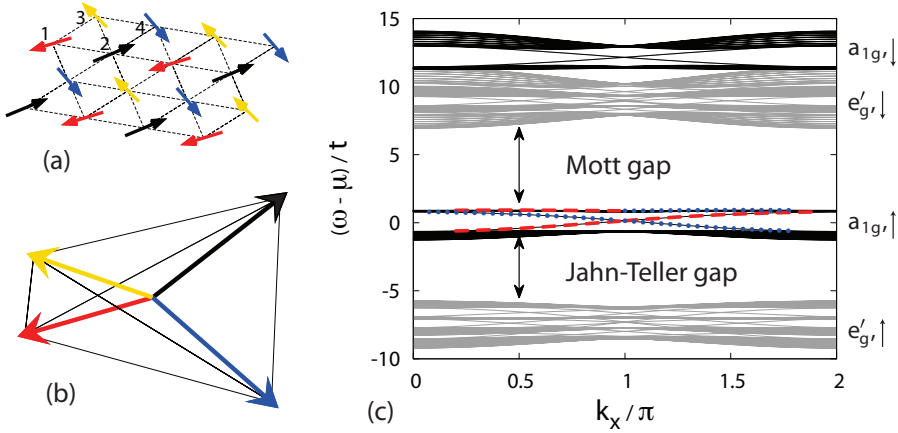
Figure 6.4: (Color online) Spin-chiral magnetic phase with topologically nontrivial bands stabilized by onsite Coulomb interactions in t_{2g} electrons on a triangular lattice. (a) Chiral magnetic order, the sites of the unit cell are labeled by 1 to 4. (b) The spins on the four sites can be seen as pointing to the corners of a tetrahedron, i.e., the pattern is non-coplanar. (c) One-particle energies on a cylinder (periodic boundary conditions along x) in the mean-field ground state of the t_{2g} multiorbital Hubbard model, which is given by the pattern shown in (a). States drawn in black (grey) have more (less) than 33% a_{1g} character, dashed and dotted lines indicates edge states with more than 33% of their weight on the top (bottom) row of sites. The arrows $\uparrow$ ($\downarrow$) indicate states with electron spin mostly (anti-)parallel to the local quantization axis, which can be seen as the lower (upper) Hubbard band. The filling is 2.5 electrons per site, slightly less than half filling. Parameters used were $t = 1$, $t_{dd} = 0$, $U/t = 12$, $J/t = 3$, $\Delta_{\mathrm{JT}}/t = -6$. The figure of merit M, which is given by the ratio of the gap separating the two a_{1g} subbands of the lower Hubbard band and the band width of the highest subband of the lower Hubbard band, is $M \approx 14$.

coupling or any explicit breaking of time-reversal symmetry.

In order to understand the origin of the spin-chiral state, it is helpful to look at the one-band Kondo-lattice model (KLM), which describes itinerant electrons coupled to localized spins. The KLM supports spin-chiral phases because of frustration between ferromagnetism (driven by double exchange, i.e., the kinetic energy of the electrons) and antiferromagnetism (driven by superexchange between the localized spins) on many frustrated lattices like the triangular [30–32, 100], pyrochlore [33], and face-centered cubic [29] lattices. Our model can be related to the KLM by noting that the half-filled e'_g levels are far from the chemical potential and act as a localized spin to which the electrons in the a_{1g} orbital are coupled via Hund's rule coupling. The antiferromagnetic superexchange arises through excitations into the upper Hubbard band. Consequently, it is suppressed by a larger Mott gap and the ground state becomes ferromagnetic for $U \gtrsim 24|t|$, as in the KLM with a large Kondo gap [31, 100]. In a large window $6 \lesssim U/|t| \lesssim 24$, the balance of kinetic energy and superexchange stabilizes a spin-chiral ground state and flat bands with $M > 5$ are found for a window of $8 \lesssim U/|t| \lesssim 20$.

Finally, we note that the fact that onsite interactions U and J are only large, but *not* infinite, is important for the spin-chiral ground state: For very large U and J, the ground state becomes a ferromagnet. [107] This can be related to the fact that the Kondo-lattice model requires either finite J_{Kondo} [31] or additional AFM inter-site superexchange [32] to support a spin-chiral instead of a FM state. At finite onsite interactions, virtual excitations with doubly occupied e'_g orbitals are possible and lead to second-order processes that are similar to the effective longer-range hoppings discussed above. In such a process, an e'_g electron hops into an occupied e'_g state at a NN site, creating a (virtual) intermediate state with energy $\propto U + J \approx U' + 3J$, and hops back in the next step. Such a process yields an energy gain $\propto t^2_{e'_g}/(U + J)$ and is only possible if the spins of the two involved electrons, which occupy the same orbital in the intermediate state, are opposite. The mechanism thus effectively provides the needed AFM intersite superexchange and the spin-chiral state becomes stable for wide parameter regimes, including ranges supporting nearly flat upper chiral sub-bands. [107]

6.5   Conclusions

The possibility of a spontaneous FQH effect without a magnetic field is currently intensely discussed, and various models have been suggested [87, 104, 106, 108, 113, 130, 131]. In these proposals, the necessary topological character of the bands was introduced by hand, the flatness of the bands needed fine-tuning and the underlying lattices were often rather exotic; an experimental realization appears therefore chal-

lenging. We have shown here that in strongly correlated t_{2g} orbitals on a triangular lattice, bands with the desired properties emerge spontaneously for wide parameter ranges and support FQH ground states. Both t_{2g} systems and triangular lattices occur in various TM oxides, and signatures of the unconventional *integer* QH state have been reported for a triangular-lattice palladium-chromium oxide [80]. This harbors the prospect that a suitable material can be synthesized in this highly versatile material class. As such a material is by default strongly correlated, one also naturally expects an inter-site Coulomb repulsion that is strong enough to stabilize spontaneous FQH states in the absence of a magnetic field.

CHAPTER 7

TRIANGULAR LATTICE FRACTIONAL CHERN INSULATOR MODEL

7.1 Introduction

The Fractional Quantum Hall effect is one of the most peculiar and intriguing states of matter. Discovered in 1982 [10], not very long after the Integer Quantum Hall effect [75], it has continued to fascinate condensed matter physicists until the present day. The key experimental characteristic of the integer quantum Hall effect is the emergence of quantum Hall plateaus, plateaus in the off diagonal Hall conductivity σ_{xy} as function of magnetic field at integer multiples of the quantum of conductance e^2/h, while the longitudinal conductivity vanishes. At particularly strong magetic fields, plateau structures are observed at non-integer, i.e. fractional (for the purpose of this chapter we will assume rational, p/q) values and these are known as the Fractional Quantum Hall effect. While the integer effect can be understood purely in terms of single-particle state physics (see also Chapter 1), its fractional counterpart is a consequence of electron-electron interaction. Even more, as the degeneracy of a magnetic Landau level scales with the magnetic field, in a very strong magnetic field all electrons will be in the lowest Landau level (LLL) and the repulsive Coulomb interaction will be the only remaining energy scale. Hence, even though superficially similar judging from their experimental signature, the integer and fractional

Quantum Hall effect are fundamentally distinct, with the fractional QHE presenting a much more difficult problem due to its quartic Hamiltonian structure.

The fascination with the Fractional Quantum Hall effect derives from its special features as a rather exotic quantum state of matter. The fractional Quantum Hall state constitutes an incompressible liquid, which sets it apart from states of matter that are classified according to broken symmetries represented by a local order parameter. An example of the latter, which naturally competes with the fractional Quantum Hall state in the presence of strong electron repulsion, is the Wigner crystal, a charge ordered state. The fractional Quantum Hall ground state is topologically ordered, implying a ground state degeneracy which depends on the topology of the manifold on wich it lives (torus, sphere, ect.). The FQH effective field theory is therefore not of Ginzburg-Landau type, but is instead a topological Chern-Simons field theory accounting phenomenologically for its physical characterics. In addition, the quasi-particles of these states have fractional charge and obey anyonic statistics, [138, 139] which can be either Abelian or non-Abelian, the latter fulfilling an essential condition for fault-tolerant quantum computation. [129]. In particular these quasiparticle properties have attracted a great deal of attention and have triggered considerbable effort in uncovering the deep physics of the FQHE.

As a consequence of the recent and tremendous surge in interest in topological states of matter, caused by the discovery of topological insulators [12, 111], new directions in fractional quantum Hall physics have been explored. In particular, since the topological insulators can be regarded as generalizations of the quantum anomalous Hall insulator, which belongs to the IQH universality class, the following question presented itself: can the FQHE be generalized to situations where external magnetic fields are absent and lattice effects cannot be ignored? This question was first addressed by [87, 108, 113]. In case of the continuum FQHE, Hilbert space is organized according to the Landau level spectrum which originates from the magnetic field. Adding interactions to the LLL yields the FQHE. In case of a lattice model described by a tight-binding hamiltonian $\hat{H}$ the first prerequisite for any hope of a possible generalized FQHE is the presence of isolated bands with nontrivial topology. Or, in other words, the band structure corresponding to $\hat{H}$ needs consist of a band with nonzero Chern number C (see Chapter 1), separated from other bands by a full energy gap. That such Hamiltonians exist in principle has been demonstrated already long ago by Haldane in 1988 [76], but the past decade has witnessed an impressive effort in devising proposals for realizing such a Hamiltonian in experimentally accessible conditions. One such realization may be found in strongly spin-orbit coupled semiconductor materials that are ferromagnetically ordered [77, 82]. Another possibility arises through the coupling of itinerant electrons to localized magnetic moments [85], for example the Kondo-lattice model on the triangular lattice supports a non-trivial magnetic texture, which induces an integer-quantized Hall conductivity of the itin-

erant electrons [30]. Note that nonzero Chern number C immediately implies the breaking of time-reversal symmetry, which is reassuring, as the uniform magnetic field breaks time-reversal in the continuum.

While the above is unambiguously sufficient to generalize integer quantum Hall physics to lattice systems without fields, fractional quantum Hall physics puts more restrictions on potential generalization schemes. If we focus on a band that has nonzero Chern number (is has become custom to call such a band *Chern band*), and compare it more closely to a Landau level, we observe that the Chern band is generally dispersive, a Landau level however is perfectly flat, i.e. all single-particle states have the same energy. This is of considerable significance, as it renders the interactions to be the only energy scale of the problem en thus by definition the dominant one. The interactions select the fractional quantum Hall liquid out of the macroscopically degenerate manifold of single-particle states. Adding interactions to a Chern band would seem to lead to a competition between kinetic and interaction energy scales, which potentially spoils the emergence of a liquid state. Hence, in order for the Chern band to mimic the Landau level as much as possible, one should require the former to have a very small bandwidth W as compared to the interaction strength V. To put it differently, minimally dispersive or *flat* Chern bands are expected to be the best candidates for hosting a lattice FQHE. Furthermore, the ordinary FQHE is most clearly observed in a strong magnetic field, which causes a large energy gap between Landau levels and concentrates all electrons in the LLL. Landau level mixing is negligible. It would consequently seem natural to demand that that band gap Δ which separates the Chern band from any other band is much larger than the interaction energy scale V. Summarizing, the following hierarchy of energy scales would need to be fulfilled to provide proper conditions for fractional quantum Hall physics confined to a Chern band

$$\Delta \gg V \gg W, \quad F \equiv \Delta/W \gg 1. \tag{7.1}$$

With this perspective in mind, the first studies of FQH generalization were undertaken [87, 104, 105, 108, 113, 131, 140]. Chern insulator models with the correct energy scale hierarchy were identified and first signatures of fractional quantum Hall type physics were obtained with numerical methods. Starting from a Chern insulator given by the non-interacting Hamiltonian

$$\hat{H}_{\text{CI}} = \sum_{\vec{K}} \hat{\psi}_\alpha^\dagger(\vec{k}) \mathcal{H}^{\alpha\beta}(\vec{k}) \hat{\psi}_\beta(\vec{k}), \tag{7.2}$$

interactions were added by including

$$\hat{H}_{\text{int}} = \sum_{ij} V_{ij}^{\alpha\beta} \hat{n}_{i\alpha} \hat{n}_{j\alpha} = \sum_{\vec{q}} V^{\alpha\beta}(\vec{q}) \hat{\rho}_\alpha(\vec{q}) \hat{\rho}_\beta(-\vec{q}), \tag{7.3}$$

and the standard approach has been to isolate the Chern band explicitly and project the interactions into that band. This requires normal ordering first and then projecting onto band n with corresponding energy $E_n(\vec{k})$, obtained afterdiagonalization of the Bloch Hamiltonian $\mathcal{H}(\vec{k})$. The eigenstates are $|\vec{k}, n\rangle = \hat{\gamma}_n^\dagger(\vec{k})|0\rangle$. The normal mode operators and orbital operators are related by a matrix $U(\vec{k})$ that contains the eigenvectors of the matrix $\mathcal{H}(\vec{k})$ in its columns, $\hat{\gamma}_n^\dagger(\vec{k}) = \hat{\psi}_\alpha^\dagger(\vec{k})U_{\alpha n}(\vec{k})$ with $\mathcal{H}_{\alpha\beta}(\vec{k})U_{\beta n}(\vec{k}) = E_n(\vec{k})U_{\alpha n}(\vec{k})$. The interaction becomes

$$\hat{H}_{\text{int}} = \frac{1}{N} \sum_{\vec{k},\vec{k}'} \sum_{\vec{q}} V^{\alpha\beta}(\vec{q})\hat{\psi}_\alpha^\dagger(\vec{k}+\vec{q})\hat{\psi}_\beta^\dagger(\vec{k}'-\vec{q})\hat{\psi}_\beta(\vec{k}')\hat{\psi}_\alpha(\vec{k})$$

$$= \frac{1}{N} \sum_{\vec{k},\vec{k}'} \sum_{\vec{q}} V^{n_1 n_2 n_3 n_4}(\vec{q}, \vec{k}, \vec{k}')\hat{\gamma}_{n_1}^\dagger(\vec{k}+\vec{q})\hat{\gamma}_{n_2}^\dagger(\vec{k}'-\vec{q})\hat{\gamma}_{n_3}(\vec{k}')\hat{\gamma}_{n_4}(\vec{k}) \qquad (7.4)$$

with

$$V^{n_1 n_2 n_3 n_4}(\vec{q}, \vec{k}, \vec{k}') =$$
$$\sum_{\alpha,\beta} V^{\alpha\beta}(\vec{q})U_{n_1\alpha}^\dagger(\vec{k}+\vec{q})U_{n_2\beta}^\dagger(\vec{k}'-\vec{q})U_{\beta n_3}(\vec{k}')U_{\alpha n_4}(\vec{k}). \qquad (7.5)$$

From the general form of this expression it is clear that the interaction contains interband scattering events. With the separation of energy scales properly in place it has become common practice to focus exclusively on the given Chern band n, neglecting the its dispersion, i.e. $E_n(\vec{k}) \to \overline{E}_n$ and keeping only the terms $n_1 = n_2 = n_3 = n_4 = n$. This approach, which then lends itself to exact diagonalization (ED) studies is in contrast to the method explained later in this chapter and implemented in [107, 141]. In the final section of this chapter we discuss the numerical signatures of FQH physics in these Chern insulators in somewhat more detail.

In the wake of these first steps towards a lattice generalization of the FQHE – quickly dubbed the *Fractional Chern Insulator* (FCI) – the question of what constitutes good Chern bands has been addressed in more detail. Is it just the hierarchy of energy scales in a Chern insulator, or can and should one identify constraints of an entirely different quality? This specific question was first considered by [142] and soon after reconsidered by [143–145]. The central results of these works is the derivation of constraint on Berry curvature fluctuations of the Chern insulator model. The key idea is that in the continuum the density operators projected onto the LLL satisfy the GMP algebra (see again Chapter 1) and in order to keep the analogy with the LLL upright, the density operators of a Chern insulator projected into the (nearly flat) Chern band, should obey an equivalent algebraic relation. The orbital dependent

density operator is given by

$$\hat{\rho}_\alpha(\vec{q}) = \frac{1}{\sqrt{N}} \sum_{\vec{k}} \hat{\psi}^\dagger_\alpha(\vec{k}+\vec{q})\hat{\psi}_\alpha(\vec{k}), \qquad (7.6)$$

and projecting this into the Chern band labeled by n, summing over α, gives

$$\tilde{\rho}(\vec{q}) \equiv \hat{P}_n\hat{\rho}(\vec{q})\hat{P}_n = \frac{1}{\sqrt{N}} \sum_{\vec{k},\alpha} U^\dagger_{n\alpha}(\vec{k}+\vec{q})U_{\alpha n}(\vec{k})\hat{\gamma}^\dagger_n(\vec{k}+\vec{q})\hat{\gamma}_n(\vec{k}) \qquad (7.7)$$

The central result obtained from aforementioned investigation of the algebraic relations of projected density operators is that in the long wave-length limit, i.e. $\vec{q}, \vec{w}$ small, and in cases when the Berry curvature may be approximated by its average, the $\tilde{\rho}(\vec{q})$ satisfy

$$[\tilde{\rho}(\vec{q}), \tilde{\rho}(\vec{w})] \approx -i(\vec{q} \times \vec{w}) \cdot \hat{z} \frac{2\pi C}{(2\pi/a)^2} \tilde{\rho}(\vec{q}+\vec{w}). \qquad (7.8)$$

This is identical to the long wave-length limit of the GMP algebra obeyed by projected density operators in the LLL. The crucial insight that the algebra of density operators reveals, is that once the GMP is valid in the Chern band for long wave-lengths, one may assume it to be valid at all wave-lengths in the thermodynamic limit, thereby establishing an a posteriori correspondence between the FCI and the FQH physics [142, 143].

Having discussed in considerable detail the prerequisites for FCI physics in Chern insulators, we state the purpose and content of this chapter. Previous chapters have demonstrated how nearly flat topological bands can arise in multi-orbital models of correlated oxides. In this chapter we map the multi-orbital model onto an effective single-orbital model, which nevertheless captures the essential features of the Chern insulator and subsequently can be used for detailed numerical study into possible FCI signatures. It will be argued that obtained triangular lattice Chern insulator shows robust features of FCI physics.

7.2 Multi-orbital nearly flat band model

In previous chapters it was shown that both e_g and t_{2g} orbital manifolds in octahedral coordination can reduce the bandwidth of topologically nontrivial bands. For a schematic illustration of orbital degeneracy in d-electron systems see Fig. 6.2. In particular, this was discussed for the spin-chiral phase arising in Kondo-lattice models on the triangular lattice at quarter and three-quarter fillings. While the flat band of

interest mixes both the $3z^2 - r^2$ and the $x^2 - y^2$ orbitals in the e_g case, it is dominated by a particular orbital state in the t_{2g} manifold, the a_{1g} state. We recall that the trigonal crystal field splits the t_{2g} manifold in an e'_g-doublet and the nondegenerate a_{1g} level. The fact that the flat mean-field Chern band of the multi-orbital model has predominantly a_{1g} character suggests that one may capture the essential physics. The program of this chapter is to systematically arrive at a simple Chern insulator model that may be used for extensive numerical calculations probing its suitability as host of FCI states. We will start from realistic multi-orbital models, in particular the band structure obtained from the mean-field treatment of local Coulomb interaction terms, as detailed in the previous chapter.

We focus exclusively on the t_{2g} triangular lattice model. In addition to an orbital degree of freedom, we consider coupling to a localized spin $\vec{S}_i$, modelled by a Kondo-lattice model, where the kinetic energy is given by hopping elements $t_{ij}^{\alpha\beta}$ taken from the matrices Eq. (6.1) or Eq. (6.4). This situation is described by

$$\hat{H} = \sum_{\langle i,j \rangle, \sigma} t_{ij}^{\alpha\beta} \hat{\psi}_{i\sigma\alpha}^{\dagger} \hat{\psi}_{j\sigma\beta} - J_{\text{Kondo}} \sum_{i,\alpha} \vec{S}_i \cdot \vec{\hat{s}}_{i\alpha} \qquad (7.9)$$

where α and β are orbital indices, $\hat{\psi}_{i\sigma\alpha}$ ($\hat{\psi}_{i\sigma\alpha}^{\dagger}$) annihilates (creates) an electron with spin σ in orbital α at site i, and $\vec{\hat{s}}_{i\alpha}$ is the corresponding vector of orbital electronic spin operators. J_{Kondo} couples the itinerant electrons to a generic localized spin $\vec{S}_i$, the origin of which is left unspecified for the moment, but will be discussed extensively later. (It will turn out to be the spin degree of freedom of the t_{2g} electrons themselves, as may be expected from 6). The coupling is assumed to be FM, as one would expect from Hund's-rule coupling. However, we are furthermore going to consider $\vec{S}_i$ as a *classical* spin, in which case AFM coupling to $\vec{S}_i$ would lead to the equivalent results.

7.2.1 Integrating out the spin-degree of freedom

For classical spins and large J_{Kondo}, it is convenient to go over to a *local* spin-quantization axis, where "↑" ("↓") refers to parallel (antiparallel) orientation of the electron's spin to the local axis. This simplifies the Kondo term to

$$\hat{H}_{\text{Kondo}} = -J_{\text{Kondo}} \sum_{i,\alpha} \vec{S}_i \cdot \vec{\hat{s}}_{i,\alpha} = -\frac{J_{\text{Kondo}}}{2} \sum_{i,\alpha} (\hat{n}_{\alpha\uparrow} - \hat{n}_{\alpha\downarrow}) , \qquad (7.10)$$

where $\hat{n}_\alpha^\uparrow$ ($\hat{n}_\alpha^\downarrow$) is the electron density at site i in orbital α with spin (anti-) parallel to the localized spin. This local spin definition is particularly convenient when going to the limit of large J_{Kondo}, where one immediately finds the low-energy states as given by only "↑" electrons.

On the other hand, the fact that the spin-quantization axis is not the same at all sites implies that the hopping no longer conserves the new spin. Instead, hopping acquires as spin-dependent factor $t_{ij}^{\alpha\beta} \to t_{ij}^{\alpha\beta\sigma\sigma'} = t_{ij}^{\alpha\beta}u_{ij}^{\sigma\sigma'}$, [28] with

$$u_{ij}^{\uparrow\uparrow} = c_i c_j + s_i s_j e^{-i(\phi_i - \phi_j)}, \tag{7.11}$$

$$u_{ij}^{\downarrow\downarrow} = c_i c_j + s_i s_j e^{i(\phi_i - \phi_j)}, \tag{7.12}$$

$$u_{ij}^{\sigma\bar{\sigma}} = \sigma(c_i s_j e^{-i\sigma\phi_j} - c_j s_i e^{-i\sigma\phi_i}),$$

where $\bar{\sigma} = -\sigma$ and $c_i = \cos\theta_i/2$, $s_i = \sin\theta_i/2$ and the set of angles $\{\theta_i\}$ and $\{\phi_i\}$ are the polar and azimuthal angles corresponding to $\{\vec{S}_i\}$, respectively. As one can see, these effective hoppings can become complex, and it has been shown that non-coplanar spin configurations can endow the electronic bands with a nontrivial topology [30, 85].

In line with the approach extensive outlined elsewhere in this thesis, we may assume strong coupling between the local moments and the itinerant electrons and take the limit of infinite Hund's rule coupling. In this case, one only keeps the $\uparrow$ electrons parallel to the local spin-quantization axis and electrons effectively become spinless fermions. For the chiral spin pattern in Fig. 6.4, which has been found as the ground state of triangular Kondo-lattice models [30–32, 100], the Berry phases between the four sites of the magnetic unit cell can be parametrized as

$$u_{1,2}^{\uparrow\uparrow} = u_{3,4}^{\uparrow\uparrow} = \frac{1}{\sqrt{3}}, \quad u_{1,3}^{\uparrow\uparrow} = -u_{2,4}^{\uparrow\uparrow} = \frac{1}{\sqrt{3}} \tag{7.13}$$

$$u_{2,3}^{\uparrow\uparrow} = u_{4,1}^{\uparrow\uparrow} = -u_{3,2}^{\uparrow\uparrow} = -u_{1,4}^{\uparrow\uparrow} = \frac{i}{\sqrt{3}}.$$

Constructing the tight-binding hopping Hamiltonian from these effective hoppings of the now effectively spinless fermions (which still have an orbital degree of freedom) reveals that even though the unit cell corresponding to the spin configuration contains four sites, the unit cell of the fermions can be reduced to two sites.

Combining the phases Eq. (7.13) with the hoppings given by Eqs. (6.1) or (6.4) and the crystal-field splitting Eq. (6.2) still gives a non-interacting model that can be easily solved in momentum space. One finds that large $|\Delta_{JT}|$, see Eq. (6.2), strongly reduces the dispersion of one subband. This can also be seen in Fig. 7.1(a), which shows the one-particle energies obtained on a cylinder. Figure 7.1(a) also reveals the edge states crossing some gaps, indicating the topologically nontrivial nature of these bands. Calculating Chern numbers C corroborates this and gives $C = \pm 1$. The band flatness can be expressed in terms of a figure of merit

$$F = \frac{\min(\overline{\Delta}_{JT}, \Delta_c)}{W}, \tag{7.14}$$
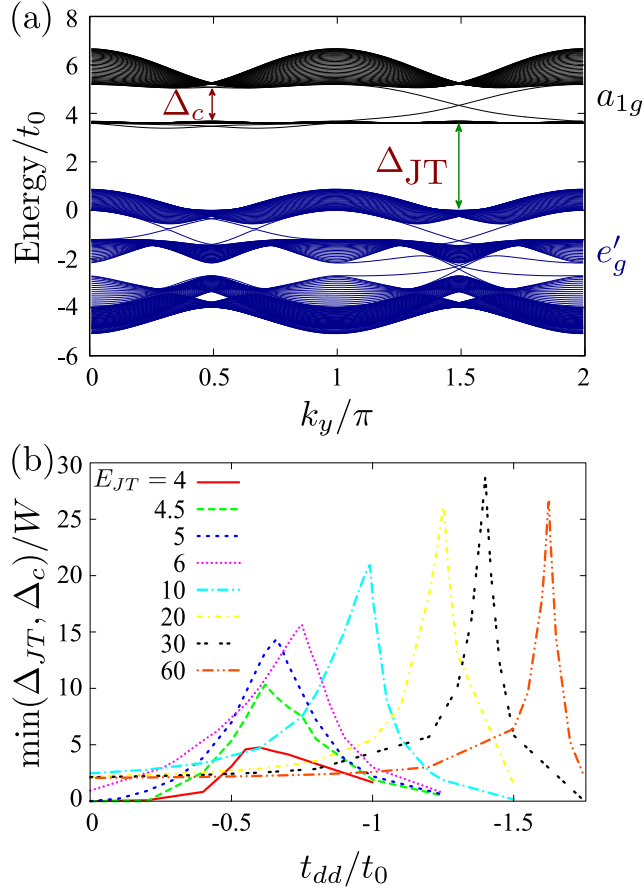
Figure 7.1: Flat lower chiral subband in the Kondo-lattice model with infinite Hund's rule coupling (double-exchange model). (a) Shows the one-particle energies of three t_{2g} orbitals coupled to localized spins, where the latter form a spin-chiral phase on a triangular lattice, [30–32, 100] see Fig. 6.4. The system is a cylinder, i.e., periodic boundary conditions along y-direction and open boundaries along x. The horizontal axis is the momentum in the direction with periodic boundaries. The gaps Δ_{JT} and Δ_c denote the gaps due to crystal-field splitting E_{JT} and to the chiral spin state. (b) shows the figure of merit M, see Eq. (7.14), for the lower a_{1g} subband. The curves for crystal-field splittings $E_{\mathrm{JT}} = 4, 4.5$, and 5 were already given in Fig. 3(b) of Ref. [**?**] and are repeated here for convenience.

where $\overline{\Delta}_{\text{JT}}$ and Δ_c are the two gaps separating the narrow band of interest from the other orbitals and from the subband with opposite Chern number and W is the width of the narrow band. As was pointed out in chapter 5, the lower subband can here become very flat, and as can be seen in Fig. 7.1(b), the flatness can be further improved by going to larger crystal fields and reaches values $M \approx 28$.

7.2.2 Integrating out the orbital degree of freedom

As these very flat bands can be achieved for large separation E_{JT} between the a_{1g} and e'_g states and as the band of interest then has almost purely a_{1g} character, it is natural to assume that one should be able to capture the most relevant processes with an effective a_{1g} model. (This is in contrast to the situation starting from e_g orbitals, where one finds intermediate E_{JT} to be optimal. In that case, the nearly flat bands can only be obtained if *both* orbitals contribute weight and one cannot easily reduce the situation to a one-band system.)

The impact of the e'_g levels on the effective a_{1g} dispersion can be taken into account in second-order perturbation theory. This includes processes where a hole hops from the a_{1g} orbital at site i to an e'_g state at j and back again to an a_{1g} state at a third site i', which may or may not be the same as i. The denominator of these terms is the crystal-filed energy E_{JT} and the numerator is obtained from the products $\widetilde{T}^{ab}_i \widetilde{T}^{ba}_j + \widetilde{T}^{ac}_i \widetilde{T}^{ca}_j$ (with a designating a_{1g} and b, c the e'_g states). In order to evaluate the second-order hopping between sites i and i', these orbital hoppings have to be multiplied by the product of the Berry phases $u^{\uparrow\uparrow}_{i,j}$ and $u^{\uparrow\uparrow}_{j,i'}$ from Eq. (7.13) for all paths connecting i and i' via one intermediate site $j \neq i, i'$. Due to destructive interference, processes connecting NN and next-nearest neighbor (NNN) sites cancel while effective third-neighbor hopping, where there is only one path, remains. Since third-neighbor spins in the chiral phase are always parallel, the total Berry phase of this process is 1 in all directions, however, the hopping via a spin of different orientation in the middle reduces the hopping amplitude by $|u^{\uparrow\uparrow}|^2 = 1/3$, leading to

$$t_3 = -\frac{2(t_0 - t_{dd})^2}{27\Delta_{\text{JT}}} \ . \tag{7.15}$$

A third-neighbor hopping $\propto \sum_i \cos 2\vec{k} \cdot \vec{a}_i$ turns out to have almost the same dispersion as the chiral subbands and can consequently almost cancel it in one subband. As its strength can be tuned by t_{dd} and Δ_{JT}, very flat subbands can be achieved, see Fig. 7.1(b).
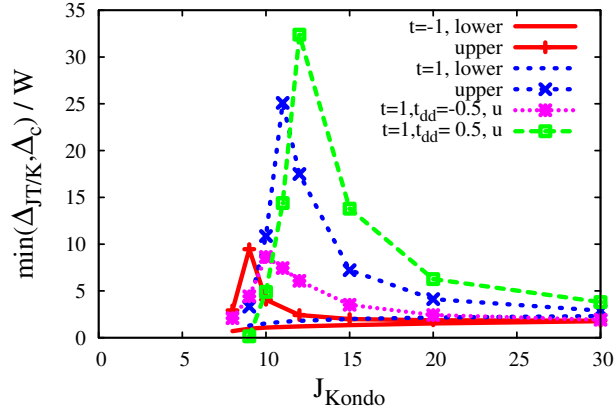
Figure 7.2: Figure of merit M, see Eq. (7.14), for finite Hund's-rule coupling J_{Kondo}/t_0 and $E_{\text{JT}} = 6t_o$. The bands designated as "upper" and "lower" refer to the two subbands of the a_{1g} states with spin parallel to the localized spin, which are separated by the gap opening in the spin-chiral phase, see Fig. 7.1(a).

7.2.3 Mapping the mean-field solution to a Chern insulator

While the previous section has illustrated how one can understand the occurrence of nearly flat bands in a three-orbital double-exchange model, i.e., for infinite Hund's rule coupling to some localized spins, this section will discuss finite Hund's rule and take the single-particle spectrum obtained from the mean-field calculation as a starting point for deriving an effective hopping model. Figure 7.2 shows the figure of merit for the band flatness Eq. (7.14) for a few sets of hopping parameters and for $\Delta_{\text{JT}} = 6t_0$ depending on Hund's rule coupling J_{Kondo} to the localized spin, see Eq. (7.10). As can be seen in Fig. 7.2, the *upper* subband of the a_{1g} sector can now become nearly flat. (For $J_{\text{Kondo}} \gg |\Delta_{\text{JT}}|$, one can of course still find flat lower subbands, as discussed above.)

The flatness of the upper subband can be explained by similar effective longer-range hoppings in second-order perturbation theory, this time also taking into account intermediate states with an electron in the upper Kondo band, i.e. with antiparallel spin. These additional terms can go either via the a_{1g} or via the e'_g orbitals and involve combined Berry phases of the form $u_{ij}^{\uparrow\downarrow} u_{ji'}^{\downarrow\uparrow}$. Again, one has to sum over all possible

intermediate sites j and finds

$$t_1 = \frac{3t + \delta t}{3} + 2\frac{(3t + \delta t)^2}{9}\frac{1}{E_2} - 2\frac{\delta t^2}{9}\frac{1}{E_3}, \tag{7.16}$$

$$t_2 = 2\frac{(3t + \delta t)^2}{9}\frac{1}{E_2} - 2\frac{\delta t^2}{9}\frac{1}{E_3}, \tag{7.17}$$

$$t_3 = 2\frac{(3t + \delta t)^2}{27}\frac{1}{E_2} + 4\frac{\delta t^2}{27}\frac{1}{E_3} + 2\frac{\delta t^2}{27}\frac{1}{E_1} . \tag{7.18}$$

The NN, NNN and third-neighbor hoppings are here denoted by t_1, t_2, and t_3. $E_1 = \Delta_{\text{JT}}$, $E_2 = J_{\text{Kondo}}$, and $E_3 = J_{\text{Kondo}} - \Delta_{\text{JT}}$ give the excitation energies of the intermediate states with (i) a hole in the e_g' states with spin parallel, (ii) an electron in the a_{1g} states with spin anti-parallel and (iii) an electron in an e_g' state with spin anti-parallel. Like the bare NN hopping, these effective hopping-matrix elements acquire an additional Berry phase $u_{ii'}^{\uparrow\uparrow}$ in the Hamiltonian, which only depends on the relative orientation of spins on the initial and final sites. NNN hopping t_2 via the upper Kondo band does not drop out, and NN hopping becomes renormalized.

The flat chiral subbands that have been observed in a three-orbital t_{2g} Hubbard model on the triangular lattice [107] arise in situations similar to the finite-J_{Kondo} scenario. Above we have shown that a mapping to the Kondo-lattice model can be constructed and that the physics of the flat band is captured by taking the other into account perturbatively. The key point of the mapping is the observation that large crystal-field splitting Δ_{JT}, see (6.2), leads to an orbital-selective Mott-insulator, where the e_g' levels are half-filled and far from the Fermi level, while the states near the Fermi level have almost only a_{1g} character. The orbital degree of freedom is consequently quenched, because orbital occupations are already fully determined. A charge degree of freedom remains, as the a_{1g} orbital contains one electron per two sites. Charge fluctuations of the half-filled e_g levels, however, are suppressed due to the large Mott gap between their occupied and empty states. They can thus be described as a spin degrees of freedom, and the situation is further simplified, because they form a total spin with $S = 1$ due to Hund's rule. The a_{1g} electron is likewise coupled via FM Hund's rule to this spin. This situation – mobile carriers coupled via FM Hund's rule to localized spin degrees of freedom – is well described by a FM Kondo-lattice model.

7.3 Triangular lattice Chern Insulator

As we have discussed in the previous section, the most realistic route to nearly flat bands with nontrivial topology on the triangular lattice arises at finite Hubbard/Kondo
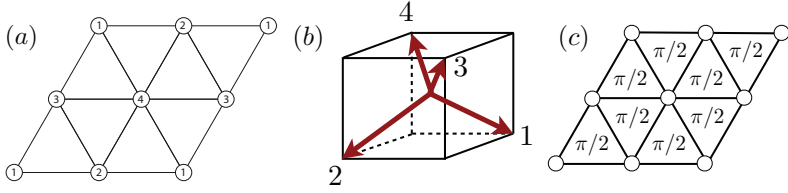
Figure 7.3: (a) Schematic illustration of the 4-site unit cell of the magnetic config-
uration on the triangular lattice where the the number labels correspond to the spins
represented in (b). (c) shows the effective single-orbital spinless model, which is that
of fermions hopping on the triangular lattice with each triangle threaded by a flux of
$\phi = \pi/2$

coupling, where effective second-neighbor hopping is generated in addition to NN
and third-neighbor terms. However, the exposition in previous sections has demon-
strated that all essential features of the band structure can be captured by using just
NN and third-neighbor hoppings. As the purpose of this chapter was to arrive a sim-
ple Chern insulator model that both captures the essential features of a more realistic
multi-orbital model of correlated oxides, and meets all requirements for showing FCI
physics, we adopt the a_{1g} model with NN and third-NN hopping for simplicity.

The essential ingredients for the triangular lattice Chern insulator model are spin-
less fermions coupled to an effective compact $U(1)$ gauge field A_{ij}. In other words,
the fermions hop in the presence of an effective flux threading the triangles. The
Hamiltonian of these fermions in momentum space is given by

$$\mathcal{H}_{\text{CI}}(\vec{k}) = 2t \sum_j \cos k_j \, \tau^j + 2t' \sum \tau^0 \cos 2k_j \, , \qquad (7.19)$$

where $\vec{a}_j$ ($j = 1, 2, 3$) denote the unit vectors on the triangular lattice, $k_j \equiv \vec{k} \cdot \vec{a}_j$, and
t and t' are the NN and third-neighbor hopping, which can be related to Eqs. (7.13)
and (7.15) for the double-exchange scenario, to Eqs. (7.16) and (7.18) for finite onsite
interactions, or which can be taken as fit parameters. Pauli matrices σ^j and unit matrix
σ^0 refer to the two sites of the electronic unit cell in the chiral state. The unit cell and
the topologically non-trivial bands are due to the symmetry breaking involved in the
underlying magnetic order. The dispersion of Eq. (7.19) is

$$E_{\pm}(\vec{k}) = \pm 2t \sqrt{\sum_j \cos^2 k_j + 2t' \sum_j \cos 2k_j}. \qquad (7.20)$$

Figure 7.3 shows pictorially how the lattice fermion model with fluxes is connected

to the spin ordered state. As panel (c) indicates, the Berry phases coming from the noncoplanar spins lead to a uniform flux arrangement that is equivalent to a uniform magnetic field perpendicular to the lattice. This is in contrast to other Chern insulator models which have a net flux of zero through the unit cell, while non-trivial fluxes do thread the individual plaquettes. This distinction must be qualified with a note of caution, however. On a lattice, the concept of "average" field is ill-defined, as one may always thread elementary flux quanta through selected plaquettes, which cannot change the physics, but does change the notion of net average field. In particular, in the present case we may group the triangles in sets of four and thread a additional flux of 2π through one of those four triangles, changing the plaquette flux to $-3\pi/2$ and making the average field zero. With this remark in mind, we choose however to think about this triangular Chern insulator model as fermions in a uniform magnetic field. From this connection we may immediately deduce that the unit cell should contain two atoms. The triangular lattice can be thought of as a square lattice with additional diagonal hoppings. It is a well established fact for the square lattice that in a magnetic field corresponding to flux $\phi = 2\pi\tilde{\phi}$, with $\tilde{\phi} = p/q$, the unit cell is q times larger. In this case a square plaquatte (two triangles) has flux $\tilde{\phi} = 1/4 + 1/4 = 1/2$ and the unit cell is doubled.

The Hamiltonian written in equation (7.19) is not in Bloch form, i.e. it does not satisfy $\mathcal{H}(\vec{k} + \vec{G}) = \mathcal{H}(\vec{k})$, where $\vec{G}$ is any reciprocal lattice vector. We wish to bring our Hamiltonian to Bloch form in order to probe to what extent we may expect this particular Chern insulator model to be a good candidate to host Fractional Chern insulator states. The introductory section already provided ways to interrogate the non-interacting Chern insulator model and will expand on that now. For convenience we make use of the aforementioned equivalence between the present Chern insulator model and lattice fermions on the square lattice in a magnetic field. The momentum space Hamiltonian of such fermions can be written as

$$\mathcal{H}(\vec{k}) = -t \begin{bmatrix} 2\cos k_y & -i(T_y T_x + T_y^*) - (1 + T_x) \\ i(T_y^* T_x^* + T_y) - (1 + T_x^*) & -2\cos k_y \end{bmatrix}, \quad (7.21)$$

with the definitions $T_x = e^{i2k_x}$ and $T_y = e^{ik_y}$. For details we refer the reader to Appendix B, and to references [146,147]. As a consequence of the flux the reciprocal lattice vectors of the magnetic Brillouin zone are $\vec{G}_1 = (\pi, 0)$ and $\vec{G}_2 = (0, 2\pi)$ in units of the inverse lattice constant. By construction, see the Appendix B, this Hamiltonian is in Bloch form.

In the introduction it was shown that fluctuations in the Berry curvature of the band one wishes to address are expected to be critical for the potential emergence and stability of FCI states resembles ordinary Fractional Quantum Hall states. We therefore calculate the Berry curvature of the occupied band of model expressed in 7.21.
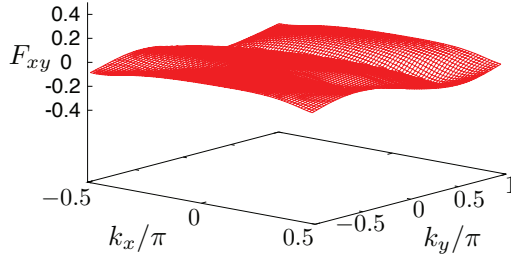
Figure 7.4: Plot of the Berry curvature in the rectified rectangular Brillouin zone of the triangular lattice Chern insulator model given by Hamiltonian (7.21).

For a tight-binding approach such as in the present case, the most convenient way to calculate the Berry curvature is borrowed from lattice gauge theory and was first introduced in [148]. The great advantage is the manifest invariance under electron wave function gauge transformations. This circumvents the cumbersome procedure of dividing the Brillouin zone in patches and finding a smooth gauge on each patch. If we take the lattice dimension in the i direction to be N_y, then we define a Brillouin zone grid of $N_x \times N_y$. We let $\vec{n} \in \mathbb{Z}_{N_x} \times \mathbb{Z}_{N_y}$ represent a site on the grid corresponding to momnetum $\vec{k} = (\pi n_x/N_x, 2\pi n_y/N_y)$. Then we define the so-called $U(1)$ *link* variables as

$$\mathcal{A}_i(\vec{n}) = \frac{\langle n, k_{\vec{n}} | n, k_{\vec{n}+\vec{u}_i} \rangle}{|\langle n, k_{\vec{n}} | n, k_{\vec{n}+\vec{u}_i} \rangle|}, \tag{7.22}$$

where $i = x, y$, $\vec{u}_i$ is unit vector in the i direction and we write $k_{\vec{n}}$ to denote the momentum $\vec{k}$ corresponding to the grid point $\vec{n}$. The field strength, or the Berry curvature, corresponding to these link variables is then expressed as

$$\mathcal{F}_{xy}(\vec{n}) = \frac{1}{2\pi} \text{Im} \ln \mathcal{A}_x(\vec{n}) \mathcal{A}_y(\vec{n}+\vec{u}_x) \mathcal{A}_x^{-1}(\vec{n}+\vec{u}_y) \mathcal{A}_y^{-1}(\vec{n}). \tag{7.23}$$

One may for instance obtain the Chern number by performing a sum on $\vec{n}$, i.e. $C = \sum_{\vec{n}} \mathcal{F}_{xy}(\vec{n})$, resembling the integral formula in the continuum. The Berry curvature this obtained is presented in Fig. 7.4. The most prominent observation we can make is that while there are fluctuations and the Berry curvature is not constant, these fluctuations do not show any singular or sharp features. To qualify this statement further we compare the Berry curvature of the triangular lattice CI to the Berry curvature of a simple two-orbital square lattice CI model. The latter is captured by a
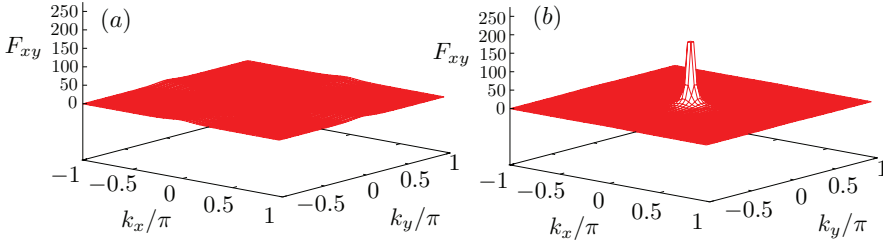
Figure 7.5: Plot of the Berry curvature for the model in (7.24) for different masses m: (a) $m = 0.8$, (b) $m = 1.9$

Hamiltonian

$$\mathcal{H}(\vec{k}) = \sin k_x \tau^1 + \sin k_y \tau^2 + (\cos k_x + \cos k_y - m)\tau^3. \qquad (7.24)$$

Without discussing the physical content of this model in too much detail, we stress that the parameter m, a *mass* parameter, controls a transition from a topologically trivial regime to a topological regime with Chern number $-\text{sign}(m)$. In particular, at $m = 2$ the system is gapless and described by a low-energy Dirac theory. Close to $m = 2$ m has the interpretation f a Dirac mass. For $|m| > 2$ the insulator is trivial, i.e. $C = 0$, while for $|m| < 2$ the insulator has Chern number $-\text{sign}(m)$. In Fig. 7.5(a) and 7.5(b) we have plotted the Berry curvature for two different values of m, namely $m = 0.8$ [7.5(a)] and $m = 1.9$ [7.5(b)]. The crucial observation to be made here is the emergence of a singularity in the Berry curvature at the Dirac point as the Dirac mass approaches zero (gapless state). Such behaviour would be expected close to a topological phase transition and it is precisely such type of singular or sharp behaviour that one wishes to avoid in a CI if it is to be a good candidate for FCI physics. Indeed, at $m = 0.8$, far away from the Dirac regime the situation is similar to our triangular lattice CI model, where deviations from constant curvature are present yet smooth. In fact, all CI models that have come into view as good candidates for FCI states on various lattices, have been shown to have Berry curvatures similar to one shown in Fig. 7.4 [87, 113, 140]. One quantitative measure of the Berry curvature fluctuations is to calculate the standard deviation of the Berry curvature, $\overline{\sigma}_{\mathcal{F}_{xy}}$. We find for the triangular lattice CI model $\overline{\sigma}_{\mathcal{F}_{xy}} = 0.061$, which is very similar to values reported for the by now highly popular kagome CI model, see for instance [149].

To conclude this section, we come to the energetics of the triangular lattice CI. We return to the model expressed in equation (7.19) and we use the effective NN hopping t as unit of energy; the band flatness can then be tuned by varying the ratio t'/t.
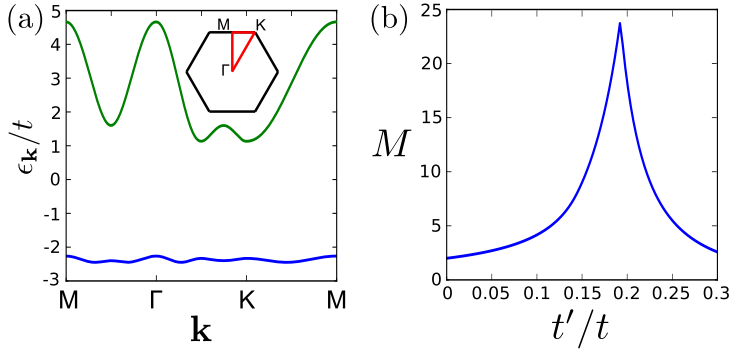
Figure 7.6: (a) Energy dispersion $E(\vec{k})$ for $t'/t = 0.2$. The inset shows the path taken through the first Brillouin zone. (b) Flatness ratio M, see Eq. (7.14), as a function of t'/t. The flatness ratio has been calculated from the dispersion along the high-symmetry directions shown in the inset on the left.

The longer range hopping t' determines the flatness of the bands of H_{kin}, which can be expressed by the figure of merit M, see Eq. (7.14). Figure 7.6 shows M depending on t', and one sees that ratios $M \gtrsim 20$ can be reached for $t' \approx 0.2$. Such flatness ratios can reasonably be achieved in the low-energy bands of a strongly correlated t_{2g} system on a triangular lattice [107]. Changing the sign of t' simply mirrors the dispersion vertically, i.e. it is then the upper band that becomes nearly flat. When going away from maximal M, the bands for smaller and larger t' differ qualitatively: For $t' < 0.2$, the Fermi surface (FS) at some fillings is almost perfectly nested.

7.4   Discussion and outlook

In the previous section we have developed and analyzed the triangular lattice Chern Insulator model from a non-interacting perspective. We have addressed the question to what extent this particular model fulfills the criteria for making a connection to the continuum Landau level problem. In order to address the question whether ground states of the CI model with interactions included actually resemble Fractional Quantum Hall states one has to resort to numerical methods. The most prominent of such numerical approaches is exact diagonalization (ED) of the Hamiltonian on a finite size cluster. Another procedure in principle appropriate to study interacting CI models is density-matrix renormalization group (DMRG) analysis, which to date has not been

used extensively, however. In the introductory section we already mentioned that to obtain FCI states the CI model is supplmented with density-density interactions, which for the present triangular lattice CI may be taken simply as (see [107, 141])

$$H_{\text{int}} = V \sum_{\langle i,j \rangle} \hat{n}_i \hat{n}_j \ . \tag{7.25}$$

There are two basic implementations of ED which have been used to study FCI states in lattice CI models. The most commen implementation uses single-particle states labeled by momentum quantum number as basis states, whereas the other approach uses real space orbitals as basis states (see [149, 150] and references therein). When using single-particle momentum eigenstates the kinetic part of the Hamiltonian is already diagonal and one needs to construct the interacting part in this basis in order to diagonalize the Hamiltonian. As such it is analogous to ED studies of the continuum problem, in which the single-particle Hilbert space consists of Landau orbitals labeled by angular momentum, and the Coulomb interaction is expanded in this basis. Another approach is to use the real space orbitals corresponding to the operators $\hat{\psi}_i$. In that case the interactions as given by equation (9.44) [or equation (7.3)] are diagonal and one needs to construct the kinetic part of the Hamiltonian in this basis. The latter approach has been used in ED studies of the triangular lattice CI [107, 141]. A widely used simplification when working in single-particle momentum space is to project out all but the flat band and in addition neglect the dispersion of this band. Working in real space effectively forces to keep the full band structure of the non-interacting CI and therefore allows to probe the interplay of energy scales.

In order to identify FCI states, i.e. states that are lattice analogs of the Fractional Quantum Hall states, one looks for spectral features that are characteristic for the Fractional Quantum Hall universality class. For instance, when the flat band is filled with a filling fraction $\nu = 1/q$, the ground state should be q-fold degenerate on the torus. On the lattice this is necessarily a quasi-degeneracy, the splitting of the ground state manifold should nevertheless vanish exponentially in the thermodynamic limit. In addition, in this limit the gap to the excited state should remain finite. Another probe of the FQH universality class is the response of the spectrum to a twist in the boundary conditions. As this represents flux threading through the handles of the torus, the ground state manifold should not be mixed with excited states upon changing the twist angle. Quasi-degenerate ground states switch places as function of inserted flux and are mapped back to themselves only after insertion of q elementary flux quanta. As a specific example of these two probes of FCI states we present results for the triangular lattice CI in Fig. 7.7 [107, 141]. The left panel, Fig. 7.7(a) shows the energy spectrum as function of total momentum, which remains a good quantum number in the presence of interactions. Three ground quasi-degenerate ground states
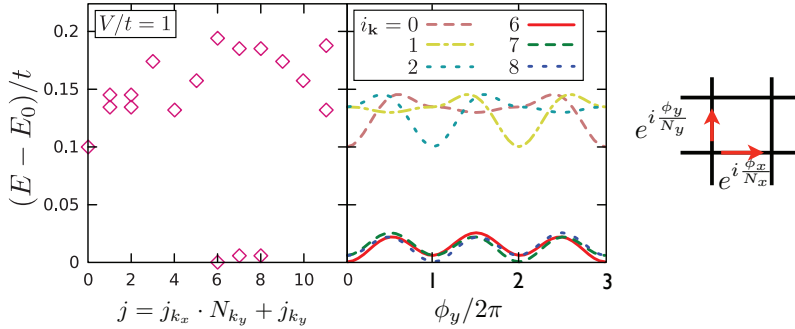
Figure 7.7: FCI state induced by NN Coulomb repulsion V in the triangular lattice CI model Eq. (7.19). (a) Energy depending on total momentum $\vec{k}$ for $V/t = 1.0$. (b) Energy depending on a flux ϕ_y added whenever an electron goes once around the whole lattice in y direction. Each addition of $\phi = 2\pi$ leads to an equivalent state, 6π to the same state. Lattice size is 4×6 sites (12 two-site unit cells), parameters in Eq. (7.19) are $t'/t = 0.2$. The filling of the flat band is $\nu = 1/3$. On the right a pictorial representation of flux insertion by adding a phase $e^{i\phi_y/N_y}$ or $e^{i\phi_x/N_x}$ to the hopping.

are clearly separated from the rest of the spectrum by an energy gap, as expected for a filling of $\nu = 1/3$. The right panel Fig. 7.7(b) shows the evolution of the ground state energies as function of adiabatic flux insertion. The spectral flow, i.e. ground states evolving into equivalent states after a single elementary flux quantum, only returning to the same state after $q = 3$ flux quanta, is in agreement with the behaviour of FQH states.

Yet another very powerful way to identify lattice analogs of FQH states is to count zero modes (ground and quasi-hole states) per momentum sector [105, 143]. For FQH states the number of zero modes per momentum sector can be obtained without diagonalizing the Hamtiltonian by just using the generalized Pauli principle applicable to the particular type of FQH state, e.g. Laughlin, composite fermion (CF), Moore-Read, ect. If the ground and quasi-hole states found by diagonalizing the FCI Hamiltonian are to be lattice analogs of the FQH states, they should obey these counting rules, as they follow from universal principles. To illustrate how such counting works for ground states we take the simplest case of a Laughlin state at filling $\nu = 1/3$, system size $N_x \times N_y = 4 \times 3$ and number of electrons $N_e = 4$. There are 12 total momenta and we organize them in a linear array with increasing j_x, i.e.

$[(j_x = 0, j_y = 0), (0, 1), (0, 2), (1, 0), (1, 1), (1, 2), (2, 0), \ldots]$. The counting rule or generalized Pauli principle applicable to this case dictates that no more than one electron can occupy three consecutive orbitals, respecting periodic boundary conditions in j. There are three different ways of distributing 4 electrons over 12 orbitals respecting these rules. Summing the total momenta we obtain the three total momenta $(j_x, j_y) = (2, 0), (2, 1), (2, 2)$. Comparing this to the specific case of the triangular lattice CI, such as presented in Fig. 7.7, which has the appropriate system size and number of electrons, using that $j = j_x \cdot N_y + j_y$, we observe that the counting agrees with numerical data.

We conclude this chapter by mentioning two features of Chern Insulator and Fractional Chern Insulator models that clearly set them apart from the continuum Landau level problem in an external magnetic field. In Chapter 1 it was demonstrated that each filled Landau level contributes e^2/h to the Hall conductivity and a Landau level therefore has Chern number one. Chern insulators mimic this in the sense that an electronic band has nonzero Chern number. While the Chern number of an electronic band in most CIs is indeed one, it is possible to construct a model in which Chern bands have higher Chern number. These bands are topologically distinct from Landau levels, as they differ in topological index. This allows for the possibility to study Fractional Quantum Hall physics starting from a Chern band with higher Chern number, a possibility which does not exist for magnetic field induced Landau levels.

A second intriguing generalization of ordinary Fractional Quantum Hall physics is to consider Quantum Spin Hall insulators instead of Chern Insulators. For the present purpose, a Quantum Spin Hall insulator may be thought of as two copies of a Chern insulator, with opposite Chern character the spin-up and spin-down states (assuming there is an invariant spin-rotation axis). Combining CIs in such a way restores time-reversal invariance and adding interactions to a fractionally filled band may lead to a time-reversal invariant analog of incompressible fractional quantum Hall liquids.

These two examples of possible generalizations point to exciting potential of FCIs to uncover new physics and lead to the discovery of new states of matter.

Part III

Symmetry and density-wave orders

CHAPTER 8

INTRODUCTION

Interactions of various degrees of freedom such as for instance electronic, lattice and spin degrees of freedom, are at the root of many intriguing phenomena in condensed matter physics. Interactions between electrons for example, can lead to metal-insulator transitionswhich may occur in combination with magnetic or orbital ordering. Both electron-electron and electron-phonon interactions can cause electrons to condense into a superconducting state, while (effective) interactions between spins are the origin of a plethora of distinct magnetic phases.

The study of these phenomena and their relation to strong correlations has a long and rich history. Depending on the energy scale of the electronic correlations as compared to the electron itineracy set by the electron bandwidth, it is appropriate to address the role of correlations either by treating the hopping of electrons as a perturbation to the interacting problem which is solved first, or by assuming the electrons in the vicinity of the Fermi surface to be perturbed by the repulsive interations between them. In the latter case the starting point is the non-interacting Fermi-liquid ground state and the prime objects of interest are the Fermi surface instabilities towards different types of electronic condensation driven by interactions. Charge or spin density wave formation are both examples of particle-hole condensation, while superconductivity originates from condensation of particle-particle pairs.

There are different ways to approach the investigation of electronic ordering tendencies, i.e. the fate of the Fermi liquid when subject to interactions. Particularly in

the weak-coupling regime, a mean field Hartree Fock approach is a well-suited first step to study the effect of correlations at zero temperature. A multitude of different schemes to subsequently include the effect of quantum fluctuations exist, all having their own advantages and drawbacks. Other more advanced methods, such as various incarnations of renormalization group schemes [151, 152], allow for an even more general and unbiased search for possible Fermi surface instabilities. These theoretical methods are at the heart of understanding the complicated behaviour of materials for which such (strong) interactions and multiple degrees of freedom are important, sharing the basic philosophy of departing from the non-interacting Fermi-liquid and then unraveling the electronic instabilities towards order. The insight such methods provide has been been of great benefit for material classes and areas of condensed matter as disparate as for instance high temperature superconducticity in the cuprates or iron pnictides [153, 154], multiferroics [155–157], Colossal Magnetoresistant manganites [27, 28] and other complex oxides [158].

Quite a number of materials which exhibit interesting and complicated behaviour due to strong electronic correlations have a layered and effectively two-dimensional structure with square symmetry. One can think of the high-temperature cuprate and iron-pnictide superconductors. However, prototypical systems with hexagonal symmetry, of which the triangular, honeycomb and kagome lattices are perhaps the most prominent representatives, have also attracted increasing attention recently due to the large variety of novel and unconventional interaction-driven electronic condensates proposed in such systems. These include chiral superconductivity [159], uniaxial and chiral spin density waves [30, 160–163] and chiral nematic phases [164, 165]. In particular particle-hole condensation with nonzero angular momentum is an exciting prospect in the context of hexagonal symmetry systems [165, 166].

The richness of the reported and anticipated phase diagrams derives from the existence of multidimensional irreducible representations with d-wave symmetry. The components of these may be combined to give to rise to intricate phases. In addition, lattices with hexagonal symmetry have a nested Fermi surface when doped to the van Hove points of the band structure. The nesting vectors are the three inequivalent M-point vectors of the hexagonal Brillouin zone (see Fig. 9.4), and the possibility to have order parameters corresponding to different M-point vectors leads to a further increase in complexity. The (near) nesting of the van Hove Fermi surface by M-point vectors in combination with a diverging density of states is a feature common to triangular lattice, honeycomb lattice and kagome lattice systems, suggesting a similarly common phenomenology of electronic instabilities for these systems with hexagonal symmetry.

The examples above highlight the importance of both electron correlation and symmetry to explain and understand the electronic properties of complex materials: electron correlations are the driving force behind a strikingly diverse collection of

electronic ordered states, while symmetry shapes the playing field of electronic ordering.

The aim of this paper is to explore these concepts in the context of a branch of condensed matter physics where electronic interactions are not immediately responsible for the physical effects under study, the field of topological states of matter, in particular the field of the topological insulators [1–5, 12, 111]. Topological insulators are electronic insulating states which are distinct from ordinary insulators. Ordinary insulators are materials which can in principle be adiabatically turned into an atomic insulator, where every atom is uniquely associated to an atom and therefore cannot move. Topological insulators are bulk insulators which have conducting edge or boundary modes, the presence of which directly follows from the topological character of the insulating state and is captured by a topological quantum number, i.e. a topological invariant. The physics of topological insulators can be understood by relying simply on non-interacting electron band theory: the topological character of an insulator is determined by and calculated from the single-particle electronic band structure [1–5]. The most prominent class of materials unambiguously identified as topological insulators both in theory and experiment is that of semi-conductors with strong spin-orbit coupling [12, 111]. The formation of a topologically insulating state can, however, also be driven by electron-electron interactions in the sense that interactions induce particle-hole condensation with a topologically nontrivial condensate mean field band structure [84]. Such a scenario has been considered in case of the two-dimensional ($2D$) honeycomb [84, 167, 168], kagome [169, 170] and checkerboard lattices [86], as well as the three-dimensional ($3D$) diamond lattice [171]. In $2D$ there are two distinct topological phases which may be dynamically generated by interactions, a Quantum Anomalous Hall (QAH) state and a Quantum Spin Hall (QSH) state. The former requires the absence of time-reversal symmetry, while the latter requires the presence of time-reversal symmetry in addition to the (partial) breaking of spin rotation symmetry.

Even though topological insulators are classified based on a topological invariant instead of a local symmetry-broken order parameter, symmetry is nevertheless of great significance for the classification of topological states, as symmetry dictates which type of topological invariant may or may not be nontrivial. The QSH state, for instance, is an example of a symmetry-protected topological state, i.e. a state which requires the presence of a symmetry to make its distinction from a topologically trivial insulator meaningful. Indeed, the QSH state cannot be adiabatically deformed to the trivial (atomic) insulator without closing the energy gap, provided time-reversal symmetry is preserved. For interaction-induced insulators this implies that *the symmetry of the condensate order parameter will is decisive for the possibility of the insulator to be topologically nontrivial*. Apart from time-reversal symmetry, other symmetries such as point group symmetries can play a key role [172]. This makes

the symmetry characterization of electronic condensates a prerequisite for identifying interaction-induced topological insulators, which is the goal of the rest of this paper.

In addition to the topological insulators, there is a class of topological states of matter called topological semimetals. These are electronic states with band structures exhibiting isolated touching points of two bands in momentum space. In $3D$ such semimetals are referred to as Weyl semimetals [173–176], as the electronic spectrum disperses linearly at the degeneracy points and the low-energy description of electrons takes the form of a two-component Dirac equation called the Weyl equation. This means that the degeneracies, i.e. the Weyl points, must come in pairs which are separated in momentum space. In $2D$ there exist two prominent types of topological semimetallic states. The first is the $2D$ version of the Weyl semimetal, i.e. a pair of linearly dispersing Weyl nodes separated in momentum space. The other is a single degeneracy with quadratic dispersion close to the degeneracy, which is characterized by a nonzero topological winding number when going around the degeneracy in momentum space [177]. Such a degeneracy is generally called a quadratic band crossing (QBC) point. In $3D$ the Weyl points are robustly protected as long as they remain separated in momentum space (momentum must be a good quantum number) since the topological invariant protecting each node does *not* require the presence of symmetries to be well-defined. In contrast, in two dimensions additional symmetries are required to protect the degeneracy which defines the semimetal, as no meaningful topological numbers can be defined without a symmetry constraint. The latter may come from the familiar time-reversal, particle-hole or point group symmetries. Interestingly, it was shown recently in the context of the simple square lattice that previously unnoticed symmetries, in particular combinations of translations and point group elements, can also protect a topological semimetallic state [178].

This establishes yet another crucial link between correlation-induced electronic states and symmetry. The symmetry of the order parameter will determine whether or not a given ordered state can protect spectral degeneracies defining a topological semimetal. A simple and well-known example of precisely such a semimetallic state is the square lattice $d_{x^2-y^2}$-density wave (DDW), believed to be relevant for cuprate pseudogap physics, which induces a pair of Weyl points in the condensate spectrum. Having identified which symmetry or combination of symmetries protects the semimetal, be it a $2D$ Weyl semimetal or a QBC, gives insight into the effect of the breaking of such symmetries on the low-energy description. Dirac nodes and QBC points may be gapped out by masses, and a QBC point may be split into two Dirac points. It is a very interesting and relevant question to what extent symmetries and symmetry breaking by itself determine the fate of these particular semimetallic states.

Motivated by these considerations, i.e. (i) the increasing attention focused on unconventional exotic electronic orders, (ii) their potential for hosting topologically

nontrivial states such as topological insulators and topological semimetals, and (iii) the key role played by symmetry, we set out to systematically investigate and organize all possible interaction-induced electronic orders of the two dimensional square lattice and the three prime hexagonal lattices based on lattice symmetry. We focus on condensates of particle-hole pairs only, i.e. density waves of the form $\langle \hat{\psi}^\dagger(\vec{k} + \vec{Q})\hat{\psi}(\vec{k})\rangle$ [166], and consider finite but commensurate ordering momenta $\vec{Q}$, which lead at most to quadrupling of the unit cell. In the present work we restrict ourselves to $2D$. The result of systematically organizing density wave orders in terms of basis functions of point group representations, employing the machinery of group theory, may be concisely summarized as follows. It provides a comprehensive and unified framework to predict and uncover (i) the possibilities for topological Mott insulating states and topological semimetallic states, and (ii) the effects of symmetry breaking condensation on the low-energy spectrum.

Considering the length and scope of the present work, it may be helpful to the reader to have a clear description of the organization of the paper, in addition to a summary of the main results presented in this work. This will be provided in the next section. We stress that in this work we do not aim to show or prove that any particular density wave state is the ground state of any particular model. Instead, our aim is to guide and complement such studies by identifying *possible* states which can and cannot arise due to interactions and their properties, on the basis of symmetry. The density waves of particle-hole condensed pairs that will be presented in this work are therefore candidates for variational ground states in specific models, in addition to being interesting objects of study in themselves from the viewpoint of symmetry and topology.

8.1   Overview

In this part of this thesis we present a symmetry perspective on density wave orders in two dimensions. In this section we give an overview of the organization of the paper and we familiarize the reader with the main results and conclusions of this work.

The key idea behind the symmetry perspective developed in this work is to organize different types of density wave order, i.e. site order, bond order and flux order, according to their transformation properties under point group operations or extended point goup operations. Extended point groups are obtained from the ordinary point group by including the effects of translational symmetry breaking and unit cell enlargement. Since we anticipate the breaking of translational symmetry by condensation at finite ordering vector, we must resort to extended point groups for a proper description of lattice symmetry breaking. The extension of a point group is generated by adding the translations which are no longer invariant translations to the rotations

and reflections of the "bare" point group. Extended point groups only depend on the symmetry class of a given lattice (defining the bare point group), and the ordering vectors $\vec{Q}$, as the latter determine the group of invariant translations. Density wave states can then be organized as basis functions of irreducible representations of the extended point group. For any specific lattice it is possible to find all irreducible representations contained in the enlarged unit cell, for each of the three types of order, by simply using elementary tools of group theory. This yields a symmetry filtered list of possible orderings [see for instance equations (9.88)-(9.90), or (9.131)-(9.136)]. The main purpose of the present work is to find out how much insight into the electronic properties of density waves can be derived from such an organization.

Let us illustrate the idea of such an organization here by considering an example of bond order on the square lattice. Assuming a quadrupling of the unit cell due to density wave modulations, the enlarged square lattice unit cell contains eight bonds. This implies eight distinct bond density waves and we will see in Section 9.3 that these are grouped in $1D$ and $2D$ representations. For instance, one such $2D$ representation corresponds to a doublet of bond order waves characterized by alternating weaker and stronger hoppings in the x and y directions [166]. In case of the x direction the density wave can be expressed as

$$\langle \hat{\psi}_\sigma^\dagger(\vec{k} + \vec{Q})\hat{\psi}_{\sigma'}(\vec{k})\rangle = i\Delta_{p_x} \sin k_x \delta_{\sigma\sigma'}, \tag{8.1}$$

where σ (σ') label the spin degree of freedom, Δ_{p_x} is the order parameter or the strength of density wave, and $\vec{Q} = (\pi, 0)$. Under a fourfold rotation this state transforms into the state with $\sin k_y$ on the right hand side and momentum $\vec{Q} = (0, \pi)$ on the left hand side. These two states, conveniently labeled p_x and p_y, are the partners of a $2D$ representation of the extended point group. Note that under a translation over one lattice constant in the x direction, the p_x state is odd, while the p_y state is even. This is what gives the two p_x and p_y density waves the interpretation of basis functions of irreducible representations of the extended group.

If we think of these two density waves as basis functions of a particular representation, we realize that nothings prevents us from choosing a different basis, i.e. performing a basis transformation on these basis functions. Using the labels p_x and p_y, we could express a possible change of basis intuitively as $p_x \to p_x + p_y$ and $p_y \to p_x - p_y$. As the density waves p_x and p_y transform into each other under rotations, combining them in some way gives the hope that the combination is invariant under rotations, or at least even or odd under bare point operations. Whether or not such a combination exists follows directly from group theory in the following way. If we for the moment call the representation of the extended point group p_x and p_y belong to E, then we can ask how E decomposes in terms of representations of the bare point group, which is a propor subgroup of the extended one. If E decom-

poses into two $1D$ irreducible representations of the bare point group, the answer is yes, such a combination exists. In the present case, the answer is indeed affirmative, and skipping ahead to Fig. 9.3(a)-(b) will show these specific density waves. An example of an extended point group doublet for which such a decomposition does not exist is obtained from equation (8.1) by simply substituting the ordering momentum $\vec{Q} = (\pi, \pi)$ for both $\sin k_x$ and $\sin k_y$. These density waves will be discussed in more detail in Section 9.3.1. In organizing the density waves according to symmetry, we will consistently seek to write density wave states in a basis which respects the subdivision of extended point group representations into distinct bare point group representations. We will elucidate the physical meaning of such a subdivision.

The great advantage of group theory is that one can obtain the symmetry of density wave states without the knowledge of explicit expressions such as equation (8.1). By simply applying representation theory one can find the distinct density waves and their symmetry properties, and we will argue and show in this work that this information alone is sufficient to make strong statements with regard to the electronic properties of the density waves, such as for instance a symmetry-mandated correspondence to a Dirac mass in the low-energy description of the (mean field) electronic structure.

In this paper we apply this scheme of listing density waves by extended point group symmetry to four lattices, the square lattice and three lattices with hexagonal symmetry, i.e. the triangular, honeycomb and kagome lattices. In all those cases we distinguish three kinds of possible orderings, which are site or charge order, bond order and flux order. Site order and bond order refer to a modulated redistribution of charge between lattice sites, $\sim \langle \hat{\psi}_i^\dagger \hat{\psi}_i \rangle$, and a modulated strengthening or weakening of bond overlaps, $\sim \mathrm{Re}\,\langle \hat{\psi}_i^\dagger \hat{\psi}_j \rangle$, respectively. By flux order we mean a modulated arrangement of spontaneously generated orbital currents. In the presence of flux order the elementary plaquettes of a lattice (squares in case of the square lattice, hexagons in case of the honeycomb lattice) are threaded by fluxes which are indstinguishable from external magnetic fluxes. However, as they are spontaneously generated and do not originate from external fields, they must average to zero over the enlarged unit cell. The fluxes derive from the imaginary part of bond order condensation, $\sim \mathrm{Im}\,\langle \hat{\psi}_i^\dagger \hat{\psi}_j \rangle$, but due to the gauge freedom associated with imaginary hoppings it is the fluxes which consitute the fundametnal objects specifying the order. We will therefore treat fluxes on equal footing with sites and bonds and thus provide a gauge invariant framework for treating all possible density wave orderings of particle-hole pairs.

Armed with the symmetry filtered listing of various orderings we proceed to systematically obtain explicit expressions for the density waves for selected cases. We investigate the mean field or single-particle band structures and this analysis will provide the foundation for the following general results and conclusions.

(i) We show how extended point group symmetries, sometimes in combination with the time-reversal operation, protect isolated spectral degeneracies and hence establish the states exhibiting these degeneracies as (topological) semimetals. In case of the square lattice, we will demonstrate the key role played by translations, which are naturally embedded in the extended point groups. In contrast, using again the structure of extended point groups, we will show how such degeneracy protection is generally not possible for systems with hexagonal symmetry. Instead, for systems with hexagonal symmetry we will show (i) the emergence of point group symmetry protected QBCs in case of M-point ordering and (ii) the emergence of Dirac nodes protected by extended point group operations, in particular and crucially the translations broken by finite Q ordering, but are resurrected as symmetries due to global spin rotations. We therefore propose extended point group elements dressed with global spin rotations as another class of hidden symmetries with the potential to protect semimetallic states.

(ii) Semimetals generally have special low-energy theories in the vicinity of the degeneracy point. We have mentioned the canonical examples of Weyl nodes and QBC points. Such semimetals may arise just from lattice topology (honeycomb and kagome lattices), or from condensation ($d_{x^2-y^2}$ density wave on the square lattice). In all these cases lattice symmetries, possibly in conjunction the anti-unitary time-reversal operation, protect the degeneracy. In the present work we address the impact of symmetry breaking by density wave formation on the low-energy theory of these semimetals. In particular, for a Dirac theory, as the low-energy description of two Weyl nodes are colloquially referred to in $2D$, we will demonstrate a robust connection between the abstract symmetry classification of density waves and their spectral effects at low energies. For instance, the two Dirac nodes can be gapped out by a mass term, or they can be energetically split by making the two nodes inequivalent. Alternatively, the two nodes can be shifted in momentum space by terms that have the appearance of static gauge fields. We will argue, based on a careful study of both a square and hexagonal symmetry Dirac theory, that the point group representations to which distinct density waves belong decide to what low-energy term they couple. In addition, the dimensionality of these representations is directly related to the degeneracy of the density waves at low energies. As an illustration and a spoiler for Section 9.4.1, we point out that the two well-known Kekule bond distortions of the graphene lattice are partners of a $2D$ representation of the extended point group, and enter as equivalent (compatible) masses in the low-energy description.

(iii) In the context of a Dirac theory, apart from Dirac mass terms leading to an energy gap, another set of interesting low-energy terms is given by the pseudomagnetic gauge fields. It is known in the community of graphene physics, the prime example of a condensed matter system hosting Dirac fermions, that strain applied to the graphene sheet as well as its intrinsic corrugation and ripples manifest themselves

as gauge fields [179]. These are different from the ordinary electromagnetic gauge field as they do not break time-reversal symmetry, but if they acquire a spatial dependence they lead to pseudo-Landau level quantization in a way analogous to the magnetic field-induced Landau levels. Recently it was demonstrated that strain fields in graphene can be naturally grouped together with translational symmetry broken charge density waves to form the components of a non-Abelian gauge field coupled to the low-energy Dirac theory [180]. This marked the first example of a set of density waves being identified as components of an $SU(2)$ gauge structure. In addition, it was argued that such gauge field components are dynamically generated if one of them causes pseudo-Landau level quantization, as they can gap out the pseudo Landau levels. Such an $SU(2)$ gauge structure in principle exists for any Dirac theory. It is however not immediately obvious what microscopic physical states, such as the charge density waves in graphene, will correspond to it. In this work we address this question and show how symmetry paves the way for a direct identification of the density waves manifesting themselves as gauge fields. The identification rule we find is simple and pertains to any given lattice. If a density wave state transforms as a $2D$ representation of the bare point group (not the extended point group), then it corresponds to low-energ gauge field component, and the same is then true for its partner. We will see how this rule emerges from a careful study of the square lattice π-flux state and the honeycomb lattice, and then see its application in action in case of the kagome lattice.

(iv) We will present an extensive study and analysis of hexagonal lattice M-point orders, i.e. ordering tendencies expected when doping these systems to the van Hove points of band structure. We specifically focus on the honeycomb lattice, the triangular lattice and the kagome lattice, but we will find that the main features of M-point ordering, such as degeneracy protection, the form of effective low-energy theories and spectral gap opening, are not lattice specific. Particle-hole condensation at finite M-point vectors causes the extended point group representations to be all $3D$. Hence, for any such representation there are three degenerate density wave components transforming into each other, which may be applied indepedently to lower condensation energy. We show how further organizing these three components according to transformation properties under rotations and reflections only, i.e. constructing basis functions of the bare point group representations, allows for general and lattice independent predictions concerning the mean field spectrum. In particular, we demonstrate that the most symmetric way of applying the three degenerate components either leads to fully gapped out Fermi surface, or a symmetry protected QBC.

For hexagonal lattice M-point order we will also give a more detailed overview of spin triplet, i.e. spinful, density waves [166]. Taking the spin degree of freedom into account explicitly introduces the notion of dressing lattice operations with rota-

tions in spin space in order to form density waves transforming as irreducible point group representations. Furthermore, as mentioned before, this dressing of translations or reflections with spin rotations can "resurrect" symmetries which appear to be broken for spinful ordering at finite order vectors. In addition, we will make contact with recent literature addressing hexagonal lattice M-point order, to show that (spin) density wave orders obtained from symmetry considerations in some cases precisely coincide with the orderings proposed to occur in specific interacting fermion models.

(v) Since there is an intimate connection between symmetry and topology, the symmetry-based organization of density wave orders is particularly helpful in identifying electronic states which can come with topological quantum numbers. The two basic topological insulating states of matter in $2D$, the QAH effect and the QSH effect, critically rely on the absence and presence of time-reversal symmetry, respectively. Lattice symmetries provide further constraints. A QAH effect cannot occur if the systems has a reflection symmetry. This limits the class of states possibly hosting a QAH, which in turn affects the interaction-induced QSH scenario of [84], as this is essentially predicated on the assumption of one QAH per spin species. The symmetry organization of density waves allows for a direct identification of putative topological Mott insulators and we demonstrate this for each lattice we consider.

We will show how for each of the hexagonal lattices considered, there is an M-point flux ordered state which hosts a QAH effect. We will furthermore discuss the various possibilities for spinful versions of this order, which in case of translational symmetry broken M-point order are not limited to the obvious version of one QAH copy per spin species with opposite sign.

Point group symmetries were shown to give rise to another type of topological quantum numbers in $2D$, which is quantized electric polarization [172]. Symmetry severely constrains the possible nontrivial values of this quantized polarization and we will discuss which density waves are compatible with these quantum numbers and if so check whether they possess them.

(vi) In this work we propose a new class of highly symmetric time-reversal invariant spin-bond ordered states existing in hexagonal lattice systems. As mentioned under *(e)*, for each of the hexagonal lattices considered we find an M-point flux ordered state. We will put forward a particular way of creating a spinful version of these states, which fully breaks spin rotation symmetry, but recovers all lattice symmetries broken in the flux ordered state. The lattice symmetries can be dressed with global spin rotations to yield good symmetries again. In particular, we will show how translational symmetry is essentially recovered. Remarkably, due to the full recovery of all lattice symmetries, there is a symmetry protected fourfold degeneracy at the M' points of the reduced Brillouin zone. Apart from this isolated degeneracy point, the nested Fermi surface at the van Hove filling is fully gapped. The resulting semitallic state is a new type of Dirac semimetal, characterized by three Dirac theories instead

of the usual single theory, one for each inequivalent M' point. We will show how seemingly trivial mass gaps give rise to a QSH state.

This concludes the preview summary of the content of this part of the thesis as well as its main results and conclusions. The aspects of particle-hole condensation listed above are the subject of this paper and will de developed in the remaining part of it. The organization of the main content of this work is as follows. In Section 9.1 we present the mathematical prerequisites for studying electronic lattice symmetries. We explicitly incorporate translational symmetry breaking due to condensation at finite wave vectors. In addition, we explain how the topological quantum numbers of electronic states can be computed. In Section 9.2 we give a detailed introduction to a mean field treatment of electron correlation, presented in a way particularly suited for the symmetry perspective of density waves adopted in this work. Following the mean field theory, Section 9.3 covers the density wave classification of square lattice density waves. After having obtained all possible condensates, we zoom in on the $d_{x^2-y^2}$ and d_{xy} density waves to show how their degeneracies are symmetry proteced and in what way symmetry breaking affects the low-energy description defined by these degeneracies. Section 9.4 then treats the density waves of hexagonal lattices, starting with the honeycomb lattice, which is discussed in most detail, then proceeding to the kagome lattice and closing with the triangular lattice. In case of the honeycomb and kagome lattices three types of density waves will be treated, (i) translationally invariant condensates (zero ordering vector), (ii) K-point order, and (iii) M-point order. K-point order affects the Dirac nodes, while M-point order is relevant for van Hove filling. For the triangular lattice we only discuss M-point order. Chapter 10 then gives an introduction to hexagonal lattice M-point spin triplet order, i.e. spinful density waves.

Chapter 11 summarizes the results and concludes part III of this thesis.

CHAPTER 9

DENSITY-WAVE STATES FROM A SYMMETRY PERSPECTIVE IN TWO DIMENSIONS

9.1 Electronic lattice symmetries

The present section will discuss in detail the mathematical prerequisites for studying the effect of lattice symmetries. We will introduce relevant notation which will be used throughout the paper. Some aspects presented below may be rather technical (even though conceptually straightforward) and upon first reading this section may just be glossed over.

9.1.1 Space group symmetries

In this work we will be mainly concerned with two-dimensional systems and we therefore describe the necessary formalism in this setting. The material presented in this section is very straightforwardly generelized to $3D$ or even arbitrary dimension, and at the very end of this work we comment on how the content and conclusions of this work may carry over to $3D$.

We denote the atomic positions in the crystal lattice by $\vec{r}_i$, where i is a label for the atomic site. The atomic position can be decomposed in terms of the Bravais lattice as

$$\vec{r}_i = \vec{x} + \vec{l}_i, \tag{9.1}$$

where $\vec{x}$ is a Bravais lattice vector and $\vec{l}_i$ denotes the position of the i-th atom with respect to the unit cell vector $\vec{x}$. The latter can be written in terms of its generators as

$$\vec{x} = \vec{x}_{n_1 n_2} = n_1 \vec{x}_1 + n_2 \vec{x}_2. \tag{9.2}$$

Here the vector $\vec{n} = (n_1, n_2) \in \mathbb{Z}^2$ is integer-valued and specifies a given Bravais lattice site. In the following we will occasionally use vectors $\vec{n}, \vec{m}, \ldots$ to refer to unit cells. For a lattice with N_{sl} different sublattices, i.e. N_{sl} atoms in the unit cell, there are N_{sl} distinct $\vec{l}$ vectors.

Space groups consist of all spatial symmetries of the crystal lattice and here we assume that the space group is symmorphic, meaning that we can always find an origin such that all space group elements are generated by translations and point group operations, which are themselves symmetries. Translations will be written as $T(\vec{x})$, representing a translation over lattice vector $\vec{x}$ and point group operations will be written as R. In two dimension, to which we particularize unless stated otherwise, and for spinless fermions the dihedral groups D_n are identical to the groups C_{nv}, wich instead of an in-plane twofold rotation axis, contain a mirror relfection. In the rest of this paper we assume the symmetry group to be C_{nv}. For spinful fermions the two symmetry groups must be distinguished as the twofold rotation and reflection act differently on the spin degree of freedom. For the most part, this difference is not important for our purposes, we have however included some details on it in Appendix C.3. In the following we will assume the equivalence of D_n and C_{nv}, but whenever appropriate or necessary we will comment on the differences. For a C_{nv} symmetric system, any element of the space group can be written in terms of the four generators $T(\vec{x}_1), T(\vec{x}_2), C_n$ and σ_v, where C_n is the n-fold rotation and σ_v is a reflection. Any element may then be specified by $T(\vec{x}_1)^{m_1} T(\vec{x}_1)^{m_2} C_n^{m_3} \sigma_v^{m_4}$ and point group operations R can be written as $R = C_n^{m_1} \sigma_v^{m_2}$.

The effect of a point group symmetry on an atomic position is represented as $R\vec{r}_i = R\vec{x} + R\vec{l}_i$. As this operation is a symmetry, $R\vec{r}_i$ is another atomic position, but possibly an inequivalent one. Hence we have $R\vec{r}_i = \vec{r}'_j = \vec{x}' + \vec{l}_j$. It is not necessarily true that $\vec{x}' = R\vec{x}$, the difference must however be some lattice vector $\vec{t}_i$, $\vec{x}' = R\vec{x} + \vec{t}_i$. $\vec{t}_i$ depends on the atom in the unit cell, hence the label i. It thus follows that $R\vec{r}_i = R\vec{x} + \vec{t}_i + \vec{l}_j$.

We now wish to find the transformation properties of the field operators and the

Hamiltonian. The creation and annihilation field operators are given by

$$\hat{\psi}_\sigma(\vec{r}_i) = \hat{\psi}_\sigma(\vec{x} + \vec{l}_i) = \hat{\psi}_{i\sigma}(\vec{x}) \equiv \hat{\Psi}(\vec{x}),$$
$$\hat{\psi}_\sigma^\dagger(\vec{r}_i) = \hat{\psi}_\sigma^\dagger(\vec{x} + \vec{l}_i) = \hat{\psi}_{i\sigma}^\dagger(\vec{x}) \equiv \hat{\Psi}^\dagger(\vec{x}) \tag{9.3}$$

Here we use the index σ to denote any additional internal degree of freedom, which is in this work will invariably be the electron spin, but in principle one may think of σ as representing the collection of internal degrees of freedom including also an electron orbital degree of freedom (p, or d-orbitals for instance). For convenience we also collec the operators $\hat{\psi}_{i\sigma}(\vec{x})$ in the vector operator $\hat{\Psi}(\vec{x})$. Note again that i labels the sublattice degree of freedom, which we explicitly distinguish from the other degrees of freedom. Defining N as the number of unit cells, the Fourier transform of the field operators is given by

$$\hat{\psi}_{i\sigma}(\vec{k}) = \frac{1}{\sqrt{N}} \sum_{\vec{x}} \hat{\psi}_\sigma(\vec{x} + \vec{l}_i) e^{-i\vec{k}\cdot\vec{x}} = \frac{1}{\sqrt{N}} \sum_{\vec{x}} \hat{\psi}_{i\sigma}(\vec{x}) e^{-i\vec{k}\cdot\vec{x}}, \tag{9.4}$$

We choose this definition of the Fourier transform, as opposed to the common tight binding Fourier exponentials $e^{-i\vec{k}\cdot(\vec{x}+\vec{l}_i)}$, to ensure that $\mathcal{H}(\vec{k} + \vec{G}) = \mathcal{H}(\vec{k})$. Below we briefly discuss this gauge choice, which one should be aware of when evaluating symmetry properties. We define the operators $\hat{U}_R$ and their Hermitian conjugates as acting on the field operators to implement the point group symmetry R. Then one has

$$\hat{U}_R \hat{\psi}_\sigma(\vec{r}_i) \hat{U}_R^\dagger = \sum_{\sigma'} U_{R\sigma\sigma'}^o \hat{\psi}_{\sigma'}(R\vec{r}_i) = \sum_{j,\sigma'} U_{R\sigma\sigma'}^o U_{Rij}^{sl} \hat{\psi}_{j\sigma'}(\vec{x}') \tag{9.5}$$

Here U_R^o is a unitary matrix that acts in the space of internal orbital degrees of freedom (hence the superscript o). The matrix U_R^{sl} acts in sublattice space. One observes easily that the combined effect on the orbital and sublattice space can be represented as $\mathcal{U}_R^\dagger = U_R^o \otimes U_R^{sl}$. To deduce the transformation properties of the field operators in momentum space, we note that $\vec{x} + \vec{l}_i = R^{-1}(\vec{x}' + \vec{l}_j)$, where $\vec{x}' = R\vec{x} + \vec{t}_i$. Thus we get

$$\hat{U}_R \hat{\psi}_{i\sigma}(\vec{k}) \hat{U}_R^\dagger = \sum_{j,\sigma'} \sum_{\vec{x}} U_{R\sigma\sigma'}^o U_{Rij}^{sl} \hat{\psi}_{j\sigma'}(\vec{x}') e^{-i\vec{k}\cdot\vec{x}}$$

$$= \sum_{j,\sigma'} \sum_{\vec{x}} U_{R\sigma\sigma'}^o U_{Rij}^{sl} \hat{\psi}_{j\sigma'}(\vec{x}') e^{-iR\vec{k}\cdot R\vec{x}}$$

$$= \sum_{j,\sigma'} \sum_{\vec{x}} U_{R\sigma\sigma'}^o U_{Rij}^{sl} \hat{\psi}_{j\sigma'}(\vec{x}') e^{-iR\vec{k}\cdot(\vec{x}'-\vec{t}_i)}$$

$$= \sum_{j,\sigma'} U_{R\sigma\sigma'}^o U_{Rij}^{sl} e^{iR\vec{k}\cdot\vec{t}_i} \hat{\psi}_{j\sigma'}(R\vec{k}) \tag{9.6}$$

For convenience we define the new matrix $U_R^{\rm sl}(\vec{k})$ to include the $\vec{k}$-dependencies $U_R^{\rm sl}(\vec{k}) = {\rm diag}(e^{iR\vec{k}\cdot\vec{t}_1}, \dots, e^{iR\vec{k}\cdot\vec{t}_{N_{\rm sl}}}) \times U_R^{\rm sl}$. Then we can write concisely $\hat{U}_R \hat{\Psi}(\vec{k})\hat{U}_R^\dagger = U_R^{\rm o} \otimes U_R^{\rm sl}(\vec{k})\hat{\Psi}(R\vec{k}) \equiv \mathcal{U}_R^\dagger \hat{\Psi}(R\vec{k})$, with a proper redefinition of $\mathcal{U}_R$ to incorporate the $\vec{k}$ dependence.

The translationally invariant Hamiltonian is generically written as

$$\hat{H} = \sum_{i,j,\sigma,\sigma'} \sum_{\vec{x},\vec{x}'} \hat{\psi}_{i\sigma}^\dagger(\vec{x})\mathcal{H}_{i\sigma,j\sigma'}(\vec{x}-\vec{x}')\hat{\psi}_{j\sigma'}(\vec{x}')$$
$$= \sum_{i,j,\sigma,\sigma'} \sum_{\vec{k}} \hat{\psi}_{i\sigma}^\dagger(\vec{k})\mathcal{H}_{i\sigma,j\sigma'}(\vec{k})\hat{\psi}_{j\sigma'}(\vec{k}) \equiv \sum_{\vec{k}} \hat{\Psi}^\dagger(\vec{k})\mathcal{H}(\vec{k})\hat{\Psi}(\vec{k}) \qquad (9.7)$$

Under the symmetry operation the Hamiltonian transforms as

$$\hat{U}_R \hat{H} \hat{U}_R^\dagger = \sum_{i,j,\sigma,\sigma'} \sum_{\vec{k}} (\mathcal{U}_R \mathcal{H} \mathcal{U}_R^\dagger)_{i\sigma,j\sigma'}(\vec{k})\hat{\psi}_{i\sigma}^\dagger(R\vec{k})\hat{\psi}_{j\sigma'}(R\vec{k}), \qquad (9.8)$$

and since this is a symmetry we must have $\hat{U}_R \hat{H} \hat{U}_R^\dagger = \hat{H}$, which implies

$$\mathcal{U}_R(\vec{k})\mathcal{H}(\vec{k})\mathcal{U}_R^\dagger(\vec{k}) = \mathcal{H}(R\vec{k}). \qquad (9.9)$$

The composition of two point group symmetries gives another element of the point group, i.e. if R_1 and R_2 are symmetries, then so is $R_3 = R_2 R_1$. This is of particular importance if we think of the point group as being generated by just two elements. The effect of such a product of symmetries (first applying R_1, then R_2) on the field operator is, using equation (9.6),

$$\hat{U}_{R_3}\hat{\Psi}(\vec{k})\hat{U}_{R_3}^\dagger = \hat{U}_{R_2}\hat{U}_{R_1}\hat{\Psi}(\vec{k})\hat{U}_{R_1}^\dagger\hat{U}_{R_2}^\dagger = \mathcal{U}_{R_1}^\dagger(\vec{k})\mathcal{U}_{R_2}^\dagger(R_1\vec{k})\hat{\Psi}(R_2 R_1\vec{k}). \quad (9.10)$$

Not only does this demontrate that one should be careful with the order in which matrix multiplications must take place, it also shows that if and only if $R\vec{k}^* = \vec{k}^*$ for some $\vec{k}^*$ in the Brillouin zone and *all* R of the point group, do the $\mathcal{U}_R$ form a representation of the group, i.e. $\mathcal{U}_{R_3} = \mathcal{U}_{R_2}\mathcal{U}_{R_1}$. If a proper subgroup of the point group leaves a certain $\vec{k}^*$ invariant, then the $\mathcal{U}_R$ will form a representaion of that subgroup.

9.1.2   Gauge dependencies

We now examine in more detail the gauge choice that is contained in the definition of the Fourier transform of the creation and annihilation operators. The choice of the previous section, as mentioned, reflects the requirement $\mathcal{H}(\vec{k}+\vec{G}) = \mathcal{H}(\vec{k})$. A

common choice in tight-binding analyses is (supressing generalized orbital indices for clarity)

$$\hat{\psi}_i(\vec{k}) = \frac{1}{\sqrt{N}} \sum_{\vec{x}} \hat{\psi}(\vec{x} + \vec{l}_i)e^{-i\vec{k}\cdot(\vec{x}+\vec{l}_i)}$$

$$= \frac{1}{\sqrt{N}} \sum_{\vec{x}} \hat{\psi}_i(\vec{x})e^{-i\vec{k}\cdot(\vec{x}+\vec{l}_i)} = \frac{e^{-i\vec{k}\cdot\vec{l}_i}}{\sqrt{N}} \sum_{\vec{x}} \hat{\psi}_i(\vec{x})e^{-i\vec{k}\cdot\vec{x}}. \qquad (9.11)$$

It is easy to see that the two choices are indeed related by gauge transformation of the form

$$\mathcal{A}(\vec{k}) = \text{diag}(e^{i\vec{k}\cdot\vec{l}_1}, \ldots, e^{i\vec{k}\cdot\vec{l}_{N_\text{sl}}}),$$
$$\mathcal{A}^\dagger(\vec{k}) = \text{diag}(e^{-i\vec{k}\cdot\vec{l}_1}, \ldots, e^{-i\vec{k}\cdot\vec{l}_{N_\text{sl}}}) \qquad (9.12)$$

We immediately deduce that the momentum dependent Hamiltonian in the new basis is written in terms of the previous choice as

$$\mathcal{H}'(\vec{k}) = \mathcal{A}^\dagger(\vec{k})\mathcal{H}(\vec{k})\mathcal{A}(\vec{k}) \qquad (9.13)$$

The vectors $\vec{l}_i$ decribe structures within the unit cell and it is therefore obviously not true that inner products with reciprocal lattice vectors will give multiples of 2π. Hence, $\mathcal{H}'(\vec{k} + \vec{G}) \neq \mathcal{H}'(\vec{k})$. This has the following consequence. Since the two Hamiltonians are unitarily equivalent, the spectrum is unaltered and will be fully revealed in the first Brillouin zone. The eigenstates however will not be periodic as expected, and show a repetitive pattern not equal to the first Brillouin zone. This should be taken into account when doing calculations, but will not be reflected in quantities of physical significance.

Repeating the same calculation as above to find the transformation properties of state operators, we deduce that

$$\hat{U}_R\hat{\psi}_i(\vec{k})\hat{U}_R^\dagger = \sum_j \sum_{\vec{x}} U_{Rij}^{\text{sl}}\hat{\psi}_j(\vec{x}')e^{-i\vec{k}\cdot(\vec{x}+\vec{l}_i)} = \sum_j \sum_{\vec{x}} U_{Rij}^{\text{sl}}\hat{\psi}_{j\sigma'}(\vec{x}')e^{-i\vec{k}\cdot R^{-1}(\vec{x}'+\vec{l}_j)}$$

$$= \sum_j \sum_{\vec{x}} U_{Rij}^{\text{sl}}\hat{\psi}_j(\vec{x}')e^{-iR\vec{k}\cdot(\vec{x}'+\vec{l}_j)} = \sum_j U_{Rij}^{\text{sl}}\hat{\psi}_{j\sigma'}(R\vec{k}), \qquad (9.14)$$

From which we conclude that with this gauge choice the matrix $\mathcal{U}_R$ is completely momentum indepdent and only contains the permutation of all the atoms in the unit cell: $\mathcal{U}_R'\mathcal{H}'(\vec{k})\mathcal{U}_R'^\dagger = \mathcal{H}'(R\vec{k})$.

It is important to be aware of this difference when studying invariant $\vec{k}$-points, i.e. momenta for which $R\vec{k}^* = \vec{k}^* \mod \vec{G}$. In that case one often needs precisely

$\mathcal{H}(\vec{k} + \vec{G}) = \mathcal{H}(\vec{k})$, so that

$$\mathcal{U}_R(\vec{k}^*)\mathcal{H}(\vec{k}^*)\mathcal{U}_R^\dagger(\vec{k}^*) = \mathcal{H}(R\vec{k}^*) = \mathcal{H}(\vec{k}^* \bmod \vec{G}) = \mathcal{H}(\vec{k}^*). \tag{9.15}$$

9.1.3   Lattice symmetries and translational symmetry breaking

When translational invariance is lost due to the interaction-induced formation of a density-wave state, the explicit operation of lattice symmetries is slightly altered. Here we show explicitly how translational symmetry breaking affects the action of lattice operations (which may even no longer be symmetries) within the formalism developed above. In light of content of this work, we demonstrate this for a specific case of translational symmetry breaking, where the generators of the remaining translations are at most doubled with respect to the fully symmetric ones, i.e. $\vec{x}_1 \to 2\vec{x}_1$ and/or $\vec{x}_2 \to 2\vec{x}_2$. This amounts to a quadrupled unit cell at most. The considerations are completely general however, and apply equivalently to situations where the unit cell is tripled, which is natural in systems with hexagonal symmetry.

The mean field Hamiltonian for given density-wave order is then written as

$$\hat{H} = \sum_{\vec{k} \in \text{rbz}} \hat{\chi}^\dagger(\vec{k})\mathcal{H}(\vec{k})\hat{\chi}(\vec{k}). \tag{9.16}$$

where the spinor $\hat{\chi}$ is given by

$$\hat{\chi}(\vec{k}) = \hat{\chi}_{\mu j}(\vec{k}) = \begin{bmatrix} \hat{\chi}_{0j}(\vec{k}) \\ \hat{\chi}_{1j}(\vec{k}) \\ \hat{\chi}_{2j}(\vec{k}) \\ \hat{\chi}_{3j}(\vec{k}) \end{bmatrix} = \begin{bmatrix} \hat{\psi}_j(\vec{k}) \\ \hat{\psi}_j(\vec{k} + \vec{Q}_1) \\ \hat{\psi}_j(\vec{k} + \vec{Q}_2) \\ \hat{\psi}_j(\vec{k} + \vec{Q}_3) \end{bmatrix}. \tag{9.17}$$

The momenta $\vec{Q}_\mu$ satisfy the relations $2\vec{Q}_\mu = \vec{0} \bmod \vec{G}$ and $\vec{Q}_1 + \vec{Q}_2 + \vec{Q}_3 = \vec{0} \bmod \vec{G}$. For convenience we set $\vec{Q}_0 = \vec{0}$. Note that these algebraic relations pertain to the case of unit cell quadrupling. Different algebraic relations hold for other patterns of translational symmetry breaking, the scheme does not depend on the specific form of these relations.

We derive that a point group operation acts on the spinor components as

$$\hat{U}_R\hat{\chi}_{\mu i}(\vec{k})\hat{U}_R^\dagger = \hat{U}_R\hat{\psi}_i(\vec{k} + \vec{Q}_\mu)\hat{U}_R^\dagger = U_{Rij}^{\text{sl}}(\vec{k} + \vec{Q}_\mu)\hat{\psi}_j(R\vec{k} + R\vec{Q}_\mu) =$$

$$U_{Rij}^{\text{sl}}(\vec{k} + \vec{Q}_\mu)\hat{\psi}_j(R\vec{k} + \vec{Q}_\nu) = U_{Rij}^{\text{sl}}(\vec{k} + \vec{Q}_\mu)U_{R\mu\nu}^{\text{sb}}\hat{\chi}_{\nu j}(R\vec{k}) =$$

$$\begin{bmatrix} U_R^{\text{sl}}(\vec{k}) & & \\ & \ddots & \\ & & U_R^{\text{sl}}(\vec{k} + \vec{Q}_3) \end{bmatrix}_{\mu\nu} U_{R\nu\eta}^{\text{sb}}\hat{\chi}_\eta(R\vec{k}), \tag{9.18}$$

Here U_R^{sb} is a matrix that acts on the momentum components μ of the spinor $\hat{\chi}$. The point group operation R generally permutes the momenta $\vec{Q}_\mu$ that represent the translational symmetry breaking (sb) and the symmetry breaking matrix U_R^{sb} implements this permutation. We stress that in the case of translational breaking we do not have the freedom to multiply the matrix $U_R^{\text{sl}}(\vec{k}) = \text{diag}(e^{iR\vec{k}\cdot\vec{t}_1}, \ldots, e^{iR\vec{k}\cdot\vec{t}_{N_{\text{sl}}}}) \times U_R^{\text{sl}}$ by an overall factor $e^{-iR\vec{k}\cdot\vec{t}_1}$. The latter is allowed in the absence of translational symmetry breaking since an overall global displacement of the unit cell is immaterial. When translational symmetry is broken $\vec{t}_j$ may no longer be good translations.

Based on the above we can write down an expression for the symmetry condition of the translationally broken mean-field Hamiltonian in momentum space. If we denote the mean-field Hamiltonian as $\mathcal{H}(\vec{k})$ and the matrix representing the symmetry operation by $\widetilde{\mathcal{U}}^\dagger(\vec{k})$, which is defined as $\hat{U}_R\hat{\chi}(\vec{k})\hat{U}_R^\dagger = \widetilde{\mathcal{U}}^\dagger(\vec{k})\hat{\chi}(R\vec{k})$, then we have

$$\widetilde{\mathcal{U}}_R(\vec{k})\mathcal{H}(\vec{k})\widetilde{\mathcal{U}}_R^\dagger(\vec{k}) = \mathcal{H}(R\vec{k}) \tag{9.19}$$

Here $\vec{k}$ is restricted to the reduced BZ (RBZ). Care must be taken when analyzing invariant $\vec{k}$-points in the reduced BZ, as these points are not invariant points in the original BZ. Using the periodicity of the RBZ is consequently nontrivial. To demonstrate this, let us imagine that we are considering a momentum $\vec{k}^*$ that is left invariant in the RBZ by the symmetry operation R. Then we would naively have $\hat{\chi}_\mu(R\vec{k}^*) = \hat{\chi}_\mu(\vec{k}^*)$. This is not correct however. The correct relation reads $\hat{\chi}_\mu(R\vec{k}^*) = \hat{\chi}_\mu(\vec{k}^* + \vec{G}_{\text{rbz}})$, where $\vec{G}_{\text{rbz}}$ is a reciprocal lattice vector of the RBZ. For the cases we have restricted ourselves to from the outset, which is commensurate $\vec{Q}_\mu$, the reciprocal lattice vectors of the RBZ are precisely the $\vec{Q}_\mu$ vectors. To see this one observes that they all get folded onto Γ by definition and thus must correspond to reciprocal lattice vectors. This means that we must have $\vec{G}_{\text{rbz}} = \vec{Q}_\mu$. In addition we know that given the commensurability assumptions the vectors $\vec{Q}_\mu$ form a group under addition. From this we conclude that the addition of a RBZ reciprocal lattive vector just permutes the $\hat{\chi}_\mu$, i.e. $\hat{\chi}_\mu(\vec{k}^* + \vec{G}_{\text{rbz}}) = U_{\mu\nu}^{\text{eq}\dagger}\hat{\chi}_\nu(\vec{k}^*)$. The matrix $U_{\mu\nu}^{\text{eq}}$ implements the equivalence of momenta in the RBZ. In particular, this means for a symmetry operation R that

$$\mathcal{H}(R\vec{k}^*) = \mathcal{H}(\vec{k}^* + \vec{G}_{\text{rbz}}) = U^{\text{eq}\dagger}\mathcal{H}(\vec{k}^*)U^{\text{eq}} \tag{9.20}$$

and hence that

$$U^{\text{eq}}\widetilde{\mathcal{U}}_R(\vec{k}^*)\mathcal{H}(\vec{k}^*)\widetilde{\mathcal{U}}_R^\dagger(\vec{k}^*)U^{\text{eq}\dagger} = \mathcal{H}(\vec{k}^*). \tag{9.21}$$

We note in passing that it is a straightforward, albeit possibly tedious, matter to change to a gauge for which $\mathcal{H}(\vec{k} + \vec{G}_{\text{rbz}}) = \mathcal{H}(\vec{k})$, where $\mathcal{H}(\vec{k})$ is the mean-field

Hamiltonian of the translational symmetry broken state. One may choose $\vec{Q}_1$ and $\vec{Q}_2$ as generators of the reciprocal lattice, for which we have $\hat{\chi}(\vec{k}+\vec{Q}_1) = U_1^{\text{eq}\dagger}\hat{\chi}(\vec{k})$ and $\hat{\chi}(\vec{k}+\vec{Q}_2) = U_2^{\text{eq}\dagger}\hat{\chi}(\vec{k})$. Clearly $\hat{\chi}(\vec{k}+\vec{Q}_1+\vec{Q}_2) = U_1^{\text{eq}\dagger}U_2^{\text{eq}\dagger}\hat{\chi}(\vec{k}) = U_2^{\text{eq}\dagger}U_1^{\text{eq}\dagger}\hat{\chi}(\vec{k})$, implying that $U_1^{\text{eq}\dagger}$ and $U_2^{\text{eq}\dagger}$ commute and are simultaneously diagonalizable. For $2\vec{Q}_1 = 2\vec{Q}_2 = 0$ we have in addition $(U_1^{\text{eq}})^2 = (U_2^{\text{eq}})^2 = 1$ mandating the eigenvalues to be $e^{i\phi_\mu}$ with $\phi_\mu = 0, \pi$. One now sets $\phi_\mu = \vec{k}\cdot\vec{x}_{1,2}$ so as to match correct value for $\vec{Q}_1\cdot\vec{x}_{1,2} = 0, \pi$ and $\vec{Q}_2\cdot\vec{x}_{1,2} = 0, \pi$ simultaneously. This then defines the gauge transformation needed to compensate the eigenvalues of U_1^{eq} and U_2^{eq}.

We close this section by showing that an analogous expression can be derived for the tight-binding gauge, i.e. $\tilde{\mathcal{H}}(\vec{k}) = \mathcal{A}^\dagger(\vec{k})\mathcal{H}(\vec{k})\mathcal{A}(\vec{k})$. In that case we obtain

$$\hat{U}_R\hat{\chi}_{\mu i}(\vec{k})\hat{U}_R^\dagger = \hat{U}_R\hat{\psi}_i(\vec{k}+\vec{Q}_\mu)\hat{U}_R^\dagger =$$
$$U_{Rij}^{\text{sl}}\hat{\psi}_j(R\vec{k}+R\vec{Q}_\mu) = U_{Rij}^{\text{sl}}\hat{\psi}_j(R\vec{k}+\vec{Q}_\nu+\vec{G}_\mu) =$$
$$U_{Rij}^{\text{sl}}(\vec{G}_\mu)U_{R\mu\nu}^{\text{sb}}\hat{\psi}_j(R\vec{k}+\vec{Q}_\nu) = U_{Rij}^{\text{sl}}(\vec{G}_\mu)U_{R\mu\nu}^{\text{sb}}\hat{\chi}_{\nu j}(R\vec{k}) =$$
$$\begin{bmatrix} U_R^{\text{sl}}\mathcal{A}^\dagger(\vec{0}) & & \\ & \ddots & \\ & & U_R^{\text{sl}}\mathcal{A}^\dagger(\vec{G}_3) \end{bmatrix}_{\mu\nu} U_{R\nu\eta}^{\text{sb}}\hat{\chi}_\eta(R\vec{k}), \tag{9.22}$$

where the crucial point to notice here is that $R\vec{Q}_\mu = \vec{Q}_\nu + \vec{G}_\mu$ with $\vec{G}_\mu$ some reciprocal lattice vector which has an effect on the state operator via $\mathcal{A}^\dagger(\vec{G}_\mu)$. This fully specifies the action of symmetry operations on state operators in the tight-binding gauge.

9.1.4 Topological characteristics of fermionic states

We now come to a brief discussion of the topological character of fermionic states. One of the main purposes of this work was to shed light on the connection between lattice symmetry and spectral properties. Symmetry broken density wave states may cause a spectral gap to open, in which case the ground state will be insulating for the appropriate filling. The presence of discrete symmetries can give rise to additional topological quantum numbers of the ground state and here we are interested in the topological structure based on lattice symmetries [172, 176, 181]. The symmetry classification of particle hole condensates proposed and worked out here allows for a characterization of these condensates in terms of additional topological quantum numbers. In characterizing the condensates we will rely on the theoretical framework developed in Refs. [172, 182]. Here we will merely summarize some the results reported in those works and adapt them slighty to the language and definitions presented here.

It is convenient to rewrite the real space basis functions as $|\vec{x}, j\rangle = \hat{\psi}_j^\dagger(\vec{x})|0\rangle$, where for convenience we collect all local degrees of freedom (sublattice, orbital, spin) in the label j. After diagonalization of the Bloch Hamiltonian $\mathcal{H}(\vec{k})$ one obtains the spectrum $E_n(\vec{k})$ where n labels the band. The eigenstates are $|\vec{k}, n\rangle = \hat{\gamma}_n^\dagger(\vec{k})|0\rangle$. The normal mode operators and orbital operators are related by a matrix $U(\vec{k})$ that contains the eigenvectors of the matrix $\mathcal{H}(\vec{k})$ in its columns, $\hat{\gamma}_n^\dagger(\vec{k}) = \hat{\psi}_j^\dagger(\vec{k})U_{jn}(\vec{k})$ with $\mathcal{H}_{ij}(\vec{k})U_{jn}(\vec{k}) = E_n(\vec{k})U_{in}(\vec{k})$. For the orbital operators we have the relation

$$\hat{U}_R\hat{\psi}_i(\vec{k})\hat{U}_R^\dagger = \mathcal{U}_{Rij}^\dagger(\vec{k})\hat{\psi}_j(R\vec{k}),$$
$$\hat{U}_R\hat{\psi}_i^\dagger(\vec{k})\hat{U}_R^\dagger = \hat{\psi}_j^\dagger(R\vec{k})\mathcal{U}_{Rji}(\vec{k}) \tag{9.23}$$

which implies for the normal mode operators

$$\hat{U}_R\hat{\gamma}_n\hat{U}_R^\dagger = U_{ni}^\dagger(\vec{k})\mathcal{U}_{Rij}^\dagger(\vec{k})U_{jm}(R\vec{k})\hat{\gamma}_m(R\vec{k}),$$
$$\hat{U}_R\hat{\gamma}_n^\dagger(\vec{k})\hat{U}_R^\dagger = \hat{\gamma}_m^\dagger(R\vec{k})U_{mj}^\dagger(R\vec{k})\mathcal{U}_{Rji}(\vec{k})U_{in}(\vec{k}) \tag{9.24}$$

These relations hold in an equivalent way for the mean-field normal modes $\hat{\gamma}_n^\dagger(\vec{k}) = \hat{\chi}(\vec{k})U_{jn}(\vec{k})$ (we use the same symbols as no confusion is expected), resulting from the mean-field Hamiltonian. Based on the expressions for the operation of symmetries on $\hat{\chi}(\vec{k})$ given in the previous sections, we simply have to substitute $\widetilde{\mathcal{U}}_R(\vec{k})$ for $\mathcal{U}_R(\vec{k})$. To establish a connection with results of [172], we define the sewing matrix $\mathcal{B}_R(\vec{k})$ corresponding to an operation R as

$$\hat{U}_R\hat{\gamma}_n^\dagger(\vec{k})\hat{U}_R^\dagger \equiv \hat{\gamma}_m^\dagger(R\vec{k})\mathcal{B}_{Rmn}(\vec{k}) \tag{9.25}$$

which may be expressed alternatively as

$$\mathcal{B}_{Rmn}(\vec{k}) = \langle R\vec{k}, m|\hat{U}_R|\vec{k}, n\rangle. \tag{9.26}$$

For condensate state which have an energy gap at the relevant filling (and under the assumption that R is indeed a symmetry) the sewing matrix will not mix occupied and unoccupied bands and therefore it is block diagonal. One can use equation (9.1.4) to write an expression for the sewing matrix in terms $\mathcal{U}_R$,

$$\mathcal{B}_R(\vec{k}) = U^\dagger(R\vec{k})\mathcal{U}_R(\vec{k})U(\vec{k}). \tag{9.27}$$

Note that the three matrix appearing in the product are not individually block diagonal in the space of (occupied and unoccupied) bands. From this specific expression it is however immediately obvious that the sewing matrix is unitary. Hence, due to the

block diagonal structure, the sewing matrix is unitary when restricted to the space of occupied bands. In accordance with custom we restrict ourselves to the space of occupied bands.

There are two distinct types of additional quantum numbers an insulating state can, or cannot, acquire in two dimensions as a consequence of lattice point group symmetries. The first is the Chern number C, an integer which labels the Quantum Hall universality class of the insulating state. Nonzero Chern number will lead to a quantized Hall response when an electric field is applied, expressing the fact that the Chern number, a topological index, physically corresponds to the Hall conductivity σ_{xy}. The Chern number is defined as

$$C = \frac{1}{2\pi} \int_{\text{bz}} d\vec{k} \operatorname{Tr}\left[F_{xy}(\vec{k})\right], \tag{9.28}$$

where $F_{xy}(\vec{k})$ is the momentum space field strength corresponding to the non-Abelian Berry gauge connection $A_i^{nm}(\vec{k})$, $i = x, y$. The latter is given by the expression

$$A_i^{nm}(\vec{k}) = -i\langle \vec{k}, n|\partial_i|\vec{k}, m\rangle \tag{9.29}$$

and the field strength is calculated in the standard way as

$$F_{ij}(\vec{k}) = \partial_i A_j(\vec{k}) - \partial_j A_i(\vec{k}) + i[A_i(\vec{k}), A_j(\vec{k})] \tag{9.30}$$

where $i, j = x, y$ and $\partial_i \equiv \partial/\partial k_i$. The non-Abelian nature of the connection A_i and the field strength F_{ij} comes from the band indices n, m, which refer to the occupied bands only. The trace in equation (9.28) should therefore be understood as restricted to the space of occupied bands.

To see how point group symmetries constrain the Chern number one first derives the transformation of the field strength F_{ij} under such a point group operation, which is

$$F_{i'j'}(R\vec{k}) = \partial_{i'} A_{j'}(R\vec{k}) - \partial_{j'} A_{i'}(R\vec{k}) + i[A_{i'}(R\vec{k}), A_{j'}(R\vec{k})] = \\ R_{i'i} R_{j'j} \mathcal{B}_R(\vec{k}) F_{ij}(\vec{k}) \mathcal{B}_R^\dagger(\vec{k}). \tag{9.31}$$

From this general transformation rule it follows that

$$F_{x'y'}(R\vec{k}) = \operatorname{Det}[R] \mathcal{B}_R(\vec{k}) F_{xy}(\vec{k}) \mathcal{B}_R^\dagger(\vec{k}), \tag{9.32}$$

which yields when tracing over the occupied bands

$$\operatorname{Tr}\left[F_{x'y'}(R\vec{k})\right] = \operatorname{Det}[R] \operatorname{Tr}\left[F_{xy}(\vec{k})\right]. \tag{9.33}$$

This relation can be directly used to deduce that if the system has a symmetry which is improper, i.e. $\mathrm{Det}\,[R] = -1$, the Chern number must vanish [172]. Hence, in $2D$ only insulating states which have rotational symmetries C_n are allowed to have nonzero Chern number. Incidentally, as was demonstrated earlier [177], the presence of time-reversal symmetry leads to the relation $\mathrm{Tr}\,[F_{xy}(-\vec{k})] = -\mathrm{Tr}\,[F_{xy}(\vec{k})]$ and mandates vanishing Chern number in the same way. Physically this is not surprising as the quantum Hall response equation itself is time-reversal odd.

Point group symmetries not only force the Chern number to be zero in some cases, they can also be used to calculate it modulo an integer number [172]. For instance, in case of C_4 symmetry, the Chern number is given by a product of eigenvalues of C_4 and C_2 modulo 4. Specifically, if we label the eigenvalue of C_4 at the square lattice Brillouin zone center Γ by $\eta_4(\Gamma)$, the C_4-eigenvalue at the Brillouin zone corner, denoted as Q_1 (see Fig. 9.1), by $\eta_4(Q_2)$, and the C_2 eigenvalue at Q_2 by $\eta_{2i}(Q_2)$ (or equivalently Q_3), then we have

$$e^{i\pi C/2} = \prod_{i\in\mathrm{occ}} \eta_{4i}(\Gamma)\eta_{4i}(Q_1)\eta_{2i}(Q_2) \tag{9.34}$$

(i indexing the bands) which shows that the Chern number C is determined by the eigenvalues of point group operations. Due to the exponential $e^{i\pi C/2}$ it is only determined modulo 4 in case of a C_4 symmetric insulating state. More generally, for a C_n invariant system ($n = 2, 3, 6$), the Cherm number is determined by the rotational eigenvlues η_n at high symmetry point modulo n [172, 183]. In case of a C_3 invariant state the expression reads

$$e^{i2\pi C/3} = \prod_{i\in\mathrm{occ}} \eta_{3i}(\Gamma)\eta_{3i}(K_+)\eta_{3i}(K_-) \tag{9.35}$$

where K_+ and K_- are the vertices of the hexagonal Brillouin zone, see Fig. 9.4. We note in passing that the presence of inversion symmetry alone (C_2) the parity of the Chern number C can be obtained from the inversion eigenvalues.

In order to evaluate these expressions in the context of translational symmetry broken density wave states, it is helpful to realize the that the product eigenvalues originates from the determinant of the sewing matrix, for example $\prod_{i\in\mathrm{occ}} \eta_{3i}(\Gamma) = \mathrm{Det}\,[\mathcal{B}_{C_3}(\Gamma)]$. In general, suppose that $\vec{k}^*$ is one of the invariant momenta, i.e. $R\vec{k}^* = \vec{k}^*$, then we know from section 9.1.3 that $\hat{U}_R\hat{\gamma}^\dagger(\vec{k}^*)\hat{U}_R^\dagger = \hat{\gamma}^\dagger(R\vec{k}^*)\mathcal{B}_R(\vec{k}^*) = \hat{\gamma}^\dagger(\vec{k}^*)U^{\mathrm{eq}}\mathcal{B}_R(\vec{k}^*) \equiv \hat{\gamma}^\dagger(\vec{k}^*)\widetilde{\mathcal{B}}_R(\vec{k}^*)$. Using the expression for the sewing matrix as given in equation 9.27, we have

$$\widetilde{\mathcal{B}}_R(\vec{k}^*) = U^{\mathrm{eq}}U^\dagger(R\vec{k}^*)\widetilde{\mathcal{U}}_R(\vec{k}^*)U(\vec{k}^*) = U^\dagger(\vec{k}^*)U^{\mathrm{eq}}\widetilde{\mathcal{U}}_R(\vec{k}^*)U(\vec{k}^*). \tag{9.36}$$

From equation 9.21 it follows that $U^{\text{eq}}\widetilde{\mathcal{U}}_R(\vec{k}^*)$ commutes with the Hamiltonian, meaning that $U(\vec{k})$ diagonalizes $U^{\text{eq}}\widetilde{\mathcal{U}}_R(\vec{k}^*)$ as well (or can be chosen to do so). This shows that $\text{Det}\,[\widetilde{\mathcal{B}}_R(\vec{k}^*)]$ is equal to the product of eigenvlues of $U^{\text{eq}}\widetilde{\mathcal{U}}_R(\vec{k}^*)$. The matrix U^{eq} should not be overlooked here.

The second kind of quantum numbers point group symmetric insulators can have in two dimensions is a set of two fractionally quantized numbers p_1 and p_2 which correspond to the electric charge polarization in the unit cell [172], defined as

$$\vec{P} = p_1\vec{x}_1 + p_2\vec{x}_2. \tag{9.37}$$

As polarization is generally only well-defined up to a lattice constant, one has $0 \leq p_i < 1$. The expression for the polarization parameters is

$$p_i = \frac{1}{2\pi} \int_0^1 dk_1 \int_0^1 dk_2 \text{Tr}\,[A_i(k_1\vec{G}_1 + k_2\vec{G}_2)]. \tag{9.38}$$

It should be stressed that these are only meaningful if the Chern number vanishes. This is a priori guaranteed for states with reflection symmetries or time-reversal symmetry. Ref. [172] discusses exhaustively how symmetry constrains the allowed values for p_1 and p_2. That lattice symmetries should put constraints on electric polarization is most easily seen in one dimensionen, where the only symmetry is inversion. If the polarization is p the inversion requires $p = -p + en$ with n integer due to fact that polarization is only defined up to a lattice vector. It follows that there are only two allowed values of electric polarization, 0 and $e/2$, which constitute distinct topological classes. Very similar reasoning using symmetries restricts the values of electric polarization in two dimensions. For instance, for C_6 symmetry p_1 and p_2 are necessarily integer and therefore there is no nontrivial charge polarization. Other constraints will be discussed and applied directly when specific lattice symmetry groups are considered in following sections. If symmetry allows for nontrivial polarization then appropriate symmetry eigenvalues at high symmetry points in the Brillouin zone can be used to calculate the p_i. In case of C_2 these eigenvalues formulas read

$$(-1)^{2p_1} = \prod_{i\in\text{occ}} \frac{\eta_{2i}(Q_2)}{\eta_{2i}(\Gamma)}, \quad (-1)^{2p_2} = \prod_{i\in\text{occ}} \frac{\eta_{2i}(Q_3)}{\eta_{2i}(\Gamma)} \tag{9.39}$$

These may be used as well in case of C_4 insulating states, in which case $p_1 = p_2$. In case of a C_3 invariant system the formula reads

$$e^{i2\pi p_{1,2}} = \prod_{i\in\text{occ}} \frac{\eta_{3i}(K_+)}{\eta_{3i}(K_-)}. \tag{9.40}$$

Yet a third topological number is given by the $\mathcal{Z}_2$ number which distinguishes time-reversal invariant trivial insulators from the QSH state in two dimensions (a generalization exists for $3D$) [1,3,184]. The crucial symmetry that allows for the definition of this number is time-reversal symmetry, i.e. time-reversal symmetry needs to be preserved to give rise to a meaningful $\mathbb{Z}_2$ topological classification of $2D$ (and $3D$) insulators. A $\mathbb{Z}_2$ classification implies there are only two flavors: trivial insulators and nontrivial insulators. The $\mathbb{Z}_2$ index ν is obtained as follows

$$(-1)^\nu = \prod_{n=1}^{4} \delta_n. \tag{9.41}$$

In general the δ_n, which take values ± 1 and where n labels one of the four time-reversal invariant momenta of the $2D$ BZ, are not easy to obtain, however, the presence of inversion symmetry (C_2 in $2D$) allows for a straightforward determination based on the formula

$$\delta_n = \prod_{i \in \text{occ}} \eta_{2i}(\Gamma_n). \tag{9.42}$$

Here Γ_n denote the time-reversal invariant momenta, η_{2i} is again the C_2 eigenvalue of the i-th band and the sum is over all occupied bands with the understanding that we only sum over one of the degenerate Kramers partners, which necessarily have the same eigenvlues. Wewill use this formula in Section 10.

9.2 Interactions and mean-field theory

The particle-hole condensates discussed in this paper are candidate ground states for interacting Hamiltonians on the respective lattices. It is therefore time to take a closer look into interacting lattice fermion models and build a genereal mean-field theory which may be used to test which condensates appear in the mean-field phase diagram for a given choice of interaction.

9.2.1 General formalism

We start from the assumption that the lattice has a basis, but neglect the internal orbital degree of freedom. The non-interacting part of the Hamiltonian is then written as

$$\hat{H}_0 = \sum_{ij} \sum_{\vec{k}} \hat{\psi}_i^\dagger(\vec{k}) \mathcal{H}_{ij}(\vec{k}) \hat{\psi}_j(\vec{k}). \tag{9.43}$$

Here and in the rest of this section we will explicitly write the sums over indices i, j as adherence to the summation convemtion may be confusing. For the interacting part of the Hamiltonian we take a density-density interaction of the form

$$
\begin{aligned}
\hat{H}_{\text{int}} &= \frac{1}{2} \sum_{ij} \sum_{\vec{x}, \vec{x}'} V_{ij}(\vec{x} - \vec{x}') \hat{n}_i(\vec{x}) \hat{n}_j(\vec{x}') \\
&= \frac{1}{2} \sum_{ij} \sum_{\vec{q}} \tilde{V}_{ij}(\vec{q}) \hat{\rho}_i(\vec{q}) \hat{\rho}_j(-\vec{q}),
\end{aligned}
\tag{9.44}
$$

Here $\hat{n}_i(\vec{x}) = \hat{\psi}_i^\dagger(\vec{x}) \hat{\psi}_i(\vec{x})$ and we have assumed translational invariance of interactions, expressed in $V_{ij}(\vec{x} - \vec{x}')$ which only depends on the difference $\vec{x} - \vec{x}'$. Observe that we have suppressed spin indices here and excluded an onsite interaction of the type $U \hat{n}_\uparrow(\vec{x}) \hat{n}_\downarrow(\vec{x})$. This type of interaction is valid for spinless systems to which we will restrict ourselves in this section so as to avoid unnecessary complication at this stage. In the next section we treat the spinful case. As mentioned elsewhere, we will touch on triplet spin-density waves only occasionally in the bulk of this paper and in the last section we take more detailed but far from exhaustive look at triplet condensates. For now we particularize to spinless fermions. Note also the appearance of the factor $1/2$ in front of the sum. This is due to the fact that we will find it convenient to enforce $V_{ij}(\vec{x}) = V_{ji}(-\vec{x})$, which has the consequence that each combination $\hat{n}_i(\vec{x}) \hat{n}_j(\vec{x}')$ occurs twice.

The momentum dependent density-operator is defined as

$$
\hat{\rho}_i(\vec{q}) = \sum_{\vec{k}} \hat{\psi}_i^\dagger(\vec{k} + \vec{q}) \hat{\psi}_i(\vec{k}),
\tag{9.45}
$$

and the Fourier transformed interaction reads explicitly

$$
\tilde{V}_{ij}(\vec{q}) = \frac{1}{N} \sum_{\vec{x}} V_{ij}(\vec{x}) e^{-i\vec{q} \cdot \vec{x}}.
\tag{9.46}
$$

Note that so far we have not made any assumptions on the range of the interaction. The property $V_{ij}(\vec{x}) = V_{ji}(-\vec{x})$ is expressed in momentum space as $\tilde{V}_{ji}(\vec{q}) = \tilde{V}_{ij}^*(\vec{q}) = \tilde{V}_{ij}(-\vec{q})$. As it is written now it generally contains interactions between nearest-neighbors, next nearest-neighbors, ect. In any specific model calculation one will always terminate this sequence somewhere and we therefore we write the interaction in momentum space as a series in which each term represents a distict range,

$$
\tilde{V}_{ij}(\vec{q}) = \frac{1}{N} \sum_n V_n \Gamma_{ij}^{(n)}(\vec{q}), \quad n = 1, 2, \ldots
\tag{9.47}
$$

where, for instance, V_1 corresponds to the interaction between nearest neighbors only. We stress that the nearest neighbor interaction pertains to the underlying lattice, and thus may be active between unit cells as well as within the unit cell.

Writing the the interaction term of equation (9.44) in terms of field operators explicitly we easily get

$$\sum_{ij} \sum_{\vec{q},\vec{k},\vec{k}'} \hat{\psi}_i^\dagger(\vec{k}+\vec{q})\hat{\psi}_i(\vec{k})\, \tilde{V}_{ij}(\vec{q})\, \hat{\psi}_j^\dagger(\vec{k}'-\vec{q})\hat{\psi}_j(\vec{k}'). \tag{9.48}$$

In the weak-coupling limit, anticipating density-wave order of some kind, it is legitimate to employ a Hubbard-Stratonovich (HS) decouplig of the interaction and look for the saddle-point solution. To that end we introduce two kinds of HS fields, one for charge order and one for bond order. At the same time, we make an assumption concerning the type of translational symmetry breaking, by specifiying the set of ordering vectors $\vec{Q}_\gamma$ which will feature in the expecation values $\langle \hat{\psi}^\dagger(k+Q_\gamma)\hat{\psi}(k)\rangle$. Consequently, the Ansatz for the HB fields corresponding to charge order are specified by the expression

$$\sum_{i,\gamma,\vec{k}} \Delta_{i\gamma}^* \,\hat{\psi}_i^\dagger(\vec{k}-\vec{Q}_\gamma)\hat{\psi}_i(\vec{k}) + \sum_{i,\gamma,\vec{k}} \hat{\psi}_i^\dagger(\vec{k}+\vec{Q}_\gamma)\hat{\psi}_i(\vec{k})\,\Delta_{i\gamma} - \sum_{i,j,\gamma} \Delta_{i\gamma}^* \tilde{V}_{ij}^{-1}(\vec{Q}_\gamma)\Delta_{j\gamma},$$

$$\tag{9.49}$$

and the saddle-point equations read

$$\begin{aligned}
\Delta_{i\gamma}^* &= \sum_{j,\vec{k}} \langle \hat{\psi}_j^\dagger(\vec{k}+\vec{Q}_\gamma)\hat{\psi}_j(\vec{k})\rangle \tilde{V}_{ji}(\vec{Q}_\gamma) \\
\Delta_{i\gamma} &= \sum_{j,\vec{k}} \tilde{V}_{ij}(\vec{Q}_\gamma)\langle \hat{\psi}_j^\dagger(\vec{k})\hat{\psi}_j(\vec{k}+\vec{Q}_\gamma)\rangle,
\end{aligned} \tag{9.50}$$

which are obviously equivalent due to $\tilde{V}_{ij}^* = \tilde{V}_{ji}$. In general, the order parameters $\Delta_{i\gamma}$ are complex, which suggests that the degrees contained in them are twice the number of lattice orbitals labeled by i times the number of ordering vectors labeled by γ. For site order this would not seem right, and indeed, given the set of $\vec{Q}_\gamma$, one may deduce relations showing the correct number of degrees of freedom. For instance, in case of $2\vec{Q}_\gamma = 0$, it is easy to show that the $\Delta_{i\gamma}$ are real.

For bond order we follow a similar recipy, by first arranging the interaction in a suitable fashion

$$-\sum_{ij} \sum_{\vec{q},\vec{k},\vec{k}'} \hat{\psi}_i^\dagger(\vec{k}+\vec{q})\hat{\psi}_j(\vec{k})\, \tilde{V}_{ij}(\vec{k}-\vec{k}')\, \hat{\psi}_j^\dagger(\vec{k}')\hat{\psi}_i(\vec{k}'+\vec{q}). \tag{9.51}$$

Note the minus sign coming from the anti-commutation of fermion operators. For the interaction as given in (9.44) and (9.47), the functions $\Gamma_{ij}^{(n)}(\vec{k} - \vec{k}')$ contained in $\tilde{V}_{ij}(\vec{k} - \vec{k}')$ are separable. Specifically, one can write $\Gamma_{ij}^{(n)}(\vec{k} - \vec{k}')$ as a sum of products of basis functions of irreducible representation of the lattice point group. This yields the expression

$$\Gamma_{ij}^{(n)}(\vec{k} - \vec{k}') = \sum_{\mathcal{I},r} \lambda_{ij}^{(n,\mathcal{I}_r)}(\vec{k}) \, \lambda_{ij}^{(n,\mathcal{I}_r)*}(\vec{k}') \tag{9.52}$$

where the sum is over irreducible representations labeled by $\mathcal{I}$ and its basis functions r (an irreducible representation may have more than one basis function). A term in the expansion defined by (9.47) then takes the form

$$-\frac{V_n}{N} \sum_{ij} \sum_{\vec{q},\vec{k},\vec{k}'} \sum_{\mathcal{I},r} \hat{\psi}_i^\dagger(\vec{k} + \vec{q})\hat{\psi}_j(\vec{k}) \, \lambda_{ij}^{(n,\mathcal{I}_r)}(\vec{k}) \, \lambda_{ij}^{(n,\mathcal{I}_r)*}(\vec{k}') \, \hat{\psi}_j^\dagger(\vec{k}')\hat{\psi}_i(\vec{k}' + \vec{q}). \tag{9.53}$$

Sticking with a term such as this one, we introduce the bond HS fields $\Delta_{ij\gamma}^{(n,\mathcal{I}_r)}$ and $\Delta_{ij\gamma}^{(n,\mathcal{I}_r)\dagger}$ as

$$-\sum_{i,j,\gamma,\vec{k}} \sum_{\mathcal{I},r} \left[\Delta_{ij\gamma}^{(n,\mathcal{I}_r)*}\lambda_{ij}^{(n,\mathcal{I}_r)*}(\vec{k}) \, \hat{\psi}_j^\dagger(\vec{k})\hat{\psi}_i(\vec{k} + \vec{Q}_\gamma) + \right.$$
$$\left. \hat{\psi}_i^\dagger(\vec{k} + \vec{Q}_\gamma)\hat{\psi}_j(\vec{k}) \, \lambda_{ij}^{(n,\mathcal{I}_r)}(\vec{k})\Delta_{ij\gamma}^{(n,\mathcal{I}_r)} \right]$$
$$+\frac{N}{V_n} \sum_{\gamma,\mathcal{I},r} \Delta_{ij\gamma}^{(n,\mathcal{I}_r)*}\Delta_{ij\gamma}^{(n,\mathcal{I}_r)} \tag{9.54}$$

for which we have the saddle-point equations

$$\Delta_{ij\gamma}^{(n,\mathcal{I}_r)*} = \frac{V_n}{N} \sum_{\vec{k}} \langle \hat{\psi}_i^\dagger(\vec{k} + \vec{Q}_\gamma)\hat{\psi}_j(\vec{k}) \rangle \lambda_{ij}^{(n,\mathcal{I}_r)}(\vec{k})$$

$$\Delta_{ij\gamma}^{(n,\mathcal{I}_r)} = \frac{V_n}{N} \sum_{\vec{k}} \lambda_{ij}^{(n,\mathcal{I}_r)*}(\vec{k}) \langle \hat{\psi}_j^\dagger(\vec{k})\hat{\psi}_i(\vec{k} + \vec{Q}_\gamma) \rangle. \tag{9.55}$$

As a consequence of translational symmetry breaking, we restrict the sum over momenta $\vec{k}, \vec{k}'$ to momenta in the reduced Brillouin zone. At the same time we must include a sum over the momenta $\vec{Q}_\mu$ for each of the momentum summations. For the

charge order parameter fields this yields explicitly

$$
\begin{aligned}
\Delta_{i\gamma} &= \sum_{j,\mu,\vec{k}\in\text{rbz}} \tilde{V}_{ij}(\vec{Q}_\gamma)\langle\hat{\psi}_j^\dagger(\vec{k}+\vec{Q}_\mu)\hat{\psi}_j(\vec{k}+\vec{Q}_\gamma+\vec{Q}_\mu)\rangle \\
&= \sum_{j,\mu,\vec{k}\in\text{rbz}} \tilde{V}_{ij}(\vec{Q}_\gamma)\langle\hat{\chi}_{\mu j}^\dagger(\vec{k})\hat{\chi}_{[\mu+\gamma]j}(\vec{k})\rangle. \quad (9.56)
\end{aligned}
$$

We have used the definition $\hat{\chi}_{\mu i}(\vec{k}) = \hat{\psi}_i^\dagger(\vec{k}+\vec{Q}_\mu)$ already introduced in Section 9.1.3. By $[\mu+\gamma]$ we mean the index ν that is the result of $\vec{Q}_\gamma + \vec{Q}_\mu = \vec{Q}_\nu$. Hence, the momenta must be added and not the indices μ and γ itself. The mean-field part of the Hamiltonian corresponding to charge order then reads

$$
\sum_{i,\mu,\gamma,\vec{k}\in\text{rbz}} \left[\Delta_{i\gamma}^* \, \hat{\chi}_{\mu i}^\dagger(\vec{k})\hat{\chi}_{[\mu+\gamma]i}(\vec{k}) + \hat{\chi}_{[\mu+\gamma]i}^\dagger(\vec{k})\hat{\chi}_{\mu i}(\vec{k}) \, \Delta_{i\gamma} \right] - \sum_{i,j,\gamma} \Delta_{i\gamma}^* \tilde{V}_{ij}^{-1}(\vec{Q}_\gamma)\Delta_{j\gamma}.
$$

$$(9.57)$$

This mean field part of the Hamiltonian containing the coupling of (charge) order parameters to the spinors $\hat{\chi}$, together with the free part $\mathcal{H}_0(\vec{k})$ constitutes the full mean field Hamiltonian of equation (9.16). The formalism laid out in the previous section can now be used to investigate the structure of symmetry breaking induced by the mean fields.

Clearly a similar expression may be written down for bond order, but instead of quoting the general result we think it will be illustrative to work out a specific case and see the formalism outlined above at work directly. We will do so in Section 9.2.3.

We close this section with some general remarks on the order parameters introduced above. By defining them such that they are labeled by the momenta $\vec{Q}_\gamma$, we have separated them automatically into translationally invariant and translational symmetry broken components. Both for bond and site order, the $\gamma = 0$ component corresponds to translationally invariant orders, while nonzero $\gamma \neq 0$ components signal the breaking of translational symmetry. The main purpose of the present mean-field theory is to find out which condensates transforming as irreducible representations of the relevant symmetry are contained in the solutions of the saddle-point equations, i.e. the site and bond order parameters. The translationally invariant components $\gamma = 0$ are written in the sublattice space basis and in order to find the irreducible representations contained in the order parameters we only have to project on the sublattice functions.

9.2.2 Interactions with spin

In this section we present the generalities of a mean-field theory for spinful interacting lattice fermion models. Based on the work already done in the first part of this section,

it is rather straightforward to include the spin degree of freedom and thereby provide a way to discuss, classify and test the stability of triplet particle-hole condensates.

There is one main difference with the spinless case, and we already commented on this following equation (9.44), which is the presence of an on-site Hubbard repulsion. Fermionic statistics allows each site to be occupied by two electrons of opposite spin species, a situation which will however lead to an energetic penalty customarily labeled U. The onsite Hubbard Hamiltonian reads

$$\hat{H}_{\mathrm{U}} = U \sum_{i,\vec{x}} \hat{n}_{i\uparrow}(\vec{x}) \hat{n}_{i\downarrow}(\vec{x}). \tag{9.58}$$

This term can be rewritten so as to allow for a decoupling in charge and spin order parameter fields separately. One easily finds that the onsite Hubbard term can be expressed as

$$\hat{H}_{\mathrm{U}} \sim U \sum_{i,\vec{x}} [\hat{\psi}^{\dagger}_{i\sigma}(\vec{x})\hat{\psi}_{i\sigma}(\vec{x})]^2 - U \sum_{i,\vec{x}} [\hat{\psi}^{\dagger}_{i\sigma}(\vec{x})\vec{\sigma}_{\sigma\sigma'}\hat{\psi}_{i\sigma'}(\vec{x})]^2. \tag{9.59}$$

Here and in the following we adopt the convention that spin indices appearing twice are assumed to be summed over, as this should not cause any confusion. The first term of equation (9.59) is a product of density operators, i.e. $\sum_{\sigma} \hat{n}_{i\sigma}(\vec{x})$, and hence can be decoupled using a charge order field. The second term is written in terms of spin operators, i.e. $\hat{\psi}^{\dagger}_{i\sigma}(\vec{x})\vec{\sigma}_{\sigma\sigma'}\hat{\psi}_{i\sigma'}(\vec{x}) \sim \vec{s}_i$ with σ^i a set of Pauli matrices acting in spin space, and corresponds to spin ordering. Transforming to momentum space, the first term of equation (9.59) is written as

$$U \sum_{i} \sum_{\vec{q},\vec{k},\vec{k}'} \hat{\psi}^{\dagger}_{i\sigma}(\vec{k}+\vec{q})\hat{\psi}_{i\sigma}(\vec{k})\hat{\psi}^{\dagger}_{i\sigma'}(\vec{k}')\hat{\psi}_{i\sigma'}(\vec{k}'+\vec{q}), \tag{9.60}$$

while the second term, containing the spin operators, takes the form

$$U \sum_{i} \sum_{\vec{q},\vec{k},\vec{k}'} \hat{\psi}^{\dagger}_{i\sigma_1}(\vec{k}+\vec{q})\sigma^a_{\sigma_1\sigma_2}\hat{\psi}_{i\sigma_2}(\vec{k})\hat{\psi}^{\dagger}_{i\sigma_3}(\vec{k}')\sigma^a_{\sigma_3\sigma_4}\hat{\psi}_{i\sigma_4}(\vec{k}'+\vec{q}). \tag{9.61}$$

In the same way as before we anticipate translational symmetry breaking with ordering vectors $\vec{Q}_{\gamma}$ forming a closed algebra under addition, and we proceed with the HS decoupling for the charge part to arrive at

$$\sum_{i,\gamma,\vec{k}} \Delta^{0*}_{i\gamma} \hat{\psi}^{\dagger}_{i\sigma}(\vec{k})\hat{\psi}_{i\sigma}(\vec{k}+\vec{Q}_{\gamma}) + \sum_{i,\gamma,\vec{k}} \hat{\psi}^{\dagger}_{i\sigma}(\vec{k}+\vec{Q}_{\gamma})\hat{\psi}_{i\sigma}(\vec{k}) \Delta^0_{i\gamma} - \sum_{i,\gamma} \Delta^{0*}_{i\gamma} U^{-1} \Delta^0_{i\gamma}. \tag{9.62}$$

We introduce the spinful HS fields $\Delta_{i\gamma}^a$ in the decoupling of the spin order term (9.61) as

$$-\sum_{i,\gamma,\vec{k}} \Delta_{i\gamma}^{a*} \hat{\psi}_{i\sigma}^\dagger(\vec{k})\sigma_{\sigma\sigma'}^a \hat{\psi}_{i\sigma'}(\vec{k}+\vec{Q}_\gamma)$$

$$-\sum_{i,\gamma,\vec{k}} \hat{\psi}_{i\sigma}^\dagger(\vec{k}+\vec{Q}_\gamma)\sigma_{\sigma\sigma'}^a \hat{\psi}_{i\sigma'}(\vec{k})\,\Delta_{i\gamma}^a + \sum_{i,\gamma} \Delta_{i\gamma}^{a*} N U^{-1} \Delta_{i\gamma}^a. \qquad (9.63)$$

Here $a = 1, 2, 3$ labels the direction in spin space and a sum over a is understood in expressions where the spin label appears twice. If we now let a take the values $a = 0, 1, 2, 3$ and define σ^0 as the identity matrix, then the self-consistent saddle-point equations for charge and spin order can be compactly written as

$$\Delta_{i\gamma}^{a*} = \frac{U}{N}\sum_{\vec{k}} \langle \hat{\psi}_{i\sigma}^\dagger(\vec{k}+\vec{Q}_\gamma)\sigma_{\sigma\sigma'}^a \hat{\psi}_{i\sigma'}(\vec{k})\rangle$$

$$\Delta_{i\gamma}^a = \frac{U}{N}\sum_{\vec{k}} \langle \hat{\psi}_{i\sigma}^\dagger(\vec{k})\sigma_{\sigma\sigma'}^a \hat{\psi}_{i\sigma'}(\vec{k}+\vec{Q}_\gamma)\rangle. \qquad (9.64)$$

We observe that the onsite interaction U can induce charge density waves and spin density waves, which the current scheme treats on equal footing. Any form of bond order is not possible for an onsite interaction only, and in order to look for a spinful generalization of bond ordering, we revisit the longer range density-density interactions of equation (9.44) including the spin degree of freedom.

The starting point is straightforward, as we only need to write the spin labels explicitly,

$$\hat{H}_V = \frac{1}{2}\sum_{ij,\sigma\sigma'}\sum_{\vec{x},\vec{x}'} V_{ij}(\vec{x}-\vec{x}')\hat{n}_{i\sigma}(\vec{x})\hat{n}_{j\sigma'}(\vec{x}'), \qquad (9.65)$$

here the sum over spin indices is written explicitly due to the number operators. Transforming to momentum space we then have

$$\sum_{ij}\sum_{\vec{q},\vec{k},\vec{k}'} \hat{\psi}_{i\sigma}^\dagger(\vec{k}+\vec{q})\hat{\psi}_{i\sigma}(\vec{k})\,\tilde{V}_{ij}(\vec{q})\,\hat{\psi}_{j\sigma'}^\dagger(\vec{k}')\hat{\psi}_{j\sigma'}(\vec{k}'+\vec{q}). \qquad (9.66)$$

This term, which is quartic in the fermion operators, can be decoupled in charge order parameters and bond order parameters, something which we alread y demonstrated for the spinless case. In the presence of spin, the bond order parameters can be further catergorized as order parameters with no spin structure and order parameters

corresponding to combined spin-bond order. The former is just a trivial generalization of equation (9.49) and the HS decoupling defining the order parameters $\Delta_{i\gamma}^0$ reads

$$\sum_{i,\gamma,\vec{k}} \Delta_{i\gamma}^{0*}\, \hat{\psi}_{i\sigma}^\dagger(\vec{k})\hat{\psi}_{i\sigma}(\vec{k}+\vec{Q}_\gamma) + \sum_{i,\gamma,\vec{k}} \hat{\psi}_{i\sigma}^\dagger(\vec{k}+\vec{Q}_\gamma)\hat{\psi}_{i\sigma}(\vec{k})\,\Delta_{i\gamma}^0 - \sum_{i,\gamma}\Delta_{i\gamma}^0 V_{ij}^{-1}(\vec{Q}_\gamma)\Delta_{j\gamma}^0.$$

(9.67)

We have chosen the same notation $\Delta_{i\gamma}^0$ for the order parameter fields as equation (9.62), since these two terms may indeed be collected into a single terms for charge order without spin structure. The self-consistent saddle-point equations for such charge order easily follow from equation (9.50) and take the form

$$\Delta_{i\gamma}^{0*} = \sum_{j,\vec{k}} \langle \hat{\psi}_{j\sigma}^\dagger(\vec{k}+\vec{Q}_\gamma)\hat{\psi}_{j\sigma}(\vec{k})\rangle \tilde{V}_{ji}(\vec{Q}_\gamma)$$

$$\Delta_{i\gamma}^0 = \sum_{j,\vec{k}} \tilde{V}_{ij}(\vec{Q}_\gamma)\langle \hat{\psi}_{j\sigma}^\dagger(\vec{k})\hat{\psi}_{j\sigma}(\vec{k}+\vec{Q}_\gamma)\rangle.$$

(9.68)

Rearranging terms in equation (9.66) yields an interaction quartic in fermion operators which can be decoupled in the bond order channel,

$$-\sum_{ij}\sum_{\vec{q},\vec{k},\vec{k}'} \hat{\psi}_{i\sigma}^\dagger(\vec{k}+\vec{q})\hat{\psi}_{j\sigma'}(\vec{k})\, \tilde{V}_{ij}(\vec{k}-\vec{k}')\, \hat{\psi}_{j\sigma'}^\dagger(\vec{k}')\hat{\psi}_{i\sigma}(\vec{k}'+\vec{q}).$$

(9.69)

Further manipulations of this interaction term lead to a form which makes the spin structure of the bond order explicit. Again using the Pauli matrices $\sigma^a = (\sigma^0, \sigma^1, \sigma^2, \sigma^3)$ we find the interaction to be equal to

$$-\frac{1}{2}\sum_{ij}\sum_{\vec{q},\vec{k},\vec{k}'} \hat{\psi}_{i\sigma_1}^\dagger(\vec{k}+\vec{q})\sigma_{\sigma_1\sigma_2}^a\hat{\psi}_{j\sigma_2}(\vec{k})\, \tilde{V}_{ij}(\vec{k}-\vec{k}')\, \hat{\psi}_{j\sigma_3}^\dagger(\vec{k}')\sigma_{\sigma_3\sigma_4}^a\hat{\psi}_{i\sigma_4}(\vec{k}'+\vec{q}).$$

(9.70)

Based on this interaction we can follow the same recipy for HS decoupling as in the spinless case, and apply it to each of the spin components a. Without explicitly writing the HS decoupling, we give the self-consistent saddle-point equations for the spinful bond order parameters, now labeled by a in addition to $(n, \mathcal{I}_r, i, j, \gamma)$,

$$\Delta_{ij\gamma}^{a(n,\mathcal{I}_r)*} = \frac{V_n}{N}\sum_{\vec{k}} \langle \hat{\psi}_{i\sigma}^\dagger(\vec{k}+\vec{Q}_\gamma)\sigma_{\sigma\sigma'}^a\hat{\psi}_{j\sigma'}(\vec{k})\rangle \lambda_{ij}^{(n,\mathcal{I}_r)}(\vec{k})$$

$$\Delta_{ij\gamma}^{a(n,\mathcal{I}_r)} = \frac{V_n}{N}\sum_{\vec{k}} \lambda_{ij}^{(n,\mathcal{I}_r)*}(\vec{k})\langle \hat{\psi}_{j\sigma}^\dagger(\vec{k})\sigma_{\sigma\sigma'}^a\hat{\psi}_{i\sigma'}(\vec{k}+\vec{Q}_\gamma)\rangle.$$

(9.71)

9.2.3 Example: honeycomb and triangular lattice

In order to show how the mean-field theory presented above may be used in a specific case we take the honeycomb lattice as an example. We will look at two sets of $\vec{Q}_\mu$, the K-points and the M-points. A mean-field theory incorporating translational symmetry breaking has been applied to the honeycomb lattice before [167, 168, 185] by working directly with a six site unit cell. This would correspond to $\vec{Q}_\mu = \vec{K}_\pm$ in our case and we must of course obtain the same results in this case.

For the honeycomb lattice we first specify an explicit form for the interaction $\tilde{V}_{ij}(\vec{q})$. The honeycomb lattice has two sublattices, A and B, and the indices i, j run over these values. We take a nearest neighbor V_1 and a next-nearest neighbor interaction V_2 into account. In defining $V_{ij}(\vec{x})$ (and consequently $\tilde{V}_{ij}(\vec{q})$), we should be careful to comply with the counting convention specified by equation (9.44), and in case of the nearest neighbor interaction we set

$$
\begin{aligned}
V_{AB}(0) = V_{AB}(\vec{x}_2) = V_{AB}(-\vec{x}_1) = \\
V_{BA}(0) = V_{BA}(-\vec{x}_2) = V_{BA}(\vec{x}_1) = V_1
\end{aligned}
\tag{9.72}
$$

and all other matrix elements are zero. This leads to the Fourier transformed expression

$$
\begin{aligned}
\Gamma_{ij}^{(1)}(\vec{q}) = \Gamma^{(1)}(\vec{q})\delta_{iA}\delta_{jB} + \Gamma^{(1)*}(\vec{q})\delta_{iB}\delta_{jA} \\
\Gamma^{(1)}(\vec{q}) = 1 + e^{i\vec{q}\cdot\vec{x}_2} + e^{-i\vec{q}\cdot\vec{x}_1}.
\end{aligned}
\tag{9.73}
$$

For the next-nearest neighbor interaction we make the following choice

$$
\begin{aligned}
V_{AA}(\vec{x}_1) = V_{AA}(\vec{x}_2) = V_{AA}(\vec{x}_1 + \vec{x}_2) = \\
V_{AA}(-\vec{x}_1) = V_{AA}(-\vec{x}_2) = V_{AA}(-\vec{x}_1 - \vec{x}_2) = V_2
\end{aligned}
\tag{9.74}
$$

and the same for V_{BB}. In Fourier space we then have

$$
\Gamma_{ij}^{(2)}(\vec{q}) = \delta_{ij}\Gamma^{(2)}(\vec{q}) = 2\delta_{ij}(\cos q_1 + \cos q_2 + \cos q_3),
\tag{9.75}
$$

where $q_i = \vec{q} \cdot \vec{x}_i$ and we have set $\vec{x}_3 = -(\vec{x}_1 + \vec{x}_2)$. Before going very specifically into the case of ordering at the K-points and subsequently M-points, we write down the decomposition of $\Gamma_{ij}^{(1)}(\vec{k} - \vec{k}')$ and $\Gamma_{ij}^{(2)}(\vec{k} - \vec{k}')$ in terms of the $\lambda_{ij}^{(n,\mathcal{I}_r)}(\vec{k})$, as these apply generally both to cases. It suffices to derive relevant expression for $\Gamma^{(1)}(\vec{k} - \vec{k}')$ and $\Gamma^{(2)}(\vec{k} - \vec{k}')$. We obtain as a general expansion

$$
\begin{aligned}
\Gamma^{(1)}(\vec{k} - \vec{k}') &= \lambda^{(1,A_1)}(\vec{k})\lambda^{(1,A_1)*}(\vec{k}') + \vec{\lambda}^{(1,E_2)}(\vec{k}) \cdot \vec{\lambda}^{(1,E_2)*}(\vec{k}') \\
\Gamma^{(2)}(\vec{k} - \vec{k}') &= \lambda^{(2,A_1)}(\vec{k})\lambda^{(2,A_1)*}(\vec{k}') + \vec{\lambda}^{(2,E_2)}(\vec{k}) \cdot \vec{\lambda}^{(2,E_2)*}(\vec{k}') \\
&\quad \lambda^{(2,B_1)}(\vec{k})\lambda^{(2,B_1)*}(\vec{k}') + \vec{\lambda}^{(2,E_1)}(\vec{k}) \cdot \vec{\lambda}^{(2,E_1)*}(\vec{k}').
\end{aligned}
\tag{9.76}
$$

The functions $\lambda^{(1,\mathcal{I}_r)}(\vec{k})$ are given explicitly in Appendix A

With this preliminary work out of the way we are in a position to particularize to a certain set of ordering vectors. As advetised we focus on K-point ordering first, and as such we work with the state operator basis

$$\begin{bmatrix} \hat{\chi}_{0i}(\vec{k}) \\ \hat{\chi}_{1i}(\vec{k}) \\ \hat{\chi}_{2i}(\vec{k}) \end{bmatrix} = \begin{bmatrix} \hat{\psi}_i(\vec{k}) \\ \hat{\psi}_i(\vec{k} + \vec{K}_+) \\ \hat{\psi}_i(\vec{k} + \vec{K}_-) \end{bmatrix} . \tag{9.77}$$

Let's consider charge order first. It is straightforward to find that $\Gamma_{ij}^{(1)}(0) = 3(\delta_{iA}\delta_{jB} + \delta_{iB}\delta_{jA})$ and that $\Gamma_{ij}^{(1)}(\vec{K}_+) = \Gamma_{ij}^{(1)}(\vec{K}_-) = 0$. As there is no contribution to Δ_{i1} and Δ_{i2} from the nearest neighbor interaction, the nearest neighbor interaction will cause translational symmetry breaking. For the next-nearest neighbor interaction we easily find that $\Gamma_{ij}^{(2)}(0) = 6\delta_{ij}$ and $\Gamma_{ij}^{(2)}(\vec{K}_+) = \Gamma_{ij}^{(2)}(\vec{K}_-) = -3\sqrt{3}\delta_{ij}$. Observe that these are all real. The order parameters of equation (9.50) become

$$\Delta_{i0} = 3\frac{V_1}{N}\sum_{\mu,\vec{k}}(\delta_{iA}\delta_{jB} + \delta_{iB}\delta_{jA})\langle\hat{\chi}_{\mu j}^\dagger\hat{\chi}_{\mu j}\rangle + 6\frac{V_2}{N}\sum_{\mu,\vec{k}}\delta_{ij}\langle\hat{\chi}_{\mu j}^\dagger\hat{\chi}_{\mu j}\rangle$$

$$\Delta_{i1} = -3\sqrt{3}\frac{V_2}{N}\sum_{\mu,\vec{k}}\delta_{ij}\langle\hat{\chi}_{\mu j}^\dagger\hat{\chi}_{[\mu+1]j}\rangle$$

$$\Delta_{i2} = -3\sqrt{3}\frac{V_2}{N}\sum_{\mu,\vec{k}}\delta_{ij}\langle\hat{\chi}_{\mu j}^\dagger\hat{\chi}_{[\mu+2]j}\rangle, \tag{9.78}$$

where we did not write the momentum dependence of the expectation values explicitly. From this is more or less directly follows that the order parameters Δ_{i1} and Δ_{i2} are not indepedent, but equivalent. Using the additive properties of the $\vec{K}_\pm$ vectors we find that $\Delta_{i1}^* = \Delta_{i2}$. This is fully consistent with the expectation that the charge order parameters must contain six independent degrees of freedom, corresponding to the six sites in the enlarged unit cell.

We proceed in the same way for bond order. For the nearest neighbor bond order the order parameters read (again suppressing some momentum dependence)

$$\Delta_{ij\gamma}^{(1,A_1)} = \frac{V_1}{N}\sum_{\mu,\vec{k}}\left[\lambda^{(1,A_1)*}(\vec{k})\delta_{iA}\delta_{jB}\langle\hat{\chi}_{\mu j}^\dagger\hat{\chi}_{[\mu+\gamma]i}\rangle + \lambda^{(1,A_1)}(\vec{k})\delta_{iB}\delta_{jA}\langle\hat{\chi}_{\mu j}^\dagger\hat{\chi}_{[\mu+\gamma]i}\rangle\right],$$

$$\vec{\Delta}_{ij\gamma}^{(1,E_2)} = \frac{V_1}{N}\sum_{\mu,\vec{k}}\left[\vec{\lambda}^{(1,E_2)*}(\vec{k})\delta_{iA}\delta_{jB}\langle\hat{\chi}_{\mu j}^\dagger\hat{\chi}_{[\mu+\gamma]i}\rangle + \vec{\lambda}^{(1,E_2)}(\vec{k})\delta_{iB}\delta_{jA}\langle\hat{\chi}_{\mu j}^\dagger\hat{\chi}_{[\mu+\gamma]i}\rangle\right]$$

$$\tag{9.79}$$

For nearest neighbor bond order we expect nine complex degrees of freedom, corresponding to the nine bonds in the enlarged unit cell. Since we have three basis functions of irreducible representations and three degrees of freedom coming from γ, we immediately see that they represent the independent degrees of freedom. Note that $\vec{\Delta}_{AB\gamma}^{(1,\mathcal{I})}$ and $\vec{\Delta}_{BA\gamma}^{(1,\mathcal{I})}$ are not independent but related by complex conjugation. Very similar expressions hold for next-nearest neighbor bond order, which are all diagonal in sublattice space. For instance, the $(2, A_1)$ order parameter reads

$$\Delta_{ij\gamma}^{(2,A_1)} = \frac{V_2}{N} \sum_{\mu,\vec{k}} \lambda^{(2,A_1)*}(\vec{k})\delta_{ij}\langle \hat{\chi}_{\mu j}^{\dagger}\hat{\chi}_{[\mu+\gamma]i}\rangle, \tag{9.80}$$

For next-nearest neighbor bond order we expect nine complex order degrees of freedom for each of the sublattices. Since we now have six basis functions of irreducible representations, we seem to have twice too many. It is however straightforward to show that all the $\Delta_{ij0}^{(2,\mathcal{I})}$ are real and that $\Delta_{ij1}^{(2,\mathcal{I})}$ and $\Delta_{ij2}^{(2,\mathcal{I})}$ are not independent. Hence, we have the correct number of degrees of freedom.

Instead of the ordering vectors $\vec{K}_{\pm}$ we may anticipate a different pattern of translational symmetry breaking, and choose the three M-point ordering vectors, which we just label $\vec{Q}_{\mu}$ (see Section 9.4.1). The mean field spinor then has four momentum components and reads

$$\begin{bmatrix} \hat{\chi}_{0i}(\vec{k}) \\ \hat{\chi}_{1i}(\vec{k}) \\ \hat{\chi}_{2i}(\vec{k}) \\ \hat{\chi}_{3i}(\vec{k}) \end{bmatrix} = \begin{bmatrix} \hat{\psi}_i(\vec{k}) \\ \hat{\psi}_i(\vec{k} + \vec{Q}_1) \\ \hat{\psi}_i(\vec{k} + \vec{Q}_2) \\ \hat{\psi}_i(\vec{k} + \vec{Q}_3) \end{bmatrix}. \tag{9.81}$$

Apart from this difference, we need to evaluate $\tilde{V}_{ij}(\vec{Q}_{\mu})$ for the three M-point momenta. Doing this we find that the charge order parameters take the form

$$\Delta_{i0} = \frac{1}{N} \sum_{\mu,\vec{k}} [6V_2\delta_{ij} + 3V_1(\delta_{iA}\delta_{jB} + \delta_{iB}\delta_{jA})]\langle \hat{\chi}_{\mu j}^{\dagger}\hat{\chi}_{\mu j}\rangle$$

$$\Delta_{i1} = \frac{1}{N} \sum_{\mu,\vec{k}} [-2V_2\delta_{ij} + V_1(\delta_{iA}\delta_{jB} + \delta_{iB}\delta_{jA})]\langle \hat{\chi}_{\mu j}^{\dagger}\hat{\chi}_{[\mu+1]j}\rangle$$

$$\Delta_{i2} = \frac{1}{N} \sum_{\mu,\vec{k}} [-2V_2\delta_{ij} - V_1(\delta_{iA}\delta_{jB} + \delta_{iB}\delta_{jA})]\langle \hat{\chi}_{\mu j}^{\dagger}\hat{\chi}_{[\mu+2]j}\rangle$$

$$\Delta_{i3} = \frac{1}{N} \sum_{\mu,\vec{k}} [-2V_2\delta_{ij} + V_1(\delta_{iA}\delta_{jB} + \delta_{iB}\delta_{jA})]\langle \hat{\chi}_{\mu j}^{\dagger}\hat{\chi}_{[\mu+3]j}\rangle. \tag{9.82}$$

Note that in this case the nearest neighbor interaction in principle contributes to the order parameters describing translational symmetry breaking, which was different for ordering at $\vec{K}$. Insofar as bond order is concerned, we can simply copy the expressions from equations (9.2.3) and (9.80), but we must interpret the sum over ordering vectors to run over $\vec{Q}_\mu$.

As an illustrative example of a spinful mean field theory we apply the general expressions to the specific case of the triangular lattice. Choosing the triangular lattice we can for the moment avoid the additional complication of sublattice structure. We assume the presence of an onsite repulsion U and a nearest neighbor repulsion $V_1 = V$. For the nearest neighbor repulsion we find that the Fourier transform is given by $\tilde{V}(\vec{q}) = V\Gamma^{(1)}(\vec{q})/N = 2V(\cos q_1 + \cos q_2 + \cos q_3)/N$, and evaluated at the orderig momenta $\vec{Q}_\mu$ it gives $\Gamma^{(1)}(\vec{Q}_\mu) = -2$, while clearly $\Gamma^{(1)}(0) = 6$. We therefore have for the charge order parameters

$$
\begin{aligned}
\Delta_0^0 &= \frac{U + 6V}{N} \sum_{\mu,\vec{k}} \langle \hat{\chi}_{\mu\sigma}^\dagger \hat{\chi}_{\mu\sigma} \rangle \\
\Delta_{\gamma=1,2,3}^0 &= \frac{U - 2V}{N} \sum_{\mu,\vec{k}} \langle \hat{\chi}_{\mu\sigma}^\dagger \hat{\chi}_{[\gamma+\mu]\sigma} \rangle,
\end{aligned}
\tag{9.83}
$$

Where we have written the expectation values in terms of the mean field spinor components $\hat{\chi}_{\mu\sigma} = \hat{\psi}_\sigma(\vec{k} + \vec{Q}_\gamma)$, while suppressing the momentum dependence. Spin density wave order parameters can only originate from the onsite repulsion and we simply have

$$
\Delta_\gamma^{a=1,2,3} = \frac{U}{N} \sum_{\mu,\vec{k}} \langle \hat{\chi}_{\mu\sigma}^\dagger \sigma_{\sigma\sigma'}^a \hat{\chi}_{[\gamma+\mu]\sigma'} \rangle.
\tag{9.84}
$$

We are left with bond order, which can be spinful or without any spin structure. The function $\Gamma^{(1)}(\vec{k} - \vec{k}')$ is written as sum of products of irreducible representations in a manner exactly equal to the honeycomb lattice next nearest neigbor function $\Gamma^{(2)}(\vec{k} - \vec{k}')$ given in equation (9.76). In total there are six irreducible representations to be summed over, for the sake of brevity we limit ourselves to writing down two of corresponding order parameters explicitly. For the triangular lattice they are

$$
\begin{aligned}
\Delta_\gamma^{a(1,A_1)} &= \frac{V}{N} \sum_{\vec{k}} \lambda^{(1,A_1)}(\vec{k}) \langle \hat{\chi}_{\mu\sigma}^\dagger \sigma_{\sigma\sigma'}^a \hat{\chi}_{[\gamma+\mu]\sigma'} \rangle, \\
\vec{\Delta}_\gamma^{a(1,E_2)} &= \frac{V}{N} \sum_{\vec{k}} \vec{\lambda}^{(1,E_2)}(\vec{k}) \langle \hat{\chi}_{\mu\sigma}^\dagger \sigma_{\sigma\sigma'}^a \hat{\chi}_{[\gamma+\mu]\sigma'} \rangle.
\end{aligned}
\tag{9.85}
$$

9.3 Condensates of the square lattice

We now take a closer look at the density wave states of the square lattice. As advertised in previous sections, the focus will be on their symmetry and the way in which they alter the low-energy electronic properties of the band structure.

An important aspect of density-wave orders is the breaking of translational symmetry by modulations at finite wave vector. Condensation of particle-hole pairs at finite vector leads to a reduced group of invariant translations as one has to remove the broken translations from the Bravais lattice translational symmetry group. This enlarges the unit cell of the system. In case of the simple square lattice, it is well known that charge or spin density-waves at ordering vector $\vec{Q} = (\pi, \pi)$ double the unit cell and, consequently, reduce the Brillouin zone to half of its size. When analyzing space group symmetries in such a situation it is appropriate to add the broken translations, which are no longer part of the set of invariant translations, to the point group of the Bravais lattice. This generates the extended point of the lattice, the point group of the enlarged unit cell, which has its own group structure and additional irreducible representations. We may put this differently by noting that generally, to find the point group of a given space group S one constructs the factor group G/T by factoring out all the translations T, the group of invariant translations. Translational symmetry breaking removes elements from T, which reappear as distinct cosets of G/T. A more detailed introduction of extended point groups is given in Appendix C. At this point it suffices to develop an intuitive understanding of the basic structure of extended point groups, so let us briefly consider an illustrative example of translational symmetry breaking. Suppose we anticipate ordering at wave vector $\vec{Q} = (\pi, \pi)$, a sensible expectation at half filling of the square lattice as Q nests the Fermi surface. In that case the generators of good translations, i.e. the group of invariant translations, are $T(\vec{x}_1 + \vec{x}_2)$ and $T(\vec{x}_1 - \vec{x}_2)$. Hence, $T(\vec{x}_1)$ is no longer a good translation and consequently becomes a member of the point group. The number of point group elements are doubled and new irreducible representations emerge, on top of the existing bare point group representations. Note that $T(\vec{x}_1)$ is its own inverse, as $2T(\vec{x}_1)$ belongs to the group of invariant translations. By the same token, even though $T(\vec{x}_2)$ is no longer a good translation, it can be written as $T(\vec{x}_1) - T(\vec{x}_1 - \vec{x}_2)$ and therefore belongs to the same coset as $T(\vec{x}_1)$.

In the following presentation of square lattice density waves, we will not restrict ourselves to the single ordering vector $\vec{Q} = (\pi, \pi)$, but instead consider more general multiple-Q ordering using the triplet of ordering momenta $\vec{Q}_1 = (\pi, \pi)$, $\vec{Q}_2 = (\pi, 0)$ and $\vec{Q}_3 = (0, \pi)$, which are shown in Fig. 9.1. This set of ordering momenta has the useful property that it is closed under addition. Specifically, the additive algebraic properties are $2\vec{Q}_\mu = 0$ (for each $\mu = 1, 2, 3$), which makes them nicely commensu-
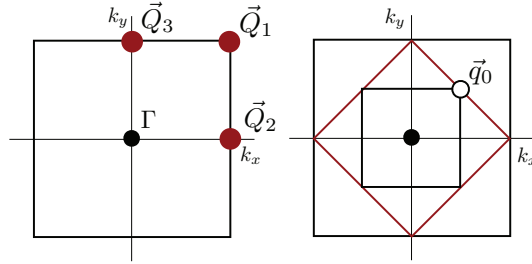
Figure 9.1: (Left) Brillouin zone of the square lattice. The momenta $\vec{Q}_1 = (\pi, \pi)$, $\vec{Q}_2 = (\pi, 0)$, and $\vec{Q}_3 = (0, \pi)$ are marked by bold red dots (Right) Outer black square represents the square lattice Brillouin zone. Red rotated square inscribed in the square lattice Brillouin zone marks the nested Fermi surface at half filling and at the same time corresponds to reduced Brillouin zone for translational symmetry breaking at wave vector $\vec{Q}_1$. Inner black square represents the reduced Brillouin zone for multiple $\vec{Q}$ ordering and $\vec{q}_0 = (\pi, \pi)/2$ denotes the location of the degeneracy point of the $d_{x^2-y^2}$ density-wave state.

rate, and $\pm \vec{Q}_1 \pm \vec{Q}_2 \pm \vec{Q}_3 = 0$. This choice of ordering vectors immediately implies that the unit cell is at most four times as large and as a consequence the three translations $T(\vec{x}_1)$, $T(\vec{x}_2)$ and $T(\vec{x}_3) \equiv T(\vec{x}_1 + \vec{x}_2)$ become members of the extended (point) symmetry group C_{4v}'''. The character table of this group listing the irreducible representations of this group is given in Appendix C and taken from [186]. Note that we altered notation with respect to [186] so as to conform to the definitions used in this work.

In this section dealing with the square lattice density waves, having fixed the set of commensurate ordering vectors, we start by listing all possible site, bond and flux ordered states by means of group theory. As advertised in Section 8.1 this will set the stage for establishing a connection between symmetry and electronic properties. We will demonstrate this in two separate subsections, the first of which provides a discussion of the specific form of the various density waves. The second then focuses on the way in which these density waves alter and affect the electronic (mean field) band structure.

There are three types of distinct orderings to consider in the context of lattice models and these are site or charge order, bond order, and time-reversal symmetry breaking flux order. Strictly speaking, the latter is also a form of bond ordering, as it is the hopping amplitudes which become complex. In order to properly account for gauge equivalence of seemingly different orderings, we distinguish them here

and treat them seperately. Having specified the structure of translational symmetry breaking simple group theory arguments suffice to obtain a general organization of density-wave states according to symmetry, without having to write down explicit expression for them. For the square lattice with an enlarged unit cell containing four sites, we collect these four sites in a vector with elements $\{s_i\}_{i=1}^4$ corresponding to the sites. Point group operations permute this set. A representation $\mathcal{P}_\mathrm{s}$ (s for site order) of the extended point is constructed by associating each element of the group with a permutation P_{ij}^s which acts on the s_i. In the same way we label the eight bonds by $\{b_i\}_{i=1}^8$ and construct a representation $\mathcal{P}_\mathrm{b}$. The permutations in both cases act explicitly as

$$s_i' = \sum_j P_{ij}^\mathrm{s} s_j, \quad b_i' = \sum_j P_{ij}^\mathrm{b} b_j. \tag{9.86}$$

These representations are clearly reducible ad may be decomposed into irreducible representations using the character table of the symmetry group. For site order we obtain the following decomposition

$$\mathcal{P}_\mathrm{s} = A_1 \oplus B_2' \oplus E_5. \tag{9.87}$$

The only representation also appearing in the point group C_{4v} is A_1, while the others are representations specific to the group C_{4v}'''. Hence, the translationally invariant content of this decomposition is A_1, which is not surprising as the only possible translationally invariant charge order on the square lattice is a uniform excess or defect charge. The other two representation correspond to translational symmetry broken charge order. It is not hard to convince oneself that the s-wave charge order at $\vec{Q}_1$ transforms as B_2'.

For bond order we find that the representation $\mathcal{P}_\mathrm{b}$ has the following decomposition

$$\mathcal{P}_\mathrm{b} = A_1 \oplus B_1 \oplus E_1' \oplus E_3 \oplus E_5, \tag{9.88}$$

where we find the translationally invariant content to be $A_1 \oplus B_1$, as expected. We will come back to the translationally variant part when we discuss the specific condensates corresponding to these representations.

We move on to flux states on the square lattice. In order to find the distinct flux states transforming according to irreducible representations of the symmetry group we associate a flux ϕ_i to each square plaquette of the lattice. Then the problem of finding the permutation corresponding to a given group member is similar to the problem of site order square lattice, since we have four fluxes as well as four sites. The crucial difference is that in case of fluxes reflections invert the sign of the fluxes and give rise to a minus sign in $\phi_i' = \sum_j P_{ij}^\phi \phi_j$. In addition, we must enforce the constraint

that the sum of fluxes in the (enlarged) unit cell is zero, up to integer multiples of the elementary flux quantum 2π. This originates from the fact that density-wave states coming from interactions cannot cause magnetic field configurations with nonzero average. Decomposing the square lattice flux representation $\mathcal{P}_\phi$ we obtain

$$\mathcal{P}_\phi = A_2 \oplus A_2' \oplus E_2, \tag{9.89}$$

The translationally invariant content is simply given by A_2, which by definition corresponds to a state with the same flux ϕ pierced through each hexagonal plaquette. Given the constraint that the flux through the unit cell must be zero up to integer multiples of 2π, we have $\phi/(2\pi) \in \mathbb{Z}$. There is one other state fulfilling the constraints, which is a π-flux state given by $\phi = \pi$. This is a consequence of the compact nature of the (electromagnetic) gauge field on the lattice, meaning that $\pi = -\pi \bmod 2\pi$. The π-flux state [92, 187] has become a ubiquitous state in condensed matter with relevance to many seemingly disparate fields. Is preserves time-reversal invariance and transforms as A_1, as any point group operation leaves the state invariant up to a gauge transformation. We will come back to it in more detail below. As will be shown below, the representation A_2' corresponds to a staggered flux state, of which the π-flux state may also be thought of as a particular case (since $\pi = -\pi$ on a lattice).

Insofar as bond ordered states are concerned, to this point we have limited ourselves to the bonds connecting nearest neighbors of the square lattice. We will find this too restrictive as it excludes interesting density waves representing diagonal bond modulations. Including the diagonal bonds in the bond vector b_i adds another 8 bonds and yields the decomposition

$$\mathcal{P}_b = 2A_1 \oplus B_1 \oplus B_2 \oplus A_1' \oplus B_2' \oplus E_1' \oplus E_2 \oplus 2E_3 \oplus E_5. \tag{9.90}$$

The double appearance of A_1 comes from the fact that next-nearest neighbor (diagonal) and nearest neighbor bonds are never mixed by point group operations, and so we might have different bond strengths for both without lowering the symmetry. We will find the state corresponding to the A_1' representation to be particularly interesting. It corresponds to the square lattice d_{xy} state, and as such is closely related to the $d_{x^2-y^2}$ state, which is the A_2' state of the flux order decomposition (9.89).

To conclude these more general considerations using just group theory, and before we come to the explicit expression for quite a number of the density wave states listed here, we demonstrate based on the elementary example of the square lattice case how the symmetry organization serves the purpose of identifying states with topological quantum numbers. In section 9.1.4 we presented two distinct possibilities for topological quantum numbers, the Chern number (connected to quantized off-diagonal conductivity) and electric polarization. Prerequisites for nonzero Chern number are time-reversal symmetry breaking and the absence of any reflection symmetries, which means we must consider the flux states given in equation (9.89). The

state corresponding to A_2' certainly breaks all reflections, but as can be seen from the character table of C_{4v}''', it is even under any reflection followed by $T(\vec{x}_i)$. The translation may be thought of as a form of gauge transformation, leaving the Hamiltonian unitarily equivalent to itself under reflections, which mandates zero Chern numbers in the same way as pure reflection do. Hence, this state by itself cannot have nonzero Chern number. The same is true for the states belonging to E_2, which are even under $T(\vec{x}_1 + \vec{x}_2)\sigma_v$.

Concerning electric polarization, we see that we may restrict the attention to states which transform as $1D$ representations of C_{4v}, as these are the only ones which have at least C_2 symmetry. This considerably limits the possibilities, as for site order we only have the state B_2' and for bond order the states A_1 and B_1 contained in E_3 which have the potential to acquire nontrivial quantum numbers, should they be insulating. The will investigate these possibilities below.

9.3.1 The density waves of the square lattice

It is now time to look at the explicit form density-wave orders transforming according to the representations just presented. We note once again that we mainly focus on spin singlet states, but we comment briefly on triplet states at the end of this section. We have stated that we are interested in density-waves at modulation vectors $\vec{Q}_\mu$, with $\vec{Q}_\mu$ defined above. A general density-wave state is then specfied by

$$\langle \hat{\psi}_\sigma^\dagger(\vec{k} + \vec{Q}_\mu)\hat{\psi}_{\sigma'}(\vec{k})\rangle = \Delta_\mu(\vec{k})\delta_{\sigma\sigma'} \tag{9.91}$$

Above we have commented on the special commensurability conditions of the ordering vectors $\vec{Q}_\mu$, which are summed up as $2\vec{Q}_\mu = 0$ and $\pm\vec{Q}_1 \pm \vec{Q}_2 \pm \vec{Q}_3 = 0$. From these properties one can easily obtain compatibility conditions of density-wave states. In particular, the fact that $2\vec{Q}_\mu = 0$ leads to (see also [166])

$$\frac{\Delta_\mu(\vec{k} + \vec{Q}_\mu)}{\Delta_\mu^*(\vec{k})} = 1, \tag{9.92}$$

or, to put it in a different form, writing $\Delta_\mu(\vec{k}) = \Delta_\mu f_\mu(\vec{k})$ explicitly, $f_\mu(\vec{k} + \vec{Q}_\mu)/f_\mu^*(\vec{k}) = \Delta_\mu^*/\Delta_\mu$. In addition there are relations between the different $\vec{Q}_\mu$, due to $\pm\vec{Q}_1 \pm \vec{Q}_2 \pm \vec{Q}_3 = 0$. We have for instance

$$\langle \hat{\psi}_\sigma^\dagger(\vec{k} + \vec{Q}_1)\hat{\psi}_{\sigma'}(\vec{k})\rangle = \Delta_1(\vec{k}) = \langle \hat{\psi}_\sigma^\dagger(\vec{k} + \vec{Q}_2 + \vec{Q}_3)\hat{\psi}_{\sigma'}(\vec{k} + \vec{Q}_2 + \vec{Q}_2)\rangle =$$
$$\langle \hat{\psi}_\sigma^\dagger(\vec{k} + \vec{Q}_2 + \vec{Q}_3)\hat{\psi}_{\sigma'}(\vec{k} + \vec{Q}_3 + \vec{Q}_3)\rangle \tag{9.93}$$

from which it easily follows that

$$\langle \hat{\psi}_\sigma^\dagger(\vec{k} + \vec{Q}_3)\hat{\psi}_{\sigma'}(\vec{k} + \vec{Q}_2)\rangle = \Delta_1(\vec{k} - \vec{Q}_2) =$$
$$\langle \hat{\psi}_\sigma^\dagger(\vec{k} + \vec{Q}_2)\hat{\psi}_{\sigma'}(\vec{k} + \vec{Q}_3)\rangle^* = \Delta_1^*(\vec{k} - \vec{Q}_3) \tag{9.94}$$

Similar relations obviously hold for the other combinations of ordering momenta and thus we obtain the additional relation

$$\Delta_{\mu_1}(\vec{k} - \vec{Q}_{\mu_2}) = \Delta_{\mu_1}^*(\vec{k} - \vec{Q}_{\mu_3}), \quad \mu_1 \neq \mu_2 \neq \mu_3 \tag{9.95}$$

Armed with these general relations we proceed to explicit expression of density-wave states on the square lattice.

The simplest and almost trivial example of an s-wave state at momentum $\vec{Q}_1$ is given by

$$\langle \hat{\psi}_\sigma^\dagger(\vec{k} + \vec{Q}_1)\hat{\psi}_{\sigma'}(\vec{k})\rangle = \Delta_{\text{CDW}}\delta_{\sigma\sigma'}. \tag{9.96}$$

This state is a site ordered state with no momentum dependence, hence the commonly used label s-wave, and represents the staggered charge-ordering as is shown graphically in Fig. 9.2(a). In the decomposition of equation (9.87) is belongs to the representation B_2'. Substituting the ordering momentum $\vec{Q}_2$ or $\vec{Q}_3$ for $\vec{Q}_1$ yields the remaining two charge-density waves, which are partners belonging to the representation E_5.

There are a number of p-wave type bond orders contained in the decomposition of equation (9.88). Two of them are associated to the ordering vector $\vec{Q}_1$ and are given by

$$\langle \hat{\psi}_\sigma^\dagger(\vec{k} + \vec{Q}_1)\hat{\psi}_{\sigma'}(\vec{k})\rangle = i\Delta_{p_x}^{E_1'} \sin k_x \delta_{\sigma\sigma'},$$
$$\langle \hat{\psi}_\sigma^\dagger(\vec{k} + \vec{Q}_1)\hat{\psi}_{\sigma'}(\vec{k})\rangle = i\Delta_{p_y}^{E_1'} \sin k_y \delta_{\sigma\sigma'}. \tag{9.97}$$

Here we have chosen $\Delta^{E_1'}$ real and therefore a factor of i is necessary due to equation (9.92). We give these states the label E_1' as they belong to this representation, and the fact that these are imaginary p waves underlines the time-reversal invariance of these bond orders. Figures 9.2(c)-(d) show these two p waves graphically. The p_x state of this doublet is seen to correspond to alternating weaker and stronger bonds in the x direction, like a Peierls distorted state, only modulated in the y direction as well. Another time-reversal invariant bond order contained in equation (9.88) is the doublet

$$\langle \hat{\psi}_\sigma^\dagger(\vec{k} + \vec{Q}_2)\hat{\psi}_{\sigma'}(\vec{k})\rangle = i\Delta_1^{E_3} \sin k_x \delta_{\sigma\sigma'},$$
$$\langle \hat{\psi}_\sigma^\dagger(\vec{k} + \vec{Q}_3)\hat{\psi}_{\sigma'}(\vec{k})\rangle = -i\Delta_2^{E_3} \sin k_y \delta_{\sigma\sigma'}. \tag{9.98}$$

(a) B_2'

(b) A_2'

(c) E_1' p_x

(d) E_1' p_y
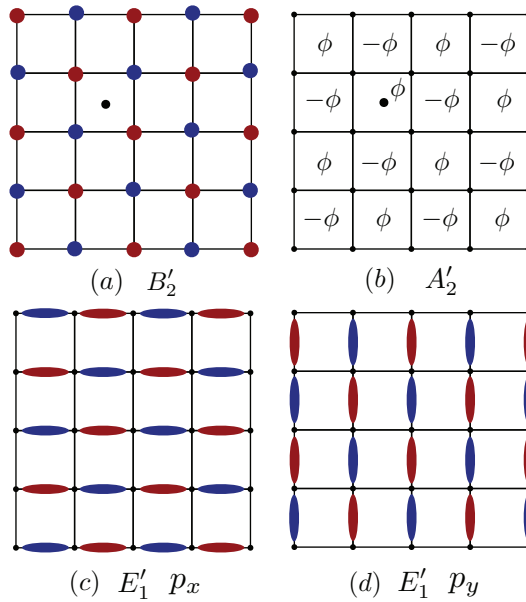
Figure 9.2: Graphical representation of some of the density wave states discussed in the main text, labeled by their irreducible representations. Red (blue) bonds represent stronger (weaker) bonds. All states have ordering vector $\vec{Q}_1$ and black dots in the center of the squares denote the origin. (a) Site ordered, or charge-density wave state, (b) $d_{x^2-y^2}$ state (which is a flux state), (c)-(d) Two partners of the bond ordered doublet E_1'.

It can be easily checked that these density-wave states transform as partners of E_3, which means that under twofold rotations C_2 they transform into themselves instead of acquiring a minus sign as strict p-wave states would. We choose not to label them explicitly as p_x and p_y waves as the decomposition of E_3 in terms of irreducible representations of C_{4v} is $E_3 = A_1 \oplus B_1$. The E_3 doublet is shown in Fig. 9.3(a)-(b).

Exchanging $\vec{Q}_2$ and $\vec{Q}_3$ in equation (9.98) yields a time-reversal symmetry breaking doublet given by

$$\langle \hat{\psi}_\sigma^\dagger(\vec{k} + \vec{Q}_3)\hat{\psi}_{\sigma'}(\vec{k})\rangle = -\Delta_{p_x}^{E_2} \sin k_x \delta_{\sigma\sigma'},$$
$$\langle \hat{\psi}_\sigma^\dagger(\vec{k} + \vec{Q}_2)\hat{\psi}_{\sigma'}(\vec{k})\rangle = \Delta_{p_y}^{E_2} \sin k_y \delta_{\sigma\sigma'}. \tag{9.99}$$

These are real p waves and we must therefore look at equation (9.89) in order to identify the irreducible representation corresponding to this doublet and we find that it is E_2, a doublet of flux states, which we show in Fig. 9.3(c)-(d) in the $A_2 \oplus B_2$ basis. To complete the identification of flux states in the decomposition (9.89), we have the d-wave staggered flux given by

$$\langle \hat{\psi}_\sigma^\dagger(\vec{k} + \vec{Q}_1)\hat{\psi}_{\sigma'}(\vec{k})\rangle = \Delta_{d_{x^2-y^2}} i(\cos k_x - \cos k_y)\delta_{\sigma\sigma'}. \tag{9.100}$$

The $d_{x^2-y^2}$ state is well-known in the context of high temperature superconductivity, as it has been discussed in connection to pseudogap physics in cuprates [188] and was found much earlier to be a mean-field solution of the Hubbard model [92, 189]. As we have already assigned the E_2 doublet and this state clearly breaks translational symmetry, it must be the A_2' state, the staggered flux as shown in Fig. 9.2(b). Direct evaluation of the relevant point group operations confirms this. Its time-reversal invariant d-wave cousin which was also mentioned earlier already is

$$\langle \hat{\psi}_\sigma^\dagger(\vec{k} + \vec{Q}_1)\hat{\psi}_{\sigma'}(\vec{k})\rangle = \Delta_{d_{xy}} \sin k_x \sin k_y \delta_{\sigma\sigma'}. \tag{9.101}$$

Note that they are just cousins and not partners of a two-dimensional representation in the context of square symmetry. The d_{xy} state transforms as A_1' as contained in the decomposition (9.90) since it is a next-nearest neighbor bond density-wave state. To complete the square lattice nearest-neighbor bond density-wave states we give an expression for the doublet states corresponding to E_5. These are

$$\langle \hat{\psi}_\sigma^\dagger(\vec{k} + \vec{Q}_3)\hat{\psi}_{\sigma'}(\vec{k})\rangle = \Delta_{p_x}^{E_5} \cos k_x \delta_{\sigma\sigma'},$$
$$\langle \hat{\psi}_\sigma^\dagger(\vec{k} + \vec{Q}_2)\hat{\psi}_{\sigma'}(\vec{k})\rangle = \Delta_{p_y}^{E_5} \cos k_y \delta_{\sigma\sigma'}. \tag{9.102}$$

Despite its appearance it makes sense to label them as p-waves, as they are odd under C_2, which is a consequence of the fact that $E_5 = E_1$ when decomposed in terms of C_{4v}.
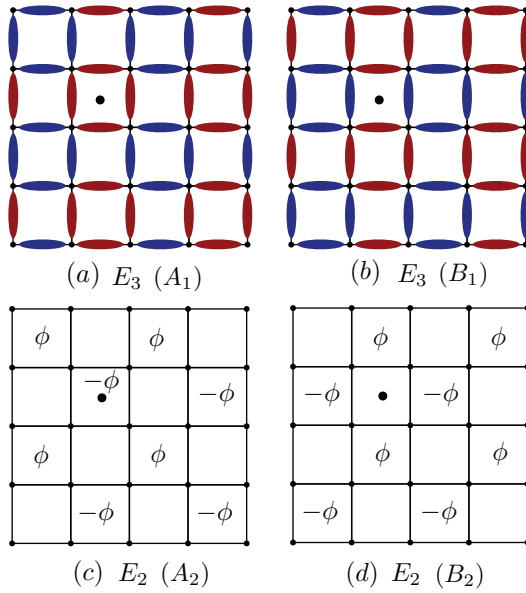
Figure 9.3: Graphical representation of square lattice density wave states at ordering vectors $\vec{Q}_2$ and $\vec{Q}_3$. (a) and (b) show the bond ordered doublet states belonging to E_3, expressed so as to transform as A_1 and B_1 of the bare point group. (c) and (d) show the flux states belonging to E_2, expressed in the A_2 and B_2 basis.

This completes the listing of density-wave states transforming as the representations in the decompositions of equations (9.87) and (9.88). In addition we have mentioned one state coming from equation (9.90), i.e. the d_{xy} state, as there is a natural connection to the $d_{x^2-y^2}$ state. Not only are they both d-wave states, their mere symmetry properties indicate that for a combined $id_{x^2-y^2} + d_{xy}$ a topological quantum number can be defined. Indeed, we had noted in the beginning of this section that the state $id_{x^2-y^2}$ transforms as A_2' and is thus even under reflections followed by translations. The combination $id_{x^2-y^2} + d_{xy}$ changes this because d_{xy} transforms as A_1'. The difference is entirely due to reflections. The d_{xy} state is even under reflections but odd under translations by a primitive lattice vector ($T(\vec{x}_1)$ or $T(\vec{x}_2)$). Hence, reflections are manifestly broken in an $id_{x^2-y^2} + d_{xy}$ state. The same is true for time-reversal symmetry, i.e. the time-reversal operation cannot be compensated by a translation, which is the case for a pure $id_{x^2-y^2}$ state. This allows for the Chern number, the topological quantum number of the state, to be nonzero and it was indeed found that the chiral $id_{x^2-y^2} + d_{xy}$ density-wave is a gapped Chern insulator state [190, 191]. We thus see how the organization of density waves in terms of symmetry serves one of the purposes laid out in the introduction. It leads in a direct way to the identification of states that can acquire additional quantum numbers of topological nature. In this case it leads us to known result, but in what follows we hope to demonstrate the general usefulness of the approach. A second intent of the symmetry perspective is to extract information on the low-energy properties of the symmetric parent state for a given filling. How the organization above serves this purpose we discuss in the next section.

As we have mentioned the Chern insulating chiral $id + d$ density wave state, we briefly comment on possible nontrivial spinful triplet states of the square lattice. Even though these are known results, they however will set the stage for similar observations in case of other lattices. Just to ease ourselves into the possible triplet states, we recall the simplest and most obvious triplet state, i.e. the antiferromagnetic spin-density wave at $\vec{Q}_1$, which is the triplet version of s-wave site order,

$$\langle \hat{\psi}_\sigma^\dagger(\vec{k} + \vec{Q}_1)\hat{\psi}_{\sigma'}(\vec{k})\rangle = \Delta_{\mathrm{SDW}}\sigma_{\sigma\sigma'}^3. \tag{9.103}$$

We might have chosen a generic spin direction $\vec{s}\cdot\vec{\sigma}_{\sigma\sigma'}$, but we shall not be concerned with global spin rotation equivalence of spin density wave states. A time-reversal invariant version of the $d_{x^2-y^2}$ state is given by

$$\langle \hat{\psi}_\sigma^\dagger(\vec{k} + \vec{Q}_1)\hat{\psi}_{\sigma'}(\vec{k})\rangle = \Delta_{\sigma d_{x^2-y^2}}i(\cos k_x - \cos k_y)\sigma_{\sigma\sigma'}^3. \tag{9.104}$$

This $\sigma id_{x^2-y^2}$ state may be thought of as two copies of the spinless $d_{x^2-y^2}$ state, with inverted fluxes for the two spin species. Time-reversal invariance follows from the inversion of both spin and flux under time-reversal. The $\sigma id_{x^2-y^2}$ is a semimetallic

state with isolated Dirac nodes, the spinless version of which will be discussed in more detail in the next section. For now it suffices to note that the combination $\sigma i d_{x^2-y^2} + d_{xy}$, in the same way as its spinless counterpart, is a gapped state with nontrivial topological character [191]. Its explicit expression reads

$$\langle \hat{\psi}^\dagger_\alpha(\vec{k} + \vec{Q})\hat{\psi}_\beta(\vec{k})\rangle = \Delta_{\text{QSH}} \left[i(\cos k_x - \cos k_y)\sigma^3_{\sigma\sigma'} + \sin k_x \sin k_y \delta_{\sigma\sigma'} \right],$$
$$(9.105)$$

Its topological character follows from a simple and well-established argument, which uses the spin-projected Chern numbers $C_\uparrow$ and $C_\downarrow$. The latter are well-defined since σ^3 represents good quantum numbers. Time-reversal symmetry requires $C_\uparrow + C_\downarrow = 0$, but their difference is nonzero, $C_\uparrow - C_\downarrow = \pm 2$, indicating that the insulating density wave state is in the Quantum Spin Hall universality class [1, 23].

9.3.2 Spectral properties and low energy effects

As laid out in the introductory sections, one of purposes of studying the symmetry of condensates is to uncover any direct relation between the preserved or broken symmetries of condensates and their impact of the electronic spectrum. Now that we have discussed quite a number of specific density wave orders in the previous section, we can turn to the question of spectral properties. Naturally, the starting point is the spectrum of electrons on the square lattice, which is trivially given by $E(\vec{k}) = -2t \sum_i \cos k_i$ where $i = x, y$. We focus on half filling, a filling at which the Fermi surface is nested by the wave vector $\vec{Q}_1 = (\pi, \pi)$, a widely known property. This is graphically depicted in Fig. 9.1. As a consequence of this nesting property, it is reasonable to expect condensates at ordering vector $\vec{Q}_1$ to have strongest impact on the Fermi surface, possibly creating a full energy gap, as the mean-field Hamiltonian will now contain terms coupling states at momenta $\vec{k}$ and $\vec{k} + \vec{Q}_1$, i.e. terms such as $\hat{\psi}^\dagger(\vec{k})\hat{\psi}(\vec{k} + \vec{Q}_1)$. Let us therefore look into these states in particular. Indeed, a textbook example of a square lattice density wave state leading to insulating behaviour is the staggered charge ordered state, given in 9.96 and its spinful cousin the (weak-coupling) antiferromagnet. The condensate functions are of s-wave type, i.e. Δ_{CDW} for the charge density wave and $\Delta_{\text{SDW}}\sigma^3$ for the (triplet) spin density wave, and therefore nodeless.

States which do have nodes in momentum space are the d-wave states given by condensate functions $\Delta_{d_{x^2-y^2}}(\vec{k}) = \Delta_{d_{x^2-y^2}} i(\cos k_x - \cos k_y)$ and $\Delta_{d_{xy}}(\vec{k}) = \Delta_{d_{xy}} \sin k_x \sin k_y$ [see the equations (9.100) and (9.101)], and these nodes coincide with the Fermi surface. The spectral consequence of this is the presence of remaining degeneracies at isolated points on the Fermi surface. Except for the isolated nodes, the spectrum is gapped out. For both of these d-wave states the degeneracies occur

at high symmetry points, which is connected to the symmetric nature of the condensate functions. We will now show explicitly that these degeneracies are protected by lattice symmetries. Based on the classification of these states in terms irreducible representations of the extended point group C_{4v}''' it is not all too diffcult to establish which symmetries mandate the presence of degeneracies.

We recall the expression for the $d_{x^2-y^2}$ state, which is

$$\langle \hat{\psi}^\dagger(\vec{k}+\vec{Q}_1)\hat{\psi}(\vec{k})\rangle = \Delta_{d_{x^2-y^2}} i(\cos k_x - \cos k_y), \qquad (9.106)$$

The nodes of this condensate function are located at the two inequivalent moment $\vec{q}_0 = (\pi,\pi)/2$ and $\vec{q}_0' = (-\pi,\pi)/2$. The node at $\vec{q}_0$ is shown in Fig. 9.1. The mean field fermion operators are given generically in equation (9.17) and for ordering at $\vec{Q}_1$ we simply have

$$\hat{\chi}(\vec{k}) = \begin{bmatrix} \hat{\chi}_0(\vec{k}) \\ \hat{\chi}_1(\vec{k}) \end{bmatrix} = \begin{bmatrix} \hat{\psi}(\vec{k}) \\ \hat{\psi}(\vec{k}+\vec{Q}_1) \end{bmatrix}. \qquad (9.107)$$

In order to study the robust symmetry protection of the degeneracies, we take $\vec{q}_0$ as an example and abbreviate the fermion operator at this point as $\hat{\Phi} = \hat{\chi}(\vec{q}_0)$. The density wave state $d_{x^2-y^2}$ preserves a number of symmetries and one can simply look up the representation A_2' in the character table to see what operations, or what combination of operations, constitutes a symmetry. A subset of these symmetries leave the point $\vec{q}_0$ invariant and can therefore be used to derive constraints on the coupling between the two degenerate states at $\vec{q}_0$. Two of such symmetries are the inversion C_2, and the combination of the reflection $\sigma_{1d} = C_4\sigma_v$ and $T(\vec{x}_1)$, where σ_v is the reflection sending $(x,y) \to (x,-y)$ (for the precise and more detailed definition of the point group operations see Appendix A and C). Separately the reflection and the translation are broken, but the combination is preserved. Equation (9.18) can now simply be applied to obtain the effect of these symmetries on $\hat{\Phi}$ and we find

$$C_2 \;\to\; \hat{\chi}(-\vec{q}_0) = \hat{\chi}(\vec{q}_0 - \vec{Q}_1) = \tau^1 \hat{\Phi}$$
$$T(\vec{x}_1)\sigma_{1d} \;\to\; \tau^3 \hat{\Phi}. \qquad (9.108)$$

Here τ^i is a set of Pauli matrices acting on the two-component state $\hat{\Phi}$. From these relations it straightforwardly follows that the presence of these symmetries protects the degeneracy at $\vec{q}_0$. At $\vec{q}_0$ the mean-field Hamiltonian must commute with both τ^1 and τ^3 and the only matrix which has this property is the unit matrix. This is fully analogous to the protection of the degeneracy at the Dirac point of the honeycob lattice, which is explicitly demonstrated in Appendix A. In the present example of the $d_{x^2-y^2}$ density wave, it is possible to show the protection of the degeneracy at $\vec{q}_0$ by a

single symmetry. Time-reversal symmetry $\mathcal{T}$ is broken for the $d_{x^2-y^2}$ density wave, but as Fig. 9.2(b) shows, the combination of $\mathcal{T}$ and $T(\vec{x}_1)$ is preserved, and maps $\vec{q}_0$ to itself. The action of $\mathcal{T}T(\vec{x}_1)$ on Φ is

$$\mathcal{T}T(\vec{x}_1) \;\rightarrow\; \mathcal{K}\tau^3\tau^1\hat{\Phi}, \tag{9.109}$$

with $\mathcal{K}$ complex conjugation, from which one obtains the condition $\tau^3\tau^1\mathcal{H}^*(\vec{q}_0)\tau^1\tau^3 = \mathcal{H}(\vec{q}_0)$. This requires $\mathcal{H}(\vec{q}_0)$ to be proportional to the identity, proving that the degeneracy is symmetry protected.

In a very similar way one can show the symmetry protection of the degeneracy at $\vec{q}_1 = (\pi, 0)$ existing in the d_{xy} state. Both time-reversal and the fourfold rotation C_4 are symmetries and it is straightforward to deduce that these act on $\hat{\chi}(\vec{q}_1)$ as $\mathcal{K}\tau^3\tau^1\hat{\chi}(\vec{q}_1)$, precluding a coupling between the two degenerate states at $\vec{q}_1$. Below we comment in more detail on the special role of the fourfold rotation C_4 [86].

In the vicinity of the degeneracies present in the two examples of d wave states, the mean-field dispersion resembles that of Dirac fermions in case of the $d_{x^2-y^2}$, and a quadratic band crossing in case of d_{xy}. Hence we may reformulate the symmetry protection by stating that both the massless Dirac fermions in one case, and the quadratic band crossing are point group symmetry protected. Because of this, it is a natural and certainly interesting question to ask how additional symmetry breaking affects these low-energy descriptions.In accordance with the general theme of this work, that is the question we will address in the next two sections. We assume that we are deep inside the d wave states and will study in which way various symmetry broken density wave orders change the low energy properties of these "root" or "parent" states. This approach is similar to a recent study of band structure effects on superconducting states [192], where different "parent states" in principle competing with superconductivity were considered in order to study their impact on superconducting instabilities.

Dirac fermions of the π-flux state

A particularly interesting parent density-wave is the $d_{x^2-y^2}$ density-wave state giving rise to Dirac nodes in the low-energy spectrum. Let us abbreviate the strength of the density wave, i.e. the order parameter $\Delta_{d_{x^2-y^2}}$, as Δ for convenience. The nodes appear for arbitrary strength $|\Delta|$ with different Fermi velocities for two orthogonal directions in momentum space, however, the specific value $|\Delta| = 2t$ realizes the π-flux state on the square lattice. For illustrative purposes we take this value to correspond to the parent state and study the low-energy physics which is governed by a Dirac Lagrangian from a symmetry perspective. Suppressing spin indices we recall

the expression for the d wave state

$$\langle \hat{\psi}^\dagger(\vec{k} + \vec{Q}_1) \hat{\psi}(\vec{k}) \rangle = \Delta i (\cos k_x - \cos k_y), \tag{9.110}$$

and as we are interested in the low-energy Dirac physics we must include $\hat{\psi}(\vec{k} + \vec{Q}_2)$ and $\hat{\psi}(\vec{k} + \vec{Q}_3)$, which are coupled as

$$\langle \hat{\psi}^\dagger(\vec{k} + \vec{Q}_2) \hat{\psi}(\vec{k} + \vec{Q}_3) \rangle = \Delta i (\cos k_x + \cos k_y). \tag{9.111}$$

The fermions field in terms of which we write the Hamiltonian is now properly four-dimensional and reads explicitly

$$\hat{\chi}(\vec{k}) = \begin{bmatrix} \hat{\chi}_0(\vec{k}) \\ \hat{\chi}_1(\vec{k}) \\ \hat{\chi}_2(\vec{k}) \\ \hat{\chi}_3(\vec{k}) \end{bmatrix} = \begin{bmatrix} \hat{\psi}(\vec{k}) \\ \hat{\psi}(\vec{k} + \vec{Q}_1) \\ \hat{\psi}(\vec{k} + \vec{Q}_2) \\ \hat{\psi}(\vec{k} + \vec{Q}_3) \end{bmatrix}. \tag{9.112}$$

For convenience we abbreviate the cosine functions as $c_+(\vec{k}) \equiv \cos k_x + \cos k_y$ and $c_-(\vec{k}) \equiv \cos k_x - \cos k_y$. The Hamiltonian is block diagonal as $\hat{\chi}_0$ and $\hat{\chi}_1$ are decoupled from $\hat{\chi}_2$ and $\hat{\chi}_3$, i.e.

$$\mathcal{H}(\vec{k}) = \begin{bmatrix} \mathcal{M}_1(\vec{k}) & \\ & \mathcal{M}_2(\vec{k}) \end{bmatrix}, \tag{9.113}$$

with the blocks given by

$$\mathcal{M}_1(\vec{k}) = -2tc_+(\vec{k})\tau^3 - 2tc_-(\vec{k})\tau^2$$
$$\mathcal{M}_2(\vec{k}) = 2tc_-(\vec{k})\tau^3 + 2tc_+(\vec{k})\tau^2 \tag{9.114}$$

where τ^i is a set of Pauli matrices. As is well-known, the spectrum corresponding to this Hamiltonian has a doubly-degenerate Dirac node at $\vec{q}_0 = (\pi/2, \pi/2)$, analogous to the case of graphene. Expanding the Hamilotnian around this point yields the linear block diagonal structure

$$\mathcal{M}_1(\vec{q}_0 + \vec{q}) = v_F(q_x\tau^3 + q_y\tau^2)$$
$$\mathcal{M}_2(\vec{q}_0 + \vec{q}) = -v_F(q_y\tau^3 + q_x\tau^2), \tag{9.115}$$

where we have rotated $\vec{q}$ with respect to $\vec{k}$ by $\pi/4$. The linearized Dirac Hamiltonian corresponds to the Dirac spinor defined as $\hat{\Phi}(\vec{q}) = \hat{\chi}(\vec{q}_0 + \vec{q})$. It is convenient to

employ a basis transformation in order to express the Hamiltonian in a simple form. Making the substitution

$$\hat{\Phi}(\vec{q}) \rightarrow \begin{bmatrix} 1 & \\ & e^{-i\pi\tau^1/4} \end{bmatrix} \hat{\Phi}(\vec{q}) \equiv \begin{bmatrix} 1 & \\ & g \end{bmatrix} \hat{\Phi}(\vec{q}), \qquad (9.116)$$

achieves this and the transformed Hamiltonian reads

$$\mathcal{H}(\vec{q}) = v_F(q_x\tau^3 + q_y\nu^3\tau^2), \qquad (9.117)$$

where ν^i denotes another set of Pauli matrices acting on an effective valley space. More specifically, the τ^i mix the states $\hat{\chi}_{0,1}$ and $\hat{\chi}_{2,3}$ between themselves, and the ν^i mix the two sets. The Hamiltonian of equation (9.117) has the familiar Dirac form and one question we may ask is what are the possible Dirac masses and what do they correspond to physically. It is straightforward to determine the possible masses by finding combinations $\nu^i\tau^j$ which anticommute with both τ^3 and $\nu^3\tau^2$ [102]. All of the matrices τ^1, $\nu^1\tau^2$ and $\nu^2\tau^2$ have this property and, in addition, anti-commute between themselves. They constitute compatible masses which add in quadrature. There is another mass matrix, $\nu^3\tau^1$, which anti-commutes with τ^3 and $\nu^3\tau^2$ but not with the other masses. Hence, this is a competing mass.

In order to establish a connection between the density-wave states discussed earlier and the present low-energy description of the π-flux state, we analyze the symmetry properties of the mass matrices and other fermion bilinears. The recipy for this analysis follows directly from the gerenal considerations of Section 9.1 as we will now demonstrate. As such, it is similar to the approach described in [186]. Using the results of Section 9.1 we evaluate the effect of operations in C_{4v}''' on $\hat{\chi}(\vec{q}_0)$. As this is a point of high symmetry in the reduced Brillouin zone, we obtain a representation of the group, which can be fully specified by the action of the generators of the group. These are the translation $T(\vec{x}_1)$, the rotation C_4 and the reflection σ_v. The only yet crucial difference with respect to general discussion of Section 9.1 is the fact that in case of the π-flux state symmetry operations may need to be supplemented by a gauge transformation, the combination of which leaves the Hamiltonian invariant. Taking this into account and using equation (9.18) we find

$$\begin{aligned} T(\vec{x}_1) &\rightarrow -iG\nu^3\tau^3\hat{\chi}(\vec{q}_0) \\ C_4 &\rightarrow i\nu^3\tau^3 V\hat{\chi}(C_4\vec{q}_0) \\ \sigma_v &\rightarrow -iG\tau^3\hat{\chi}(\sigma_v\vec{q}_0) \end{aligned} \qquad (9.118)$$

where V originates from the interchange of $\hat{\chi}_2$ and $\hat{\chi}_3$ and G is the necessary gauge transformation. They are given by

$$V = \begin{bmatrix} 1 & \\ & \tau^1 \end{bmatrix}, \quad G = \nu^1 g = \nu^1 e^{-i\pi\tau^1/4}. \qquad (9.119)$$

As discussed earlier, even though $\vec{q}_0$ is invariant under all operations in the reduced BZ, it is not so in the original BZ, and we must therefore bring it back to itself by adding proper reciprocal lattice vector of the reduced BZ. Consequently, we find

$$\begin{aligned} \hat{\chi}(C_4\vec{q}_0) &= \hat{\chi}(\vec{q}_0 + \vec{Q}_2) = \nu^1\hat{\chi}(\vec{q}_0) \\ \hat{\chi}(\sigma_v\vec{q}_0) &= \hat{\chi}(\vec{q}_0 + \vec{Q}_3) = \nu^1\tau^1\hat{\chi}(\vec{q}_0). \end{aligned} \tag{9.120}$$

In a similar manner we can obtain the representation of time-reversal, which also should be supplemented by a gauge transformation in the present case. One finds

$$\mathcal{T} \to G\mathcal{K}\hat{\chi}(-\vec{q}_0) = G\mathcal{K}\tau^1\hat{\chi}(\vec{q}_0), \tag{9.121}$$

where $\mathcal{K}$ is complex conjugation. As these expressions determine the action of the group generators, the action of the group is fully specified. Simplifying the combinations of Pauli matrices somewhat we obtain the following set of operators acting on $\hat{\Phi}$, where we stress that is not the transformed $\hat{\Phi}$ defined by equation (9.116),

$$\begin{aligned} T(\vec{x}_1) &\to -ig\nu^2\tau^3\hat{\Phi} \\ C_4 &\to -i\nu^2\tau^2V\hat{\Phi} \\ \sigma_v &\to g\tau^2\hat{\Phi} \\ \mathcal{T} &\to g\mathcal{K}\nu^1\tau^1\hat{\Phi}. \end{aligned} \tag{9.122}$$

Then, using the unitary transformation expressed in equation (9.116), we obtain a representation of the group that can be used to classify all fermion bilinears $\hat{\Phi}_i^\dagger M_{ij}\hat{\Phi}_j$ with M some tensor product of Pauli matrices, i.e. $M_{ij} = (\nu^k\tau^l)_{ij}$. Let us first take a look at the mass matrices, which are of particular interest. The mass term τ^1 is found to transform according to B_2'. In addition, we find that the masses $\nu^1\tau^2$ and $\nu^2\tau^2$ transform as partners of the two-dimensional representation E_3. From this it immediately follows which density-wave states presented in Section 9.3.1 correspond to these mass terms and will therefore gap out the parent π-flux state. These are, respectively, the site ordered state at ordering vector $\vec{Q}_1$ given in equation (**??**) and the bond order doublet transforming as E_3, which is the real bond order doublet contained in the decomposition (9.88) and which we will see below is a flux-preserving generalization of equation (9.98). Here we observe how the symmetry of interaction-induced density wave orders allows for a direct identification of the impact of such density wave states at low energies. The three masses just identified are full analogs of masses (insulating states) in graphene [193–195]. We will analyze this connection in more detail below when we come to the honeycomb lattice itself, but for completeness we already mention what they correspond to in graphene. The site ordered state is trivially seen to correspond to a site ordered state on the honeycomb lattice, with

Irreps of C_{4v}'''	B_2'	E_3	E_2	E_1'	E_5
Irreps of C_{4v}	B_2	$A_1 \oplus B_1$	$A_2 \oplus B_2$	E_1	E_1
Basis functions	τ^1	$\nu^1\tau^2,$	$\nu^1,$	$\tau^2,$	$\frac{1}{\sqrt{2}}(\nu^1 - \nu^2\tau^1),$
		$\nu^2\tau^2$	ν^2	$\nu^3\tau^3$	$\frac{1}{\sqrt{2}}(\nu^2 - \nu^1\tau^1)$

Table 9.1: This table summarizes the identification of low-energy fermion bilinears as basis functions of irreducible representations of C_{4v}'''. In addition we present the irreducible representations of C_{4v} contained in those of C_{4v}'''.

a charge imbalance between the two sublattices (hence sometimes referred to as sublattice potential). The other two masses can be mapped onto the Kekule bond order in graphene.

Before we move on to establish a connection between other density-wave states listed in Section 9.3.1 and the Dirac matrices, we comment on the explicit expressions for mass generating density-wave states. The nature of the parent state we are considering here, i.e. the π-flux state, prevents us from directly associating the expressions written down in Section 9.3.1 with the mass matrices presented here. This is a consequence of the π-flux threading each square and the fact that some symmetry operations must be dressed with gauge transformation in order to leave the Hamiltonian invariant. The mass matrices $\nu^1\tau^2$ and $\nu^2\tau^2$ are time-reversal invariant and must therefore correspond to a flux-preserving density wave state. The doublet of equations (9.98) and (9.99) by themselves are not π-flux-preserving (even though the doublet (9.98) clearly preserves zero flux, the parent). We must therefore form appropriate linear combinations in order to form states that transform as E_3 under the symmetry operations of the parent state. We find that the following linear combinations have this property

$$
\begin{aligned}
\langle \hat{\psi}_\sigma^\dagger(\vec{k} + \vec{Q}_2)\hat{\psi}_{\sigma'}(\vec{k}) \rangle &= -i\eta_1 \Delta_{\eta_1\eta_2}(\sin k_x + i\eta_2 \sin k_y)\delta_{\sigma\sigma'}, \\
\langle \hat{\psi}_\sigma^\dagger(\vec{k} + \vec{Q}_3)\hat{\psi}_{\sigma'}(\vec{k}) \rangle &= \Delta_{\eta_1\eta_2}(\sin k_x + i\eta_2 \sin k_y)\delta_{\sigma\sigma'}.
\end{aligned}
$$
(9.123)

Here $\eta_i = \pm$ and we have not only formed combinations of the E_2 and E_3 doublets as specified by (9.98) and (9.99), we have also constructed the condensates so as to form basis functions of the two A_1 representations of C_{4v} contained in E_3. This is reflected in the appearance of $p_x + ip_y$ functions. As there are two indices η_i both taking two values, they represent four distinct condensates. Let's first take $\eta_1 = +$. Then we find that the two density-wave states $\eta_2 = \pm$ are precisely the flux-preserving mass terms transforming as $E_3 = A_1 \oplus B_1$. Hence, these are the condensate functions which

directly correspond to the Dirac masses $\nu^1\tau^2$ and $\nu^2\tau^2$. Since they were obtained by taking linear combinations of E_1 and E_2 functions of the zero flux root state, it is natural to expect that we may form very similar linear combinations to obtain expressions for doublet functions belonging to E_2 of the π-flux state. Indeed, taking $\eta_1 = -$ yields the two ($\eta_2 = \pm$) partners of the E_2 representation, which do change the flux away from π. The Dirac matrices ν^1 and ν^2 provide the low-energy fermion bilinears belonging to these states. They are not masses which gap out each of two Dirac cones, but instead split the two Dirac cones in energy. One may call them masses in "valley space".

Now that we have seen how density wave states, based on symmetry arguments, have the interpretation of Dirac masses at low energies, we proceed to establish a connection between some other density-wave states and Dirac matrices. In particular the doublets E_1' and E_5, which are part of (9.88) and were defined in the previous section, have an interesting low-energy structure. Taking the E_1' as an example, we may find Dirac matrices which transform as partners of this representation, by requiring that they are odd under the translations $T(\vec{x_1})$ and $T(\vec{x_2})$, while being odd under C_2 as well. Two matrices satisfying these constraints are τ^2 and $\nu^3\tau^3$, which are indeed the partners of E_1'. Similar reasoning leads to the combinations of Dirac matrices $(\nu^1 - \nu^2\tau^1)/\sqrt{2}$ and $(\nu^2 - \nu^1\tau^1)/\sqrt{2}$ belonging to E_5. As such, they correpond to the terms in the low-energy coming from the density waves transforming accordingly. What is the precise structure of these terms? To see this, we first define the three Dirac matrices $\Omega^1 = \nu^1\tau^3$, $\Omega^2 = \nu^1\tau^3$ and $\Omega^3 = \nu^3$. Note that these satisfy the $su(2)$ algebra $[\Omega^i, \Omega^j] = 2i\epsilon^{ijk}\Omega^k$, and we can therefore use them as gauge charges of an $SU(2)$ gauge field A_α as $A_\alpha = A_\alpha^i\Omega^i$ ($\alpha = x, y$) and couple this gauge field to the low-energy Dirac fermions of the π-flux state as

$$\mathcal{H}(\vec{q}) = \hbar v_F \left[\tau^3(q_x - A_x^i\Omega^i) + \nu^3\tau^2(q_y - A_y^i\Omega^i) \right]. \tag{9.124}$$

Looking at what the products $\tau^3\Omega^i$ and $\nu^3\tau^2\Omega^i$ amount to, we see that one precisely obtains ν^1, ν^2 and $\nu^3\tau^3$ in case of the former, and $\nu^2\tau^1$, $\nu^1\tau^1$ and τ^2 in case of the latter. This leads to the conclusion that density wave states transforming as E_1' and E_5 enter to lowest order as gauge-fields in the low-energy Dirac theory of the parent π-flux state. As such they do not gap out the linear Dirac nodes, but shift them away from $\vec{q_0}$ in the Brillouin zone. Non-Abelian gauge fields appearing in a low-energy Dirac theory of a condensed matter system have been discussed in the context of graphene [180] (to which we come back later) and we observe here that the translational symmetry broken density wave states belonging to the E_1' and E_5 representation are direct square lattice analogs of these.

Table (9.1) summarizes the identification of Dirac matrices as basis functions of irreducible representations. In essence, as was demonetrated above, this table allows to directly interpret the effect of interaction induced site or bond ordered states

on the low-energy theory of the fully symmetric patent state, the π-flux state. Table (9.1) highlights an important conclusion which follows from the symmetry analysis presented here and which will reappear in the context of hexagonal lattices. All condensates which belong to representations that can be reduced in terms of "bare" point group representations (C_{4v} for the square lattice) as $1D$ representations enter as masses in the low-energy description, either in valley space or providing a full spectral gap. This was demonstrated for $E_3 = A_1 \oplus B_1$, which lead to genuine masses and therefore spectral gaps, and $E_2 = A_2 \oplus B_2$, states of which have the effect of a valley-mass. In contrast, condensates transforming according to representations that contain only $2D$ representations of the "bare" point group are found to correspond to gauge fields in the context of a low-energy Dirac description. These statements will be found to hold true for hexagonal lattices with symmetry protected Dirac points as well, such as the honeycomb and kagome lattice. In addition, we will find a more general connection between condensate functions transforming as $1D$ representation and the presence of spectral gaps when looking at nested Fermi surfaces of the hexagonal lattice free dispersions.

Quadratic band crossing

After this extensive exposition on the π-flux root state, we come now to the second parent state of interest. Whereas the π-flux state is essentially a $d_{x^2-y^2}$ state, the other state we focus on is the d_{xy} state given in equation (9.101). Assuming we are very deep inside the d_{xy} state and writing the strength as $\Delta = t_2$ we start from the following root state

$$\langle \hat{\psi}^\dagger(\vec{k} + \vec{Q}_1)\hat{\psi}(\vec{k})\rangle = t_2 \sin k_x \sin k_y,$$
$$\langle \hat{\psi}^\dagger(\vec{k} + \vec{Q}_2)\hat{\psi}(\vec{k} + \vec{Q}_3)\rangle = -t_2 \sin k_x \sin k_y \qquad (9.125)$$

We choose to work again in the four-dimensional spinor basis specified in equation (9.112). As was the case for the π-flux state, the Hamiltonian is block diagonal, with the blocks defined as $\mathcal{M}_i$. The low-energy theory (at half filling) of the d_{xy} state is that of a quadratic band crossing (QBC) at Γ, i.e. an isolated degeneracy in the vicinity of which the dispersion is quadratic. The QBC exists in the $\mathcal{M}_2$ block of the Hamiltonian, which reads

$$\mathcal{M}_2(\vec{k}) = 2t(\cos k_x - \cos k_y)\tau^3 - t_2 \sin k_x \sin k_y \tau^1, \qquad (9.126)$$

while the $\mathcal{M}_1$ block contains the high-energy modes at Γ. Hence, for the low-energy description we need to project into the subspace spanned by $\hat{\chi}_2$ and $\hat{\chi}_3$ and the low-

energy spinor is then given by

$$\hat{\Phi}(\vec{q}) = \begin{bmatrix} \hat{\chi}_2 \\ \hat{\chi}_3 \end{bmatrix} = \begin{bmatrix} \hat{\psi}(\vec{Q}_2) \\ \hat{\psi}(\vec{Q}_3) \end{bmatrix} \tag{9.127}$$

The low-energy Hamiltonian for small momenta $\vec{q}$ takes the form

$$\mathcal{H}(\vec{q}) = 2t(q_x^2 - q_y^2)\tau^z - 2t_2 q_x q_y \tau^1, \tag{9.128}$$

which directly follows from (9.126). We have seen above that the d_{xy} state transforms according to A_1', which essentially means that it is odd under the translations $T(\vec{x}_i)$. The action of the generators of the group C_{4v}''' on the low-energy degrees of freedom is derived in the same way as before [see again equation (9.116)], and after projecting onto the low-energy subspace

$$T(\vec{x}_1) \rightarrow -\tau^3 \hat{\Phi}$$
$$C_4 \rightarrow -i\tau^2 \hat{\Phi}$$
$$\sigma_v \rightarrow \tau^3 \hat{\Phi}$$
$$\mathcal{T} \rightarrow \mathcal{K}\hat{\Phi}. \tag{9.129}$$

Based on the action of these operators we can deduce the effect on the d_{xy} root state, of density waves which lower the symmetry. Two well-known properties of QBC points [86] follow immediately from them. The first is that an energy gap is forbidden by time-reversal invariance. The opening of a gap would come from a constant term in (9.128) proportional to τ^2, which is odd under time-reversal. The second is the protection of the QBC by C_4 symmetry. In general a perturbation may split the QBC into two Dirac points, which is not possible however in the presence of C_4 symmetry [86]. Intuitively this is obvious, as the splitting in two nodes away from Γ clearly violates fourfold rotational symmetry. From the above relations we see that C_4 is the only operation acting as τ^2, which anticommutes with both τ^1 and τ^3, making them both odd under a fourfold rotation, precluding a constant term proportional to these matrices. Hence, the combined operation of time-reversal and fourfold rotation robustly protects the QBC at Γ in the RBZ.

We observe that the matrix τ^1 is odd under the vertical reflection σ_v and would therefore transform as B_2'. Indeed the CDW at ordering vector $\vec{Q}_1$ couples to such a term. This would correspond to a splitting of the QBC point into two Dirac points. The time-reversal odd matrix τ^2, the only matrix available to open up a spectral gap, couples to the density staggered flux state of equation (9.100). For any generic QBC point a spectral gap can only be opened by breaking time-reversal symmetry. This is due to the fact that a gapped QBC intrinsically carries a nonzero Chern number [86],

which is not compatible with time-reversal invariance. These two density waves, i.e. the B_2' and the A_2' state, are both modulated by $\vec{Q}_1$ and therefore directly affect the QBC point due to the relation $\langle \hat{\psi}^\dagger(\vec{k} + \vec{Q}_1)\hat{\psi}(\vec{k})\rangle = \langle \hat{\psi}^\dagger(\vec{k} + \vec{Q}_2)\hat{\psi}(\vec{k} + \vec{Q}_3)\rangle$. The same is true for the time-reversal invariant bond order doublet of equation (9.97). As these are p-wave states they enter in the low-energy description as $q_x \tau^2$ and $q_y \tau^2$, where the momentum dependence ensures time-reversal invariance.

9.4   Condensates of hexagonal lattices

The second class of lattices for which we present an extensive and detailed discussion of the symmetry organization of particle-hole condensation are the hexagonal lattices. Two-dimensional lattices with hexagonal symmetry play are ubiquitous in condensed matter physics, the honeycomb lattice realized in graphene being the highlight example. The kagome lattice, to name another well-known example, has attracted much attention since materials which have this basic lattice structure are considered to be prime candidates for intriguing physics such as spin liquid behaviour. At the same time, recent studies of hexagonal lattice fermion models with strong electronic interactions point towards new and unconventional correlated electronic phases, which are believed to originate from the hexagonal symmetry of such systems. With this in mind, in this section we will apply the method outlined in Section 9.1, and applied to the square lattice in 9.3, to three specific lattices, the honeycomb lattice, the kagome lattice and the triangular lattice.

The hexagonal lattices all have a triangular Bravais lattice and their first Brillouin zone takes the shape of a hexagon, which is shown in Fig. 9.4. In the followig we will focus on translational symmetry breaking at two different sets of commensurate wave vectors. The first set consists of the corners of the Brillouin zone hexagon, a set which contains two inequivalent wave vectors $\vec{K}_+$ and $\vec{K}_-$, the socalled K-points, see Fig. 9.4. The second set consists of the centers of the hexagon faces, the so-called M-points, also shown in Fig. 9.4. There are three inequivalent M-points and we will write them as $\vec{Q}_\mu$, with $\mu = 1, 2, 3$. The algebraic properties under addition are distinct for these two sets of ordering momenta. The K-points are related by $\vec{K}_- = 2\vec{K}_+$ and $3\vec{K}_+ = 0$, from which it follows that $\vec{K}_- = -\vec{K}_+$. Observe that the K-points are generated by a single vector $\vec{K}_+$ (or $\vec{K}_-$ obviously). The M-points in the hexagonal Brillouin have the property $2\vec{Q}_\mu = 0$, which is equivalent to $\vec{Q}_\mu$ defined for square symmetry systems. Indeed, the M-points satisfy $\pm\vec{Q}_1 \pm \vec{Q}_2 \pm \vec{Q}_3 = 0$. The difference with respect to the square lattice $\vec{Q}_\mu$ is that all M-points are mixed by point group operations, while $\vec{Q}_1 (= (\pi, \pi))$ is always mapped to itself for systems with square symmetry. Translational symmetry breaking at the K-points amounts a

tripling of the unit cell and is expected in case of the honeycomb and kagome lattices when these systems are doped to the Diracpoints of band structure, as K connects the Dirac nodes in momentum space. In contrast, translational symmetry breaking at the M-points leads to a quadrupled unit cell, and is expected to occur for all three hexagonal lattices when their band structure is filled to the van Hove points.

The rest of this section is divided into three parts, corresponding to the three lattices that will be discussed. The first part deals with the honeycomb lattice, while the second and third part focus on the kagome and triangular lattice, respectively. The most detailed treatment will be presented for the honeycomb lattice, as it will serve to highlight the features common to all three lattices. All three parts start with a group theoretical analysis of all the possible site, bond and flux density waves and then proceed to finding the explicit forms of these density waves in order to characterize their electronic properties. The honeycomb lattice part is subdivided into five distinct parts, the first three of which discuss the density waves of translationally invariant, K-point, and M-point density waves, respectively. In particular M-point ordering on the honeycomb lattice will treated in great detail as we will introduce a formalsim for obtaining density waves of definite symmetry that will find more general application in the context of the other hexagonal lattices. The last two parts focus on the spectral characterization of these density waves and its connection to the representations to which they belong. For K-point order the relevant low-energy description of the electronic systems is a Dirac theory located at those K-points and we will carefully study how the various density waves enter in such a Dirac theory, in a similar fashion as for the square lattice. For M-point order the relevant starting point for describing low-energy electrons is a hexagonal Fermi surface, energetically located at the van Hove points of band structure, and nested by the M-points. We will derive and present an effective low-energy theory around those M-points and show, using only symmetry arguments, how density wave states enter in such an effective description. Both of these parts are based on the honeycomb lattice, but the results and conclusions presented there apply to all hexagonal lattices. For this reason, the discussion of the kagome and triangular lattices will be more brief as we can draw from insight gained in the context of the honeycomb lattice. Specifically, in case of the kagome lattice we will combine the explicit construction of symmetric density waves and their impact on the mean field spectrum for the purpose of illustrating the power and utility of the lattice symmetry organization of the density waves. We will do the same for the triangular lattice, in which case we content ourselves with M-point ordered states, for the most part because we use the triangular lattice as the prime example illustrating spinful M-point condensates in Chapter 10.
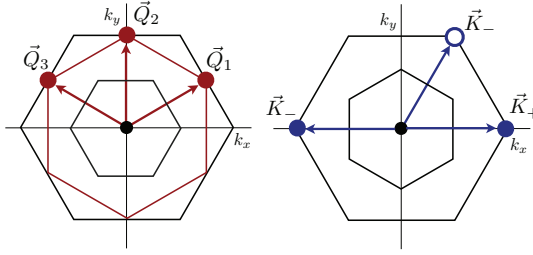
Figure 9.4: (Left) Outer black lined hexagon denotes the first Brillouin zone of hexagonal lattices (for instance honeucomb, kagome, but also triangular lattices). Bold red dots mark the M-point ordering vectors $\vec{Q}_\mu$ (for the definition see Appendix A) and the red hexagon connecting these M-points denotes the Fermi surface at a specific lattice depedent filling fraction, which in case of the honeycomb lattice would be $3/8$. Inner black hexagon denotes the reduced Brillouin zone corresponding to M-point order (b) First Brillouin zone of the hexaginal lattices, with bold blue dots denoting the hexagon vertices $\vec{K}_\pm$. Inner black rotated hexagon denotes the reduced the reduced Brillouin zone corresponding to ordering at $\vec{K}_\pm$.

9.4.1 Honeycomb lattice

The honeycomb lattice is a lattice structure which has acquired fame since the isolation of single-atom graphite layers now known as graphene [98, 196]. The honeycomb lattice has a triangular Bravais lattice with a two-atom unit cell, and we follow the convention of labeling the atoms A and B. Details of Bravais and reciprocal vectors in addition to the real space positions of the unit cell atoms, definition of real space origin and lattice symmetries are given in Appendix A. We will first look at translationally invariant density-wave states, and then proceed to discuss translational symmetry broken states, at K-points and M-points respectively. Before we go into the details of these classes of condensates we employ straightforward group theory methods to derive which irreducible representations are expected for a given choice of translational symmetry breaking. As was the case for the square symmetry groups, translational symmetry breaking removes a certain set of translations from the translational symmetry group corresponding to the Bravais lattice. Adding these translations to the point group of the original Bravais lattice gives the extended points groups. In case of the hexagonal space group lattices, these extended groups are C_{6v}'' and C_{6v}''' for K-point ordering and M-point ordering, respectively. The number of primes pertain to the number of translations added to the point group C_{6v}. For more details we refer to Appendix C.

For density wave states at both K- and M-points we distinguish site order, bond order and flux states. Let us defer flux states for the moment and focus attention on site and bond order first. The general procedure is to label all sites and bonds within the unit cell by s_i and b_i, respectively. The index i runs over the number of sites or bonds in the unit cell, which depends on the modulation (ordering) vectors under consideration. For instance, for K-point ordering, we have 6 sites in the unit and 9 bonds. We then construct a representation of the extended point groups by associating each element of the group with a permutation $P_{ij}^{\mathrm{s,b}}$, which follows from the way the group element permutes the sets $\{s_i\}_{i=1}^6$ and $\{b_i\}_{i=1}^9$, i.e.

$$s_i' = \sum_j P_{ij}^{\mathrm{s}} s_j, \quad b_i' = \sum_j P_{ij}^{\mathrm{b}} b_j. \tag{9.130}$$

These representations, denoted as $\mathcal{P}_{\mathrm{s,b}}$, may be decomposed into irreducible representations using the character table of the symmetry group. The decomposition then tells us how all possible condensates may be organized according to their transformation properties under symmetry group elements.

In case of site order at the K-points we find the following decomposition in terms of irreducible representations of C_{6v}''

$$\mathcal{P}_{\mathrm{s}}^{\mathrm{K}} = A_1 \oplus B_2 \oplus G', \tag{9.131}$$

whereas we find for M-point ordering

$$\mathcal{P}_{\mathrm{s}}^{\mathrm{M}} = A_1 \oplus B_2 \oplus F_1 \oplus F_4, \tag{9.132}$$

which in this case is a decomposition in terms of irreducible representations of C_{6v}'''. These two decompositions share the combination $A_1 \oplus B_2$ which is the translationally invariant content of the decomposition. It is not surprising that this is also contained in the decomposition of larger reducible representations of translational symmetry broken states. The combination $A_1 \oplus B_2$ may also be obtained in a direct manner by focusing exclusively on the translationally invariant unit cell structures. The two sublattices corresponding to the A and B are either left invariant or interchanged by an element of C_{6v}, yielding a two-dimensional reducible representation of the symmetry group. Decomposing it in terms of irreducible representations simply gives $A_1 \oplus B_2$. As a spoiler of what follows, we note that B_2 corresponds to a charge-density wave that corresponds to the sublattice potential often discussed in the context of graphene.

Repeating the same procedure for bond ordering we obtain for K-point ordering

$$\mathcal{P}_{\mathrm{b}}^{\mathrm{K}} = A_1 \oplus E_2 \oplus E_1' \oplus G', \tag{9.133}$$

and for ordering at the M-points we find

$$\mathcal{P}_{\text{b}}^{\text{M}} = A_1 \oplus E_2 \oplus F_1 \oplus F_3 \oplus F_4. \tag{9.134}$$

Here we observe that the translationally invariant content is $A_1 \oplus E_2$. At this stage we leave these results for what they are, but will come back to them extensively when we discuss the explicit expressions of the density-wave states transforming according to the representations featuring in the decompositions derived here.

   We now go into the details of flux states on the honeycomb lattice. In order to find the various flux states transforming according to irreducible representations of the relevant symmetry group we associate a flux ϕ_i to each hexagonal plaquette of the honeycomb lattice. As such, the problem of finding the permutation corresponding to a given is similar to the problem of site order on the triangular lattice, with the crucial difference that reflections invert the flux and give rise to a minus sign. In addition, we must again enforce the constraint that the sum of fluxes in the unit cell is zero up to integer multiples of the elementary flux quantum 2π. Working out the permutation representation and decomposing it into irreducible representations of C_{6v}'' we find

$$\mathcal{P}_{\phi}^{\text{K}} = A_2 \oplus E_2'. \tag{9.135}$$

The translationally invariant content is simply given by A_2, which by definition corresponds to a state with the same flux ϕ pierced through each hexagonal plaquette. To find the flux patterns contained in E_2' we first decompose it in irreducible representations of C_{6v} and find $E_2' = A_2 \oplus B_2$.

   An analogous calculation for flux patterns coming from M-point ordering yields the decomposition

$$\mathcal{P}_{\phi}^{\text{M}} = A_2 \oplus F_2, \tag{9.136}$$

where the F_2 representation can be further decomposed into $A_2 \oplus E_2$.

   In the same way as for the square lattice, we can use the obtained representations for the different types of ordered states to analyse whether or not additional quantum numbers connected to topological characteristics can in principle be acquired by the condensates. The simplest task to identify orderings that are compatible with nonzero Chern number. We stress that we do not assume anything with regard to the spectral properties such as the existance of an energy gap, which is a necessary condition of a well-defined integer Chern number. Based on symmetry alone it is possible to narrow the possibilities down considerably. In particular, as was noted in Section 9.1.4, time-reversal symmetry mandates vanishing Chern number and therefore we are forced to consider the flux states. The translationally invariant state we already excluded, which leaves us with E_2' in case of K-point ordering, and F_2 in case of M-point ordering.

We had already taken the effort of decomposing them further in terms of C_{6v} and found that both in case of K-point and M-point ordering there is a state A_2 which breaks all reflections. Both are contained in larger dimensional representations of C_{6v}'' and C_{6v}''', the partners of which are mixed by the point group translations $T(\vec{x}_i)$. Hence, translations cannot compensate the odd reflections as was the case for the square lattice. These states are therefore genuine candidates for nontrivial topology and we will investigate this specifically once we have obtained explicit expression for them.

Insofar as quantized electric polarization is concerned, hexagonal symmetry restricts the possibilities. We iterate that hexagonal symmetry here refers strictly to the rotations and reflections, the bare point group elements. As stated in section 9.1.4, when C_6 rotational symmetry is present, no nontrivial electric polarization is possible. The threefold rotational symmetry C_3 restricts the polarization $p_1 = p_2$ to be multiples of $1/3$. If, in addition, there exists a reflection (or two-fold rotation from D_3) then it precludes nontrivial polarization if one of the lattice vectors $\vec{x}_i$ is in the reflection plane (or one of its C_3 equivalents). The point group C_{6v} has four representations which have C_3 symmetry, which are all the $1D$ representations. Two must be excluded as they have C_6 in addition. Two other are B_1 and B_2, only one of which admits nontrivial polarization due to the reflection. Which one depends on the translational symmetry breaking, in the sense that for K-point ordering the unit lattice vectors are $2\vec{x}_1 + \vec{x}_2$ and $\vec{x}_1 + 2\vec{x}_2$. For M-point ordering they are $2\vec{x}_1$ and $2\vec{x}_2$, which has the consequence that for translationally invariant order and order at M-points B_2 states admit nontrivial polarization, while B_1 states admit nontrivial polarization for K-point order. Based on these considerations we conclude that for site order the C_3 symmetric state contained in the M-point triplet F_4, which is a B_2 state may have nontrivial polarization. For bond order we have the K-point candidate B_1 contained in E_1' and the M-point candidate B_2 contained in F_4.

Before we start building the general particle-hole condensates on the honeycomb lattice, we note that we will use the matrix functions τ^i (Pauli matrices), which operate on the sublattice degree of freedom.

Translationally invariant singlet states at Γ

We start by considering translationally invariant states, some of which are nontrivial due to the sublattices of the honeycomb lattice. A general density-wave state with sublattice structure can then be written as

$$\langle \hat{\psi}_{i\sigma}^\dagger(\vec{k})\hat{\psi}_{j\sigma'}(\vec{k}) \rangle = \vec{\Delta}(\vec{k}) \cdot \vec{\tau}_{ij}\delta_{\sigma\sigma'} \tag{9.137}$$

Here the τ-matrices are Pauli matrices acting on the sublattice degree of freedom $i, j = A, B$. The simplest translationally invariant state we can write is the CDW

state which makes the two sublattices inequivalent and breaks inversion symmetry.

$$\langle \hat{\psi}_{i\sigma}^{\dagger}(\vec{k}) \hat{\psi}_{j\sigma'}(\vec{k}) \rangle = \Delta_{\mathrm{CDW}} \tau_{ij}^{3} \delta_{\sigma\sigma'} \tag{9.138}$$

The Pauli matrix τ^{3} transforms according to B_2 and this CDW state consquently transforms as B_2. Note that $\Delta_{\mathrm{CDW}} = \Delta_{\mathrm{CDW}}^{*}$. Intuitively this is immediately obvious, since the two sublattices are inequivalent and hence all operations that exchange A and B sites no longer constitute symmetries.

Next we look at translationally invariant bond-order states. There are three bonds in the unit cell which transform into each other under point group operations. In accordance with equation (9.133) we expect a one-dimensional representation A_1, which corresponds to the fully symmetric state, and a two-dimensional d-wave-like representation E_2. The state transforming as A_1 is simply a uniform renormalization of the bond strength and therefore the overlap integral (hopping). The other two bond density-wave states transform accoring to d-wave functions (E_2) and are given by

$$\langle \hat{\psi}_{i\sigma}^{\dagger}(\vec{k}) \hat{\psi}_{j\sigma'}(\vec{k}) \rangle = \frac{\Delta_{x^2-y^2}}{3} \tau_{ij}^{x^2-y^2}(\vec{k}) \delta_{\sigma\sigma'}$$

$$\langle \hat{\psi}_{i\sigma}^{\dagger}(\vec{k}) \hat{\psi}_{j\sigma'}(\vec{k}) \rangle = \frac{\Delta_{xy}}{\sqrt{3}} \tau_{ij}^{xy}(\vec{k}) \delta_{\sigma\sigma'} \tag{9.139}$$

Here the matrix $\tau^{x^2-y^2}(\vec{k})$ is defined as

$$\tau^{x^2-y^2}(\vec{k}) = \begin{bmatrix} & f_{x^2-y^2}(\vec{k}) \\ f_{x^2-y^2}^{*}(\vec{k}) & \end{bmatrix}, \tag{9.140}$$

and $\tau^{xy}(\vec{k})$ is defined similarly. The functions $f_{x^2-y^2}$ and f_{xy} are given by

$$f_{x^2-y^2}(\vec{k}) = (-2e^{-i\vec{k}\cdot\vec{\delta}_1} + e^{-i\vec{k}\cdot\vec{\delta}_2} + e^{-i\vec{k}\cdot\vec{\delta}_3})e^{i\varphi(\vec{k})}$$

$$f_{xy}(\vec{k}) = (e^{-i\vec{k}\cdot\vec{\delta}_2} - e^{-i\vec{k}\cdot\vec{\delta}_3})e^{i\varphi(\vec{k})}. \tag{9.141}$$

which may be immediately recognized as real d-wave combinations of the three exponentials $e^{i\vec{k}\cdot\vec{\delta}_i}$, which transform into each other under the operations of the point group. The exponential $e^{-i\varphi(\vec{k})} \equiv e^{-i\vec{k}\cdot\vec{\delta}_1}$ is included to enforce the gauge choice of equation (9.4). We adopt the convention of including the factor $e^{-i\varphi(\vec{k})}$ explicitly so as not to risk obscuring the three nearest-neighbor exponentials.

What we have not discussed in the introdcution to this honeycomb lattice section, are bond density waves which emerging on next-nearest neighbor bonds. All bond order decompositions, equations (9.133) and (9.134), pertain to nearest neighbor bonds connecting the two sublattices. Even though we have not derived the decompositions,

we nevertheless briefly discuss the next-nearest neighbor bond order since it plays an important role in the literature [84, 167, 168]. Intra-sublattice bond order intabilities have been at the heart of recent studies on topological particle-hole condensates on the honeycomb lattice.

We proceed to writing $k_j = \vec{k} \cdot \vec{x}_j$ where $\vec{x}_j$ are the Bravais lattice vectors (see also Appendix A.3 for more on these definitions). Using this, we can directly write orbital momentum basis functions which transform as $1D$ representations under all elements of the point group.

$$
\begin{aligned}
f_{A_1}(\vec{k}) &= \cos k_1 + \cos k_2 + \cos k_3 \\
f_{B_1}(\vec{k}) &= \sin k_1 + \sin k_2 + \sin k_3
\end{aligned}
\tag{9.142}
$$

These functions may be combined with sublattice functions (Pauli matrices) to construct states with specific symmetry. Let us start by considering the most famous example of a condensate functions that may be constructed in such a way. We can combine f_{B_1} with τ^3, which transform as B_1 and B_2, respectively, to obtain a density-wave state that transforms as $A_2 = B_1 \otimes B_2$, as expected from the character table. The expression for the condensate reads

$$
\langle \hat{\psi}^\dagger_{i\sigma}(\vec{k}) \hat{\psi}_{j\sigma'}(\vec{k}) \rangle = \Delta_{A_2} f_{B_1}(\vec{k}) \tau^3_{ij} \delta_{\sigma\sigma'}
\tag{9.143}
$$

Note that we need to have $(\Delta_{A_2})^* = \Delta_{A_2}$ hence we have one real parameter. This state does not break any rotational symmetries, however, the point group reflections are all broken, together with time-reversal symmetry. The state described by this condensate function has a gapped mean-field spectrum and is in fact precisely the state introduced by Haldane [76] in order to demonstrate as a matter of principle that a Quantum Hall effect can occur in a lattice system in the absence of external magnetic fields. It has been argued in the literature that such a density wave state indeed emerges from next-nearest neighbor interactions in a mean field treatment [84].

Another example of a density wave state we can form simply by combining functions of specific symmetry, is a state which does not break any lattice symmetries, but does however break the particle-hole symmetry of the bare honeycomb lattice. It is obtained by combining the f_{A_1} function with the unit matrix δ_{ij}. The condensate function reads

$$
\langle \hat{\psi}^\dagger_{i\sigma}(\vec{k}) \hat{\psi}_{j\sigma'}(\vec{k}) \rangle = \Delta_{A_1} f_{A_1}(\vec{k}) \delta_{ij} \delta_{\sigma\sigma'}
\tag{9.144}
$$

Also in this case one has $(\Delta_{A_1})^* = \Delta_{A_1}$.

As we are considering intra-sublattice bond order, the two available sublattice functions are δ_{ij} and τ^3_{ij}. Combining them with the two orbital momentum functions f_{A_1} and f_{B_1} yields four different states, two of which we have just discussed. The

others must have symmetries $B_1 = A_1 \otimes B_1$ and $B_2 = B_2 \otimes A_1$. The condensate functions are then give by

$$\langle \hat{\psi}_{i\sigma}^\dagger(\vec{k}) \hat{\psi}_{j\sigma'}(\vec{k}) \rangle = \Delta_{B_1} f_{B_1}(\vec{k}) \delta_{ij} \delta_{\sigma\sigma'},$$
$$\langle \hat{\psi}_{i\sigma}^\dagger(\vec{k}) \hat{\psi}_{j\sigma'}(\vec{k}) \rangle = \Delta_{B_2} f_{A_1}(\vec{k}) \tau_{ij}^3 \delta_{\sigma\sigma'} \tag{9.145}$$

Note that the second of these two transforms as B_2, which is the same as the site ordered state of equation (9.138). Hence, already anticipating the conclusion of Section 9.4.1, this density wave state opens up a gap in the mean-field spectrum.

Translational symmetry breaking at $\vec{K}_\pm$

We move on to translational symmetry broken states at wave-vector $\vec{K}_\pm = \pm(4\pi/3, 0)$. We will start with site order and then discuss bond-density wave orders. For site order we expect states corresponding to representations contained in (9.131). As we already found the translationally symmetric A_1 and B_2 states, we are left to identify the $G'(= E_1 \oplus E_2)$ states.

In the case of site order the relevant sublattice functions are $\tau^0 = \delta$ and τ^3. We will look for condensates which transform as G' and are simultanesouly organized as partners of E_1 and E_2 contained in G'. Such condensates are pedagogically derived in real space. We start from a properly modulated state on the A-sublattice (suppressing spin indices for the sake of brevity)

$$\langle \hat{\psi}_A^\dagger(\vec{x}) \hat{\psi}_A(\vec{y}) \rangle = \Delta \cos(\vec{K} \cdot \vec{x}) \delta_{\vec{x}, \vec{y}}. \tag{9.146}$$

Since the little group of $\vec{K}_\pm$ is C_{3v} (see also above) it is sensible to first build a set of three objects which transform into each other under the threefold rotation. Doing this for the expectation value in equation (9.146) we find the two related states

$$C_3 \rightarrow \langle \hat{\psi}_A^\dagger(\vec{x}) \hat{\psi}_A(\vec{y}) \rangle = \Delta \cos(\vec{K} \cdot \vec{x} + \vartheta) \delta_{\vec{x}, \vec{y}}$$
$$C_3^{-1} \rightarrow \langle \hat{\psi}_A^\dagger(\vec{x}) \hat{\psi}_A(\vec{y}) \rangle = \Delta \cos(\vec{K} \cdot \vec{x} + 2\vartheta) \delta_{\vec{x}, \vec{y}} \tag{9.147}$$

where $\vartheta = 2\pi/3 = -i \ln \omega$. In general, for three objects $|a\rangle, |b\rangle, |c\rangle$ related by a three-fold rotation, one may form a fully symmetric combination, i.e. $|a\rangle + |b\rangle + |c\rangle$ and a doublet of states transforming as partners of the two-dimensional representation of C_{3v}. The latter doublet is written as $|E, 1\rangle = (-2|a\rangle + |b\rangle + |c\rangle)/3$ and $|E, 2\rangle = (|b\rangle - |c\rangle)/\sqrt{3}$. Now if we make the identification $|a\rangle = \cos(\vec{K} \cdot \vec{x}) \equiv \cos a$, $|b\rangle = \cos(\vec{K} \cdot \vec{x} + \vartheta) \equiv \cos b$ and $|c\rangle = \cos(\vec{K} \cdot \vec{x} + 2\vartheta) \equiv \cos c$ an expression for the doublets of E_1 and E_2 is immediately obtained. We are left with finding expressions for the B

sublattice. They are fixed by the character table of C_{6v} in the sense that the character table tells us that the partners of E_1 are odd under C_2, while the partners of E_2 are even. As the inversion C_2 exchanges sublattices this uniquely fixes $\langle \hat{\psi}_B^\dagger(\vec{x})\hat{\psi}_B(\vec{y})\rangle$. Is is important to realize that the threefold rotation C_3 maps A and B atoms to different unit cells. This is reflected in the expression for the condensate expectation value on the B-sublattice, which read $(-2\cos c + \cos b + \cos a)/3$ and $(\cos b - \cos a)/\sqrt{3}$. Transforming to momentum space yields expressions for the four density wave states transforming as $G' = E_1 \oplus E_2$, i.e. for E_2 (reinstating spin)

$$\langle \hat{\psi}_{i\sigma}^\dagger(\vec{k} + \vec{K}_+)\hat{\psi}_{j\sigma'}(\vec{k})\rangle = \frac{\Delta_{x^2-y^2}^1}{3}(-2 + \omega + \omega^2)\underline{\tau}_{ij}\delta_{\sigma\sigma'}$$

$$\langle \hat{\psi}_{i\sigma}^\dagger(\vec{k} + \vec{K}_+)\hat{\psi}_{j\sigma'}(\vec{k})\rangle = \frac{\Delta_{xy}^1}{\sqrt{3}}(\omega^2 - \omega)\underline{\tau}_{ij}\delta_{\sigma\sigma'}, \tag{9.148}$$

and for the E_1 doublet

$$\langle \hat{\psi}_{i\sigma}^\dagger(\vec{k} + \vec{K}_+)\hat{\psi}_{j\sigma'}(\vec{k})\rangle = \frac{\Delta_{xz}^2}{3}(-2 + \omega + \omega^2)[\underline{\tau}\tau^3]_{ij}\delta_{\sigma\sigma'}$$

$$\langle \hat{\psi}_{i\sigma}^\dagger(\vec{k} + \vec{K}_+)\hat{\psi}_{j\sigma'}(\vec{k})\rangle = \frac{\Delta_{yz}^2}{\sqrt{3}}(\omega^2 - \omega)[\underline{\tau}\tau^3]_{ij}\delta_{\sigma\sigma'}. \tag{9.149}$$

Note that $\langle \hat{\psi}_{i\sigma}^\dagger(\vec{k} + \vec{K}_+)\hat{\psi}_{j\sigma'}(\vec{k})\rangle^* = \langle \hat{\psi}_{j\sigma}^\dagger(\vec{k} + \vec{K}_-)\hat{\psi}_{i\sigma'}(\vec{k})\rangle$. Here the matrix $\underline{\tau}$ accounts for the fact that threefold rotations do not preserve the honeycomb unit cell and is given by

$$\underline{\tau} = \begin{bmatrix} 1 & \\ & \omega \end{bmatrix}. \tag{9.150}$$

One observes that in momentum space the d-wave nature of these doublets is reflected in the combinations of phases $(-2 + \omega + \omega^2)/3$ and $(\omega - \omega^2)/\sqrt{3}$. They are easily seen to be equal to $(-2 + \omega + \omega^2)/3 = -1$ and $(\omega - \omega^2)/\sqrt{3} = i$. Based on this it is also straightforward to see that the symmetric combination $\cos a + \cos b + \cos c \to 1 + \omega + \omega^2$ vanishes. This is not surprising as the symmetric combination, combined with either τ^0 or τ^3 would transform as a $1D$ representation and there are no such translational symmetry broken states, as we learned from (9.131). Before we proceed to bond order, we note that

$$(-2\cos a + \cos b + \cos c)/3 \sim \cos(\vec{K} \cdot \vec{x})$$

$$(\cos b - \cos c)/\sqrt{3} \sim \sin(\vec{K} \cdot \vec{x}), \tag{9.151}$$

which relates the density wave states derived here purely on symmetry grounds to CDWs discussed in the context of graphene [180]. These CDWs were shown to

(a) E_2' (B_2)

(b) E_2' (A_2)

(c) E_1' (A_1)

(d) E_1' (B_1)
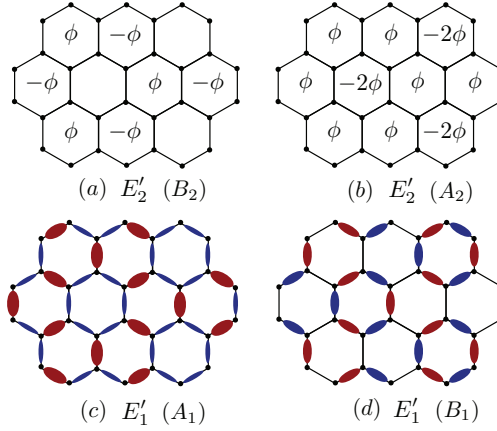
Figure 9.5: Graphical representation of some density wave orders on the honeycomb lattice. (a)-(b) denote the flux states which are partners of the E_2' doublet, while (c)-(d) denote the bond ordered states transforming as E_1', which are nothing but the two linearly independent Kekule distortions known to gap out the honeycomb Dirac fermions.

correspond to non-Abelian gauge fields in the low-energy theory of graphene, which we will comment on more extensively below. In addition, this reduction shows that starting with a cosine in equation (9.146) did not constitute a loss of generality.

After having exhaustively discussed and classified site order based on symmetry, we move on to translational symmetry broken bond order. It makes sense to explicitly distinguish nearest-neighbor and next-nearest neighbor bond order and we choose to focus mainly on the former. In fact, the decomposition of bond order states in equation (9.133) refers to nearest neighbor bond order exclusively. The translational symmetry broken content of the decomposition is $E_1' \oplus G'$, which may be decomposed further into $A_1 \oplus B_1 \oplus E_1 \oplus E_2$ in terms of representations of C_{6v}. In the following we identify the states corresponding to these representations and we will see that they are actually very familiar states.

We start with some general relations which hold for any hexagonal symmetry system with sublattices. A general bond order state is specified by the expectation value

$$\langle \hat{\psi}_{i\sigma}^{\dagger}(\vec{k} + \vec{K}_{\pm}) \hat{\psi}_{j\sigma'}(\vec{k}) \rangle = [\hat{\Delta}_{\pm}(\vec{k})]_{ij}, \tag{9.152}$$

where $\hat{\Delta}_{\pm}(\vec{k})$ is a matrix valued function in sublattice space. Using the properties of

the $\vec{K}_\pm$ one can deduce the following relations

$$\langle \hat{\psi}_{i\sigma}^\dagger(\vec{k})\hat{\psi}_{j\sigma'}(\vec{k}+\vec{K}_\pm)\rangle = [\hat{\Delta}_\pm(\vec{k})]_{ij}^\dagger$$
$$\langle \hat{\psi}_{i\sigma}^\dagger(\vec{k})\hat{\psi}_{j\sigma'}(\vec{k}+\vec{K}_\mp)\rangle = [\hat{\Delta}_\pm(\vec{k}+\vec{K}_\mp)]_{ij}$$
$$\langle \hat{\psi}_{i\sigma}^\dagger(\vec{k}+\vec{K}_\mp)\hat{\psi}_{j\sigma'}(\vec{k})\rangle = [\hat{\Delta}_\pm(\vec{k}+\vec{K}_\mp))]_{ij}^\dagger$$
$$\langle \hat{\psi}_{i\sigma}^\dagger(\vec{k}+\vec{K}_\mp)\hat{\psi}_{j\sigma'}(\vec{k}+\vec{K}_\pm)\rangle = [\hat{\Delta}_\pm(\vec{k}+\vec{K}_\pm)]_{ij}$$
$$\langle \hat{\psi}_{i\sigma}^\dagger(\vec{k}+\vec{K}_\pm)\hat{\psi}_{j\sigma'}(\vec{k}+\vec{K}_\mp)\rangle = [\hat{\Delta}_\pm(\vec{k}+\vec{K}_\pm)]_{ij}^\dagger \tag{9.153}$$

In particular, these constraints imply for the honeycomb lattice that bond order is fully determined by $[\hat{\Delta}_\pm(\vec{k})]_{AB} = \Delta_\pm(\vec{k})$ and we only need to specify these two functions to distinguish different condensates. In addition, time-reversal invariance imposes the constraint $\Delta_-(\vec{k}) = (\Delta_+(-\vec{k}))^*$ on the condensate functions. As long as this constraint is satisfied the density wave states will be part of the decomposition in (9.133).

We first look at the states corresponding to the E_1' doublet. The two partners of this doublet are contained in the functions

$$\Delta_+(\vec{k}) = \Delta_{E_1'}\omega^2(e^{-i\vec{k}\cdot\vec{\delta}_1} + \omega^2 e^{-i\vec{k}\cdot\vec{\delta}_2} + \omega e^{-i\vec{k}\cdot\vec{\delta}_3})e^{i\varphi(\vec{k})},$$
$$\Delta_-(\vec{k}) = \Delta_{E_1'}^*\omega(e^{-i\vec{k}\cdot\vec{\delta}_1} + \omega e^{-i\vec{k}\cdot\vec{\delta}_2} + \omega^2 e^{-i\vec{k}\cdot\vec{\delta}_3})e^{i\varphi(\vec{k})}. \tag{9.154}$$

The order parameter $\Delta_{E_1'}$ is complex and the two partners of the doublet are given by the real and imaginary parts of the order parameter $\Delta_{E_1'}$. We find in addition that the real and imaginary parts are precisely the states transforming as A_1 and B_1 of the group C_{6v}. What is the interpretation of these states? They are actually very familiar bond ordered states on the honeycombl lattice, as they are nothing else than the Kekule distortions of the hopping texture [197]. This is not very hard to believe, as the Kekule pattern is known to be tied to a tripling of the unit cell, and by inspecting a typical Kekule bond modulation it is easy to identify it as a state that is even under all rotatations and reflections (for properly chosen origin), therefore transforming as A_1. In graphene, the hallmark condensed matter example of a honeycomb lattice, the Kekule modulations have been discussed as perturbations generating a mass for the low-energy Dirac fermions. We will come back to the low-energy description of this E_1' doublet from the perspective of symmetry.

Before we take a closer look at the precise structure of the E_1' doublet functions, we show that the time-reversal breaking doublet E_2' which is part of the flux state decomposition of equation (9.135), is easily obtained by using the time-reversal odd-ness condition $\Delta_-(\vec{k}) = -(\Delta_+(-\vec{k}))^*$. Indeed, the E_2' flux doublet is simply given

by

$$\Delta_+(\vec{k}) = \Delta_{E_2'}\omega^2(e^{-i\vec{k}\cdot\vec{\delta}_1} + \omega^2 e^{-i\vec{k}\cdot\vec{\delta}_2} + \omega e^{-i\vec{k}\cdot\vec{\delta}_3})e^{i\varphi(\vec{k})},$$
$$\Delta_-(\vec{k}) = -\Delta_{E_2'}^*\omega(e^{-i\vec{k}\cdot\vec{\delta}_1} + \omega e^{-i\vec{k}\cdot\vec{\delta}_2} + \omega^2 e^{-i\vec{k}\cdot\vec{\delta}_3})e^{i\varphi(\vec{k})}. \tag{9.155}$$

While not as widely known as the Kekule distortion, these states have been discussed as time-reversal symmetry broken states with nontrivial topological characteristics emerging as mean-field solutions of an interacting honeycomb lattice model away from half filling [185, 198]. Based on the symmetry classification presented here it is now straightforward to see why one of these states permits additional topological quantum numbers. As we had noted in the beginning of this section, the flux doublet E_2' is further decomposed in terms of the rotational and reflection elements as $E_2' = A_2 \oplus B_2$. Hence only one of these flux states breaks all reflections allowing for nontrivial topological Fermi surface properties [177]. In particular, if such a state would induce gaps in the spectrum, the Chern number may be nonzero. The spectral effects of all density waves constructed from K-point momenta will be discussed in more detail in Section 9.4.1, but here we already disclose that the A_2 state is not gapped, making the Chern number a meaningless quantity. However, one may still calculate the off-diagonal (Hall) conductivity and find that it is nonzero in case of the A_2 state [185], but not quantized. Any unbroken reflection would necessarily imply vanishing Hall conductivity.

In the introductory part of this section, where we showed which irreducible representations are contained in the site, bond and flux order representations for a given type of translational symmetry breaking, we had identified one state which may have quantized electric polarization. This is the B_1 bond order state coming from the E_1' doublet. The mean field spectrum of this state is in fact gapped, as it is one of the Kekule partners. However, a simple argument shows that evaluating equation (9.40) must yield a trivial result for the appropriate filling (half filling). As the B_1 state belongs to the doublet E_1' with the A_1 state as its partner, it is possible to adiabatically deform one state into th other without closing the energy gap, indeed a known property of the two Kekule distortions. Hence, the B_1 state must have the same topological characteristics as the A_1 state.

Before we continue and look at density wave states at M-point wave vectors, we make three comments. The first comment concerns the bond order doublets. From the general decompostion of K-point bond order in equation (9.133), it is clear that in addition to the aforementioned translational symmetry broken doublet E_1', there is a collection of states transforming as $G' = E_1 \oplus E_2$. These are easily constructed from the functions of the Kekule modulations, by just taking the usual d-wave and combinations, $(x^2 - y^2, xy)$ and (xz, yz). For instance, the E_2 condensates are given

by

$$\Delta_+^{x^2-y^2}(\vec{k}) = \Delta_{x^2-y^2}\frac{\omega^2}{\sqrt{3}}(-2e^{-i\vec{k}\cdot\vec{\delta}_1} + \omega^2 e^{-i\vec{k}\cdot\vec{\delta}_2} + \omega e^{-i\vec{k}\cdot\vec{\delta}_3})e^{i\varphi(\vec{k})},$$

$$\Delta_+^{xy}(\vec{k}) = \Delta_{xy}\omega^2(\omega^2 e^{-i\vec{k}\cdot\vec{\delta}_2} - \omega e^{-i\vec{k}\cdot\vec{\delta}_3})e^{i\varphi(\vec{k})} \tag{9.156}$$

where $(\Delta_{x^2-y^2}, \Delta_{xy})$ are both real in this case, and $\Delta_-(\vec{k})$ is given by the time-reversal invariance condition. d-wave doublets that break time-reversal invariance do not need to be considered as they cannot give any new state. This immediately follows from equation (9.135), which states that the only distinct flux states are A_2 and E_2', which we have already identified.

The second comment we wish to add concerns the precise structure of the translational symmetry broken condensate functions. Sticking to the Kekule bond order functions given in equation (9.154), and rearranging terms by working out the complex factors ω and ω^2, we can write $\Delta_\pm(\vec{k})$ (for the Re $\Delta_{E_1'}$ state) as

$$\Delta_+(\vec{k}) \sim [-\lambda_1^{(1,E_2)*}(\vec{k}) - i\lambda_2^{(1,E_2)*}(\vec{k})],$$

$$\Delta_-(\vec{k}) \sim [-\lambda_1^{(1,E_2)*}(\vec{k}) + i\lambda_2^{(1,E_2)*}(\vec{k})] \tag{9.157}$$

This rearrangement shows that the E_1' condensates are specific linear combinations of the doublet orbital functions $\vec{\lambda}^{(1,E_2)}$, which are explicitly given in Appendix A. In light of the earlier discussion of charge order, we can go one step further and present the coefficients of the terms in a more suggestive form. It was shown that $-1 = (-2+\omega+\omega)/3$ and $i = (\omega - \omega^2)/\sqrt{3}$, which we may collect in a vector $\vec{d}^{E_2}$. In this way we can write the functions $\Delta_\pm(\vec{k})$ as

$$\Delta_+(\vec{k}) \sim [\vec{d}^{E_2} \cdot \vec{\lambda}^{(1,E_2)}(\vec{k})]^*,$$

$$\Delta_-(\vec{k}) \sim \vec{d}^{E_2} \cdot \vec{\lambda}^{(1,E_2)}(-\vec{k}). \tag{9.158}$$

Written in this way, the nature of these condensates as basis functions which transform as A_1 and B_1 under operations of the group C_{6v} is most apparent. For instance, simple inner products of vectors transforming as E_2 will be functions transforming as A_1. In general, taking inner products as $\vec{d}^{E_2} \cdot M\vec{\lambda}^{(1,E_2)}$ is expected to yield functions transforming as $1D$ representations for $M = \tau^0, \tau^2$, while choosing $M = \tau^1, \tau^3$ gives the two partners of a $2D$ representation. This holds true for the case of the Kekule distortions, as $[\vec{d}^{E_2} \cdot \vec{\lambda}^{(1,E_2)}]^*$ and $[\vec{d}^{E_2} \cdot \tau^2\vec{\lambda}^{(1,E_2)}]^*$ indeed correspond to Re $\Delta_{E_1'}$ and Im $\Delta_{E_1'}$, respectively.

We therefore observe how the condensate functions are structured in terms of group theory.

Translational symmetry breaking at $\vec{Q}_\mu$

This part deals with the second set of hexagonal lattice ordering vectors leading to translational symmetry broken density waves, the M-points of the hexagonal Brillouin zone. We have shown that in case of the honeycomb lattice there are six distinct translational symmetry broken site ordered states and nine distinct bond ordered states. For site order they transform as $F_1 \oplus F_4$, which is sensible as $F_4 = B_2 \otimes F_1$. The sublattice function relevant for site order is τ^3 and it indeed transforms as B_2. In what follows we systematically derive the density-wave states transforming as these representations, where we first focus on site order and then move on to bond order. More specifically, the aim will be to derive condensate functions that transform as the representations of the bare point group C_{6v} contained in the F_i repesentations of C_{6v}'''. We anticipate this to be the most convenient basis in which to express the density wave states so as to relate their symmetry properties to spectral properties at relevant densities. Before we start with site order however, it is helpful to go through some generalities of ordered states with modulation vectors $\vec{Q}_\mu$, i.e. the M-point vectors. This general setting will allow to derive the symmetric states in a straightforward way.

To express the most general real space modulations given a certain set of wave vectors $\vec{Q}_\mu$ one needs the linearly independent functions $\cos(\vec{Q}_\mu \cdot \vec{x})$ and $\sin(\vec{Q}_\mu \cdot \vec{x})$. In the case of M-point vectors the functions $\sin(\vec{Q}_\mu \cdot \vec{x})$ are identically zero, as $2\vec{Q}_\mu = 0$ which leaves only two possible values for the inner products $\vec{Q}_\mu \cdot \vec{x} = 0, \pi$. Hence one only requires the cosine functions, which incidentally is consistent with the unit cell quadrupling. The three functions $\cos(\vec{Q}_\mu \cdot \vec{x})$ may be conveniently collected in a vector $\vec{\xi}(\vec{x})$ as $\xi_\mu = \xi_\mu(\vec{x}) = \cos(\vec{Q}_\mu \cdot \vec{x})$. We stress here that this pertains to all lattices with hexagonal symmetry. Even more, one can now deduce the effect of space group operations on the vector $\vec{\xi}$ and exploit this later. Translations for instance are given by $\xi_\mu(\vec{x} + \vec{x}_j)$, which is easily seen to reduce to $\xi_\mu(\vec{x} + \vec{x}_j) = [G_j]_{\mu\nu}\xi_\nu(\vec{x})$, where G_j is some matrix depending on j and summation over repeated indices is implied. We define and find that

$$
\begin{aligned}
\vec{\xi}(\vec{x} + \vec{x}_1) &= G_1\vec{\xi}(\vec{x}) = \begin{bmatrix} -1 & & \\ & -1 & \\ & & 1 \end{bmatrix} \vec{\xi}, \\
\vec{\xi}(\vec{x} + \vec{x}_2) &= G_2\vec{\xi}(\vec{x}) = \begin{bmatrix} 1 & & \\ & -1 & \\ & & -1 \end{bmatrix} \vec{\xi}, \\
\vec{\xi}(\vec{x} + \vec{x}_1 + \vec{x}_2) &= G_3\vec{\xi}(\vec{x}) = G_1 G_2 \vec{\xi}
\end{aligned}
\tag{9.159}
$$

All G_j commute, square to one, and multiplying two of them gives the third.

With regard to point group operations, any point group element may be uniquely written in terms of two generators, i.e. $C_6^{m_2}\sigma_v^{m_1}$. We thus need the action of the generators on $\vec{\xi}$. We first look at the rotational generator and define the matrix X to correspond to the permutation of ξ_μ as a consequence of C_6, i.e.

$$\vec{\xi}(C_6\vec{x}) = X\vec{\xi}(\vec{x}), \quad X = \begin{bmatrix} 0 & 0 & 1 \\ 1 & 0 & 0 \\ 0 & 1 & 0 \end{bmatrix} \tag{9.160}$$

Note that X has the property $X^3 = 1$ and thus $X^{-1} = X^2$. In addition the relation $X^{-1} = X^T$ holds, where X^T is the transpose. It thus follows that $\vec{\xi}(C_3\vec{x}) = X^T\vec{\xi}(\vec{x})$ and $\vec{\xi}(C_2\vec{x}) = \vec{\xi}(\vec{x})$. For the reflection σ_v we have that

$$\vec{\xi}(\sigma_v\vec{x}) = Y\vec{\xi}(\vec{x}), \quad Y = \begin{bmatrix} 0 & 0 & 1 \\ 0 & 1 & 0 \\ 1 & 0 & 0 \end{bmatrix} \tag{9.161}$$

Some useful relations between the G_j and X and Y are collected in Appendix C.2.1.

As stated, the aim for both site and bond order is to derive condensate functions based on their transformation properties under point group operations alone. In the case of site order we may start with the most general real space M-point condensate

$$\langle \hat{\psi}_{i\sigma}^\dagger(\vec{x})\hat{\psi}_{j\sigma'}(\vec{y})\rangle = \Delta\, \vec{\zeta}_i \cdot \vec{\xi}(\vec{x})\, \delta_{\vec{x},\vec{y}}\delta_{ij}\delta_{\sigma\sigma'} \tag{9.162}$$

where the two real vectors $\vec{\zeta}_A$ and $\vec{\zeta}_B$ fully specify the site ordered state, each vector giving the linear combination of ξ_μ functions on sublattice. The idea now is to derive constraints on the $\vec{\zeta}_i$ given a set of symmetries the density wave state should preserve or break. The symmetry constraints we should impose follow directly from the decomposition of F_1 and F_4 in terms of representations of C_{6v} and we simply find that $F_1 = A_1 \oplus E_2$, while $F_4 = B_2 \oplus E_1$. It is best to start with the $1D$ representations A_1 and B_2. A look at the character table of the group C_{6v}, which is given in Appendix **??**, tells us that all functions transforming as any of the four $1D$ irreducible representations must be even under the threefold rotations. It seems therefore natural to first impose this condition. The effect of a point group operation R is to act on the vectors $\vec{\zeta}_i$ with a matrix composed of the G_i, X and Y elements. In case of the threefold rotation we fond that they act as

$$\begin{aligned} C_3 &: \quad \vec{\zeta}_A \rightarrow G_2 X^T \vec{\zeta}_A \\ C_3^{-1} &: \quad \vec{\zeta}_A \rightarrow G_3 X \vec{\zeta}_A = (G_2 X^T)^2 \vec{\zeta}_A \end{aligned} \tag{9.163}$$

and similarly, the effect of the threefold rotations on $\vec{\zeta}_B$ is given by

$$C_3 \; : \quad \vec{\zeta}_B \; \rightarrow \; G_3 X^T \vec{\zeta}_B$$
$$C_3^{-1} \; : \quad \vec{\zeta}_B \; \rightarrow \; G_1 X \vec{\zeta}_B = (G_3 X^T)^2 \vec{\zeta}_B \tag{9.164}$$

From this, and the fact that $(G_2 X^T)^3 = (G_3 X^T)^3 = 1$, we conclude that the following choice will correspond to a density wave state symmtric under the threefold rotations

$$\vec{\zeta}_A \; \rightarrow \; \frac{1}{3}(1 + G_2 X^T + G_2 X^T G_2 X^T) \vec{\zeta}_A'$$
$$\vec{\zeta}_B \; \rightarrow \; \frac{1}{3}(1 + G_3 X^T + G_3 X^T G_3 X^T) \vec{\zeta}_B' \tag{9.165}$$

The three diagonal reflections do not change the sublattices either and we can look at the constraints they impose on the newly defined $\vec{\zeta}_i'$. We derive that all three reflections lead to the same constraint on each of the $\vec{\zeta}_i'$, which are given by

$$X^T Y \vec{\zeta}_A' = \vec{\zeta}_A'$$
$$G_3 Y \vec{\zeta}_B' = \vec{\zeta}_B' \tag{9.166}$$

Note that in principle we should have allowed states to be even or odd under reflections, but the two states we are after are both even under reflections and we therefore exclude the odd states. The constraints coming from these reflections already narrow the choices for $\vec{\zeta}_i'$ down. Indeed, both $X^T Y$ and $G_3 Y$ should be interpreted as elements of $SO(3)$ acting on the vectors $\vec{\zeta}_i'$, and it is certainly not surprising that both are reflections in $SO(3)$. Reflections leave a plane invariant and equation (9.166) consequently restricts the $\vec{\zeta}_i'$ to lie in precisely the invariant plane. That still leaves two independent degrees of freedom and we need further constraints to find the unique solutions corresponding to states of symmetry A_1 and B_2. Point group elements left to consider all exchange sublattice, and in case of for instance the inversion C_2, we obtain the relations

$$G_3 \vec{\zeta}_A' = \pm \vec{\zeta}_B'$$
$$G_3 \vec{\zeta}_B' = \pm \vec{\zeta}_A', \tag{9.167}$$

which may be combined to give the trivial relation $(G_3)^2 \vec{\zeta}_A' = \vec{\zeta}_A'$. Triviality follows from $(G_3)^2 = 1$. Also note that in case of inversion we need to distinguish A_1 and B_2, as the latter is odd. We find that the definitive constraint can be derived from the

sixfold rotation, which leads to

$$X\vec{\zeta}'_A = \pm\vec{\zeta}'_B$$
$$G_3\vec{\zeta}'_B = \pm\vec{\zeta}'_A. \tag{9.168}$$

These expressions can be combined to give $G_3 X\vec{\zeta}'_A = \vec{\zeta}'_A$. Again interpreting the matrix $G_3 X$ as an $SO(3)$ element, we see that it describes a rotation of the vector it acts on. In particular the constraint $G_3 X\vec{\zeta}'_A = \vec{\zeta}'_A$ means that the vector $\vec{\zeta}'_A$ is left invariant by the rotation $G_3 X$, from which it directly follows that $\vec{\zeta}'_A$ must be proportional to the axis of rotation and therefore is uniquely fixed up to a sign. The vector $\vec{\zeta}'_B$ is then immediately determined by the constraints as well. We find that the solutions for $\vec{\zeta}'_i$ are given by

$$\vec{\zeta}'_A = \frac{1}{\sqrt{3}}\begin{bmatrix} -1 \\ -1 \\ 1 \end{bmatrix}, \quad \vec{\zeta}'_B = \pm\frac{1}{\sqrt{3}}\begin{bmatrix} 1 \\ -1 \\ -1 \end{bmatrix} \tag{9.169}$$

where the overall sign (which is immaterial) has been fixed by fully specifying $\vec{\zeta}'_A$. The relative sign distinguishing between A_1 and B_2 is incorporated in $\vec{\zeta}'_B$, consistent with the sublattice function τ^3. At this point we should remember that the condensate functions were formulated in terms of $\vec{\zeta}_i$ and we should use equation (9.165) to obtain these vectors. We find that the $\vec{\zeta}_i$ are exactly equal to the $\vec{\zeta}'_i$, i.e. $\vec{\zeta}_i = \vec{\zeta}'_i$. One way to explain this seemingly surprising fact is to note that the constraints coming from the sixfold rotation C_6 are the same for both $\vec{\zeta}_i$ and $\vec{\zeta}'_i$. Since these constraints, expressed in equation (9.168), are strong enough to uniquely fix both $\vec{\zeta}_i$ and $\vec{\zeta}'_i$, we conclude that they must be the same. At the same time this raises the question why one would consider the constraints coming from C_3, or σ_d, in the first place. The reason is that considering the action of C_3 yields the building blocks for constructing the doublets contained in F_1 and F_4, as will be demonstrated just below.

First we write down the condensate functions in momentum space now that we have found the $\vec{\zeta}_i$. Based on the above they can simply be expressed as

$$\langle\hat{\psi}^\dagger_{i\sigma}(\vec{k}+\vec{Q}_\mu)\hat{\psi}_{j\sigma'}(\vec{k})\rangle = \frac{1}{\sqrt{3}}\Delta^{F_1}_{A_1}\zeta^\mu_i\delta_{ij}\delta_{\sigma\sigma'}$$
$$\langle\hat{\psi}^\dagger_{i\sigma}(\vec{k}+\vec{Q}_\mu)\hat{\psi}_{j\sigma'}(\vec{k})\rangle = \frac{1}{\sqrt{3}}\Delta^{F_4}_{B_2}\zeta^\mu_i\tau^3_{ij}\delta_{\sigma\sigma'} \tag{9.170}$$

Before we come to the specific expressions of the doublets, we take an alternative look at the way to derive the $\vec{\zeta}'_i$ and in particular why it is helpful to define the $\vec{\zeta}'_i$ with equation (9.165). By looking at the action of the threefold rotation we identified

three objects transforming into each other under threefold rotations. Forming the symmetric combination for each of the sublattices led to equation (9.165). Taking the A sublattice as an example we can define the matrix of the symmetric combination as P, i.e. $P = (1 + G_2X^T + G_2X^TG_2X^T)/3$. Then we find that $P^2 = P$ and therefore P is a projector having two possible eigenvalues, 0 and 1. It follows that a nontrivial (zero) solution for $\vec{\zeta}_i'$ must belong to the subspace mapped to 1, while it simultaneously shows that necessarily $\vec{\zeta}_i = \vec{\zeta}_i'$. This subspace is found to be spanned specisely by $\vec{\zeta}_A'$ given in equation (9.169), while an exactly analogous calculations confirms that for the B sublattice the nontrivial subspace is spanned by $\vec{\zeta}_B'$ given in equation (9.169). The kernel of P (for the A-sublattice), i.e. the subspace mapped to 0, is found to be spanned by

$$\left\{ \frac{1}{\sqrt{2}} \begin{bmatrix} 1 \\ -1 \\ 0 \end{bmatrix}, \frac{1}{\sqrt{6}} \begin{bmatrix} 1 \\ 1 \\ 2 \end{bmatrix} \right\}, \tag{9.171}$$

which corroborates that there are no more site ordered states corresponding to $1D$ representations of C_{6v}.

The doublets contained in F_1 and F_2 can be simply obtained by first defining a triple of vectors for each sublattice which transform into each other under the three-fold rotations. Per the above they are given by

$$\vec{\zeta}_{Aa} = \frac{1}{3}(G_2X^T)^a\vec{\zeta}_A', \quad \vec{\zeta}_{Ba} = \frac{1}{3}(G_3X^T)^a\vec{\zeta}_B', \tag{9.172}$$

where $a = 1, 2, 3$. It is crucial to note that the $\vec{\zeta}_i'$ here are *different* from the ones just found for the $1D$ representations. The task here is to find the proper $\vec{\zeta}_i'$ consistent with d-wave and/or p-wave symmetry doublets E_2 and E_1. For each sublattice we expect doublet functions of the form $x^2 - y^2 \sim (\zeta_{i1}^a + \zeta_{i2}^a - 2\zeta_{i3}^a)/\sqrt{3}$ and $xy \sim \zeta_{i1}^a - \zeta_{i2}^a$. In order to find the proper $\vec{\zeta}_i'$ we define the matrices

$$P_{x^2-y^2} = \frac{1}{3}(-2 + G_2X^T + G_2X^TG_2X^T)$$

$$P_{xy} = \frac{1}{3}(G_2X^T - G_2X^TG_2X^T) \tag{9.173}$$

and similarly for B of course. For these objects we derive the relations $P_{x^2-y^2}^2 = -P_{x^2-y^2}$ and $P_{xy}^2 = P_{x^2-y^2}$, where the latter leads additionally to $P_{xy}^4 = -P_{x^2-y^2}$. The property $P_{x^2-y^2}^2 = -P_{x^2-y^2}$ implies that $P_{x^2-y^2}$ is also a projector of some form, having eigenvalues -1 and 0. Examining the kernel of the linear mapping $P_{x^2-y^2}$ and the subspace corresponding to eigenvalue -1, we find that the vector

$[-1, -1, 1]^T/\sqrt{3}$ now spans the kernel, while the subspace given in Eq. (9.171) is the eigenspace corresponding to eigenvalue -1. This provides two indepedent vectors that are valid choices for $\vec{\zeta}'_A$. Repeating the same calculation for the B-sublattice we find that the vector $[1, -1, -1]^T/\sqrt{3}$ is in the kernel of $P_{x^2-y^2}$, while the subspace

$$\left\{ \frac{1}{\sqrt{2}} \begin{bmatrix} 1 \\ 1 \\ 0 \end{bmatrix}, \frac{1}{\sqrt{6}} \begin{bmatrix} -1 \\ 1 \\ -2 \end{bmatrix} \right\}, \tag{9.174}$$

constitutes the -1 eigenspace. The relation between $\vec{\zeta}'_A$ and $\vec{\zeta}'_B$ is then fixed by considering the inversion C_2. As found earlier we have $G_3 \vec{\zeta}'_A = \pm \vec{\zeta}'_B$. Hence, if we fix

$$\vec{\zeta}'_A = \frac{1}{\sqrt{2}} \begin{bmatrix} 1 \\ -1 \\ 0 \end{bmatrix}, \quad \vec{\zeta}'_B = \frac{1}{\sqrt{2}} \begin{bmatrix} -1 \\ -1 \\ 0 \end{bmatrix} \tag{9.175}$$

we can incorporate the sublattice sign difference by using τ^3. Note that we could have chosen the other vector, i.e. $[1, 1, 2]^T/\sqrt{6}$ and correspondingly for B, but as it turns out this does not generate anything new.

We are now in a position to write down the expressions for two doublets, one of which transforms as E_2 in F_1 and the other as E_1 in F_4. The former doublet reads

$$\langle \hat{\psi}^\dagger_{i\sigma}(\vec{k} + \vec{Q}_\mu) \hat{\psi}_{j\sigma'}(\vec{k}) \rangle = \frac{1}{\sqrt{3}} \Delta_{x^2-y^2} (\zeta^\mu_{i1} + \zeta^\mu_{i2} - 2\zeta^\mu_{i3}) \delta_{ij} \delta_{\sigma\sigma'}$$

$$\langle \hat{\psi}^\dagger_{i\sigma}(\vec{k} + \vec{Q}_\mu) \hat{\psi}_{j\sigma'}(\vec{k}) \rangle = \frac{1}{\sqrt{3}} \Delta_{xy} (\zeta^\mu_{i1} - \zeta^\mu_{i2}) \delta_{ij} \delta_{\sigma\sigma'}, \tag{9.176}$$

whereas the latter takes the form

$$\langle \hat{\psi}^\dagger_{i\sigma}(\vec{k} + \vec{Q}_\mu) \hat{\psi}_{j\sigma'}(\vec{k}) \rangle = \frac{1}{\sqrt{3}} \Delta_{xz} (2\zeta^\mu_{i3} - \zeta^\mu_{i1} - \zeta^\mu_{i2}) \tau^3_{ij} \delta_{\sigma\sigma'}$$

$$\langle \hat{\psi}^\dagger_{i\sigma}(\vec{k} + \vec{Q}_\mu) \hat{\psi}_{j\sigma'}(\vec{k}) \rangle = \frac{1}{\sqrt{3}} \Delta_{yz} (\zeta^\mu_{i1} - \zeta^\mu_{i2}) \tau^3_{ij} \delta_{\sigma\sigma'} \tag{9.177}$$

A similar approach leads to the construction of symmetric bond density wave order. Again the explicit derivation is most conveniently carried out in real space. We expect translational symmetry broken states transforming as $F_1 \oplus F_3 \oplus F_4$, and proceeding as before to express them in a basis consistent with the decompositions in terms of C_{6v}, we set out to find basis functions of $A_1 \oplus B_1 \oplus B_2 \oplus 2E_1 \oplus E_2$.
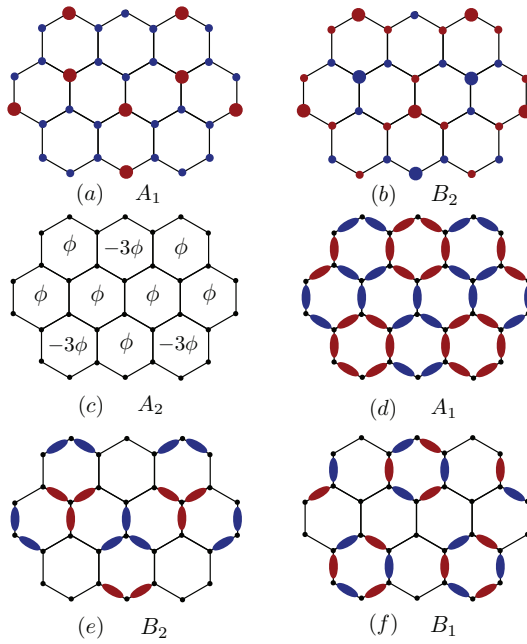
Figure 9.6: Site, bond and flux ordered density wave states on the honeycomb lattice with M-point vector modulations. (a), (b) Site ordered states with A_1 and B_2 symmetry. (c) Flux ordered state with A_2 symmetry. (d)-(f) Bond ordered states with A_1, B_2 and B_1 symmetry, coming from F_1, F_4 and F_3, respectively.

The starting point are bond order condensate functions parametrized by $\vec{\zeta}_i$ with $i = 1, 2, 3$,

$$
\begin{aligned}
\langle \hat{\psi}_{A\sigma}^\dagger(\vec{x}) \hat{\psi}_{B\sigma'}(\vec{y}) \rangle &= \Lambda + \Delta \, \vec{\zeta}_1 \cdot \vec{\xi}(\vec{x}) \, \delta_{\vec{x},\vec{y}} \delta_{\sigma\sigma'} \\
\langle \hat{\psi}_{A\sigma}^\dagger(\vec{x}) \hat{\psi}_{B\sigma'}(\vec{y}) \rangle &= \Lambda + \Delta \, \vec{\zeta}_2 \cdot \vec{\xi}(\vec{x}) \, \delta_{\vec{x}-\vec{x}_1,\vec{y}} \delta_{\sigma\sigma'} \\
\langle \hat{\psi}_{A\sigma}^\dagger(\vec{x}) \hat{\psi}_{B\sigma'}(\vec{y}) \rangle &= \Lambda + \Delta \, \vec{\zeta}_3 \cdot \vec{\xi}(\vec{x}) \, \delta_{\vec{x}+\vec{x}_2,\vec{y}} \delta_{\sigma\sigma'}.
\end{aligned}
\tag{9.178}
$$

The action of point group operations provides us with constraints on the $\vec{\zeta}_i$, which we summarize here more concisely than in the case of site order. The threefold rotations give relations $\vec{\zeta}_2 = G_2 X^T \vec{\zeta}_1$ and $\vec{\zeta}_3 = (G_2 X^T)^2 \vec{\zeta}_1$. The sixfold rotations give the relations $G_2 X \vec{\zeta}_1 = \pm \vec{\zeta}_3 = \pm (G_2 X^T)^2 \vec{\zeta}_1$ and $X^T \vec{\zeta}_1 = \pm \vec{\zeta}_2 = \pm G_2 X^T \vec{\zeta}_1$. Both lead to the same constraint $G_3 \vec{\zeta}_1 = \pm \vec{\zeta}_1$. The diagonal reflections all impose the constraint $G_3 Y \vec{\zeta}_1 = \pm \vec{\zeta}_1$, while the vertical reflections impose the constraint $Y \vec{\zeta}_1 = \pm \vec{\zeta}_1$. All these constraints can be solved to obtain solutions for $\vec{\zeta}_1 = \vec{\zeta}$, for which we may as well drop the index, since there is only one to consider. The equation $G_3 \vec{\zeta} = \vec{\zeta}$ gives the immediate and unique solution

$$
\vec{\zeta} = \begin{bmatrix} 0 \\ 1 \\ 0 \end{bmatrix},
\tag{9.179}
$$

and it is a simple matter to check that this state transforms as A_1 by evaluating the other constraints. The equation $G_3 \vec{\zeta} = -\vec{\zeta}$ on the other hand, admits a solution of the form $\vec{\zeta} = [\zeta_1, 0, \zeta_3]^T$. The constraints of the reflections lead to the relations $\zeta_1 = \pm \zeta_3$, or in other words

$$
\vec{\zeta} = \frac{1}{\sqrt{2}} \begin{bmatrix} 1 \\ 0 \\ \pm 1 \end{bmatrix}.
\tag{9.180}
$$

Evaluating the constraints it is straightforward to check that the solution with $+1$ corresponds to the B_1 representation, while the -1 solution corresponds to the B_2 representation.

In momentum space the condensate functions are generically expressed as

$$
\langle \hat{\psi}_{i\sigma}^\dagger(\vec{k} + \vec{Q}_\mu) \hat{\psi}_{j\sigma'}(\vec{k}) \rangle = [\hat{\Delta}_\mu(\vec{k})]_{ij},
\tag{9.181}
$$

where the $\hat{\Delta}_\mu(\vec{k})$ should be read as a matrix in sublattice space. Using the properties of the ordering momenta $\vec{Q}_\mu$ we establish the relations

$$
\begin{aligned}
\langle \hat{\psi}_{i\sigma}^\dagger(\vec{k}) \hat{\psi}_{j\sigma'}(\vec{k} + \vec{Q}_\mu) \rangle &= [\hat{\Delta}_\mu(\vec{k})]_{ij}^\dagger \\
\langle \hat{\psi}_{i\sigma}^\dagger(\vec{k}) \hat{\psi}_{j\sigma'}(\vec{k} + \vec{Q}_\mu) \rangle &= [\hat{\Delta}_\mu(\vec{k} + \vec{Q}_\mu)]_{ij},
\end{aligned}
\tag{9.182}
$$

and, in addition we easily find that

$$\langle \hat{\psi}_{i\sigma}^{\dagger}(\vec{k} + \vec{Q}_{\gamma})\hat{\psi}_{j\sigma'}(\vec{k} + \vec{Q}_{\nu})\rangle = [\hat{\Delta}_{\mu}(\vec{k} + \vec{Q}_{\nu})]_{ij}, \qquad (9.183)$$

where $\mu \neq \nu \neq \gamma$. These relations fully fix the bond order density-wave state in terms of the four matrices $\hat{\Delta}_{\mu}(\vec{k})$. These matrices are however not independent, which follows directly from $\langle \hat{\psi}_{i\sigma}^{\dagger}(\vec{k} + \vec{Q}_{\mu})\hat{\psi}_{j\sigma'}(\vec{k})\rangle = [\hat{\Delta}_{\mu}(\vec{k} + \vec{Q}_{\mu})]_{ij}^{\dagger}$. Bond ordered states on the honeycomb lattice are therefore specified completely by the four complex functions $[\hat{\Delta}_{\mu}(\vec{k})]_{AB} = \Delta_{\mu}(\vec{k})$.

In order to write down explicit condensate functions, we recall that we defined

$$\vec{\zeta}_a = (G_2 X^T)^a \vec{\zeta}, \qquad (9.184)$$

where the label a corresponds to one of the three elementary bonds, and per the above we have three independent choices for $\vec{\zeta}$, one for each of the states transforming as $1D$ representations. The bond density waves corresponding to A_1, B_1 and B_2 are then simply obtained by substituting the appropriate $\vec{\zeta}$ of equations (9.179)-(9.180) into (9.184) first and then write

$$\Delta_{\mu}(\vec{k}) = (\zeta_1^{\mu} e^{-i\delta_1 \cdot \vec{k}} + \zeta_2^{\mu} e^{-i\delta_2 \cdot \vec{k}} + \zeta_3^{\mu} e^{-i\delta_3 \cdot \vec{k}})e^{i\varphi(\vec{k})}. \qquad (9.185)$$

The doublets are simply obtained by forming d-wave type combinations $\sim \zeta_1 + \zeta_2 - 2\zeta_3$ and $\sim \zeta_1 - \zeta_2$. This then completes the description of the condensate functions encoding bond order coming from the decomposition (9.134).

This brings us to the final case of honeycomb lattice M-point order we discuss here, which is the flux ordered state contained in the flux decomposition of equation (9.136) and transforming as A_2. The good news is that we already went through quite some effort when deriving symmetric bond ordered states and an explicit expression for the A_2 flux ordered state is almost directly obtained by making the condensate function of equation (9.185) imaginary. We thus write

$$\Delta_{\mu}(\vec{k}) = i(\zeta_1^{\mu} e^{-i\delta_1 \cdot \vec{k}} + \zeta_2^{\mu} e^{-i\delta_2 \cdot \vec{k}} + \zeta_3^{\mu} e^{-i\delta_3 \cdot \vec{k}})e^{i\varphi(\vec{k})}, \qquad (9.186)$$

and the only task left is to check which one of the three choices for $\vec{\zeta}$ given in equations (9.179)-(9.180) yields a state with nonzero flux. As there is no other flux ordered state transforming as a $1D$ representation according to equation (9.136), we know that two of the three choices for $\vec{\zeta}$ correspond to a state which is gauge-equivalent to a bond ordered state already obtained. Checking symmetries we find that $\vec{\zeta} = (1, 0, 1)^T$ generates the A_2 symmetric state when substituted into equation (9.184) and (9.186). In the introductory part of this honeycomb lattice section we have argued that the A_2 flux ordered state is symmetry-compatible QAH effect. Now that we have an explicit expression of this density wave state, we can analyze the mean field spectrum

and find out whether it does indeed host a QAH effect. The first point to address is the insulating nature of the ground state. We find that the presence of the density wave does indeed open up a full spectral gap, thus making the ground state insulating. The second question is whether or not the Chern number, which characterizes the topological nature of the insulating state, is nonzero. To this end we simply employ formula (9.35) to conclude that the insulating ground state is indeed a Chern insulator. This is an interesting result, as it demonstrates that a Chern insulator on the honeycomb lattice can in principle be realized with purely nearest neighbor hoppings, modulated by M-point ordering vectors. On top of that, the exposition of M-point order on the kagome and triangular lattices following below will highlight that such a Chern insulating is not a peculiarity of the honeycomb lattice, but exists for all lattices with hexagonal symmetry. Finally, in Section 10 we will explain in detail how these flux ordered states on various lattices transforming as A_2 have very interesting spinful generalizations, such as for instance QSH states.

As this flux ordered state is of wider interest than just the honeycomb lattice or its concomitant Quantum Anomalous Hall effect, we take a closer look at the functions $\Delta_\mu(\vec{k})$ of equation (9.186). Substituting the $\vec{\zeta}_a$ one finds

$$
\begin{aligned}
\Delta_1(\vec{k}) &= i(e^{-i\delta_1 \cdot \vec{k}} - e^{-i\delta_3 \cdot \vec{k}})e^{i\varphi(\vec{k})}/\sqrt{2}, \\
\Delta_2(\vec{k}) &= i(e^{-i\delta_3 \cdot \vec{k}} - e^{-i\delta_2 \cdot \vec{k}})e^{i\varphi(\vec{k})}/\sqrt{2}, \\
\Delta_3(\vec{k}) &= i(e^{-i\delta_1 \cdot \vec{k}} - e^{-i\delta_2 \cdot \vec{k}})e^{i\varphi(\vec{k})}/\sqrt{2}.
\end{aligned}
\tag{9.187}
$$

Inspecting the structure of these condensate functions, we see that they have the form of a d-wave function. The two particular exponentials appearing for each of the $\vec{Q}_\mu$ are the ones which get mapped onto each other by the reflections leaving the respective $\vec{Q}_\mu$ invariant. The relative sign difference ensures relfection symmetry breaking. We therefore note for future reference, that for each $\vec{Q}_\mu$, the condensate functions ($\Delta_\mu(\vec{k})$ in this case) should tranform as representations of C_{2v}. This is the complementary momentum space view on constructing density wave states with specific symmetry, which we will come back to in Section 9.4.3 as well.

To conclude this section on the honeycomb lattice we address the remaining open question regarding topological quantum numbers associated to M-point ordered states. In the beginning of this honeycomb lattice section we had identified two candidate states with C_3 symmetry to have quantized electric polarization. Both states have B_2 symmetry and derive from F_4 representations. One is the site order state of equation (9.170) and the other is a bond order state, which is obtained from equation (9.185) by substituting the proper $\vec{\zeta}_i$. The B_2 site ordered state is found not to be gapped, but instead to have an isolated, albeit accidental, degeneracy. The B_2 bond order state is gapped, however we find the ground state not to have quantized

fractional polarization according to an evaluation of equation (9.40). Hence, there are no M-point condensates with nontrivial polarization quantum numbers on the honeycomb lattice.

Low-energy description: Dirac points

One of the most famous and intriguing characteristics of the honeycomb lattice, is the conic degeneracy of the electronic spectrum at the Brillouin zone vertices [76, 98, 199, 200]. In the vicinity of these degeneracies, which are located at momenta $\vec{K}_{\pm} = \pm(4\pi/3, 0)$ (see Fig. 9.4) and are often referred to as "valleys", the low-energy electronic degrees of freedom can be described by a Dirac Hamiltonian of a massless particle. Indeed, expanding the unperturbed Hamiltonian of electrons hopping on a honeycomb lattice around $\vec{K}_{\pm}$ in small momenta $\vec{q}$ one finds the low-energy Hamiltonian [199]

$$\mathcal{H}(\vec{q}) = \hbar v_F (q_x \nu^3 \tau^1 + q_y \tau^2) \tag{9.188}$$

(where $v_F = \sqrt{3}ta/(2\hbar)$) acting on the Dirac spinor $\hat{\Phi}(\vec{q})$ which is defined by

$$\hat{\Phi}(\vec{q}) = \begin{bmatrix} \hat{\psi}_A(\vec{K}_+ + \vec{q}) \\ \hat{\psi}_B(\vec{K}_+ + \vec{q}) \\ \hat{\psi}_A(\vec{K}_- + \vec{q}) \\ \hat{\psi}_B(\vec{K}_- + \vec{q}) \end{bmatrix}. \tag{9.189}$$

Here we have chosen the Pauli matrices τ^i to act on the sublattice degree of freedom, while the set of matrices ν^i acts on the valley degree of freedom. One often finds it convenient to express the Dirac Hamiltonian in a different basis, a basis which corresponds to the chiral representation of the Dirac theory. This is achieved by exchanging the A and B sublattice in one of the valleys [the matrix V of equation (9.119) implements this transformation], such as $\vec{K}_-$. In the chiral representation one then has

$$\mathcal{H}(\vec{q}) = \hbar v_F \nu^3 \vec{q} \cdot \vec{\tau}. \tag{9.190}$$

Note that other basis choices, such as the valley isotropic basis, have also found use in the literature [200].

The spectral degeneracy at the Brillouin zone vertices $\vec{K}_{\pm}$ is required by point group symmetries [76, 201, 202], as is explained and demonstrated in Appendix A. The breaking of point group symmetries, such as for instance the threefold rotation C_3, will allow the degeneracy to move away $\vec{K}_{\pm}$, or will lead to the lifting of the degeneracy and consequently the opening of a spectral gap, which is allowed when

the reflection σ_v is broken. Even in case of rotational symmetry breaking, i.e. C_3, the gapless Dirac nodes are still protected by the combination of inversion C_2 and time-reversal symmetry $\mathcal{T}$, but they are no longer required to be located a $\vec{K}_\pm$. In the langauge of [201], point group symmetries cause the degeneracies to be essential at the invariant points $\vec{K}_\pm$, while they are accidental under $\mathcal{T}C_2$.

The peculiar electronic properties of the honeycomb lattice have been known since long [199], but since the isolation of graphene [196], a single one-atom-thick layer of graphite realizing the two-dimensional honeycomb lattice structure, interest in the fundamental aspects of graphene physics has surged massively. Due to its particular low-energy electronic Dirac structure graphene has become a prime condensed matter playground to study and observe phenomena usually confined to the realm of high-energy physics. In addition, an impressive amount of research has been dedicated to the unique potential of graphene for technological application. Good reviews of graphene physics include [98, 179, 200, 203]. One of the main challenges is to make graphene semiconducting by opening a controllable spectral gap, which in the language of Dirac theory means making the low-energy electrons massive. Both from the fundamental and the applied perspective, the Dirac Hamiltonian of equation (9.190) is generally the starting point to study the electronic properties of electrons on the honeycomb lattice. What we will attempt here is, far from redisovering widely known facts about the low-energy description of honeycomb lattice electrons, to establish a connection between the symmetry properties of lattice density waves, i.e. intrinsic condensed matter phenomena, and the impact at low energies of these density waves. In doing so we adopt the same approach as for the square lattice π-flux state in Section 9.3.2. We first classify all Dirac fermion bilinears based on their transformation properties under lattice symmetries and then associate them to the site, bond and flux ordered density waves modulated by $\vec{K}$-vectors. Based on this symmetry connection, and using the results of the square lattice Dirac theory, will argue for very general statements regarding the lattice symmetry properties of density waves and their low-energy interpretation.

In case of the honeycomb lattice, the effect of the generators of the group C_{6v}''' on the Dirac spinor (9.189) can be worked out to obtain a full representation of the symmetry group. In the same way as for the square lattice these are then used to classify the fermion bilinears $\hat{\Phi}_i^\dagger M_{ij} \hat{\Phi}_j$ based on extended point group symmetry. The specifics of this can be found in the Appendix, as the technical details are not of general interest, and here we will simply draw from these results. Incidentally, a discussion of fermion fields not very dissimilar to the present one has appeared in the context of electron-phonon coupling in graphene [204, 205].

We divide the Dirac matrices and the density waves into two groups, i.e. one which collects all translationally invariant states and the other group collects the translational symmetry broken states. Starting with states that do not break translational

invariance, we find that in the chiral representation there are two mass terms, i.e. Dirac matrices which anti-commute with $\nu^3\tau^1$ and $\nu^3\tau^2$ and these are given by $\nu^3\tau^3$ and τ^3. It is shown in Appendix A.3 that $\nu^3\tau^3$ is time-reversal invariant and transforms as B_2, while τ^3 breaks time-reversal and transforms as A_2. This allows for the immediate identification of these mass matrices with density wave states. Both the site ordered state of equation (9.138) and the next nearest neighbor bond ordered state of equation (9.4.1) transform as B_2 and therefore correspond to a mass term in the low-energy theory. It is indeed a very well-known fact that making the two sublattices of graphene energetically inequivalent will open up a spectral gap. The time-reversal breaking bond density wave of equation (9.143) transforms as A_2 and thus corresponds to the mass matrix τ^3. Such a mass term was first discussed by Haldane [76] who went on to show that such a Dirac mass leads to a topologically nontrivial insulating state, providing the first example of a Quantum Hall state without external magnetic fields.

There are three more Dirac matrices which commute with the translations $T(\vec{x}_1)$ and $T(\vec{x}_1 + \vec{x}_2)$ and these are ν^3, τ^1 and τ^2. The matrix ν^3 transforms as B_1 and we can identify it with the bond ordered state of equation (9.4.1). This state preserves the reflections which leave the valleys $\vec{K}_\pm$ invariant and we therefore expect the degeneracies not to be preserved as well. It does however make the valleys inequivalent, which causes the Dirac points at $\vec{K}_+$ and $\vec{K}_-$ to be no longer degenerate.

The two Dirac matrices (τ^1, τ^2) form a doublet together, transforming as E_2. We have found the the bond order components $(\Delta_{x^2-y^2}, \Delta_{xy})$ of equation (9.4.1) to have precisely this symmetry and we therefore identify the doublet with this unit cell preserving bond order doublet. Working out the low-energy term in the low-energy mean field spectrum we find that

$$\mathcal{H}_{E_2} = -\Delta_{x^2-y^2}\tau^1 + \Delta_{xy}\nu^3\tau^2. \tag{9.191}$$

This may be rewritten slightly and combined with the free low-energy Hamiltonian of equation (9.190) to obtain

$$\mathcal{H}_0 + \mathcal{H}_{E_2} = \hbar v_F \left[\nu^3\tau^1(q_x - A_{5x}\nu^3) + \nu^3\tau^2(q_y - A_{5y}\nu^3) \right], \tag{9.192}$$

where $\vec{A}_5$ has been introduced as an axial gauge field. It couples to an axial gauge charge ν^3, which can be recognized as γ^5 when writing everything in Lorentz covariant form (see for instance [102, 206]). We thus conclude that the two density-wave partners correspond to an axial gauge field at low energies

$$(\Delta_{x^2-y^2}, \Delta_{xy}) \;\leftrightarrow\; (A_{5x}, -A_{5y}). \tag{9.193}$$

Axial gauge fields in a honeycomb lattice system have been discussed to great extent in the context of strain fields in graphene [98, 179]. In fact, recent experimental

data shows the observation of such strain engineered gauge fields in graphene-like systems [81].

Proceeding to the translational symmetry broken states, we first observe that they all couple the two valleys and will therefore correspond to Dirac matrices proportional to ν^1 or ν^2. Let us get organized by listing all Dirac matrices of this form. Tey are $\nu^1\tau^i$ and $\nu^2\tau^i$, where $i = 0, 1, 2, 3$ and so includes the unit matrix τ^0. Density wave states which break translational symmetry we found to transform as $G' = E_1 \oplus E_2$ for site order, $E_1' \oplus G' = A_1 \oplus B_1 \oplus E_1 \oplus E_2$ in case of bond order and $E_2' = A_2 \oplus B_2$ in case of flux order. We therefore have to consider the doublets E_1' and E_2', which are further decomposed into $1D$ irreducible representations, and G' which consists of two $2D$ representations.

Starting with the two doublets E_1' and E_2', it is shown in Appendix A.3 that the two Dirac matrices ν^1 and ν^2 transform according to E_1' and the matrices $\nu^1\tau^3$ and $\nu^2\tau^3$ transform according to E_2'. The former are time-reversal invariant while the latter break time-reversal symmetry. In addition, in Appendix A.3 we write the explicit basis functions of the representations A_1, A_2, B_1 and B_2 contained in E_1' and E_2'. Based on this we can write down the low-energy effective mean field Hamiltonian for the E_1' states as

$$\mathcal{H}_{\text{Kekule}} = (\Delta_{A_1}^{E_1'} \cos\theta - \Delta_{B_1}^{E_1'} \sin\theta)\nu^1 + (\Delta_{A_1}^{E_1'} \sin\theta + \Delta_{B_1}^{E_1'} \cos\theta)\nu^2. \quad (9.194)$$

where $\theta = \pi/3$. As these terms correspond to the condensate expressions of equation (9.154), we have chosen to label the Hamiltonian $\mathcal{H}_{\text{Kekule}}$. Indeed, it may be simply checked that both ν^1 and ν^2 anti-commute with the Dirac matrices of equation (9.190) and therefore constitute compatible masses. The two matrices $\nu^1\tau^3$ and $\nu^2\tau^3$ on the other hand, do not enter as masses and do not open up a spectral gap. Instead they enter equivalently as ν^3, shifting the Dirac nodes energetically with respect to each other.

What is left to consider is the set of Dirac matrices corresponding to the G'-symmetric density wave states. The remaining translational symmetry breaking Dirac matrices are $\nu^1\tau^1$, $\nu^2\tau^1$, $\nu^1\tau^2$ and $\nu^2\tau^2$, which indeed transform as a quartet according to G'. The low-energy Dirac structure of G' symmetric states is most powerfully demonstrated and explained by combining all Dirac matrices, and hence density wave states, which transform as $2D$ representations of the point group C_{6v}. We had found the doublet (τ^1, τ^2) to transform as E_2 and together with the $G' = E_1 \oplus E_2$ symmetric matrices we have the six terms

$$\tau^1, \ \tau^2, \ \nu^1\tau^1, \ \nu^2\tau^1, \ \nu^1\tau^2, \ \nu^2\tau^2. \quad (9.195)$$

A key observation is that all of these Dirac matrices can be generated by the triple (ν^1, ν^2, ν^3) in the following way. The two Dirac matrices appearing in (9.190) are

$\nu^3\tau^1$ and $\nu^3\tau^2$. The multiplication $\nu^3\tau^1\nu^i$ and $\nu^3\tau^2\nu^i$ then straighforwardly give all six Dirac matrices listed here. This means for the low-energy Dirac Hamiltonian that we can write a general expression incorporating the effect of these density waves, which reads

$$\mathcal{H}(\vec{q}) = \hbar v_F \left[\nu^3\tau^1(q_x - A_x^i\Omega^i) + \nu^3\tau^2(q_y - A_y^i\Omega^i) \right]. \qquad (9.196)$$

Here we have defined the three matrices $\Omega^i \equiv \nu^i$, which then obey the $su(2)$ algebraic relations generating the $SU(2)$ gauge field $\vec{A}^i$, i.e. $[\Omega^i, \Omega^j] = 2i\epsilon^{ijk}\Omega^k$. We can put this differently by saying that density waves transforming as E_2 or G', all $2D$ irreducible representations of C_{6v}, act as components of a non-Abelian gauge field in the low-energy description of the mean field spectrum.

The equations (9.148) and (9.149) provide explicit expressions for the site ordered states transforming as G' and per the above we can conclude that they enter, together with the bond ordered state of equation (9.4.1), as the components of one non-Abelian gauge field $\vec{A}^i$. The identification of translational symmetry broken charge density waves as components of a gauge was already reported in [180], which highlighted the possibility of a condensed matter realization of non-Abelian gauge fields in graphene. What we have shown here is how symmetry can be used to establish wich density wave states correspond to gauge field components in the low-energy description of the electronic degrees of freedom. In demonstrating this, we have used the same approach and reasoning as for the case of the square lattice in Section 9.3.2, which dealt with the Dirac theory of the π-flux state with C_{4v}. The key observations which hold true in both cases and are therefore independent of symmetry class (square or hexagonal), can be summed up as follows.

When the low-energy electronic spectrum exhibits symmetry protected Dirac points, then the impact of additionally induces density waves on the low-energy Dirac theory can be predicted based on the lattice symmetry breaking properties of such density waves. Density waves which are either even or odd under the rotations and reflections, i.e. transform as $1D$ representations, will either correspond to a Dirac mass gapping out the spectrum, or lift the degeneracy between the inequivalent Dirac nodes (the valleys). Density waves which have a partner and transform together as a $2D$ repressntation of the group of rotations and reflections will have the low-energy interpretation of gauge fields. Constant gauge fields merely shift the Dirac nodes away from their high symmetry mandated location, while spatially dependent gauge fields give rise to pseudo-Landau level quantization [180]. We propose that these statements have general validity, indepedent of lattice and symmetry class. This means that decompositions such as in equations (9.131) and (9.133) already provide quite some information on properties of the mean field spectra, without the need to calculate them. For any specific lattice one may proceed to derive the lattice symmetry

group representation on the Dirac spinor $\hat{\Phi}$ in order to classify the fermion bilinears in terms of lattice symmetries and obtain a more detailed identification of density waves and Dirac matrices. The full potential of such a symmetry perspective will be demonstrated with the help of a specific example below when we discuss the kagome lattice.

Low-energy description: Van Hove-singularities

The Dirac points at $\vec{K}_{\pm}$ provide a natural low-energy setting for discussing the impact of density wave states at these ordering momenta, as they couple the two inequivalent Dirac points. For the low-energy physics to be captured by the relativistic Dirac equation, the filling needs to be appropriate, i.e. one electron per two sites in case of spinless fermions. Ordering at the M points, contrary to K-point ordering, is expected not to couple the Dirac points, but instead couple Fermi surface arcs at filling $n = 3/8$. At this particular filling the Fermi surface on the honeycomb lattice is a hexagon inscribed in the Brillouin zone hexagon, as shown in Fig. 9.4, and is perfectly nested by the three vectors $\vec{Q}_{\mu}$. The M-point vectors $\vec{Q}_{\mu}$ are also shown in Fig. 9.4 and are explicitly given in Appendix A. Condensation at finite M-point wave vectors is therefore expected to be relevant for this filling, and possibly other commensurate fillings $n = p/8$. We furthermore anticipate that such M-point condensation will address the the nested Fermi surface in an analogous way as (π, π) ordering in case of the nested Fermi surface of the square lattice at half filling. We recall that the two s-wave condensates, i.e. charge and spin density waves, gap out the full Fermi surface, while the two d-wave condensates gap out the Fermi surface except for isolated points in momentum space. Here we take a detailed look at how M-point condensates alter the spectrum by focussing on energies and fillings appropriate for the nested hexagonal Fermi surface. We stress that even though we present the results in the honeycomb lattice setting, they pertain to all hexagonal lattices, a point we come back to below.

Figure 9.7(a) shows the folding of the nested Fermi surface in the reduced Brillouin zone for M-point ordering. In the reduced Brillouin zone the Fermi surface constists of line segments connecting Γ to all M'-points of the reduced Brillouin zone. It follows from the folding that each line segment is doubly degenerate in the reduced zone. The symmetry of density wave orders will determine the way in which the Fermi surface is altered. In general we expect two scenarios in the presence of at least a three-fold symmetry C_3 of the physical system. They are schematically depicted in Fig. 9.7(b). The right side shows a full lifting of the Fermi surface degeneracy at generic $\vec{k}$, except for the high symmetry points Γ and M', whiich may or may not have residual degeneracies protected by symmetry. The left figure depicts the scenario of a shifting and change in shape of the degenerate acrs in momentum
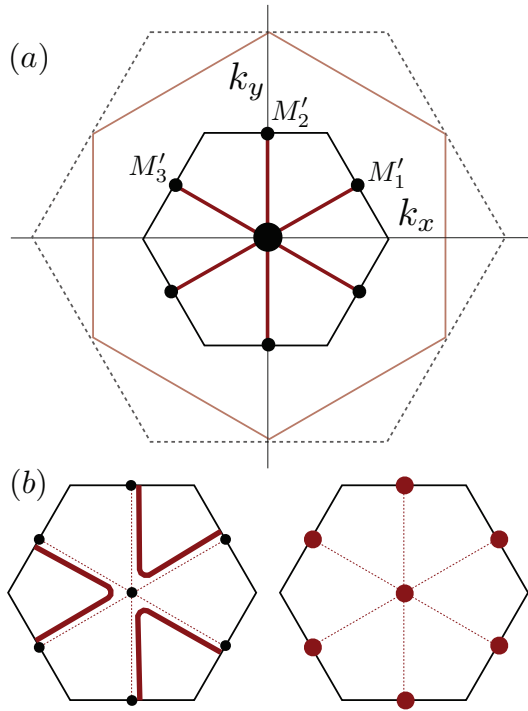
Figure 9.7: (Above) Folding of the Brillouin zone as a consequence of M-point order. Outer dashed transparent hexagon represents the hexagonal Brillouin zone, red transparant hexagonal is the M-point nested Fermi surface. Inner solid black hexagon is the reduced Brillouin zone and red lines in the reduced Brillouin zone represent the folded Fermi surface, which is doubly degenerate everywhere in the reduced BZ except Γ where it is treefold degenerate. (Below) A schematic picture of the possible effect of particle-hole condensation on the (mean field) spectrum with on the right the gapping out of the Fermi surface, i.e. lifting of the degeneracies, possibly except for high symmetry points Γ and M'. On the left the possible shifting of the degenerate arcs, a situation which requires the breaking of time-reversal symmetry.

space. It is clear that this is only possible when time-reversal symmetry and the six-fold rotation C_6 are broken. In what follows we will focus on the first scenario as the singlet density waves we have identified so far cannot lead to the second scenario. We come back to the second scenario in the context of triplet condensates.

At the high symmetry points Γ and $\vec{M}'_\mu$ degeneracies may be symmetry protected and due to this we examine these isolated points in more detail. Let us start with Γ and construct an 8-dimensional spinor $\hat{\Phi}_\Gamma$ as

$$
\hat{\Phi}_\Gamma = \begin{bmatrix} \hat{\psi}_j(\vec{0}) \\ \hat{\psi}_j(\vec{Q}_1) \\ \hat{\psi}_j(\vec{Q}_2) \\ \hat{\psi}_j(\vec{Q}_3) \end{bmatrix}, \tag{9.197}
$$

with $j = A, B$. In the absence of any particle-hole condensation all point group operations C_{6v}''' are good symmetries and we can build a representation of this group by considering how the generators of C_{6v}''' act on $\hat{\Phi}_\Gamma$. For the translation $T(\vec{x}_1)$ we have

$$
T(\vec{x}_1) \quad \rightarrow \quad \begin{bmatrix} 1 & & & \\ & -1 & & \\ & & -1 & \\ & & & 1 \end{bmatrix} \hat{\Phi}_\Gamma, \tag{9.198}
$$

while the six-fold rotation C_6 leads to the matrix

$$
C_6 \quad \rightarrow \quad \begin{bmatrix} \tau^1 & & & \\ & & \tau^3\tau^1 & \\ & & & \tau^3\tau^1 \\ & \tau^1 & & \end{bmatrix} \hat{\Phi}_\Gamma, \tag{9.199}
$$

and the reflection σ_v gives rise to

$$
\sigma_v \quad \rightarrow \quad \begin{bmatrix} \tau^1 & & & \\ & & & \tau^1 \\ & & \tau^1 & \\ & \tau^1 & & \end{bmatrix} \hat{\Phi}_\Gamma. \tag{9.200}
$$

These operations define a reducible representation of C_{6v}''' which can be decomposed into irreducible representations as $A_1 \oplus B_2 \oplus F_1 \oplus F_4$. The two one-dimensional representations correspond to high energy modes coming from $\hat{\psi}_j(\vec{0}) = \hat{\chi}_{0j}(\vec{0})$, while the two $3D$ representations correspond to the folded M-points at Γ. The honeycomb lattice with nearest neighbor hopping only is particle-hole symmetric and a nested

Fermi surface exist both at filling $n = 3/8$ and $n = 5/8$. Each of the two $3D$ representations corresponds to one of these fillings. The dimensionality of these two irreducible representations mandates a threefold degeneracy at Γ, which is just a restatement of the intuitively clear fact that energy levels at M-point in the original Brillouin zone must be degenerate for C_{6v} symmetry. When translational symmetry is broken by M-point ordering we are forced to consider the group of remaining symmetries and see how this group will affect degeneracies. If the group of remaining symmetries is C_{6v}, i.e. the density wave still has C_{6v} symmetry, we decompose $F_1 \oplus F_4$ further into irreducible representations of C_{6v}, which we already know to result in $A_1 \oplus B_2 \oplus E_2 \oplus E_1$. From this we conclude that while the three-fold degeneracies in general will be lifted, two-fold degeneracies must remain at Γ. We can go one step further and assume an even smaller group of remaining symmetries, which is C_{3v}. There are two distinct possibilities corresponding to the two distinct sets of reflections which are part of C_{6v}. To put it differently, the particle-hole condensate lowering the symmetry down to C_{3v} may transform as B_1 or B_2 of C_{6v}. In case of the former, i.e. B_1, we find that $F_1 \oplus F_4 = A_1 \oplus A_2 \oplus 2E$, while in the latter we find that $F_1 \oplus F_4 = 2A_1 \oplus 2E$. Hence, even in case of C_{3v} symmetry the two-fold degeneracies are protected.

In the same way we can study the M'-points of the reduced Brillouin zone (see Fig. 9.7). The symmetry group is different from the Γ point, as the M'-points are left invariant only by the inversion C_2 and two reflections, leading to a little group C_{2v}. The group C_{2v} only has $1D$ representations and therefore cannot protect degeneracies by itself. If translations are inlcuded to generate the group C_{2v}''' degeneracies are protected. Details are presented in Appendix A as they are of less significance. For our purposes at this point it is sufficient to conclude that particle-hole condensation will generally lift the M'-point degeneracy as it breaks translations.

Based on these considerations we make predictions concerning the spectral effects of particle-hole condensates with specific symmetries. For reasons of definiteness let us focus on the lower part of the honeycomb lattice spectrum, i.e. the filling $n = 3/8$. All condensates constructed from $\vec{Q}_\mu$ components that transform as $1D$ representations of C_{6v} have C_{3v} as a remaining symmetry group, except for A_2 states which we discuss separately below. Therefore, at Γ the three-fold degeneracy will generically be lifted and result in a non-degenerate energy level plus a two-fold level. Symmetry does not tell us a priori what the order is, i.e. whether the non-degenerate level is higher in energy or lower, but it is clear that there are only these two options. If the degenerate level is lower in energy, then for reasons of band connectivity we expect a full energy gap to develop. In contrast, if the non-degenerate level is lower in energy the existance of a Fermi surface is expected. These two different situations are graphically depicted in Fig. 9.8, where we plot the lowest four electron bands along a path in the reduced BZ for the site ordered density wave state transforming as A_1
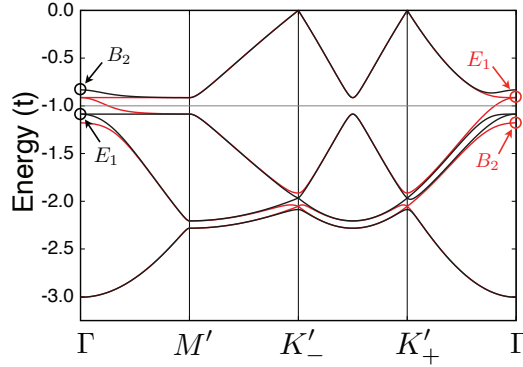
Figure 9.8: Folding of the Brillouin zone as a consequence of M-point order. Red lines in the reduced Brillouin zone represent the folded Fermi surface.

of equation (9.170), by way of example. Black and red spectra correspond to positive and negative sign of $\Delta_{A_1}^{F_1}$, respectively. At the relevant filling $n = 3/8$ we see that the two spectra differ precisely as expected and the order in which the doublet and non-degenerate level split is apparently controlled by the sign of $\Delta_{A_1}^{F_1}$.

In order to gain more insight into the way particle-hole condensation affects the nested Fermi surface, effect let us take a closer look at the low energy description at Γ. First, we organize the components of $\hat{\Phi}_\Gamma$ according to the triplets F_1 and F_3. Using obvious notation, we find that

$$\hat{\Phi}_{F_1} = \begin{bmatrix} \hat{\chi}_{1A} - \hat{\chi}_{1B} \\ \hat{\chi}_{2A} + \hat{\chi}_{2B} \\ -\hat{\chi}_{3A} + \hat{\chi}_{3B} \end{bmatrix}, \quad \hat{\Phi}_{F_4} = \begin{bmatrix} \hat{\chi}_{1A} + \hat{\chi}_{1B} \\ \hat{\chi}_{2A} - \hat{\chi}_{2B} \\ -\hat{\chi}_{3A} - \hat{\chi}_{3B} \end{bmatrix}, \tag{9.201}$$

where $\hat{\Phi}_{F_4}$ is relevant operator for $n = 3/8$, while is $\hat{\Phi}_{F_1}$ is a basis for the three-fold degeneracy at $n = 5/8$. Expanding the Hamiltonian to second order in momentum and projecting into the bases $\hat{\Phi}_{F_1}$ and $\hat{\Phi}_{F_4}$ we obtain

$$\mathcal{H}(\vec{q}) = \pm \begin{bmatrix} -q_1 q_3 & & \\ & -q_2 q_1 & \\ & & -q_3 q_2 \end{bmatrix}, \tag{9.202}$$

where $+ (-)$ refer to F_1 (F_4). We continue to rewrite the basis states $\hat{\Phi}_F \equiv [\hat{\Phi}_1, \hat{\Phi}_2, \hat{\Phi}_3]^T$ in such way that they will be the proper basis states of the representations $A_{1/2}$ and

E of C_{3v}. This gives the generic states

$$\hat{\Phi}_A = \frac{1}{\sqrt{3}}(\hat{\Phi}_1 + \hat{\Phi}_2 + \hat{\Phi}_3) \tag{9.203}$$

$$\hat{\Phi}_E = \begin{cases} \frac{1}{\sqrt{6}}(\hat{\Phi}_1 + \hat{\Phi}_2 - 2\hat{\Phi}_3) \\ \frac{1}{\sqrt{2}}(-\hat{\Phi}_1 + \hat{\Phi}_2) \end{cases}. \tag{9.204}$$

Writing the Hamiltonian of equation (9.202) in this basis we obtain the diagonal blocks $\mathcal{H}_A(\vec{q})$, which is given by

$$\mathcal{H}_A(\vec{q}) = \mp(q_1 q_3 + q_2 q_1 + q_3 q_2)/3, \tag{9.205}$$

and $\mathcal{H}_E(\vec{q})$ which after implementing a unitary transformation is given by

$$\mathcal{H}_E(\vec{q}) = \pm\frac{1}{4}q^2 \pm \frac{1}{4}\left[(q_x^2 - q_y^2)\tau^3 + 2q_x q_y \tau^1\right] \tag{9.206}$$

Note that the blocks coupling these two sectors do not vanish. The clear advantage of the present basis is revealed when expressing the possible spectral impact of general density wave states. For all density wave states that have at least C_{3v} symmetry, the allowed term in the low-energy Hamiltonian at Γ reads

$$\mathcal{H} = \begin{bmatrix} \Delta_A & & \\ & \Delta_E & \\ & & \Delta_E \end{bmatrix}. \tag{9.207}$$

It is the sign of $\Delta_A - \Delta_E$ that determines whether or not a gap will open up. At the filling $n = 3/8$ a gap opens up if $\Delta_A - \Delta_E > 0$, while it is the other way around at $n = 5/8$.

Armed with this general framework we are in a position to take a specific look at the density wave states that were derived in the previous section. Starting with site ordered states, we recall that there are two states with $\vec{Q}_\mu$ components which have residual C_{3v} symmetry. These are states transforming as A_1 and B_2, both given in equation (9.170). The lower part of the spectrum of the A_1 is presented in Fig. 9.8 and we have already pointed out the significance of the sign of the density wave strength $\Delta_{A_1}^{F_1}$. We note here that the situation is exactly opposite for $n = 5/8$ to the one at $n = 3/8$. When a gap is opened up at $n = 3/8$, then a degeneracy remains at $n = 5/8$ originating from the fact that the energetic order of the non-degenerate level and the degenerate levels is the same for both fillings. The B_2 state exhibits a threefold degeneracy at Γ, both at $n = 3/8$ and $n = 5/8$, and this is a purely accidental fact. The degeneracy is not symmetry protected. Apart from this degeneracy at Γ, the Fermi surface is completely gapped out.

Coming back again to the A_1 site ordered state and restricting ourselves to $n = 3/8$, we notice that in case of $\Delta_A - \Delta_E < 0$ the description of low-energy excitations close to Γ is fully governed by the Hamitonian $\mathcal{H}_E(\vec{q})$, which we recognize to have the generic structure of a quadratic band crossing (QBC) Hamiltonian. The emergence of such a QBC point in the context of M-point ordering was first noticed in Ref. [163], which derived the QBC Hamiltonian for uniaxial spin density wave with $\vec{Q}_\mu$-vector modulations. In the present case we have established the existence of a QBC purely based on symmetry arguments and the particular case of the uniaxial spin density wave follows from these more general arguments. Indeed, even though we have have assumed the absence of any structure in spin space so far, the result of Ref. [163] is readily understood based on the present discussion. The uniaxial spin density wave of [163] and [160, 162] can be thought of as two copies of the A_1 site order state, one for each spin species with opposite sign. Hence, the spectrum is precisely that shown Fig. 9.8, where the colors can be interpreted as spin up and spin down bands. We have shown that the QBC point arising from particle-hole condensation is protected by the residual C_{3v} symmetry, which in case of the uniaxial spin density wave may be considered to apply to each species separately. In Section 10 we will discuss the symmetries of spin triplet condensates in more detail in the context of M-point order on the triangular lattice. Here we just conclude that in the spinless case the only option apart from the appearance of a full spectral is gap, is the emergence of a QBC point in the low energy description of the M-point.

We have obtained three bond ordered states with residual C_{3v} symmetry, an A_1, B_1 and B_2 state, originating from the triplets F_1, F_3 and F_4, and collective represented in equation (9.185). Per the above, we can ask a simple question to find out what the spectral effects of these density waves are. What is the sign of $\Delta_A - \Delta_E$? We find the remarkable result that for both B_1 and B_2 symmetric bond density waves the non-degenerate level is higher in energy then the degenerate doublet at $n = 3/8$ (and vice versa for $n = 5/8$), amounting to the opening of a full energy gap. For these two states this is independent of the sign of $\Delta_{B_1}^{F_3}$ or $\Delta_{B_2}^{F_4}$ and as a result the situation of a QBC point does not occur. Even the simple triplet version of these bond density waves, which is just two copies of the density wave state for each spin species but with opposite sign, is gapped due the sign indepedence. In addition, we can argue that the spectral gaps caused by these distinct density waves are compatible, in the sense that if a density wave develops which is an arbitrary combination of these states, the total energy gap is always larger than the individual gaps. This follows in part from the fact that to lowest order, the structure of the low-energy Hamiltonian at Γ associated to the density waves, is given by equation (9.207), in a basis which is valid for all three density waves. Since we find that both these bond orders have the same order of energy levels, the values of $\Delta_A - \Delta_E$ simply add. We find the same to be true at the M'-points, which indeed shows that the gaps are compatible. In case

of the A_1 bond density wave both situations $\Delta_A - \Delta_E > 0$ and $\Delta_A - \Delta_E < 0$ can occur, depending on the sign of $\Delta_{A_1}^{F_1}$. It is therefore not necessarily compatible with the B_1 and B_2 induced gaps, but instead, its spectral impact is equivalent with the site ordered A_1 state. In particular, creating a uniaxial spin-bond ordered state out of the A_1 state results in a QBC point for one spin species and gapped excitations for the other.

Up to this point the emphasis has been on the assumption of residual C_{3v} symmetry, which holds for the states we have considered to far. We have not treated the case of C_6 symmetry (representation A_2), or the doublet states contained in the F representations of C_{6v}'''. If only C_6 rotational symmetry is left no degeneracies can be symmetry protected as Abelian groups such as C_6 have only $1D$ representations. We had derived one density wave with C_6 symmetry, given in equation (9.186). Indeed, the mean field spectrum of this density wave does not show any degeneracies at Γ or M'. Following equation (9.186) it was already noted that the spectrum is fully gapped, with nontrivial topological ground state. Insofar as the doublets are concerned the remaining symmetry is at most C_{2v}, which cannot lead to any symmetry protection of degeneracies either. An interesting common property of all doublet states we have verified, is that none of them lead to an immediate opening of a mean field spectral gap. Instead, we find that doublet states transforming as partners of E_1 or E_2 all have a mean field spectrum with a remaining Fermi surface at the van Hove filling for weakly developed density waves.

We conclude this discussion of the spectral effects of M-point modulated density waves at the Van Hove filling, by stressing the general validity and applicability of the results presented here. The dispersion of electrons hopping on the triangular or kagome lattices, two other ubiquitous examples of lattices with hexagonal symmetry, exhibits the same Fermi surface with Van Hove singularities for appropriate fillings as the honeycomb lattice. The $\vec{Q}_\mu$ vectors again connect arcs of the Fermi surface and M-point order is therefore expected to alter the spectrum in similar ways as outlined above. In order to gain deeper insight into the general, i.e. lattice independent, feautures of M-point order, we review a number of observations detailed above which hold true for the triangular and kagome lattice as well.

Based on the example of the honeycomb lattice, we showed that in the absence of translational symmetry (extended point group elements $T(\vec{x}_1)$ and $T(\vec{x}_2)$ are broken) the two-fold degeneracy at the M'-points and the threefold degeneracy at Γ are generally lifted. This statement only relies on symmetry, as it follows from the dimensionality of irreducible representations, and therefore directly applies to other lattices with hexagonal symmetry. In particular, by focusing on the Γ point, we have demonstrated that in the presence of at least C_{3v} symmetry, a two-fold degeneracy at Γ is protected. For any of the lattices with hexagonal symmetry the Van Hove singularities are located at Γ of the reduced Brillouin zone and the state vectors corresponding

to this subspace can be denoted as $\hat{\Phi}_F \equiv [\hat{\Phi}_1, \hat{\Phi}_2, \hat{\Phi}_3]^T$. Full symmetry makes these three states partners of a $3D$ representations causing the three-fold degeneracy. Lowering the symmetry down to C_{3v} lifts this degeneracy to a $2 + 1$ degeneracy, with corresponding states given by equation (9.203). The low-energy theory in terms of these basis states takes the generic form presented in equations (9.205) and (9.206), meaning in particular that all C_{3v} symmetric density waves will enter as (9.207). The sign of $\Delta_A - \Delta_E$ will then determine whether a full gap exists or the low-energy theory is captured by a QBC theory. Hence, many of the spectral effects and effective low-energy descriptions of electronic degrees of freedom in the presence of density wave states ar very general. We will come to this briefly in Section 9.4.3) when focusing on the triangular lattice. It should be stressed though that these considerations are based on symmetry. There may be accidental degeneracies at Γ or even M' in addition to the degeneracies required by symmetry.

9.4.2 Kagome lattice

After this long and detailed discussion of honeycomb lattice density waves, we focus attention on the second example of a well-known lattice with hexagonal symmetry, the kagome lattice. The kagome lattice has three inequivalent sites in its unit cell, instead of two in case of the honeycomb lattice, wich leads to more possibilities for both site and bond ordered states. The specific aim of this section is not only to provide the symmetry-based framework for classifying kagome lattice density waves, but also to highlight the utility and power of the lattice symmetry perspective. The insight into the strong link between organizing density waves as basis functions of irreducible representations and physical electronic properties of these condensates, gained both from the the square lattice and honeycomb lattice cases, will be applied to the kagome lattice. Therefore, the structure of this kagome lattice section will be as follows. We start by listing the decompositions of site, bond and flux order in the same way as for the square and honeycomb lattices, and both for K-point ordering and M-point ordering. Then we briefly discuss the prominent features of the free kagome lattice spectrum which make the kagome lattice a desirable object of study. These are the presence of Dirac fermions at the touching of the lowest two bands, a QBC point at the touching between the upper two bands, and van Hove singularities in combination with a nested Fermi surface in each of the lower two bands. Armed with the decompositions of site, bond and flux order we can make predictions concerning the mean field spectral effects of the condensates. Before we then come to a more elaborate discussion of translationally invariant order, i.e. K-point order, and M-point orderings, we introduce the sublattice functions, i.e. the kagome lattice equivalents of the Pauli matrices τ^i, and show how their transformation properties can be used to straightforwardly write down explicit condensate functions corresponding to the

irreducible representations obtained from group theory. The more detailed discussion of density waves, the construction of their explicit expression and electronic properties is divided into two parts. The first part deals with translationally invariant and K-point ordered density waves, as both of these classes affect the low-energy physics at the Dirac points, while the second part will deal with M-point ordering relevant for Fermi surface instabilities at van Hove fillings. In both of these parts we will not attempt an exhaustive characterization of all density waves, but instead limit ourselves to interesting examples. In case of the honeycomb lattice we have discussed the mean field spectrum of the density waves in a separate section. Here we integrate this part into the discussion of the density waves, their explicit form and their characteristics.

Following the same group theoretical recipy that was used for the honeycomb lattice, details of which are presented in Appendix C, we find the irreducible representations of the extended groups C_{6v}'' and C_{6v}''' present in the decompostions of site, bond and flux order representations. The decomposition for kagome lattice site order with K-point ordering vectors is given by

$$\mathcal{P}_s^K = A_1 \oplus E_2 \oplus E_1' \oplus G' \tag{9.208}$$

whereas we have for M-point ordering

$$\mathcal{P}_s^M = A_1 \oplus E_2 \oplus F_1 \oplus F_3 \oplus F_4. \tag{9.209}$$

The translationally invariant content of these two decompositions is $A_1 \oplus E_2$, which shows that in addition to the trivial A_1 state there is a translationally invariant site order doublet. For K-point order the translational symmetry broken states transform as $E_1' \oplus G'$, which differs from the honeycomb lattice decomposition [equation (9.131)] in the presence of E_1' states. Both the K-point and M-point site order decompositions are seen to be identical to the honeycomb lattice bond order decompositions, i.e. equations (9.133) and (9.134), which is a consequence of the kagome lattice being the line graph of the honeycomb lattice.

Moving on to bond order decompositions, we find that K-point order can be broken up into the following representations,

$$\mathcal{P}_b^K = A_1 \oplus B_2 \oplus E_1 \oplus E_2 \oplus E_1' \oplus E_2' \oplus 2G', \tag{9.210}$$

while the M-point order decomposition reads

$$\mathcal{P}_b^M = A_1 \oplus B_2 \oplus E_1 \oplus E_2 \oplus 2F_1 \oplus F_2 \oplus F_3 \oplus 2F_4. \tag{9.211}$$

The translationally invariant part of the decomposition, i.e. $A_1 \oplus B_2 \oplus E_1 \oplus E_2$, tells us that there is a $1D$ representation present, in addition to the fully symmetric A_1 state. We come back to these decompositions below, after we have briefly introduced

the low-energy physics corresponding to electron filling fractions where these density waves are expected to have significant impact.

The third type of order, flux order, leads to the following decomposition for translational symmetry breaking at K

$$\mathcal{P}_\phi^{\mathrm{K}} = 2A_2 \oplus B_1 \oplus E_2' \oplus G', \tag{9.212}$$

and for translational symmetry breaking at M-points one finds

$$\mathcal{P}_\phi^{\mathrm{M}} = 2A_2 \oplus B_1 \oplus 2F_2 \oplus F_3. \tag{9.213}$$

Contrary to all the other examples of flux order decompostions we have seen so far, the translationally invariant part contains the representation A_2 twice. This suggests the possibility of a realizing a density wave state breaks both time-reversal symmetry and all reflections, while at the same time leading to a flux pattern that averages to zero over the unit cell and corresponding to an insulating QAH state. The existance of such a state has in fact been known for some time [85], and here we see why it is particular to the kagome lattice. In addition to this QAH state, symmetry-based flux order decompositions teach us there are translational symmetry broken candidates for such insulators, which are contained in $E_2' = A_2 \oplus B_2$ (K) and $F_2 = A_2 \oplus E_2$ (M). From the symmetry of these density waves we can actually make more precise statements concerning their characteristics as we now proceed to argue in the context of low-energy spectral effects.

In case of the kagome lattice there are a number of interesting electron fillings worth considering, reflecting the spectral features of electrons hopping in the kagome lattice. For the filling $n = 1/3$ the Fermi surface consists of isolated points, i.e. Dirac points, which are located at the vertices of the Brillouin in the same way as for the honeycomb lattice. Therefore, in much the same way we can expand the spectrum around these Dirac points to obtain an effective Dirac theory capturing the electronic properties at low energies. The only technical difference is the fact that at both $\vec{K}_\pm$ one has to project the three-component eigenstates into the subspace corresponding to the Dirac nodes. If we label the set of states spanning the space of the Dirac nodes as $|+, j\rangle$ and $|-, j\rangle$ ($j = 1, 2$) for $\vec{K}_+$ and $\vec{K}_-$, respectively, then we derive a Dirac Hamiltonian which has exactly the same structure as for the honeycomb lattice (details in Appendix A.4),

$$\mathcal{H}(\vec{q}) = \hbar v_F \nu^3 \vec{q} \cdot \vec{\tau}, \tag{9.214}$$

[compare also equation (9.190)] where here we have $\sqrt{3}at/\hbar$. The Dirac spinor is

given by

$$\hat{\Phi}(\vec{q}) = \begin{bmatrix} \hat{\psi}_1(\vec{K}_+ + \vec{q}) \\ \hat{\psi}_2(\vec{K}_+ + \vec{q}) \\ \hat{\psi}_1(\vec{K}_- + \vec{q}) \\ \hat{\psi}_2(\vec{K}_- + \vec{q}) \end{bmatrix} . \tag{9.215}$$

As the structure is indeed equal to the honeycomb lattice Dirac theory, we can borrow the interpretation of Dirac matrices $\nu^i \tau^j$ from Section 9.4.1, where it should be understood that the ν^i act on the valley degree of freedom, i.e. $\pm$, and τ^j on the effective sublattice degree of freedom labeled by $j = 1, 2$. For instance, we direactly conclude that the Dirac matrices $\nu^3 \tau^3$, ν^1 and ν^2 constitute the compatible Dirac masses, while $\nu^1 \tau^3$ and $\nu^2 \tau^3$ make the two valleys inequivalent by separating the two nodes in energy.

Can the symmetry decompositions of equations (9.208), (9.210) and (9.212) assist us in assigning the density waves to the Dirac matrices describing their effect at the Dirac nodes? The answer to this question is yes. Let us look at site order and take the states $E_1' = A_1 \oplus B_1$ as an example. These can be written as basis functions of $1D$ representations of the bare point group C_{6v} and according to our proposition they must therefore couple to mass matrices. Indeed, as site order does not break time-reversal symmetry, valley mass terms must be excluded. As is detailed in Appendix A.4, an organization of the Dirac masses in terms of lattice symmetries indeed establishes the Dirac masses ν^1 and ν^2 as terms coupling to $E_1' = A_1 \oplus B_1$. This immediately implies the same interpretation of the bond density waves transforming as E_1'. Furthermore, there is a bond density wave which does not break translational symmetry and transforms as B_2. We can directly assign it the same character as the honeycomb lattice site order state with that same symmetry, i.e. the third Dirac mass. Another assignment that is easy to make in light of the symmetry perspective, is that of the translationally invariant site order doublet E_2 as a gauge field component. Some of these states have been found and discussed in mean field treatments or related studies [169, 170, 207]. The symmetry perspective adopted here provides a complete classification of density waves and their mean field spectral effects in the context of a Dirac theory.

Apart from Dirac nodes at filling $n = 1/3$ the kagome lattice spectrum exhibits two other types of spectral regimes which we have already encountered in this study. At filling $n = 2/3$, when two of the three bands are filled, the second filled band and the upper empty touch at the Γ point, making this degeneracy point a QBC. Even though this is an interesting property of the kagome lattice, as all the generic and peculiar features of a QBC apply directly, we will not address this point in more detail for the kagome lattice. Instead, we will be interested in the other special fillings

fractions, i.e. $n = 3/12$ and $n = 5/12$, which are the van Hove fillings of the kagome band structure. At these van Hove points the Fermi surface is shape-equivalent to the Fermi surface of the honeycomb and triangular lattice for corresponding fillings, meaning a hexagon nested by the three inequivalent M-point vectors.

Before we zoom in on the specific density waves both at K-points and at M-points and explain how to obtain explicit expressions using symmetry, it will be helpful to take a look at the kagome generalizations of the Pauli matrices, i.e. matrices which encode the sublattice structure of the lattice. For any lattice with two sublattices the Pauli matrices (in this work we consistently use the set τ^i) form a set of functions which transform as irreducible representations of the point group. In case of the kagome lattice, which has three sublattices, the appropriate set of functions is the the collection of Gell-Mann matrices. The latter span the space of 3×3 Hermitian matrices and are listed in Appendix A.4. We have organized them in three distinct sets, i.e. $\vec{\Lambda}_a$, $\vec{\Lambda}_b$, and $\vec{\Lambda}_c$. The first two sets only have off-diagonal elements and therefore connect two sites, making them bond order functions. The set $\vec{\Lambda}_a$ is real while $\vec{\Lambda}_b$ is imaginary, meaning that the former preserves and the latter breaks time-reversal symmetry. The third set collects matrices with diagonal entries oonly and therefore pertains to site order. We can extract the irreducible representations of the point group C_{6v} contained in these three sets and with this information one can straightforwardly write down condensate function, which will be demonstrated in the next subsection.

We use the set $\vec{\Lambda}_a$ as example. Using equation 9.6, in particular the matrices U_R^{sl} (R being an element of the point group), we can derive how the $\vec{\Lambda}_a$ transform under point group operations. In the present case of the kagome lattice, the matrices U_R^{sl} are generated by the two permutations X and Y as defined in equations (9.160) and (9.160). Take the six-fold rotation C_6 for instance. It corresponds to $U_{C_6}^{\mathrm{sl}} = X$ and we therefore have

$$U_{C_6}^{\mathrm{sl}\dagger} \Lambda_{1a} U_{C_6}^{\mathrm{sl}} = X^T \Lambda_{1a} X = \Lambda_{3a}, \qquad (9.216)$$

and similarly we find for the other Λ_a that $\Lambda_{2a} \to \Lambda_{1a}$ and $\Lambda_{3a} \to \Lambda_{2a}$. This can be summarized as

$$C_6 \quad \to \quad X\vec{\Lambda}_a. \qquad (9.217)$$

We can proceed in this way to find the representation of C_{6v} acting on $\vec{\Lambda}_a$, which for definiteness we write as $\mathcal{P}_a$. It is then a simple matter to decompose $\mathcal{P}_a$ into irreducuble representations and one finds $\mathcal{P}_a = A_1 \oplus E_2$, which does not surprise given the translationally invariant content of the bond order decompositions. Repeating the same calculation for the representation $\mathcal{P}_b$ acting on $\vec{\Lambda}_b$ we find that $\mathcal{P}_a = A_2 \oplus E_2$. Similarly we find $\vec{\Lambda}_c$ to transform according to E_2.

We are now in the possession necessary ingredients to find and characterize the kagome lattice density waves and we wil do so in the next two sections. Instead of aiming for a complete listing of all density obtained from group theory, we will focus on the most illustrative cases in order to demonstrate the utility and relevance of the symmetry-based organization.

Density waves at Γ and $\vec{K}_\pm$

Consider first the site ordered doublet E_2 of equation (9.208) representing a translationally invariant state. Since it transforms as E_2 it is d-wave-like. We have seen that there is precisely such a doublet among the sublattice matrix functions, given by $\vec{\Lambda}_c$, and as these are the only functions corresponding to site order, we can directly use them to write down the condensate functions

$$\langle \hat{\psi}_{i\sigma}^\dagger(\vec{k}) \hat{\psi}_{j\sigma'}(\vec{k}) \rangle = \Delta_{x^2-y^2} [\Lambda_{1c}]_{ij} \delta_{\sigma\sigma'}$$
$$\langle \hat{\psi}_{i\sigma}^\dagger(\vec{k}) \hat{\psi}_{j\sigma'}(\vec{k}) \rangle = \Delta_{xy} [\Lambda_{2c}]_{ij} \delta_{\sigma\sigma'}. \tag{9.218}$$

As a density wave doublet, which does not couple the low-energy Dirac nodes, we expect the presence of these condensates to alter the mean field spectrum at the Dirac points as an effective axial gauge field. This is analogous to the bond order E_2 doublet of the honeycomb lattice. Indeed, such site ordered states we indeed found to have the interpretation of an axial gauge field at low energies [169, 207], and in the chiral representation chosen here (just as for the honeycomb lattice) the Dirac matrices are τ^1 and τ^2.

There is one bond ordered state and one flux ordered state we wish to mention explicitly here. Both transform as $1D$ representations, do not break translational symmetry, and both are obtained from the sublattice functions $\vec{\Lambda}_b$ which break time-reversal symmetry. For bond order these sublattice should acquire a momentum dependence and for each functions we are naturally presented two choices, i.e. $\cos k_i$ and $\sin k_i$, where $k_i = \vec{\delta}_i \cdot \vec{k}$ with $\vec{\delta}_i$ the nearest neighbor vectors defined in Appendix A.4. It is important to note here that the use of the sine and cosine functions imply the standard tight-binding gauge, which we have avoided consistently throughout this paper. In this particular case we temporarily adopt this gauge as it makes the presentation a great deal more transparent. For instance, it easy to convince oneself that the cosine functions, $\cos k_i$, transform into each other under point group operations and are always even. The sine functions on the other hand, $\sin k_i$ transform into each as well, but acquire a minus sign for the six-fold rotations the reflection σ_d (and its threefold equivalents). We can exploit this to construct combinatons of sublattice and orbital momentum functions which yield the condensate functions of

desired symmetry. As an example consider the combination

$$\sin k_1 \Lambda_{1b} + \sin k_2 \Lambda_{2b} + \sin k_3 \Lambda_{3b}. \qquad (9.219)$$

It is a symmetric superposition of Λ_b matrices and therefore its basic symmetry is A_2, as the decomposition of $\mathcal{P}_b$ shows. However, the sine functions provide additional minus signs for all the elements which are odd under B_1. This leads to an overall symmetry of $\sim B_1 \otimes A_2 = B_2$, and we have consequently identified the B_2 bond order state. Note that the sine functions compensate the oddness of $\vec{\Lambda}_b$ under time-reversal. Physically this density wave corresponds to alternating bond modulations. Depending on the strength of the density wave, the order parameter Δ_{B_2}, the up triangles acquire stronger (weaker) bonds while the down triangles have weaker (stronger) bonds.

In constrast, the cosine functions preserve time reversal and are even under all point group operations (they do of course transform into each other). Hence, forming an analogous combination with the $\cos k_i$ one obtains

$$\cos k_1 \Lambda_{1b} + \cos k_2 \Lambda_{2b} + \cos k_3 \Lambda_{3b}, \qquad (9.220)$$

which inherits all its symmetry from the $\vec{\Lambda}_b$ set, i.e. it transforms as A_2. We have therefore identified the time-reversal breaking A_2 flux ordered state.

For completeness we write down the full condensate functions for both density wave states,

$$\langle \hat{\psi}_{i\sigma}^\dagger(\vec{k}) \hat{\psi}_{j\sigma'}(\vec{k}) \rangle = \Delta_{B_2} (\sum_n \sin k_n \Lambda_{nb})_{ij} \delta_{\sigma\sigma'}$$

$$\langle \hat{\psi}_{i\sigma}^\dagger(\vec{k}) \hat{\psi}_{j\sigma'}(\vec{k}) \rangle = \Delta_{A_2} (\sum_n \cos k_n \Lambda_{nb})_{ij} \delta_{\sigma\sigma'}. \qquad (9.221)$$

We had already identified the B_2 state as a Dirac mass, i.e. the $\tau^3 \tau^3$ matrix, and based on symmetry it is a rather simple matter to identify the A_2 state with the time-reversal breaking mass τ^3, sometimes known as Haldane mass.

Let us now consider translational symmetry broken density waves with K-point ordering vectors. Here we will limit ourselves to site ordered states as they provide particularly nice examples of the way in which symmetry arguments can be employed to find explicit expressions for density waves.

Consider first the site ordered doublet E_1'. We know from the honeycomb lattice that this representation can be further decomposed as $E_1' = A_1 \oplus B_1$, meaning that it contains two states transforming as $1D$ representations of the bare point group. All $1D$ representations of the hexagonal point group preserve the threefold rotation C_3 and, in addition, the ordering vectors $\vec{K}_\pm$ are invariant under the threefold rotations.

This motivates the definition of a vector of phase factors, which was already encountered in equation (9.158), in order to describe the translational symmetry breaking at K. Such a vector of phase vectors is given by

$$\vec{d} = \begin{bmatrix} d_1 \\ d_2 \end{bmatrix} = \frac{1}{\sqrt{2}} \begin{bmatrix} \frac{1}{\sqrt{3}}(\omega + \omega^{-1} - 2) \\ \omega - \omega^{-1} \end{bmatrix} \tag{9.222}$$

Here the cubic roots of unity, ω, ω^{-1} and 1 come from the Fourier transform of the real space cosine functions $\cos(\vec{K} \cdot \vec{x} + j\vartheta)$ which modulate the site order. The key point to stress here is that the vector $\vec{d}$ can be thought of as (i) encoding the K-point modulations, and (ii) to transform as the $2D$ representation E of the group C_{3v}, which is the group that leaves unit cells invariant. At the same time, the sublattice matrices $\vec{\Lambda}_c$ transform as E as well. This allows for a rather elegant derivation of condensate functions. It is clear that in order write down these function we need a sublattice part (the $\vec{\Lambda}_c$ matrices) and a translational symmetry breaking part (the vector $\vec{d}$). Both transform as E and therefore products of them will transform as $E \otimes E = A_1 \oplus A_2 \oplus E$. The $1D$ representations $A_1 \oplus A_2$ correspond to the $A_1 \oplus B_1$ representations of C_{6v} that are contained in E_1'. Using standard recipies from group theory designed to obtain basis functions of tensor product representations, we find straightforwardly

$$\begin{aligned} A_1, \ A_1 \quad &\sim \quad d_1 \Lambda_{1c} + d_2 \Lambda_{2c} \\ A_2, \ B_1 \quad &\sim \quad d_1 \Lambda_{2c} - d_2 \Lambda_{1c}. \end{aligned} \tag{9.223}$$

These expressions are all we need as ingredients for the condensate functions belonging to the doublet E_1'. They take the form

$$\langle \hat{\psi}_{i\sigma}^\dagger(\vec{k} + \vec{K}_\pm)\hat{\psi}_{j\sigma'}(\vec{k}) \rangle = \Delta_{A_1}(d_1 \Lambda_{1c} \pm d_2 \Lambda_{2c})_{ij} \delta_{\sigma\sigma'}$$
$$\langle \hat{\psi}_{i\sigma}^\dagger(\vec{k} + \vec{K}_\pm)\hat{\psi}_{j\sigma'}(\vec{k}) \rangle = \Delta_{B_1}(d_1 \Lambda_{2c} \mp d_2 \Lambda_{1c})_{ij} \delta_{\sigma\sigma'}. \tag{9.224}$$

Note that $\langle \hat{\psi}^\dagger(\vec{k} + \vec{K}_+)\hat{\psi}(\vec{k}) \rangle$ is related to $\langle \hat{\psi}^\dagger(\vec{k} + \vec{K}_-)\hat{\psi}(\vec{k}) \rangle$ by complex conjugation and therefore these are not independent.

These two charge density waves modulated by K-point vectors are the kagome lattice equivalents of the honeycomb lattice Kekule bond ordered states. They share the same symmetry and consequently they also have the same impact on the low-energy electrons. Indeed, as we already mentioned, they correspond to the compatible Dirac masses ν^1 and ν^2. In fact, these site ordered states have been found in a mean field study of the kagome lattice where the band structure was doped to the Dirac points [169]. Based on symmetry grounds we concluded that there is an equivalent correspondence between the bond ordered states with E_1' symmetry and

the Kekule bond density waves of the honeycomb lattice. For both these types of density waves we therefore expect the same intriguing physics to be possible as for the Kekule distortions. Most notably, topological defects in the order parameter of the two compatible mass states should come with fractionally charged excitations and anyonic statistics.

In case of the honeycomb lattice we had found the translational symmetry broken site ordered states to correspond to low-energy gauge fields. This originated from their point group representation, which we found to be $G' = E_1 \oplus E_2$. Site ordered states of the same symmetry exist for the kagome lattice, as equation (9.208) shows, and they have the same low-energy interpretation. All charge density waves on the kagome lattice constituting doublets, i.e. $E_2 \oplus G'$, are components of a non-Abelian $SU(2)$ gauge field within the low-energy Dirac theory. The translationally invariant states we already identified and it is straightforward to find the other two doublets. Actually, one of them we already obtained when decomposing the products of $\vec{d}$ and $\vec{\Lambda}$ into $E \otimes E = A_1 \oplus A_2 \oplus E$. The doublet on the right hand side is one of the gauge field components. Using the same group theory recipy the condensate functions of the doublet are spanned by

$$E \quad \sim \quad \begin{cases} d_1\Lambda_{1c} - d_2\Lambda_{2c} \\ d_1\Lambda_{2c} + d_2\Lambda_{1c}. \end{cases} \tag{9.225}$$

Translationally symmetry breaking at $\vec{Q}_\mu$

Let us finally come to the M-point ordered density waves, which are composed of the ordering vectors $\vec{Q}_\mu$ pictorially shown in Fig. 9.4 and specified for the kagome lattice in Appendix A.4. We will discuss the site ordered, bond ordered and flux ordered states of equations (9.209), (9.211) and (9.213), but instead of presenting the derivation of explicit based on the real space formalism laid out in Section 9.4.1, we will show these density waves graphically and analyse their mean field spectral characteristics based on symmetry. In the same way as for K-point order this will serve to illustrate that obtaining information on electronic properties is intimately related to knowing the symmetry of a density wave state.

As was highlighted in Section 9.4.1, the honeycomb lattice has been presented as a study case for both K-point and M-point order, but the general conclusions apply to all hexagonal lattices. In particular, the low-energy description of electronic degrees of freedom at the M-points given in Section 9.4.1 is valid for the kagome lattice as well. The kagome lattice has two van Hove fillings corresponding to the saddle points of band structure with a Fermi surface looking exactly like Fig. 9.7. These fillings are given by $n = 3/12$ and $n = 5/12$. In the same way as for the honeycomb lattice we can project into the low-energy subspace at Γ by choosing
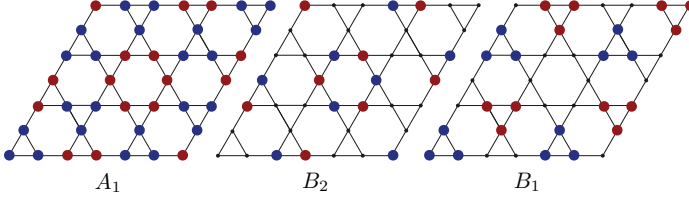
Figure 9.9: Graphical representation of kagome lattice site order with M-point ordering vectors . (upper left) the A_1 state, (upper right) the B_2 state and (below) the B_1 state.

state vectors that transform according to the $3D$ representations F_j. This yields the generic basis states $\hat{\Phi}_F \equiv [\hat{\Phi}_1, \hat{\Phi}_2, \hat{\Phi}_3]^T$, the explicit form of which in terms of $\hat{\chi}_{\mu j}$ depends on the lattice and the specific van Hove filling. We can always perform a basis transformation which leaves us with the combinations

$$\hat{\Phi}_A = \frac{1}{\sqrt{3}}(\hat{\Phi}_1 + \hat{\Phi}_2 + \hat{\Phi}_3) \tag{9.226}$$

$$\hat{\Phi}_E = \begin{cases} \frac{1}{\sqrt{6}}(\hat{\Phi}_1 + \hat{\Phi}_2 - 2\hat{\Phi}_3) \\ \frac{1}{\sqrt{2}}(-\hat{\Phi}_1 + \hat{\Phi}_2) \end{cases} . \tag{9.227}$$

We have demonstrated that in case of C_{3v} symmetry, the double degeneracy of the $\hat{\Phi}_E$ is protected. For the kagome lattice, as well as for the honeycomb lattice, the only allowed term in the low-energy Hamiltonian is

$$\mathcal{H} = \begin{bmatrix} \Delta_A & & \\ & \Delta_E & \\ & & \Delta_E \end{bmatrix} . \tag{9.228}$$

Having reviewed these basic features of M-point spectral features, we come to the specific density wave states.

The translational symmetry broken content of the kagome lattice site order decomposition is $F_1 \oplus F_3 \oplus F_4$ and this gives the $1D$ bare point group representations A_1, B_1 and B_2. The density wave states transforming as such are shown in Fig. 9.9. The A_1 state has the same mean field spectral properties as the honeycomb lattice A_1 states, both the site and bond ordered states. The sign of the order parameter $\Delta_{A_1}^{F_1}$ determines the sign of $\Delta_A - \Delta_E$ and therefore decides between a gap and a QBC at the lower van Hove filling ($n = 3/12$), while at $n = 5/12$ the doublet is always lower in energy leading to a QBC. In case of the B_1 and B_2 states we find the mean field
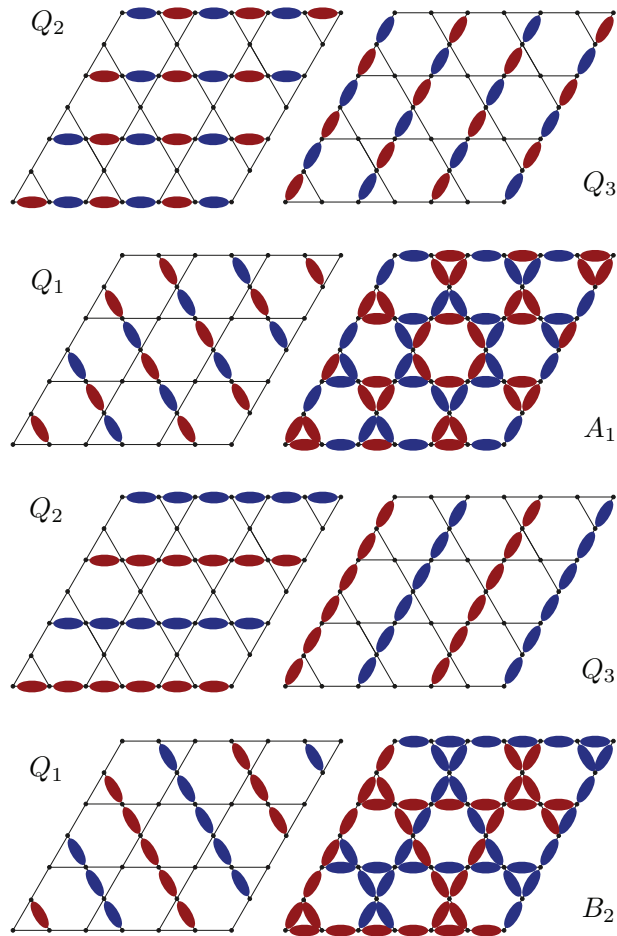
Figure 9.10: Graphical representation of kagome lattice bond order with M-point ordering vectors. We show the three individual components of F_1 (above) and F_4 (below) which transform as basis functions of these representations, in addition to the combination of these three components yielding the A_1 and B_2 states, respectively. We label the three components by their corresponding ordering vector Q_μ. As before, red (blue) bonds represent stronger (weaker) bonds.

spectrum not to depend on sign of the order parameter, in accordance with results of the honeycomb lattice. The mean field spectrum of the B_1 shows QBC's at both can Hove fillings while in case of the B_2 state the lower van Hove point is gapped out and the one at $n = 5/12$ shows a QBC. We note that in both cases, B_1 and B_2, the low-energy terms are not first order in the desnity wave strength (order parameter), but higher order.

Moving on to bond order, we recall that the translational symmetry broken states transform as $2F_1 \oplus F_2 \oplus F_3 \oplus 2F_4$. Note the appearance of the F_2 representation, which we had only encountered in time-reversal symmetry breaking flux order decompositions so far. A closer look at these states reveals that they can be organized in two series, wich are $2F_1 \oplus F_2$ and $2F_4 \oplus F_3$, where the second is obtained from the first by multiplication with B_2. As mentioned, explicit expression are worked out in Appendix A.4, and here we show them graphically in Figs. 9.10, 9.11 and 9.12. For convenience and completeness we have chosen not only to show the $1D$ states contained in the F_i representations, but instead to show the three components transforming as F_i as well.

The generic spectral features of these states again depend on symmetry only. The mean field spectra of both the A_1 states derived from the two F_1 representation and given in Figs. 9.10 and 9.11 depend on the sign of the order parameter, which in case of the van Hove filling $n = 3/12$ always decides between a gap and QBC. For the other van Hove filling, $n = 5/12$, the A_1 state of Fig. 9.11 always leads to a QBC. The mean field spectra of the two B_2 states obtained from these states (shown the same figures) does not depend on the sign of the order parameter. For both of these states the van Hove point at $n = 3/12$ is gapped out as the doublet is lower in energy. Instead, at $n = 5/12$ a QBC emerges, with an accidental degeneracy of the doublet $\hat{\Phi}_E$ and $\hat{\Phi}_A$ state in case of the B_2 state given in Fig. 9.10.

The other two bond order representations related to each other are F_2 and F_3, wich contain the $1D$ representations A_2 and B_1. They are shown in Fig. 9.12. The appearance of a time-reversal invariant state with A_2 symmetry is new. So far we only found flux ordered states with A_2 symmetry. For the latter type of states we noticed that degeneracies are in general not protected as the point group is Abelian. In the presence of time-reversal symmetry the situation changes and we can use the low-energy description at Γ to elucidate how. In the absence of C_{3v} symmetry the doublet states $\hat{\Phi}_E$ corresponding to the Hamiltonian (see also Section 9.4.1)

$$\mathcal{H}_E(\vec{q}) = \pm\frac{1}{4}q^2 \pm \frac{1}{4}\left[(q_x^2 - q_y^2)\tau^3 + 2q_x q_y \tau^1\right] \tag{9.229}$$

are no longer protected by pure point group operations. However, the combination of C_6 symmetry and time-reversal symmetry robustly protects a QBC [86] and the double degeneracy is therefore still protected. This is indeed relfected in the mean
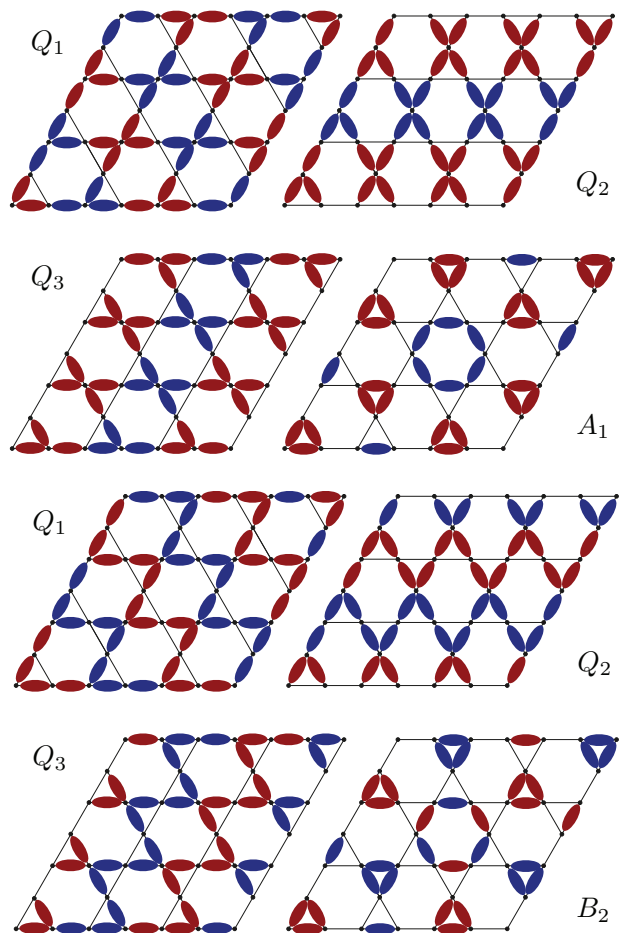
Figure 9.11: Same as in Fig 9.10, but for the other F_1 and F_4 represetations contained in the bond order decomposition.
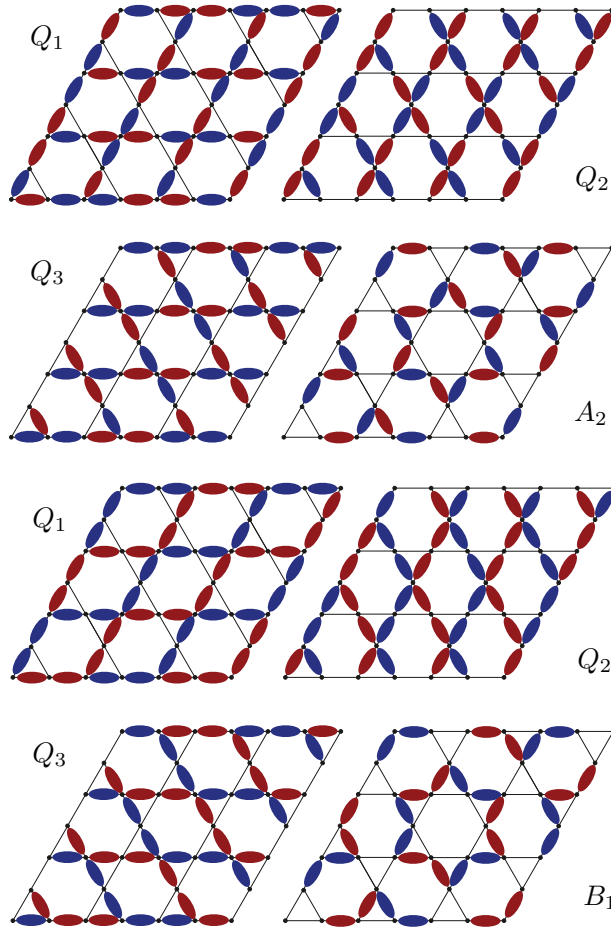
Figure 9.12: Same as in Fig 9.10 and Fig. 9.11, but for the F_2 and F_3 bond order representations. The A_2 and B_1 states that can be formed as linear combinations of the three components are shown as well.
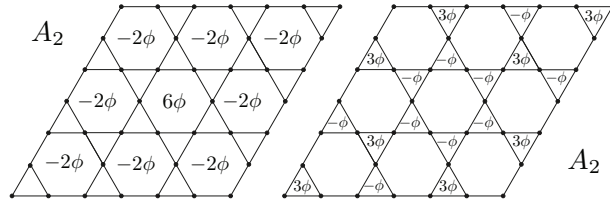
Figure 9.13: Graphical representation of kagome lattice flux order with M-point ordering vectors. On the left and right we show the two independent flux ordered states which transform as A_2 and come from the two F_2 representations contained in the flux order decompositions.

field spectrum. In particular, in case of the A_2 density wave state the low-energy theory at both van Hove points is that of a QBC. In contrast, for the B_1 state the order of singlet and doublet is such that a gap emerges for both van Hove points. For both states the sign of the order parameter is immaterial.

Finally, we come to M-point flux order on the kagome lattice. There are two independent F_2 representations contained in the flux order decomposition, both leading to A_2 time-reversal breaking $1D$ representations. In Fig. 9.13 we show these two independent A_2 states. For both states the original three-fold degereacy at Γ is fully lifted and no degeneracies remain. Both of these states can and do in fact lead to a fully gapped mean field spectrum and an insulating QAH ground state.

The kagome lattice M-point states provide additional evidence that the symmetry of density wave allows to make specific statements regarding the low-energy electronic properties. They show that while details may depend on lattice, states of the same symmetry have the same generic features, independent of lattice.

9.4.3   Triangular lattice

In this last part of the present section focusing lattices with hexagonal symmetry, we turn to the simplest of them, the triangular lattice. Even though the lattices considered up to this point, honeycomb and kagome, have already served to uncover the general structure and shared features of density waves on hexagonal lattices at specific ordering vectors, for completeness, but most of all as a warm up for the spin triplet condensates, we treat the triangular lattice case as well. The triangular lattice does not have a sublattice, which makes it similar to the square lattice. Nevertheless, its hexagonal symmetry puts it on the same footing with the honeycomb and kagome lattices, as we will demonstrate below. The hexagonal symmetry of the triangular

lattice is its most fundamental property in the context of density waves.

Contrary to the honeycomb and kagome cases, we will restrict ourselves to ordering at the M-points. As mentioned, all three hexagonal lattices here presented have a Fermi surface nested by the $\vec{Q}_\mu$ vectors and a logarithmically diverging density of states for appropriate filling. For the triangular lattice this filling is $n = 3/4$ and we therefore present the potential condensates for this filling in what follows.

The recipy is well-established and familiar by now, and we content ourselves with quoting the symmetry decomposition for site, bond and flux order. For site order we find the irreducible representations A_1 and F_1, i.e.

$$\mathcal{P}_s^M = A_1 \oplus F_1. \tag{9.230}$$

The triangular lattice has no basis and M-point ordering quadruples the unit cell, which yields the four distinct site ordered states. We have already seen a number of times that the representation F_1 decomposes further into A_1 and E_2 of the point group C_{6v}. For bond order we find the decomposition

$$\mathcal{P}_b^M = A_1 \oplus E_2 \oplus F_1 \oplus F_3 \oplus F_4, \tag{9.231}$$

which is equal to the decomposition for honeycomb bond order. Not surprising, as there is an equal number of bonds in the enlarged unit cell and both lattices do have the same symmetry. Hence, in the same way as for the honeycomb lattice, there will be three condensates transforming as $1D$ representations of C_{6v}, which are A_1, B_1 and B_2, coming from F_1, F_3 and F_4, respectively. To conclude, in case of flux order we find

$$\mathcal{P}_\phi^M = A_2 \oplus B_1 \oplus F_2 \oplus F_3. \tag{9.232}$$

For the purposes of this work we will be interested exclusively in the state transforming as A_2 and coming from the triplet F_2. This state has the potential of having nonzero Chern number, see Section 9.1.4, and based on the results obtained for honeycomb and kagome lattices, we strongly suspect that it will be a gapped state carrying a QAH effect.

For triangular lattice condensates, the compatibility and consistentie relations of equations (9.92) and (9.95) carry over in the same form. In addition, since we focus on M-point ordering, the definitions and formalism of Section 9.4.1 apply directly to the present case.

Starting with site order we can write the generic condensate expression in real space as

$$\langle \hat{\psi}_\sigma^\dagger(\vec{x}) \hat{\psi}_{\sigma'}(\vec{y}) \rangle = \Delta \, \vec{\zeta} \cdot \vec{\xi}(\vec{x}) \, \delta_{\vec{x},\vec{y}} \delta_{\sigma\sigma'}, \tag{9.233}$$

We are looking for a state which respects all operations of C_{6v} and this leads immediately to the requirements that $X\vec{\zeta} = \vec{\zeta}$ and $Y\vec{\zeta} = \vec{\zeta}$. The is only one vector satisfying this and it is $\vec{\zeta} = (1, 1, 1)^T/\sqrt{3}$. The density wave corresponding to F_1 and transforming as A_1 is therefore given in momentum space as

$$\langle \hat{\psi}_\sigma^\dagger(\vec{k} + \vec{Q}_\mu)\hat{\psi}_{\sigma'}(\vec{k})\rangle = \frac{1}{\sqrt{3}}\Delta_{A_1}^{F_1}\,\delta_{\sigma\sigma'}. \tag{9.234}$$

The site ordered doublet contained in F_1 is straightforwardly obtained by solving the equation $(-2 + X + X^T)\vec{\zeta} = \vec{\zeta}$, but we will leave it at this for now and continue to bond order.

In line with the approach so far we write down a general real space expression and evaluate the constraints imposed by symmetry. For the bonds in the $\vec{x}_1$ direction we can write down the general bond order form

$$\langle \hat{\psi}_\sigma^\dagger(\vec{x})\hat{\psi}_{\sigma'}(\vec{y})\rangle = \Delta\,\vec{\zeta}\cdot\vec{\xi}(\vec{x})\,(\delta_{\vec{x}+\vec{x}_1,\vec{y}} + \delta_{\vec{x},\vec{y}+\vec{x}_1})\delta_{\sigma\sigma'}. \tag{9.235}$$

For the other bond directions, $\vec{x}_2$ and $\vec{x}_3$, the corresponding expressions are automatically obtained using the threefold rotation, which yields $X\vec{\zeta}$ and $X^T\vec{\zeta}$ respectively. In order to find the unique expressions for $\vec{\zeta}$ corresponding to the translational symmetry broken states A_1, B_1 and B_2 we study the effect of the inversion C_2. The state transforming as A_1 should be invariant under inversion, while the other two should be odd. Applying C_2 we find the condition $G_1\vec{\zeta} = \pm\vec{\zeta}$ and this immediately fixes the $\vec{\zeta}$ vectors. The solution associated to the plus sign is given by $\vec{\zeta} = (0, 0, 1)^T$ and constitutes the A_1 state. There are two solutions associated to the minus sign, which are given by $\vec{\zeta} = (1, \pm 1, 0)^T/\sqrt{2}$ and they correspond to B_1 (+) and B_2 (−).

In order to write compact expressions in momentum space we define the triad of vectors $\vec{\zeta}_1 = \vec{\zeta}$, $\vec{\zeta}_2 = X\vec{\zeta}$ and $\vec{\zeta}_3 = X^T\vec{\zeta}$, where $\vec{\zeta}$ is one of the three vectors just identified. Furthermore, we define the functions $\cos k_j = \cos \vec{k}\cdot\vec{x}_j$ with $\vec{x}_3 = -\vec{x}_1 - \vec{x}_2$. Then, choosing $\vec{\zeta} = (0, 0, 1)^T$, we have the A_1 condensate expression

$$\langle \hat{\psi}_\sigma^\dagger(\vec{k} + \vec{Q}_\mu)\hat{\psi}_{\sigma'}(\vec{k})\rangle = \Delta_{A_1}^{F_1}\zeta_j^\mu \cos k_j \delta_{\sigma\sigma'}. \tag{9.236}$$

Very similar expressions are then simply obtained for the B_1 and B_2 states. Substituting the proper vectors $\vec{\zeta}$ one has

$$\langle \hat{\psi}_\sigma^\dagger(\vec{k} + \vec{Q}_\mu)\hat{\psi}_{\sigma'}(\vec{k})\rangle = i\Delta_{B_{1/2}}^{F_{3/4}}\zeta_j^\mu \sin k_j \delta_{\sigma\sigma'} \tag{9.237}$$

The last state of the triangular we present here is the flux state transforming as A_2 and coming from F_2. We must have imaginary hoppings in this state and we therefore start from the Ansatz

$$\langle \hat{\psi}_\sigma^\dagger(\vec{x})\hat{\psi}_{\sigma'}(\vec{y})\rangle = \Delta\,i\vec{\zeta}\cdot\vec{\xi}(\vec{x})\,(\delta_{\vec{x}+\vec{x}_1,\vec{y}} - \delta_{\vec{x},\vec{y}+\vec{x}_1})\delta_{\sigma\sigma'}. \tag{9.238}$$

Again the other directions are obtained using the threefold rotation. The state A_2 must be invariant under the inversion C_2 and we find this demand to yield the constraint $G_1 \vec{\zeta} = -\vec{\zeta}$, which we have seen to give solutions $\vec{\zeta} = (1, \pm 1, 0)^T / \sqrt{2}$. Evaluating the action of the reflection σ_v shows that the correct choice for A_2 is $\vec{\zeta} = (1, -1, 0)^T / \sqrt{2}$. In momentum space the condensate expression is

$$\langle \hat{\psi}_\sigma^\dagger(\vec{k} + \vec{Q}_\mu) \hat{\psi}_{\sigma'}(\vec{k}) \rangle = i \Delta_{A_2}^{F_2} \zeta_j^\mu \cos k_j \delta_{\sigma\sigma'}. \tag{9.239}$$

Inspecting the momentum space expressions just derived from a real space persective, we see that for each order parameter component $\vec{Q}_\mu$ they transform according to an irreducible representation of the group of $\vec{Q}_\mu$, which is C_{2v}. Indeed, $\cos k_2$ is invariant under all operations leaving $\vec{Q}_1$ invariant. In the same way the functions $\sin k_3 \pm \sin k_1$ and $\cos k_3 - \cos k_1$ transform according to irreducible representations of C_{2v}. Individually these components are basis functions of the $3D$ F_i representations of C_{6v}''' and forming proper comninations gives basis functions of the $1D$ and $2D$ representations of F_i. In particular for the triangular lattice, which has no basis, an alternative way to construct the condensates is therefore to work directly in momentum space, find functions transforming as the group of the wave vector $\vec{Q}_\mu$ use the compatability and consistency relations of equations (9.92) and (9.95) and form the proper combinations.

We close this section with some remarks on the spectral effects of the site, bond and flux ordered states. To this end we can use the general features of the low-energy structure applicable to a Fermi level close to the Van Hove singularities of hexagonal lattices, which we discussed in the context of the honeycomb lattice in section 9.4.1. First, we note that at the Van Hove singularities the perfectly nested Fermi surface (only nearest-neighbor hopping) has exactly the same form in the reduced Brillouin zone as depicted in Fig. 9.7. The relevant high symmetry points, where degeneracies may be symmetry protected are the Γ point and the M' points. The degeneracy protection is the same as was found for the honeycomb lattice. Specifically, in the presence of full C_{6v}''' symmetry, the two-fold degeneracy at each M' point is protected, while breaking of translational symmetry lift this degeneracy in general. At the Γ point, the representation of the symmetry group C_{6v}''' on $\hat{\Phi}_\Gamma = [\hat{\chi}_0, \hat{\chi}_1, \hat{\chi}_2, \hat{\chi}_3]^T$ can be decomposed into $A_1 \oplus F_1$. Losing translational symmetry but retaining C_{6v} symmetry then yields $2A_1 \oplus E_2$, which is replaced with $2A_1 \oplus E$ in case of residual C_{3v} symmetry. Furthermore, as was mentioned already in section 9.4.1, expanding the dispersion around the Γ gives the same low-energy structure that was obtained for the honeycomb lattice. At Γ the basis states corresponding to the non-degenerate and

doubly degenerate levels are given by

$$\hat{\Phi}_A = \frac{1}{\sqrt{3}}(\hat{\psi}(\vec{Q}_1) + \hat{\psi}(\vec{Q}_2) + \hat{\psi}(\vec{Q}_3)) \tag{9.240}$$

$$\hat{\Phi}_E = \begin{cases} \frac{1}{\sqrt{6}}(\hat{\psi}(\vec{Q}_1) + \hat{\psi}(\vec{Q}_2) - 2\hat{\psi}(\vec{Q}_3)) \\ \frac{1}{\sqrt{2}}(-\hat{\psi}(\vec{Q}_1) + \hat{\psi}(\vec{Q}_2)) \end{cases}. \tag{9.241}$$

In terms of these states, the lowest order term of density wave states in the effective low-energy theory is precisely given by equation (9.207). Therefore, it is again the sign of $\Delta_A - \Delta_E$ which decides between the two possibilities of a full gap and a symmetry protected QBC point. For the triangular lattice, we find that both the site ordered and the bond ordered A_1 states lead to either a gap or a QBC depending on the sign of $\Delta_{A_1}^{F_1}$, in way equivalent to honeycomb lattice A_1 site order. The two bond ordered states transforming as B_1 and B_2 both have a threefold degeneracy at Γ, which is consequence of the sine functions: at Γ the density wave state does not alter the Hamiltonian. This degeneracy is not symmetry protected. To conclude we mention here that the flux ordered state A_2 gaps out the full Fermi surface. Due to the absence of reflection symmetries there is no two-fold degeneracy at Γ. Direction calculation reveals that the energy gap at filling $n = 3/4$ is a nontrivial gap and the insulating state hosts a Quantum Hall effect marked by a nonzero Chern number.

CHAPTER 10

INTRODUCTION TO TRIPLET STATES: SPIN-DENSITY WAVES

10.1 General considerations

The purpose of the present section is to provide more insight into triplet particle-hole condensates, i.e. density wave states which break spin rotation symmetry. Up until this point spin triplet states have been mentioned only occasionally and briefly, such as QSH effects obtained from QAH effects (see for instance section 9.3.1), or uniaxial spin density waves obtained from charge order (see section 9.4.1). All of these examples have in common that they constitute the simplest class of spin triplet states, more or less trivially obtained from spinless states. Indeed, in essence they can be thought of as two copies of spinless states, one for each spin species, but with opposite sign for the two species. To put this more succinctly, they are obtained from the singlet states by replacing all $\delta_{\sigma\sigma'}$ with $\sigma^3_{\sigma\sigma'}$.

In quite a number of cases, such as the QSH effects, these triplet states are degenerate with the singlet states on a mean field level, precisely because the former comprise two copies of the latter. A notable exception are the uniaxial spin density waves of section 9.4.1, where the relative sign difference of the two copies is reflected in a different energy spectrum for the two species. Spinful condensates proportional to σ^3 break spin rotation symmetry partially, and for this reason are certainly proper

triplet states. However, the unbroken generator of spin rotations σ^3 signals that they far from exhaust the possible triplet condensates. Therefore, we take a closer look at spin triplet states in this section. We stress that we have no intention of being complete, but merely wish to present some of the general aspects of spinful condensates which go beyond the partial breaking of spin rotation reflected in the exchange $\delta_{\sigma\sigma'} \leftrightarrow \sigma^3_{\sigma\sigma'}$. We will do so with the help of selected lattices and example condensates. We will restrict ourselves to lattices with hexagonal symmetry and focus exclusively on ordering at the M-points. This will serve the purpose of demonstrating the most salient features characteristic of nontrivial triplet states. Specifically, the focus will be on two main concepts connected to the full breaking of spin rotation symmetry. The first is the possibility to dress lattice symmetries which are broken in the condensed state with a unitary global spin rotation, restoring them as symmetries. The second is the existance of time-reversal invariant spin-bond density waves, which will be introduced as a novel class of candidate interaction-induced topological insulators as well as topological semimetals. Both of these concepts will be shown to illustrate how the symmetry structure of spin density waves can be lifted from the spinless (spin rotation invariant) density waves.

In section 9.2.2 the foundations for a spinful mean field theory were presented, providing a possible context for the emergence of spinful density waves from electronic correlations in the same way as for spinless (or spin rotation invariant) case. Indeed, the triplet condensates may be taken as candidate ground states for mean field treatments, or considered variational states in the context of other approaches. In this section we repeatedly seek to establish a connection between a systematic development of spin rotation symmetry broken density waves and results from recent literature, which has reported a number of such density waves as dominant electronic instabilities or mean field ground states.

When it comes to lattice symmetries in two dimensions, the symmetry groups D_n and C_{nv} are distinct in the presence of spin degrees of freedom. In section 9.1.1 we have mentioned this distinction briefly and referred to the Appendix for details. As the differences do not significantly alter the observations and conclusions to come, we do the same here and content ourselves with focusing on the main features of lattice symmetries in the presence of spin, which are shared between the groups D_n and C_{nv}. Lattice symmetries act in spin space as a unitary $SU(2)$ matrix associated to the $SO(3)$ element acting on spatial coordinates. In addition, time-reversal symmetry now takes the form $\mathcal{T} = e^{i\pi\sigma^2/2}\mathcal{K}$, which has important the property $\mathcal{T}^2 = -1$. Triplet condensates therefore necessarily break time-reversal invariance, as all the three Pauli matrices σ^i are odd under time-reversal. Notice however that in case of the uniaxial density waves, i.e. $\sim \sigma^3$, applying a global spin rotation after time-reversal (a rotation of π around for instance the x axis) brings the state back to itself. Hence,

the time-reversed mean field Hamiltonian is unitarily equivalent to itself, effectively restoring time-reversal symmetry.

This brings us to the broader principle of spin rotation equivalence, which we take some time to introduce here before zooming in on specific lattices and particular states. For any spinful condensate a global spin rotation cannot change the spectrum or the free energy as the interacting Hamiltonian is $SU(2)$ invariant. For the mean field Hamiltonian this means that a global spin rotation yields a unitarily equivalent Hamiltonian which necessarily has the same spectrum. When considering lattice symmetries such as rotation, reflection and translation, global spin rotation equivalence comes into play in an important and consequential way. There are spinful density waves which have the property that the application of a lattice operation can be compensated by a global spin rotation. To put it in a different way, application of a lattice operation may result in a physical state which is related to the initial state by a global spin rotation. Let us make this statement more specific and tangible. We are going to study condensates of hexagonal lattices with M-point ordering only, and we therefore recall that the real space M-point modulation functions have been defined as $\vec{\zeta} \cdot \vec{\xi}(\vec{x})$ and fully specify a given type of M-point order. A general spinful ordering needs three of these functions, one for each spin direction. Instead of a vector $\vec{\zeta}$ it therefore makes sense to use a matrix $\mathcal{M} = \mathcal{M}_{i\mu}$ to encode the degrees of freedom for spinful M-point order, where $i = 1, 2, 3$ corresponding to σ^i, i.e.

$$\sigma^i \mathcal{M}_{i\mu} \xi_\mu(\vec{x}), \tag{10.1}$$

which can alternatively and more concisely written as $\vec{\sigma} \cdot \vec{\mathcal{M}}(\vec{x}) = \vec{\sigma} \cdot \vec{\mathcal{M}}_\mu \xi_\mu(\vec{x})$. Lattice symmetries can be represented by their action on $\vec{\xi}$. For instance, we have seen that $X\vec{\xi}(C_3\vec{x}) = \vec{\xi}(\vec{x})$ and $G_1\vec{\xi}(\vec{x} + \vec{x}_1) = \vec{\xi}(\vec{x})$. In particular translational symmetry was always broken for M-point modulations. To see how global spin rotations can come to the rescue, let us take such a translation, i.e. $T(\vec{x}_1)$, as an example. The effect of the translation on the spin order is

$$\vec{\sigma} \cdot \vec{\mathcal{M}}(\vec{x} + \vec{x}_1) = \sigma^i \mathcal{M}_{i\mu}[G_1]_{\mu\nu} \xi_\nu(\vec{x}). \tag{10.2}$$

We would like this to be equal to a global spin rotation $\mathcal{R}$ (depending on G_1) of the form

$$\vec{\sigma} \cdot \mathcal{R}\vec{\mathcal{M}}(\vec{x}). \tag{10.3}$$

Therefore, the translation $T(\vec{x}_1)$ can be compensated by a global spin rotation if and only if the following relation is satisfied

$$\sigma^i \mathcal{M}_{i\mu}[G_1]_{\mu\nu} \xi_\nu(\vec{x}) = \sigma^i \mathcal{R}_{ij} \mathcal{M}_{j\mu} \xi_\mu(\vec{x}). \tag{10.4}$$

This relation expresses the condition that the action on $\vec{\xi}$ can be carried over to $\vec{\mathcal{M}}$ and therefore to $\vec{\sigma}$. In other words, the translation can be compensated by a global rotation if G_1 acting on $\mathcal{M}$ from the right is identical to some $O(3)$ matrix $\widetilde{G}_1$ acting on $\mathcal{M}$ from the left, i.e. on its spin indices. Suppose for instance we have $\mathcal{M}_{11} = \mathcal{M}_{22} = \mathcal{M}_{33} = 1$ and all other elements zero. Then $\mathcal{M}$ is simply the identity and G_1 commutes with it so that $\mathcal{R} = G_1$. The translation can be compensated by a rotation of π around the z-axis, as this is the interpretation of G_1 as an element of $O(3)$. This follows from the fact that a general $O(3)$ matrix $\mathcal{R}$ acting on $\mathcal{M}$ gives $\vec{\sigma} \cdot \mathcal{R}\vec{\mathcal{M}}(\vec{x})$, and we can associate an $SU(2)$ matrix U with $\mathcal{R}$ such that

$$\vec{\sigma} \cdot \vec{\mathcal{M}} = U^{\dagger}\vec{\sigma} \cdot (\mathcal{R}\vec{\mathcal{M}})U. \tag{10.5}$$

In contrast, had we chosen instead $\mathcal{M}_{31} = \mathcal{M}_{32} = \mathcal{M}_{33} = 1$ and all other elements zero, the condition of equation (10.4) cannot be fulfilled and translational symmetry is manifestly broken. The physical significance of these two seemingly arbitrary choices for $\mathcal{M}$ will be clarified below when discussing the triangular lattice.

The concept of global spin rotation equivalence and its connection to lattice symmetries has appeared before in the context of classical spin models [208]. There it was employed to derive classical spin states which are invariant under all lattice operations, modulo a global spin rotation. Since translations are a subset of the lattice operations, these "classical spin liquids" must necessarily have a uniform spin length at every site. In the present case, where we study electronic density wave states, we find these fully symmetric spin density waves as a subset of a larger class of spinful density waves, which also includes spin-bond density waves and translational symmetry broken spin density waves, the uniaxial spin density waves being an example of the latter.

A key difference between the classical spin liquids of [208], i.e. classical spin states invariant under all lattice operations up to an $O(3)$ rotation, and electronic spinful density waves is the treatment of improper global rotations needed to promote lattice operations to symmetries. Elements of $O(3)$ are divided into two groups, the proper and improper rotations, which are distinguished by their determinant, i.e. Det $[\mathcal{R}] = \pm 1$. Improper elements can always be written as the product of a proper rotation $\mathcal{R}' \in SO(3)$ and the inversion operations, $\mathcal{R} = -\mathcal{R}'$. The relevance if this distinction follows from the need to associate an $SU(2)$ matrix U with $\mathcal{R}$, which is only possible for proper $\mathcal{R}$. In particular this means that if $\mathcal{R}$ is improper, the state is odd under the operations corresponding to $\mathcal{R}$, i.e.

$$\vec{\sigma} \cdot (\mathcal{R}\vec{\mathcal{M}}) \rightarrow -\vec{\sigma} \cdot (\mathcal{R}'\vec{\mathcal{M}}) = -U\vec{\sigma} \cdot \vec{\mathcal{M}}U^{\dagger}, \tag{10.6}$$

where the matrix U is the $SU(2)$ equivalent of $\mathcal{R}'$. In case of hexagonal lattice M-point we already observed in Section 9.4.1 that an $O(3)$ representation of the group

of lattice symmetries is generated by their action on $\vec{\xi}(\vec{x})$. The generators of this representation are G_i, X, X^T and Y. Equation (10.4) states that it is these generators which determine $\mathcal{R}$. Only the element Y is improper, implying that all reflections are associated with an improper rotation. Below we will illustrate in specific cases how this affects the electronic symmetries of given density waves.

10.2 Triangular lattice triplet states

Spin density waves in hexagonal lattice systems modulated by the M-piont vectors are currently attracting much attention, with the triangular lattice being one of the most prominent represenatives of lattices with hexagonal symmetry. One of the first examples of such a novel spin density wave state, proposed in the context of pre-formed classical local moments coupled to electrons, has been a noncoplanar chiral spin state [30]. It was shown in [30] that this state can also be thought of as a proper density wave spontaneously formed by onsite Hubbard-like interactions, in the same spirit which is at the heart of the present framework. The chiral spin density wave gaps out the electronic spectrum and leads to a Quantum Anomalous Hall ground state. In later works, the problem of spin density wave physics was revisited in a broader setting, pertaining to more general lattices with hexagonal lattices with hexagonal symmetry [160], but taking the honeycomb lattice as an example. Already briefly mentioned in section 9.4.1, the main result of this work and subsequent studies [162, 163] was the prediction of a thermal phase transition to a uniaxial translational symmetry broken spin density wave. In all of the hexagonal lattices we consider in this work, both types of spin density wave states, the uniaxial and the chiral density waves, fit into the scheme of lifting particle-hole triplet condensates with specific symmetry from the corresponding spinless site ordered states. More specifically, they can be understood by consering a single root state, the A_1 symmetric site ordered state for each of the lattices. This is most easily demonstrated for the case of the triangular lattice.

10.2.1 Spin density wave states

The A_1 symmetric site ordered state was given in equation (9.234). There are two rather straightforward ways to take this as a root state and make it spinful. One is obvious: just create two copies for both spin species and give them a relative minus sign. This yields

$$\langle \hat{\psi}_\sigma^\dagger(\vec{k} + \vec{Q}_\mu)\hat{\psi}_{\sigma'}(\vec{k}) \rangle = \frac{1}{\sqrt{3}}\Delta_{\text{uniax}}\, \sigma_{\sigma\sigma'}^3, \qquad (10.7)$$

and it exactly corresponds to the uniaxial spin density wave. It represents a manifestly translational symmetry broken state, preserving however C_{6v} (or alternatively D_6) symmetry, up to global rotation. In real space we can denote it as

$$\sigma^3 \mathcal{M}_{3\mu} \xi_\mu(\vec{x}), \quad \mathcal{M}_{31} = \mathcal{M}_{32} = \mathcal{M}_{33} = 1. \tag{10.8}$$

Following equation (10.4) we have already discussed this possibility as a case where translations cannot be saved by global spin rotations. This is different for the second way of incorporatig the spin degree of freedom, which is

$$\langle \hat{\psi}_\sigma^\dagger(\vec{k} + \vec{Q}_\mu) \hat{\psi}_{\sigma'}(\vec{k}) \rangle = \frac{1}{\sqrt{3}} \Delta_{\text{chiral}} \, \sigma_{\sigma\sigma'}^\mu. \tag{10.9}$$

Each of the order parameter components $\vec{Q}_\mu$ is associated with a different spin Pauli matrix, and in real space this can be represented as

$$\sigma^i \mathcal{M}_{i\mu} \xi_\mu(\vec{x}), \quad \mathcal{M} = I, \tag{10.10}$$

where I is the unit matrix. Now translations can be compensated by global spin rotations and the point group operations must be combined with global spin rotations as well to leave the spin density wave invariant. In particular, the effect of reflections on $\vec{\xi}$ always contains the element Y, which we have mentioned to be an improper element of $O(3)$. Indeed, $-Y$ is a rotation of π around the z-axis, followed by a rotation of $-\pi/2$ around the y-axis. Hence, the chiral spin density wave state is odd under all reflections, indeed a necessary condition to host a QAH effect which is a property well-established for this particular spin density wave [30] and its generalizations to other hexagonal lattices [40, 209, 210].

10.2.2   Spin-flux ordered states

As a second class of spinful condensates on the triangular lattice, we now focus on a particularly interesting combination of spin and flux ordered states. Spin density waves break time-reversal symmetry and so does flux order. Above we have seen that the chiral spin density waveof equation (10.9) causes a spectral gap and leads to a QAH effect. The same is true for the flux ordered state contained in the decomposition (9.232) and explicitly defined in equation (9.239). This motivates the question whether symmetric combinations of spin and flux order exist, which are possibly energetically favorable and host nontrivial physical effects. Since both constituents of such spinful flux ordered states, i.e. the spin part and the flux part, are time-reversal odd, the combination of the two should be time-reversal symmetric. Even more strikingly, not only are such states be time-reversal invariant, lattice symmetries such as

reflections and translations which are broken by the constituent orders may be resurrected, as global spin rotations can be employed to bring the mean field Hamiltonian back to itself. We will now demonstrate this using two examples on the triangular lattice, which however easily generalize to other well-known hexagonal lattices, i.e. the honeycomb and kagome lattices.

In case the triangular lattice we have derived a flux ordered state transforming as A_1 and given in equation (9.239). Translational symmetry is manifestly broken in this state. To see how appropriate spinful versions of this state can be constructed which recover (part of) the broken lattice symmetries, it is most convenient to adopt the real space perspective [see also equation (9.238)]. This requires three matrices $\mathcal{M}_i$, one for each bond direction, in the same way as three $\vec{\zeta}_j$ are required for any bond order including flux order. Following equation (9.238) it was shown that flux order is specified by $\vec{\zeta}_1 = \vec{\zeta}$, $\vec{\zeta}_2 = X\vec{\zeta}$ and $\vec{\zeta}_3 = X^T\vec{\zeta}$ with $\vec{\zeta} = [1, -1, 0]^T$. Spin-bond ordered states are then generically specified by

$$\sigma^i[\mathcal{M}_j]_{i\mu}\xi_\mu(\vec{x}), \tag{10.11}$$

and here we construct them explicitly by embedding the $\vec{\zeta}_j$ in the matrices $\mathcal{M}_j$. One such embedding yields a highly symmetric electronic state and it is obtained by putting the $\vec{\zeta}_j$ on the diagonal of the corresponding $\mathcal{M}_j$, with all off-diagonal elements zero. As both the $\mathcal{M}_j$ matrices and the G_j matrices representing the translations only have diagonal elements, they commute, having the consequence that translations can be compensated by global proper spin rotations. Mathematically this embedding can be concisely written as

$$[\mathcal{M}_j]_{i\mu} = \zeta_j^\mu \delta_{i\mu}. \tag{10.12}$$

The flux ordered state of equations (9.238) and (9.239) is odd under all reflections. In the presence of spin structure global spin rotations can recover these symmetries. Taking the reflection σ_v as an example, we have that

$$\vec{\sigma} \cdot \mathcal{M}_j \cdot \vec{\xi}(\vec{x}) \to \vec{\sigma} \cdot \mathcal{M}_j \cdot Y\vec{\xi}(\vec{x}), \tag{10.13}$$

where it is important to note that the reflection exchanges $j = 1$ and $j = 2$ and maps $j = 3$ to itself. We then find that $\mathcal{M}_3 Y = -Y\mathcal{M}_3$ and $\mathcal{M}_1 Y = -Y\mathcal{M}_2$, which proves that the proper rotation $-Y$ compensates for the reflection, reinstitating it as a symmetry. Hence, the only symmetry broken by this particular density wave state is spin-rotation symmetry.

A second natural embedding of the $\vec{\zeta}_j$ is to associate each of the $\vec{\zeta}_j$ with a different direction in spin space, i.e. to choose a different spin projection for each bond direction $\vec{x}_j$. This can be concisely captured by the expression

$$[\mathcal{M}_j]_{i\mu} = \zeta_j^\mu \delta_{ij}, \tag{10.14}$$

where δ_{ij} associates the spin label i with the bond label j. This however has the consequence that the matrices $\mathcal{M}_j$ are not diagonal, which precludes the recovery of translational invariance. Even though translational invariance is now manifestly broken, we can recover the reflections as $\mathcal{M}_3 Y = -Y\mathcal{M}_3$ and $\mathcal{M}_1 Y = -Y\mathcal{M}_2$ still holds. We conclude that this embedding yields a spin-rotation symmetry and translational symmetry broken state, which preserves the C_{6v} (or D_6) operations.

The real space perspective is perhaps the most convenient in highlighting the symmetry properties. Transforming to momentum space gives the condensate functions given by

$$\langle \hat{\psi}_\sigma^\dagger(\vec{k} + \vec{Q}_\mu)\hat{\psi}_{\sigma'}(\vec{k})\rangle = i\Delta_{\text{Dirac}}\zeta_j^\mu \cos k_j \; \sigma_{\sigma\sigma'}^\mu, \tag{10.15}$$

(no summation over μ on the right hand side) in case of the first embedding, and

$$\langle \hat{\psi}_\sigma^\dagger(\vec{k} + \vec{Q}_\mu)\hat{\psi}_{\sigma'}(\vec{k})\rangle = i\Delta_{\text{QSH}}\sum_j \zeta_j^\mu \cos k_j \; \sigma_{\sigma\sigma'}^j, \tag{10.16}$$

in case of the second embedding. The spectral properties of the mean field Hamiltonian corresponding to these spin-flux (or spin-bond) ordered states turn out to be rather intriguing. We now discuss them in more detail, which will explain the labeling Δ_{Dirac} and Δ_{QSH}. We start with the highly symmetric state given in equation 10.15.

The mean field spectrum of the highly symmetric state given in equation (10.15) is presented in Fig. 10.4. We observe that the spectrum consists of four bands, which is a consequence of a combined time-reversal symmetry and inversion symmetry, mandating a two-fold degeneracy for each energy level at every $\vec{k}$. The high symmetry of this state leads to additional spectral degeneracies, the most notable being the four-fold degeneracy at all the M' points. The nested Fermi surface at filling $n = 3/4$ is gapped out except for these isolated remaining degeneracies at the M' points, which we soon show follows from the fact that all lattice symmetries are essentially preserved. In that sense, the remaining degeneracies are very similar to the isolated degeneracies of the staggered flux order on the square lattice [see equation (9.100) and Section 9.3.2]. In the latter case, degeneracies at isolated points in the reduced Brillouin zone define Dirac nodes, i.e. in the vicinity of these points the dispersion is linear. The same is true in the present case. At each of the three M' points of the low-energy excitations are described a pair of Dirac nodes transforming into each other under the time-reversal operation, which is the reason we have denoted the state as Δ_{Dirac}. The square lattice staggered flux state breaks some lattice symmetries, in addition to time-reversal symmetry, but preserves spin rotation symmetry. The present spin-flux ordered state does not break any lattice symmetries and preserves time-reversal, but it breaks spin rotation symmetry. Furthermore, the low-energy theory of the staggered flux state consists of two Dirac nodes instead of
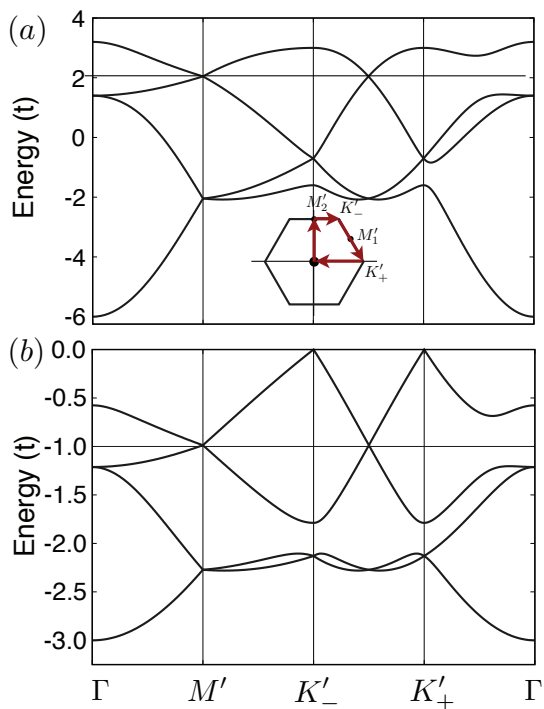
Figure 10.1: (a) Energy bands of the triangular lattice in the presence of the triplet density wave state given in equation (10.15). At the $\vec{M}'$ points in the reduced Brillouin zone the red circles point to the Dirac nodes. (b) Mean field spectrum of the equivalent state on the honeycomb lattice.

six (two for each of the three M' points). In that respect, the spin-flux ordered state is reminiscent of the three dimensional spin-orbit coupled diamond lattice model [3], which at half filling gives rise to a low-energy $3D$ Dirac theory at three inquivalent points in the $3D$ Brillouin zone. We come back to this reminiscence below.

We first show explicitly that the Dirac nodes at the $\vec{M}'$ points are protected by the symmetries which leave them invariant. Crucially, this includes the translations combined with global spin rotations and we use the relation between lattice operations and spin rotations establsihed in Appendix C.3. For the sake of definiteness we choose $\vec{M}_2'$ to demonstrate the degeneracy. The basis state at the $\vec{M}_2'$ point takes the form

$$\hat{\Phi}_{\vec{M}'} = \begin{bmatrix} \hat{\psi}_\sigma(\vec{M}_2') \\ \hat{\psi}_\sigma(\vec{M}_2' + \vec{Q}_1) \\ \hat{\psi}_\sigma(\vec{M}_2' + \vec{Q}_2) \\ \hat{\psi}_\sigma(\vec{M}_3' + \vec{Q}_3) \end{bmatrix}, \tag{10.17}$$

where σ labels the spin degree of freedom. In order to analyse the effect of lattice symmetries we choose a set of Pauli matrices σ^i to act on the spin degree of freedom, a set of matrices τ^i to act within the blocks $(\vec{M}_2', \vec{M}_2' + \vec{Q}_1)$ and $(\vec{M}_2' + \vec{Q}_2, \vec{M}_2' + \vec{Q}_3)$, and a set matrices ν^i to act on the block degree of freedom. It turn out to be convenient to start with the inversion C_2, which has the effect

$$C_2 \quad \rightarrow \quad \begin{bmatrix} \hat{\psi}_\sigma(-\vec{M}_2') \\ \hat{\psi}_\sigma(-\vec{M}_2' + \vec{Q}_1) \\ \hat{\psi}_\sigma(-\vec{M}_2' + \vec{Q}_2) \\ \hat{\psi}_\sigma(-\vec{M}_3' + \vec{Q}_3) \end{bmatrix} = \nu^1 \hat{\Phi}_{\vec{M}'}. \tag{10.18}$$

From this we conclude that the Hamiltonian at $\vec{M}_2'$ can only have terms $\sigma^i \tau^j$ or $\sigma^i \tau^j \nu^1$, where it is understood that $i, j = 0, 1, 2, 3$. The translation $T(\vec{x}_2)$ is associated with G_2 and can be compensated by a rotation around the x-axis by π, which gives

$$T(\vec{x}_2) \quad \rightarrow \quad -i\sigma^1 \nu^3 \hat{\Phi}_{\vec{M}'}. \tag{10.19}$$

This leaves us with allowed terms τ^j, $\sigma^1 \tau^j$, $\sigma^2 \tau^j \nu^1$ and $\sigma^3 \tau^j \nu^1$. The translation $T(\vec{x}_3)$ is associated with G_3 and a rotation by π around the y-axis will make it a symmetry. The action on the basis state is

$$T(\vec{x}_3) \quad \rightarrow \quad -i\sigma^2 \tau^3 \hat{\Phi}_{\vec{M}'}, \tag{10.20}$$

which leaves us with the following allowed terms

$$\tau^3, \ \sigma^1\tau^1, \ \sigma^1\tau^2, \ \sigma^2\nu^1, \ \sigma^2\tau^3\nu^1,$$
$$\sigma^3\tau^1\nu^1, \ \sigma^3\tau^2\nu^1. \tag{10.21}$$

What is left to consider is the two reflections which leave $\vec{M}_2'$ invariant. We consider $C_2\sigma_v$, which leads to

$$C_2\sigma_v \quad \rightarrow \quad -ie^{i\pi\sigma^2/4}\sigma^3 \begin{bmatrix} 1 & & & \\ & & & 1 \\ & & 1 & \\ & 1 & & \end{bmatrix} \hat{\Phi}_{\vec{M}'}. \tag{10.22}$$

The spin rotation $-ie^{i\pi\sigma^2/4}\sigma^3$ is the global spin rotation necessary to compensate Y. This transformation leads to the immediate exclusion of the terms $\sigma^2\tau^3\nu^1$ and $\sigma^2\nu^1$. The term τ^3 is clearly left invariant. The other four terms must be combined in order to represent invariant terms, and the final terms which are allowed by symmetry are

$$\tau^3, \ \tau^1(\sigma^1 - \sigma^3\nu^1), \ \tau^2(\sigma^1 - \sigma^3\nu^1). \tag{10.23}$$

Subjecting them to a basis transformation $e^{-i\pi\sigma^1\nu^1/4}e^{i\pi\sigma^3/8}$ brings them into a very simple form, and we obtain $\sigma^1\tau^1$, $\sigma^1\tau^2$ and τ^3. These three matrices anti-commute between each other and this leads to the conclusion that the most general symmetry allowed Hamiltonian at the $\vec{M}'$-points, $\mathcal{H} = m_1\sigma^1\tau^1 + m_2\sigma^1\tau^2 + m_3\tau^3$, has two eigenvalues $\pm\sqrt{m_1^2 + m_2^2 + m_3^2}$, with each eigenvalue being fourfold degenerate.

This proves that the fourfold degeneracy at the $\vec{M}'$ points is in fact symmetry protected. As we have already shown in quite a number of cases before, such as the square lattice π-flux state in Section 9.3.2, one can take the low-energy Dirac description of this spin-flux state as a starting point for studying the effect of additional symmetry breaking. We recall that in case of the square lattice π-flux state all lattice symmetries were left unbroken, because a gauge transformation could be employed to bring the Hamiltonian back to itself. In the present case a global spin rotation acts as the unitary operation bringing the Hamiltonian back to itself, and in the same way as was presented in Section 9.3.2 we can list the effect of lattice symmetry breaking in terms of the Dirac language. A key aspect of the lattice symmetric spin-flux state is the need to be careful to account for the spin rotation symmetry breaking and the nontrivial spin structure of the Dirac spinors. We leave such a detailed account of the low-energy Dirac theory following from the spin-fux state for future study.

Let us now come to the second spin-flux state given in equation (10.16) and in equation (10.14). We had already observed that translational symmetry is broken
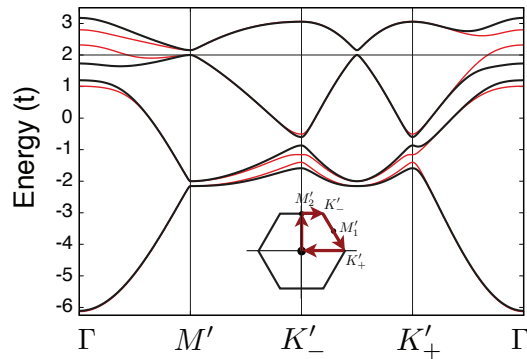
Figure 10.2:   Energy bands of the triangular lattice in the presence of the triplet density wave state given in equation (10.16). The black (red) spectrum corresponds to the density wave strength $\Delta_{\text{QSH}} = -0.4$ ($\Delta_{\text{QSH}} = 0.4$). An energy gap emerges in case of $\Delta_{\text{QSH}} < 0$ at the $\vec{M}'$ points in the reduced Brillouin zone and an evaluation of the inversion eigenvalues (C_2 eigenvalues) at these $\vec{M}'$ shows that the insulating ground state is a QSH state. Note that all bands are doubly degenerate due to the presence of both time-reversal and inversion symmetry. Inset shows the path through the reduced BZ.

in this state and we therefore do not a priori expect any degeneracies at the M'-points other than the ones required by the presence of both time-reversal and inversion symmetry. The mean field energy bands are presented in Fig. 10.2, where we show two different spectra corresponding to positive and negative sign of the density wave strength. The spectra show that indeed no additional degeneracies exist and in case of $\Delta_{\text{QSH}} < 0$ a full energy gap is emerges, which is however second order in the density wave strength. For the resulting insulating state we can calculate the $\mathbb{Z}_2$ topological invariant written in equation (9.42) and we find that this state is a non-trivial QSH state.

This shows that embedding flux order in a spinful setting can lead to two distinct time-reversal invariant topological states of matter: a $2D$ symmetry protected Weyl semimetal and an insulating QSH state. Both of these spinful density waves preserve all point group symmetries, but they differ with respect to translations. The $2D$ Weyl semimetal preserves all translations, which is the origin of its symmetry protection.

10.3   Honeycomb lattice

In order to inspire confidence in the general applicability of the results on M-point ordered triplet density waves in systems with hexagonal symmetry, which we have presented with the help of the triangular lattice above, we briefly show how these results carry over to the honeycomb lattice. Specifically, we will discuss the honeycomb lattice realizations of the uniaxial and chiral spin density waves, as they have generated considerable interest recently [40, 160, 162, 163]. In addition, we show explicitly that the fully symmetric spin-flux ordered state exists on the honeycomb lattice as well and has the same key properties as on the triangular lattice.

In the same way as for the triangular lattice, the starting point for the spin density waves are the expressions for the site ordered states derived in Section 9.4.1. Site ordered states transforming as irreducible representations of the lattice symmetry group were specified by two vectors, i.e. $\vec{\zeta}_A$ and $\vec{\zeta}_B$ [see equations (9.169) and (9.170)], and the job here is to embed them in two matrices $\mathcal{M}_A$ and $\mathcal{M}_B$ representing the spin order. With this sublattice degree of freedom taken into account, the general spin ordered state is written as

$$\sigma^i[\mathcal{M}_j]_{i\mu}\xi_\mu, \tag{10.24}$$

and using that general form we can write the uniaxial spin density waves obtained from the site order expressions as

$$[\mathcal{M}_A]_{3\mu} = \zeta_A^\mu, \quad [\mathcal{M}_B]_{3\mu} = \pm\zeta_B^\mu. \tag{10.25}$$

We had found two site ordered states transforming as $1D$ representations of C_{6v}, an A_1 state and a B_2, which are distinguished by the relative sign between the sublattices. In case of uniaxial spin density wave order, this is captured by the overall sign of $\mathcal{M}_B$, as equation (10.25) shows. The specific uniaxial spin density wave reported in [160, 162, 163] is corresponds to the choice $[\mathcal{M}_B]_{3\mu} = +\zeta_B^\mu$ and breaks translational symmetry but preserves the rotations and reflections. The mean field spectral properties, in particular the emergence of a QBC point at Γ [163], have been mentioned already in Section 9.4.1, as they follow straightforwardly from considering the two spin species separately.

The second choice for embedding the $\vec{\zeta}_j$ in the matrices $\mathcal{M}_j$ is to put the vectors on the diagonal of the corresponding matrices. This can be simply written as

$$[\mathcal{M}_A]_{i\mu} = \zeta_A^\mu \delta_{i\mu}, \quad [\mathcal{M}_B]_{i\mu} = \pm\zeta_B^\mu \delta_{i\mu}. \tag{10.26}$$

As we have already observed in case of the triangular lattice spin density waves, the fact that the matrices $\mathcal{M}_j$ only have diagonal entries has the consequence that the effects of lattice translations can be compensated by global spin rotations. Both spin states (distinguished by $\pm$) are therefore translationally invariant. The state constructed from the A_1 site ordered state, i.e. the $+$ choice, still preserves all rotations, but breaks all reflections as they can only be compensated by improper elements of $O(3)$ and therefore this spin density wave has lower symmetry then its site ordered parent state (A_2 instead of A_1). The other spin density wave, coming from the B_2 site ordered state, becomes a B_1-symmetric state. The broken reflections become good symmetries again, as the improper $O(3)$ rotation necessary to bring the state back to itself provides an additional minus sign. In turn, the minus sign coming from the improper rotation is responbible for the breaking of the σ_d reflections.

The spin density wave transforming as A_2 first appeared in the literature as the honeycomb lattice generalization of the chiral triangular lattice spin density wave [40]. Indeed, it has the same symmetry properties and since it breaks all reflections in addition to time-reversal, it can host a Quantum Anomalous Hall effect. In [40] it was demonstrated that the formation of this noncoplanar spin density wave gaps out the Fermi surface at the van Hove singularities and the the insulating ground state is indeed a Chern insulator. Furthermore, it was shown in [163] that the emergence of the noncoplanar electronically insulating spin density wave at very low temperatures can be understood starting from the uniaxial spin density wave. The low-energy theory of the electronic degrees of freedom takes the form of a QBC point, as was noted in Section 9.4.1, and when the uniaxial spin density wave starts to develop noncoplanar components at low temperatures [160] this introduces a time-reversal breaking mass in the low-energy description. A gapped QBC point necessarily leads to a QAH ground state. Hence, we see how the spin density waves we simply obtained from

site ordered states transforming as $1D$ representations of the point group, are related to each other and are found to be the lowest energy states in both a mean-field treatment [40] and a Ginsburg-Landau free energy approach [160].

It is interesting to note another property of the noncoplanar spin density waves specified by equation 10.26 and which transform as A_2 and B_1 under rotations and reflections. As was mentioned, these spin density waves are translationally invariant up to global spin rotations. In fact, if one considers them as classical spin states, they are invariant under all lattice symmetries, as the proper or improrer nature of the $O(3)$ rotation needed to compensate a given lattice operation is immaterial. As such, these two spin states are examples of what has been named *regular magnetic orders* [208], i.e. classical spin states which preserve all lattice symmetries up to a global spin rotation. In [208] all regular magnetic orders were derived for the triangular, honeycomb and kagome lattices and it is a simple matter to check that all spin states with a quadrupled unit cell, meaning ordering at the M-points, coincide with the spin density waves we construct from site-order by embedding them in a translationally invariant way. The formalism developed and presented in Section 9.4.1 to find the ordered M-point states thus systematically yields the specific subset of regular magnetic orders modulated by M-point vectors.

We conclude this brief overview of honeycomb lattice spin triplet density waves by commenting on the honeycomb lattice version of the spin-flux state which we introduced above for the triangular lattice. We simlpy start from the M-point ordered flux state which transforms as A_2, which was obtained from triplet F_2 in Section 9.4.1. The spinful version of this state, which preserves all lattice symmetries and time-reversal symmetry, is straightforwardly obtained by associating each $\vec{Q}_\mu$ with a different σ^μ, giving

$$\langle \hat{\psi}_{i\sigma}^\dagger(\vec{k} + \vec{Q}_\mu)\hat{\psi}_{j\sigma'}(\vec{k})\rangle = [\hat{\Delta}_\mu(\vec{k})]_{ij}\sigma^\mu_{\sigma\sigma'}, \tag{10.27}$$

(no sum implied on the RHS). The explicit expression of the $\hat{\Delta}_\mu(\vec{k})$ have been given in 9.4.1 following equation 9.186 and can just be taken from there. The mean field energy bands of the honeycomb spin-flux ordered state are presented in Fig. 10.4(b), which immediately shows the resemblance between the honeycomb and triangular lattice spectra. In fact, the main point we wish to stress here is that the key features of the electronic symmetries and spectra are shared between these hexagonal symmetry spin-flux orders. While spin-rotation symmetry is broken, lattice symmetries are all preserved up to global spin rotation and time-reversal symmetry is recovered by combining flux and spin type order. At the same time, the low-energy theory is in both cases (in all cases in fact) governed by a Dirac equation at each of the M'-points.

10.4   Common features of condensates with M-point order

To conclude this section on M-point spin triplet density waves with hexagonal symmetry, we the take the opportunity to summarize and review some of the key features of such density waves.

The exposition of spinful density waves presented above has made it clear how spin density waves with specific symmetry, i.e. transforming according to irreducible representations of the lattice symmetry group, can be obtained from corresponding spinless density waves. In case of the pure spin density waves (no bond or flux order), we have demonstrated both for the triangular and the honeycomb lattices that site ordered states can be taken as "parent" states, by embedding them in a spinful setting. Site ordered states with M-point ordering vectors on the triangular lattice transform according to the representation $F_1 = A_1 \oplus E_2$ (see Section 9.4.3), while honeycomb lattice site order was shown to be decomposed as $F_1 \oplus = A_1 \oplus B_2 \oplus E_1 \oplus E_2$ (see Section 9.4.1). Only focusing on the $1D$ representations (it would work in the same way for $2D$ representations), i.e. the two A_1 states and the B_2 state, we have outlined two ways of constructing spin density waves of dinstinct symmetry. The first may be referred to as the uniaxial scheme, in which the spin density waves inherit the symmetry from the site ordered states, i.e. they are also A_1 and B_2 states but break spin-rotation invariance partially. The second would be chiral scheme, in which the symmetry of the spin density waves changes from A_1 to A_2 and B_2 to B_1 ($= B_2 \otimes A_2$) as compared to the parent site order. In the chiral scheme the resulting spin density wave states are non-coplanar. These schemes can be directly applied to the kagome lattice, for which we derived the $1D$ site order representations A_1, B_1 and B_2. From these we can construct a set of uniaxial spin density waves of the same symmetry (A_1, B_1 and B_2), or a set of chiral spin density waves with representations obtained from multiplication by A_2 (A_2, B_2 and B_1).

Let us take a closer look at the unaxial A_1 and chiral A_2 spin density waves on each of these three lattices. The spin density waves are graphically represented in Fig. 10.3. On the left side of (a)-(c) we show the uniaxial A_1 states, from which we see that while on the triangular and honeycomb lattices the spin lengths are not equal, the spin moments of the kagome lattice state are of equal length. The spin length of all the states on the right side of Fig. 10.3(a)-(c) is necessarily equal due to translational invariance. We observe a deep connection between the three unaxial A_1 and chiral A_2 spin density waves, as we find that they not only have the same symmetry, but also the same electronic properties. The uniaxial spin density waves (see also Section 9.4.1) all share the same low-energy description at Γ of the reduced (folded) Brillouin zone. Specifically, for appropriate fillings these are semimetallic states with a QBC point for

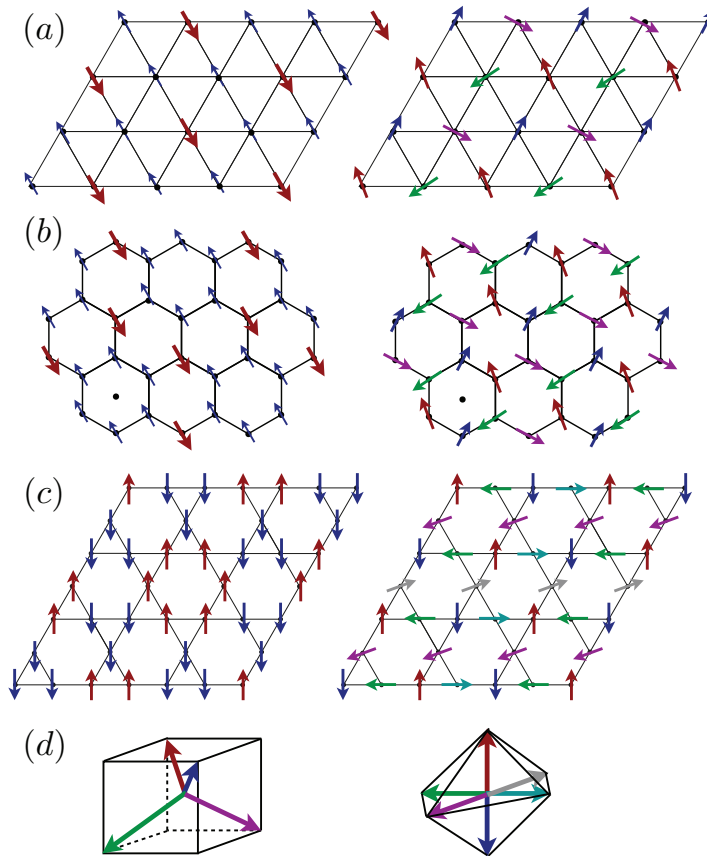**Figure 10.3:** Spin density waves of hexagonal lattices with A_1 and A_2 symmetry obtained from embedding site order in a spinful setting (a) A_1 (left) and A_2 (right) density waves of the triangular lattice, and the same for (b) the honeycomb lattice and (c) the kahome lattice. (d) shows the non-coplanar spins of the A_2 states of the triangular and honeycomb lattices (left), and the kagome lattice (right).
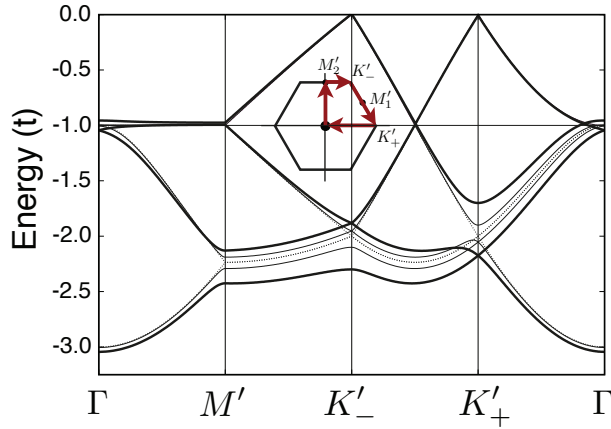
Figure 10.4: Honeycomb lattice energy bands for the B_1 chiral spin density wave. Thin dashed lines correspond to the free honeycomb band structure, solid thin lines to a weakly developed B_1 spin density wave and thick solid lines to a density wave with considerable strength. Between the lowest two bands a (doubly degenerate) Dirac node appears at K'_+.

one of the spin species, also referred to as half metallic states [160], while excitations involving the other spin species are gapped. Instead, the chiral spin density waves are all gapped for appropriate fillings and the insulating ground state is a QAH state. As was pointed out in [163], the A_1 and A_2 spin density waves are closely related in the sense that a smooth interpolation from the A_1 state to the gapped A_2 exists, which has the low-energy interpretation of gapping out the QBC point by a manifest breaking of time-reversal symmetry. The symmetry perspective developed in this work reveals and formalizes both the deep connection between the A_1 and A_2 density waves and the lattice independence of their (low-energy) electronic properties.

Interestingly, not only the A_1 and A_2 spin density waves have properties which transcend the lattice specific setting, but also the two chiral B_1 spin density waves on the honeycomb and kagome lattices. Incidentally, such a state does not exist for the triangular lattice. At the van Hove fillings these states lead to a change in shape of the Fermi surface that is schematically captured by the lower left part of Fig. 9.7. This is in agreement with symmetry, as time-reversal symmetry is broken by the spin density wave and B_1 symmetry implies that the reflection planes bisecting the vertices of the BZ are still good reflection planes, while the other set of reflections is broken. The most important feature of the mean field spectrum corresponding to these states, both

on the hobeycomb and the kagome lattice, is the appearance of Dirac nodes at K'_+ (or K'_-, depending on the sign of the order parameter) in the form isolated touchings between the *lowest two* bands. That they should appear only at one of the two valleys which are each others time-reversal partners is again in agreement with the breaking of this symmetry.

A different class of spinful density waves is derived from spin rotation invariant bond ordered states, or, more specifically flux ordered states. The structure of this derivation is essentially the same as for the pure spin density waves. Starting from the A_2 flux ordered states, which exist for all three hexagonal lattices considered in this work and come from the F_2 representation, we have discussed three schemes of constructing spin rotation symmetry breaking density waves. The first is straightforward and involves the global exhange of $\delta_{\sigma\sigma'}$ and $\sigma^3_{\sigma\sigma'}$ (the "two copies with opposite sign" scenario), creating an insulating time-reversal invariant density wave with the same mean field spectrum for up and down electrons, but opposite Chern numbers $C_\uparrow - C_\downarrow \neq 0$. The second scheme amounts to assigning a different spin Pauli matrix σ^i to each of the three hopping directions of a hexagonal lattice, i.e. $\vec{x}_i$. This spin-flux ordered state fully breaks spin rotation symmetry, and translational symmetry, while preserving all point group operations. The mean field spectrum is gapped and corresponds to a QSH state. In the third scheme one assigns a different Pauli matrix σ^i to each of the three M-point ordering momenta $\vec{Q}_\mu$. For the triangular lattice we showed in detail how such an embedding preserved all lattice symmetries, including the translations that are broken in the M-point flux ordered state. As a consequence of this high degree of symmetry there are protected degeneracies at the M' points of the reduced Brillouin zone, in addition the Kramers degeneracy mandated by time-reversal symmetry. The spectrum disperses linearly in all directions around these M' points making this particular spin-flux ordered state a Dirac semimetal. Time-reversal symmetry requires two degenerate Dirac nodes per M' point. To summarize these three schemes, all of them yield time-reversal invariant yet spin rotation symmetry broken density waves. In case of the first two, they transform as A_1 but break translational symmetry. The third scheme of constructing spinful bond density waves results in a fully lattice symmetric state. Again, these statements apply to all three lattices and should be considered a property of the hexagonal symmetry class more than of particular lattices.

The highly symmetric nature of the Dirac semimetal is a result of the embedding of the A_2 flux ordered state in a spinful setting. It allows for translations to be dressed with global spin rotation to be become good symmetries again, inspite of the underlying M-point order. Furthermore, the reflections broken in the flux state become good symmetries again, because they come dressed with improper rotations restoring the them as symmetries. The protection of the Dirac semital at the M' critically relies on the presence of translational symmetry, as we have seen in Section 9.4.1. This not
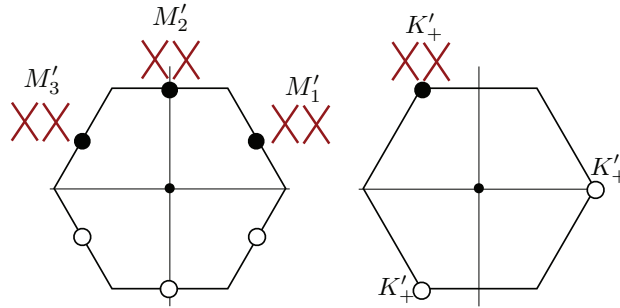
Figure 10.5: (left) Schematic representation of the double Dirac nodes at the three *inequivalent* M'-points of the reduced hexagonal Brillouin zone in the presence of the spin-flux density wave. (right) Schematic representation of the double Dirac nodes at the three *equivalent* K'_+-points in the presence of B_1 symmetric spin density wave order on for instance the honeycomb or kagome lattice.

only illustrates the principle of global spin rotation equivalenceitself, i.e. applying lattice operations yields a unitarily equivalent Hamiltonian, but it also exemplifies its importance for protecting topological semimetals.

The fully lattice symmetric spin-flux density wave states and the B_1 spin density wave states are two examples of classes of states for which translational symmetry is preserved. In both cases translational invariance plays a role in the protection of the semimetallic Dirac points and their twofold degeneracy. Both semimetallic states constitute new symmetry-protected topological semimetals. One breaks time-reversal symmetry the other preserves it. The two Dirac theories are schematically summarized in Fig. 10.5. In case of the time-reversal symmetric spin-flux state the low-energy Dirac theory consists of six Dirac nodes, two for each inequivalent M' point. Instead, the B_1 symmetric time-reversal breaking states have a double node at the K'_+ (or K'_-) point.

The concept of global spin rotation equivalence in relation to lattice symmetries was introduced for classical spin models in [208], which coined the notion of classical spin liquids. They are defined as classical spin states which do not break any lattice symmetries, up to a global $O(3)$ spin rotation. In [208] a projective symmetry group analysis was employed to systematically derive spin states which satisfy this condition for selected lattices. For hexagonal lattices, a subset of these classical spin liquids is build from M-point ordering vectors. This subset of classical spin liquids is automatically generated as a by-product of the symmetry organization of density

waves detailed in this work. To see this, let us go back again to spin density waves obtained from site order. In the second scheme of embedding, i.e. the chiral scheme, we put the vectors specifying site order $\vec{\zeta}_i$ (i labeling the sublattice) on the diagonal of the corresponding matrix $\mathcal{M}_i$, which restores translational invariance. If instead of constructing a an electronic spin density wave, i.e. $\vec{\sigma} \cdot \vec{\mathcal{M}}_i$, for the which the $\mathbb{Z}_2$ content of $O(3) = \mathbb{Z}_2 \times SO(3)$ matters, we construct a classical spin state $\vec{\mathcal{S}}_j(\vec{x})$ of the form

$$\vec{\mathcal{S}}_j(\vec{x}) = \vec{\mathcal{M}}_j(\vec{x}) = [\vec{\mathcal{M}}_j]_\mu \xi_\mu(\vec{x}), \tag{10.28}$$

we have obtained a classical spin liquid. To put it differently, if we interpret the chiral spin density waves as classical spin states, they satisfy the criteria for a classical spin liquid. Take for instance the kagome lattice. The kagome lattice allows for three M-point ordered classical spin liquids [208], which are immediately obtained from the three site ordered states A_1, B_1 and B_2 by putting the vectors $\vec{\zeta}_i$ (see Section) on the diagonal of $\mathcal{M}_i$. We therefore close by mentioning that classical spin liquids may be obtained in straightforward manner by taking the $1D$ site order representations and embedding appropriately in spin space. Of course this requires specifying M-point order ahead of time.

CHAPTER 11

SUMMARY AND CONCLUSIONS

In this final section we give an account of the main results and conclusions that follow from this work. We summarize and discuss the key results of our work point by point.

(i) In this work we presented a detailed discussion of $2D$ particle-hole condensates from a symmetry perspective. For the square lattice and three representative hexagonal lattices we have decomposed all possible density waves for specified translational symmetry breaking based on lattice symmetries, yielding an arganization of these density waves in terms of basis functions of irreducible representations of the extended and bare points groups. Differentiating between site order (charge density waves), bond order (time-reversal preserving bond density waves), and flux order (imaginary bond density waves) has allowed for a gauge invariant classification of all distinct density waves just using a group theory toolkit.

(ii) The organization of density waves in terms lattice symmetries provided the framework to identify topological states of matter induced by interactions. In two dimensions there are two main classes of topological states: the QAH states which break time-reversal symmetry, and the QSH states which preserve time-reversal symmetry but must break spin rotation symmetry at least partially. When looking for candidate QAH states it is therefore sufficient to consider flux ordered states and spin density waves as these are time-reversal breaking states. Furthermore – and this is where the symmetry organization proves very powerful – only density wave formation breaking all reflection symmetries of the system can lead to QAH states,

meaning that only states transforming as A_2 allow for Chern insulators. Such states are straightforwardly identified within the group theoretical scheme producing a list of all possible flux ordered states of a given lattice and a given set of broken translations. We have demonstrated how known and well-studied flux ordered QAH states on for instance the honeycomb and kagome lattices (Haldane state [76] and chiral spin state [85]) follow directly from deriving and constructing flux states with proper symmetry.

In addition to these well-known QAH states, all of which do not break translational symmetry, we have shown the existance of a new class of QAH states of lattices with hexagonal symmetry, i.e. the flux ordered density waves. Guided purely by symmetry arguments we have identified flux density waves with M-point ordering vectors transforming as A_2 and leading to an insulating condensate ground state. Another class of M-point modulated QAH states on hexagonal lattices is given by the noncoplanar chiral spin density waves discussed in Section 10. The existence of such chiral states and their spontaneous QAH effects was shown for the triangular and honeycomb lattices in the context of local moment Kondo-Lattice [30, 40] and interacting single-band Hubbard models [160]. In the present work we show how these particular examples are part of a fundamental sequence of M-point hexagonal lattice spin density waves with a A_2 symmetry that do not break translational symmetry in spite of finite wave vector condensation. We refer to these states as part of a *fundamental sequence* since they all follow from the same underlying symmetry principle. Applying this principle to the kagome lattice, we identify a kagome lattice spin density wave with exactly the same properties.

In the context of interaction-driven topological insulating states the numerous possibilities arising from M-point order are particularly interesting as precisely the M-point vectors nest the Fermi surface of hexagonal lattices at the van Hove fillings where the density of states diverges. This inpsires hope that even infinitesimal interactions induce such states due to dominant instabilities towards such states. In fact, such an argument was put forward in case of triangular and honeycomb lattice spin density waves [160]. In contrast, interaction-induced topological states originating from low-energy Dirac fermions becoming massive, for instance within a mean field treatment of the honeycomb [84, 168], square [167] and kagome lattices [169, 170], require finite and large interaction strengths as a consequence of the linearly vanishing density of states at the Dirac points. This makes the scenario of spontaneously gapping out Dirac cones problematic, as recently shown in Refs. [211], because quantum fluctuations prevent the QAH state from fully developing.

The two sequences of hexagonal symmetry M-point ordered QAH states, i.e. flux order and spin density wave order, are of great significance for the second kind of topological states in $2D$, i.e. the QSH states. In this work we have explained how QSH states are trivially obtained from QAH states by constructing two copies of the

latter for each of the two spin species with a relative sign difference. In that case the condensate function is proportional to $\vec{N} \cdot \vec{\sigma}$, with $\vec{N}$ the vector order parameter in spin space. This implies spin rotation symmetry around $\vec{N}$ is not broken, leading to a quantized spin Hall conductance. Full breaking of spin rotation symmetry, for instance by Rashba-type terms, does not immediately destroy the QSH state, but is generally harmful to its existence, as is signaled by the spin Hall conductance being no longer quantized [1]. In this work we propose a class of hexagonal spin triplet condensates which constitute QSH phases characterized by a matrix order parameter $\mathcal{R}$ instead of a vector $\vec{N}$ and fully break spin rotation symmmetry. They derive from a combination of spin and flux ordering with M-point ordering vectors.

(iii) In this work we have demonstrated how interaction-induced semimetallic states are protected by lattice symmetries and the anti-unitary time-reversal symmetry. We have focused on two types of semimetallic states in $2D$, which are the Weyl semimetals (alternatively referred to as Dirac semimetal) and the QBC points. Both are characterized by topological winding numbers which rely on the presence of symmetries to make their definition and use meaningful. Our symmetry analysis of density waves provides a comprehensive and systematic framework to determine the symmetries which protect isolated degeneracies definining the semimetal. Both translations and global spin rotations can act as degeneracy protecting operations in combination point group elements.

In case of the square lattice the two density waves which are semimetals, $d_{x^2-y^2}$ (Weyl or Dirac semimetal) and d_{xy} (QBC), transform as $1D$ representations of the extended point group and one may therefore select symmetries thereof to prove the spectral degeneracy at high symmetry points of the Brillouin zone. For square lattice systems combinations of (bare) point group operations and translations can form good symmetries protecting degeracies. This is different in case of hexagonal lattice systems, where we found global spin rotations to have the potential to protect degeneracies for spinful M-point ordered condensates. In particular, we have seen how the chiral spin density waves are in fact translationally invariant states regardless of finite ordering vector condensation, which is a consequence of global spin rotations compensating the translation. Perhaps most remarkably, we have demonstrated how M-point modulated spin-flux density waves become symmetry protected semimetallic states and the protection crucially relies on global spin rotation equivalence.

In the presence of these spin-flux density waves, the nested hexagonal Fermi surface at van Hove fillings is gapped out except for the protected degeneracies located located at each of the inequivalent M' points of the reduced BZ (see Fig. 9.7). Degeneracies at the M' points are only protected if none of the lattice symmetries are broken. Indeed, we found in Section 9.4.1 that the degeneracy at M' is generally lifted by translational symmetry breaking. For the spin-flux density waves translations combined with (unitary) global spin rotations are symmetries and key in pro-

tecting the degeneracy. The spin-flux density waves only break spin rotation symmetry and preserve all lattice symmetries. The low-energy description around the degeneracy points at M' takes the form of a Dirac theory, but instead of the common double-node theory, it is a six-node theory, i.e. two nodes for each inequivalent M' point. As such the spin-flux density waves constitute a new $2D$ semimetallic state. Interestingly, it is possible to superimpose a spin rotation and time-reversal invariant density wave on this Dirac semital with the result of gappig out the Dirac nodes yielding an insulating QSH ground state. This is contrary to the canonical example of a spin-orbit coupling-induced Dirac mass in the spin-rotation invariant low-energy theory of graphene [1, 23]. In the latter case it is the *breaking* of spin rotation symmetry which induces a QSH mass gap.

In addition to these time-reversal invariant semimetallic states with six Dirac nodes, we have shown the emergence of another distinct semitallic state from time-reversal breaking spin density wave formation. Both the honeycomb and kagome lattices allow for translationally invariant M-point spin density waves with B_1 symmetry. The mean field spectrum of such a state is allowed to have Dirac nodes only at the K'_+ points of the reduced BZ, but not at the K'_-. We have found precisely this situation to occur for the B_1 M-point ordered spin density waves: two Dirac nodes at the equivalent K'_+ points (and none at K'_-) for commensurate electron fillings, which are however not equal to the van Hove fillings. As such, representing a time-reversal broken state, these density waves would appear to be similar to the square lattice $d_{x^2-y^2}$ state. It is however a truly distinct state, as it manifestly breaks time-reversal, instead of preserving a combination of time-reversal and translation. It therefore constitutes another new semimetallic state of hexagonal lattice systems.

We have seen examples of the second type of semimetals, the QBC points, in the context of both the square and hexagonal lattices. As noted, in case of the square lattice the d_{xy} state gives rise to a QBC point which is protected by a fourfold rotation and time-reversal symmetry. We have demonstrated that a QBC point can occur in hexagonal lattice systems for various cases of M-point ordering, as long as the system has C_{3v} symmetry. In particular, we have identified the occurance of QBC points as one of two possibilities in case of such M-ordering with C_{3v} symmetry within a low-energy description at the Γ point of the reduced BZ. Such a low-energy description is independent of the specific lattice. Generically QBC points can be destroyed by breaking the symmetries that protect it. Specifically, the opening of a gap is intrinsically connected to time-reversal symmetry breaking and it was shown recently [163] how the QBC of a uniaxial A_1 M-point ordered spin density wave is gapped out by developing a finite scalar spin chirality, reducing the symmetry to A_2. In the present work we embed this result in a general low-energy theory for M-point ordering in hexagonal lattices based on symmetry.

(iv) We have established a robust connection between the *symmetry* of density

waves and their *low-energy interpretation* within the framework of a Dirac theory. The back bone of this connection is the rule which assigns density waves transforming as $1D$ representations the meaning of generalized masses, either gapping out the spectrum or making the two valleys inequivalent. In turn, density waves transforming as $2D$ representations have the interpretation of gauge field components in the low-energy Dirac theory, shifting the Dirac nodes in momentum space. We have shown in case of the kagome lattice, where we apply this rule, how decomposing site, bond and flux order using group theory is sufficient to determine the nature of their electronic properties.

In particular, the symmetry organization of density waves provides a straightforward way to find density waves states which enter as gauge field components in the Dirac theory. Such states may arise as a consequence of electronic interactions, but could alternatively be induced by application of external fields such as strain or modulated substrate potentials [180]. Knowledge of which states correspond to gauge fields allows to assess in which systems such gauge fields may be generated by either one of those mechanisms. This opens up the possibility to address and study the physics of non-Abelian $SU(2)$ fields in a condensed matter setting in a general way.

(v) The organization of density waves as basis functions of irreducible representations of extended point groups reveals their degeneracies. Density waves which are partners belonging to a larger dimensional extended point group representation will be energetically degenerate. If there is a dominant electronic instability towards the formation of such a state, then it applies to all partners in the representation. An illustrative example of such kind of partnership is given by the two independent hexagonal lattice K-point density waves corresponding Kekule masses (see Sections 9.4.1 and 9.4.2). Both for the honeycomb and kagome lattices these transform as E_1', a $2D$ representation of C_{6v}''. This is reflected in the low-energy theory as they correspond to compatible Dirac mass gaps, making them energetically equivalent.

For hexagonal lattice M-point ordering the irreducible representations of the extended point group C_{6v}''' are all three-dimensional, a consequence of the three inequivalent M-points. The three partners of such a representation are energetically equivalent from an electronic instability point of view. If the system gains condensation energy by the formation of one of such states in the triplet, then it will gain energy linearly and independently by forming the other partners as well. This is why our convention of decomposing these $3D$ representations into sums of representations of the bare group is particularly useful and relevant. Each of those triplets is decomposed as the sum of a $1D$ and a $2D$ representation and the $1D$ representation corresponds to a state which is the most symmetric superposition of the partners which transform into each other under rotations (in other words behave as the $\vec{Q}_\mu$ vectors). We therefore expect these states, i.e. states transforming as $1D$ bare point group representations, to develop from electronic instabilities favoring the given triplet representation. Hence,

the symmetry organization gives insight into condensation energetics.

(vi) A large part of this work is devoted to hexagonal lattice density waves. We have discussed three prominent examples of hexagonal lattices and have found remarkable similarities. Again focusing on the case of M-point ordering, we have shown explicitly that density waves of the same symmetry have the same physical properties, independent of the lattice considered. To give an example, the uniaxial spin density waves of A_1 symmetry, which exist for all three lattices considered, are topological semimetals with a QBC point in either the spin-up or spin-down sector. The chiral spin density waves with A_2 symmetry, which are closely related to the uniaxial A_1 spin density waves, are all gapped for appropriate filling and correspond to a Chern insulating state. In addition, for both the honeycomb and kagome lattices there is a noncoplanar spin density wave with B_1 symmetry which induces Dirac points at the K'_+ (or K'_-) points for commensurate fillings ($n = 1/8$ for honeycomb, $n = 1/12$ for kagome). All of these key electronic characteristics are connected to the symmetry of the (spin) density wave and transcend the lattice specific setting. The same is true for the time-reversal invariant spin-flux density waves. We have explicitly shown the equivalent electronic properties for such a state on the triangular and honeycomb lattices. We found these particular density waves to break no other symmetry than spin-rotation symmetry, leading to a new kind of $2D$ semimetallic state not specific to a lattice structure.

The importance of symmetry rather than lattice structure also manifests itself in the context of K-point ordering. For instance, both for the honeycomb and kagome lattices, we found that any E'_1 doublet corresponds to two independent yet compatible Dirac masses. In case of the honeycomb lattice there only exists such a bond order doublet, while for the kagome lattice there is a site and bond order doublet. In the same way any E'_2 doublet leads to a Dirac valley inequivalence, separating the Dirac nodes in energy but not in momentum.

These examples mentioned here highlight the general conclusion that density waves with the same symmetry affect the electronic properties in the same way if the low-energy description of the electronic degrees of freedom is equivalent. Indeed, all the hexagonal lattices have an M-point nested Fermi surface at van Hove fillings and both the kagome and honeycomb spectra exhibit Dirac nodes. It is the symmetry of the density waves which is decides what happens to the electrons close to the Fermi surface or Fermi points.

Appendices

DETAILS OF LATTICES

In the present Appendix we collect all details and relevant definitions pertaining to the four lattices that have been treated in the main text. These include explicit expressions for lattice vectors, reciprocal lattice vectors, special ordering momenta, and the Hamiltonians for lattice fermions hopping on the respective lattices. We first give the details of the square lattice and then present details of the hexagonal lattices. In case of the triangular and honeycomb lattices we include expressions for the mean field orbital momentum basis functions. For both the honeycomb and kagome lattices we also provide a more detailed derivation of the lattice symmetries of Dirac matrices, the results of which are used in the main text. In case of the kagome lattice we provide more details on explicit expressions for density wave states discussed in main text.

Before we come to the individual lattices, let us list a number of general definitions applicable to all lattives in order to avoid repetition. In Section 9.1.1 the lattice basis vectors were defined as $\vec{x}_1$ and $\vec{x}_2$. In expressions for Hamiltonians in momentum space it is convenient to abbreviate the inner products $\vec{k} \cdot \vec{x}_i$ as k_i and we will consistently do so. In addition, we write T_i for the exponentials $T_i \equiv e^{i\vec{k}\cdot\vec{x}_i}$.
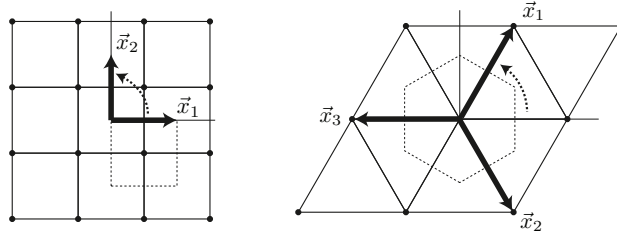
Figure A.1: Schematic picture of two of the four lattices considered in this work. (left) the square lattice, (right) triangular lattice. Lattice basis vectors are represented as thick back arrows, the hexagonal lattices also show $\vec{x}_3 = -\vec{x}_1 - \vec{x}_2$. The curved dashed arrows indicate the fourfold (C_4) and sixfold (C_6) rotations of the square and hexagonal lattices, respectively.

A.1   Square lattice

The square Bravais lattice is defined in terms of the lattice basis vectors

$$\vec{x}_1 = a \begin{bmatrix} 1 \\ 0 \end{bmatrix}, \qquad \vec{x}_2 = a \begin{bmatrix} 0 \\ 1 \end{bmatrix}, \tag{A.1}$$

which generate the translations $T(\vec{x}_1)$ and $T(\vec{x}_2)$. Here a is the lattice constant, i.e. the distance between two nearest neighbors of the square lattice. The reciprocal lattice is a square lattice in momentum space generated by the vectors

$$\vec{G}_1 = \frac{2\pi}{a} \begin{bmatrix} 1 \\ 0 \end{bmatrix}, \qquad \vec{G}_2 = \frac{2\pi}{a} \begin{bmatrix} 0 \\ 1 \end{bmatrix}, \tag{A.2}$$

A schematic picture of both the real space lattice and the reciprocal lattice is presented in Figs. A.1 and A.3. As is shown in Fig. A.1, in this work we choose to place the origin at the center of a square. We found this to be the most convenient choice, in addition to being consistent with the (obvious) choices made for the hexagonal lattices (see below). This choice does however have the consequence that the atomic positions are displaced from the Bravais lattice vectors by an amount

$$\vec{l} = \frac{a}{2} \begin{bmatrix} 1 \\ -1 \end{bmatrix}. \tag{A.3}$$

Contrary to the convention of equating the atomic positions and Bravais lattice vectors, the present choice implies that point group operations must be associated with a

nontrivial lattice translation $\vec{t}$ when acting on an atomic position. For example, referring to Section 9.1.1, we have $C_4\vec{l} = \vec{x}_2 + \vec{l}$ where $\vec{t} = \vec{x}_2$. This minor complication notwithstanding, it is the most convenient and consistent convention.

The square lattice Hamiltonian $\hat{H}$ and corresponding electronic dispersion are simply given by

$$\hat{H} = \sum_{\vec{k}} E(\vec{k}) \hat{\psi}^\dagger(\vec{k}) \hat{\psi}(\vec{k}), \quad E(\vec{k}) = -2t \sum_{i=1}^{2} \cos k_i. \tag{A.4}$$

A.2 Triangular lattice

The triangular Bravais lattice is generated by the two lattice basis vectors

$$\vec{x}_1 = \frac{a}{2} \begin{bmatrix} 1 \\ \sqrt{3} \end{bmatrix}, \quad \vec{x}_2 = \frac{a}{2} \begin{bmatrix} 1 \\ -\sqrt{3} \end{bmatrix}, \tag{A.5}$$

and in addition to these we define for convenience the (linearly dependent) lattice vector $\vec{x}_3 = -\vec{x}_1 - \vec{x}_2$. Again, a is the lattice constant. In case of the triangular lattice we choose the origin to at one of the Bravais lattice points, as indicated in Fig. A.1 on the upper right.

The reciprocal lattice of a triangular lattice is a triangular lattice and the reciprocal lattice vectors are given by

$$\vec{G}_1 = \frac{2\pi}{a} \begin{bmatrix} 1 \\ 1/\sqrt{3} \end{bmatrix}, \quad \vec{G}_2 = \frac{2\pi}{a} \begin{bmatrix} 1 \\ -1/\sqrt{3} \end{bmatrix}. \tag{A.6}$$

The corresponding first Brillouin zone is graphically shown in Fig. A.3. The M-point ordering momenta $\vec{Q}_\mu$ are shown in Fig. A.3 by full red dots and their explicit expressions are

$$\vec{Q}_{1,3} = \frac{\pi}{a\sqrt{3}} \begin{bmatrix} \pm\sqrt{3} \\ 1 \end{bmatrix}, \quad \vec{Q}_2 = \frac{2\pi}{a\sqrt{3}} \begin{bmatrix} 0 \\ 1 \end{bmatrix}. \tag{A.7}$$

The triangular lattice Hamiltonian $\hat{H}$ and corresponding electronic dispersion are simply given by

$$\hat{H} = \sum_{\vec{k}} E(\vec{k}) \hat{\psi}^\dagger(\vec{k}) \hat{\psi}(\vec{k}), \quad E(\vec{k}) = -2t \sum_{i=1}^{3} \cos k_i. \tag{A.8}$$

A.2.1 Mean field orbital momentum basis functions

In Section 9.2.3 we have discussed how to set up a triangular lattice spinful mean-field theory anticipating translational symmetry breaking due to finite $\vec{Q}_\mu$ ordering vectors. The nearest neighbor interaction V_{ij} required a decomposition into the orbital momentum functions transforming as irreducible representations of the hexagonal point group. Here we list these functions explicitly.

In general the orbital momentum functions $\lambda^{(n,\mathcal{I}_r)}(\vec{k})$ are labeled by n (n-th nearest neighbor) and $\mathcal{I}_r$ (irreducible representation $\mathcal{I}$ and partner r). In case of the triangular lattice we have only considered $n = 1$ and found that we need to sum over four irreducible representations, two of them $1D$ and two of them $2D$. The $1D$ representation A_1 and the $2D$ representation E_2 functions are constructed from cosine functions and take the form

$$\lambda^{(1,A_1)}(\vec{k}) = \frac{1}{\sqrt{3}}(\cos k_1 + \cos k_2 + \cos k_3)$$

$$\vec{\lambda}^{(1,E_2)}(\vec{k}) = \frac{1}{\sqrt{2}}\begin{bmatrix} \frac{1}{\sqrt{3}}(-2\cos k_1 + \cos k_2 + \cos k_3) \\ \cos k_2 - \cos k_3 \end{bmatrix}.$$

$$(A.9)$$

Instead, the $1D$ representation B_1 and the $2D$ representation E_1 functions are constructed from sine functions and read

$$\lambda^{(1,B_1)}(\vec{k}) = \frac{1}{\sqrt{3}}(\sin k_1 + \sin k_2 + \sin k_3)$$

$$\vec{\lambda}^{(1,E_1)}(\vec{k}) = \frac{1}{\sqrt{2}}\begin{bmatrix} \frac{1}{\sqrt{3}}(-2\sin k_1 + \sin k_2 + \sin k_3) \\ \sin k_2 - \sin k_3 \end{bmatrix}.$$

$$(A.10)$$

The triangular lattice function $\Gamma^{(1)}(\vec{k} - \vec{k}')$ can therefore be expanded in separable functions $\lambda^{(1,\mathcal{I}_r)}(\vec{k})$ and $\lambda^{(1,\mathcal{I}_r)}(\vec{k}')$ as

$$\Gamma^{(1)}(\vec{k} - \vec{k}') = \sum_{\mathcal{I},r} \lambda^{(1,\mathcal{I}_r)}(\vec{k})\lambda^{(1,\mathcal{I}_r)}(\vec{k}') \tag{A.11}$$

with $\mathcal{I} = A_1, E_2, B_1, E_1$. Since all functions are real we have suppressed the complex conjugation operation.

A.3 Honeycomb lattice

The Bravais lattice of the honeycomb lattice is a triangular lattice and the honeycomb lattice unit cell contains two inequivalent atoms, which are labeled as the A and B
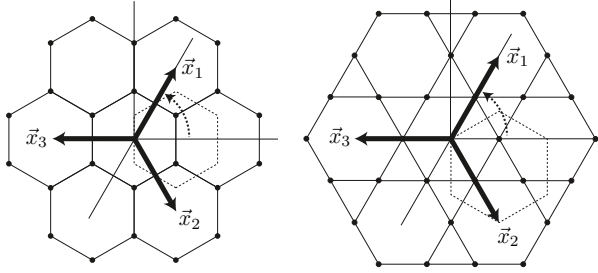
Figure A.2: Schematic picture of two of the four lattices considered in this work. (left) the honeycomb lattice, (right) kagome lattice. Lattice basis vectors are represented as thick back arrows, the hexagonal lattices also show $\vec{x}_3 = -\vec{x}_1 - \vec{x}_2$. The curved dashed arrows indicate the sixfold (C_6) rotations of the hexagonal lattices.

sublattices. The unit vectors of the triangular Bravais lattice are taken to be the same as in Eq. (A.5),

$$\vec{x}_1 = \frac{a}{2}\begin{bmatrix} 1 \\ \sqrt{3} \end{bmatrix}, \qquad \vec{x}_2 = \frac{a}{2}\begin{bmatrix} 1 \\ -\sqrt{3} \end{bmatrix}, \tag{A.12}$$

where a is again the lattice consant, which in case of the honeycomb lattice is not the distance between nearest neighbors (i.e. the carbon-carbon distance in graphene). As was the case for the triangular lattice, we define $\vec{x}_3 \equiv -\vec{x}_1 - \vec{x}_2$. The origin is taken to be the center of a hexagon and two vectors $\vec{l}_A$ and $\vec{l}_B$, specifying the positions of the A and B atoms in the unit cell with respect to the origin, are given by

$$\vec{l}_A = \frac{a}{2}\begin{bmatrix} 1 \\ -1/\sqrt{3} \end{bmatrix}, \qquad \vec{l}_B = \frac{a}{2}\begin{bmatrix} 1 \\ 1/\sqrt{3} \end{bmatrix}. \tag{A.13}$$

Taking the A sublattice as a reference sublattice, we define the three nearest neighbor vectors connecting the sublattices as

$$\vec{\delta}_1 = \vec{l}_B - \vec{l}_A, \quad \vec{\delta}_2 = \vec{\delta}_1 - \vec{x}_1, \quad \vec{\delta}_3 = \vec{\delta}_1 + \vec{x}_2. \tag{A.14}$$

The reciprocal lattice of a triangular lattice is a triangular lattice, as was noted previously, and in the case of the honeycomb lattice the reciprocal lattice vectors coincide with those of the triangular lattice,

$$\vec{G}_1 = \frac{2\pi}{a}\begin{bmatrix} 1 \\ 1/\sqrt{3} \end{bmatrix}, \qquad \vec{G}_2 = \frac{2\pi}{a}\begin{bmatrix} 1 \\ -1/\sqrt{3} \end{bmatrix}. \tag{A.15}$$

The electronic honeycomb lattice Hamiltonian is given by

$$\hat{H} = \sum_{\vec{k}} \hat{\psi}_i^\dagger(\vec{k}) \mathcal{H}_{ij}(\vec{k}) \hat{\psi}_j(\vec{k}), \tag{A.16}$$

where i, j label the sublattices and the $\vec{k}$-dependent matrix takes the form

$$\mathcal{H}(\vec{k}) = -t \begin{bmatrix} 0 & 1 + T_2 + T_1^* \\ 1 + T_2^* + T_1 & 0 \end{bmatrix} \tag{A.17}$$

with the T_i as defined at the beginning of this appendix. It is a very well-known fact that the honeycomb band structure displays band touchings at the Brioullin zone vertices $\vec{K}_\pm$ which are given by

$$\vec{K}_\pm = \frac{4\pi}{3} \begin{bmatrix} \pm 1 \\ 0 \end{bmatrix}. \tag{A.18}$$

At these isolated band touchings, which are protected by lattice symmetries (c.f. section A.3.1), the electronic bands disperse linearly, and the nodes are therefore referred to as Dirac points, or K-points. These Dirac points are shown in Fig. A.3 on the left side by large blue dots. In the main text we have discussed K-point ordering on the honeycomb lattice.

The M-point ordering momenta are the same as for the triangular lattice (and shown in Fig. A.3) and we quote them here again for completeness

$$\vec{Q}_{1,3} = \frac{\pi}{a\sqrt{3}} \begin{bmatrix} \pm\sqrt{3} \\ 1 \end{bmatrix}, \quad \vec{Q}_2 = \frac{2\pi}{a\sqrt{3}} \begin{bmatrix} 0 \\ 1 \end{bmatrix}. \tag{A.19}$$

A.3.1 Point group protection of honeycomb Dirac points

In the Brillouin zone of the honeycomb lattice (one may think of graphene), or any other lattice with point group C_{6v} such as triangular and kagome, there are special $\vec{k}$ points that are left invariant under certain point group operations. Of particular, even profound, interest are the corners of the Brillouin zone hexagon given by $\vec{K}_\pm$ (see previous subsection), also called K-points or valleys. The terminology valley is inspired by the fact that at these points $\mathcal{H}(\vec{K}_\pm) = 0$, leading to a degeneracy in the spectrum. The little cogroup of each $\vec{K}_\pm$ is C_{3v} and consists of the threefold rotations $C_3 = C_6^2$ and $C_3^{-1} = C_6^4$ of the honeycomb lattice and the three reflection bisecting the bonds of the hexagon. These reflections exchange the A and B sublattice. The group C_{3v} admits a two dimensional irreducible representation, which is realized by
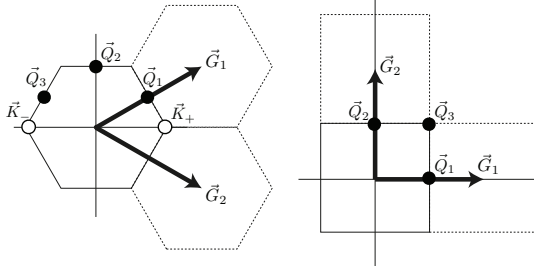
Figure A.3: Depiction of the Brillouin zones of the hexagonal lattices (left) and the square lattice (right). The reciprocal lattice vectors are denoted as $\vec{G}_1$ and $\vec{G}_2$. The special commensurate ordering momenta are indicated. For both the square and the hexagonal lattices there is a set $\vec{Q}_\mu$ (full dots), while in case of the hexagonal lattices there is a second set of two ordering vectors $\vec{K}_+$ and $\vec{K}_-$ (open dots).

the matrices $\mathcal{U}_R$ of equation (9.6) with $R \in C_{3v}$. Also note the remark following equation (9.10). In fact, by working out these matrices we derive the representation for $\vec{K}_+$ as

$$\mathcal{U}_I = \begin{bmatrix} 1 & 0 \\ 0 & 1 \end{bmatrix}, \quad \mathcal{U}_{C_3} = \begin{bmatrix} \omega & 0 \\ 0 & \omega^{-1} \end{bmatrix}, \quad \mathcal{U}_{C_3^{-1}} = \begin{bmatrix} \omega^{-1} & 0 \\ 0 & \omega \end{bmatrix},$$

$$\mathcal{U}_{\sigma v1} = \begin{bmatrix} 0 & 1 \\ 1 & 0 \end{bmatrix}, \quad \mathcal{U}_{\sigma v2} = \begin{bmatrix} 0 & \omega \\ \omega^{-1} & 0 \end{bmatrix}, \quad \mathcal{U}_{\sigma v3} = \begin{bmatrix} 0 & \omega^{-1} \\ \omega & 0 \end{bmatrix}. \tag{A.20}$$

where we defined $\omega = e^{2\pi i/3}$. Strictly speaking, the representation for $\vec{K}_-$ is obtained by $\omega \leftrightarrow \omega^{-1}$. These matrices act on the Hamiltonian at the K-points, i.e. $\mathcal{H}(\vec{K}_\pm)$, which can be expanded in Pauli matrices τ^i. As $\vec{K}_\pm$ are invariant points under R we have $\mathcal{U}_R \mathcal{H}(\vec{K}_\pm) \mathcal{U}_R^\dagger = \mathcal{H}(\vec{K}_\pm)$, or $[\mathcal{U}_R, \mathcal{H}(\vec{K}_\pm)] = 0$. We may take $\mathcal{U}_{C_3}$ and $\mathcal{U}_{\sigma v1}$ to show that this mandates $\mathcal{H}(\vec{K}_\pm) = I$ and the degeneracy is therefore protected exactly at $\vec{K}_\pm$ making it an essential degeneracy. To demontrate the vanishing of the commutator we just have to observe that $\mathcal{U}_{\sigma v1} = \tau^1$ and $\mathcal{U}_{C_3}$ contains τ^3. The only matrix commuting with both is the unit matrix.

A.3.2 Symmetry of Dirac matrices

In this part we provide more details on the low-energy theory of the honeycomb lattice at half filling, which is described by a $2D$ Dirac Lagrangian. For an extensive discussion on the connection to $2 + 1D$ QED see [206]. Here we will be concerned

with symmetries of the dicrete point groups C_{6v} and C_{6v}'' and more specifically the symmetry properties of low-energy spinor bilinears.

The low-energy theory in the vicinity of the two inequivalent valleys $\vec{K}_\pm$ is obtained by expanding the dispersion around these valleys $\vec{K}_\pm$ in small momenta $\vec{q}$. One obtains the Dirac Hamiltonian

$$\mathcal{H}(\vec{q}) = \hbar v_F (q_x \nu^3 \tau^1 + q_y \tau^2) \tag{A.21}$$

(where $v_F = \sqrt{3}ta/(2\hbar)$) acting on the spinor $\Phi(\vec{q})$ which is given by

$$\hat{\Phi}(\vec{q}) = \begin{bmatrix} \hat{\psi}_A(\vec{K}_+ + \vec{q}) \\ \hat{\psi}_B(\vec{K}_+ + \vec{q}) \\ \hat{\psi}_A(\vec{K}_- + \vec{q}) \\ \hat{\psi}_B(\vec{K}_- + \vec{q}) \end{bmatrix}. \tag{A.22}$$

The set of Pauli matrices ν^i acts on the valley degree of freedom and the τ^i matrices on the sublattice degre of freedom. Exchanging A and B sublattice for the $\vec{K}_-$ by a unitary transformation we obtain the chiral representation of the low-energy Hamiltonian

$$\mathcal{H}(\vec{q}) = \hbar v_F \nu^3 \vec{q} \cdot \vec{\tau}. \tag{A.23}$$

This chiral basis is the basis in which we will state the results. As the Dirac points have been folded to Γ the effect of the generators of the space is found by making use of equation (9.18). The generators may be used directly to generate all operations in the space group. Note that

$$\hat{\Phi} \equiv \hat{\Phi}(\vec{0}) = \begin{bmatrix} \hat{\chi}_{A1}(\vec{0}) \\ \hat{\chi}_{B1}(\vec{0}) \\ \hat{\chi}_{A2}(\vec{0}) \\ \hat{\chi}_{B2}(\vec{0}) \end{bmatrix}. \tag{A.24}$$

With this it is straightforward to dedude that the translation operator $T(\vec{x}_1)$ acts as

$$T(\vec{x}_1) \quad \rightarrow \quad \begin{bmatrix} \omega & & & \\ & \omega & & \\ & & \omega^{-1} & \\ & & & \omega^{-1} \end{bmatrix} \hat{\Phi}, \tag{A.25}$$

(again $\omega = e^{2\pi i/3}$) while the six-fold rotation C_6 acts as

$$
C_6 \quad \rightarrow \quad \begin{bmatrix} & & & 1 \\ & & \omega & \\ & 1 & & \\ \omega^{-1} & & & \end{bmatrix} \hat{\Phi}, \tag{A.26}
$$

note that this is diagonal in valley space as the six-fold rotation exchanges $\vec{K}_\pm$. The reflection σ_v acts as

$$
\sigma_v \quad \rightarrow \quad \tau^1 \hat{\Phi}. \tag{A.27}
$$

In addition to the space group generators it will be convenient to classify low-energy bilinears based on their transformation property under time-reversal. Hence, time-reversal is found to be represented by

$$
\mathcal{T} \quad \rightarrow \quad \mathcal{K} \nu^1 \hat{\Phi}, \tag{A.28}
$$

where $\mathcal{K}$ denotes complex conjugation. Note that this implies that $\nu^3 \tau^1$ and τ^2 are both odd, as they should be. They are coupled linearly to $\vec{q}$, which is also odd.

The free Dirac Hamiltonian consists of the matrices $\nu^3 \tau^1$ and τ^2. Spectral gaps are generated by Dirac matrices which anti-commute with these. It is a simple matter to find the four matrices which have this property, and they are found to be τ^3, $\nu^3 \tau^3$, $\nu^1 \tau^1$ and $\nu^2 \tau^1$. Using the action of time-reversal one easily sees that while $\nu^3 \tau^3$ is odd, the other three are even under time-reversal. The time-reversal invariant Dirac matrices all anti-commute between themselves and together with $\nu^3 \tau^1$ and τ^2 they constitute the set of maximally anti-commuting Hermitian 4×4-matrices. Based on the action of the generators of the symmetry group, we can assign the masses to representations of C_{6v}''' and C_{6v}. Taking the time-reversal invariant masses first, we find that τ^3 transforms as B_2, while $\nu^1 \tau^1$ and $\nu^2 \tau^1$ are partners of the representation E_1'. The latter can be decomposed into $A_1 \oplus B_1$ and the following linear combinations are found to correspond to this decomposition

$$
\begin{aligned}
A_1 &\rightarrow \cos\theta \nu^1 \tau^1 + \sin\theta \nu^2 \tau^1 \\
B_1 &\rightarrow -\sin\theta \nu^1 \tau^1 + \cos\theta \nu^2 \tau^1,
\end{aligned} \tag{A.29}
$$

where $\theta = \pi/3$ The time-reversal breaking mass term $\nu^3 \tau^3$ is found to transform as A_2. There are three Dirac matrices which lift the degeneracy between the valleys, but preserve the twofold degeneracy within each valley and since they distinguish the valleys at $\vec{K}_\pm$ which are related by time-reversal, all three are time-reversal symmetry breaking. The three matrices are ν^3, $\nu^1 \tau^2$ and $\nu^2 \tau^2$. The matrix ν^3 can be shown

Irreps of C_{6v}'' Irreps of C_{6v}	A_2	B_1	B_2	E_1	E_2
(standard)	$\nu^3\tau^3$	ν^3	τ^3	$\nu^3\tau^1, \tau^2$	$\tau^1, \nu^3\tau^2$
(chiral)	τ^3	ν^3	$\tau^3\tau^3$	$\nu^3\tau^1, \nu^3\tau^2$	τ^1, τ^2

	E_1'	E_2'	G'	
	$A_1 \oplus B_1$	$A_2 \oplus B_2$	$E_1 \oplus E_2$	
	$\nu^1\tau^1, \nu^2\tau^1$	$\nu^1\tau^2, \nu^2\tau^2$	$\nu^1, \nu^2, \nu^1\tau^3, \nu^2\tau^3$	
	ν^1, ν^2	$\nu^1\tau^3, \nu^2\tau^3$	$\nu^1\tau^1, \nu^2\tau^1, \nu^1\tau^2, \nu^2\tau^2$	

Table A.1: This table summarizes the identification of low-energy fermion bilinears as basis functions of irreducible representations of C_{6v}'''. In addition we present the irreducible representations of C_{6v} contained in those of C_{6v}''.

to transform according to B_1, while $\nu^1\tau^2$ and $\nu^2\tau^2$ are partners of E_2'. They can be written as basis functions transforming as A_2 and B_2 in the following way

$$
\begin{aligned}
A_2 &\rightarrow \sin\theta\nu^1\tau^2 + \cos\theta\nu^2\tau^2 \\
B_2 &\rightarrow \cos\theta\nu^1\tau^2 - \sin\theta\nu^2\tau^2.
\end{aligned}
\tag{A.30}
$$

Of the remaining six Dirac matrices, two are diagonal in valley space, while the other four exchange valleys. The former are τ^1 and $\nu^3\tau^2$, which are time-reversal invariant and are partners of E_2. Indeed, as they do not originate from a coupling of $\vec{K}_\pm$ they should correspond to the translationally invariant content of the symmetry classification. The set of matrices which do originate from coupling are $\nu^1, \nu^2, \nu^1\tau^3$ and $\nu^2\tau^3$, all of which are time-reversal invariant. Together they transform as G' of the group C_{6v}'''.

A.3.3   Lifting of degeneracies at M' points

We now present the details of degeneracy protection and lifting at the M' points of the reduced BZ corresponding to M-point order, i.e. order parameter components at $\vec{Q}_\mu$. It was mentioned in Section 9.4.1, if the translations $T(\vec{x}_i)$ and the M'-invariant elements C_{2v} are good symmetries then two-fold degeneracies at the M' points are protected, while in case of C_{2v} symmetry only, i.e. broken translations, there are no symmetry protected degeneracies. Here we demonstrate this explicitly. The recipy is

by now familiar and we write the state operator at $\vec{M}' = \vec{Q}_2/2$ as.

$$\hat{\Phi}_{M'} = \begin{bmatrix} \hat{\psi}_j(\vec{M}') \\ \hat{\psi}_j(\vec{M}' + \vec{Q}_1) \\ \hat{\psi}_j(\vec{M}' + \vec{Q}_2) \\ \hat{\psi}_j(\vec{M}' + \vec{Q}_3) \end{bmatrix}. \tag{A.31}$$

The action of the translations $T(\vec{x}_1)$ and $T(\vec{x}_2)$ (up to global $U(1)$ phases) is easily derived to be

$$T(\vec{x}_1) \rightarrow \begin{bmatrix} 1 & & & \\ & -1 & & \\ & & -1 & \\ & & & 1 \end{bmatrix} \equiv \rho^3 \nu^3 \tag{A.32}$$

where the matrix entries should be understood as 2×2 unit matrices (τ^0) and we have introduced another set of Pauli matrices ρ^i to generate the 8×8 representation. Then $T(\vec{x}_2)$ is given by ρ^3. For the C_2 element we derive

$$C_2 \rightarrow \begin{bmatrix} & & \tau^1 & \\ & & & -\tau^1 \\ \tau^1 & & & \\ & \tau^1 & & \end{bmatrix} \equiv \rho^1 \nu^3 \tau^1. \tag{A.33}$$

Symmetry dictates that the Hamiltonian at M' must commute with these elements. Taking just these translation and the inversion we simply see that the only allowed terms are $\nu^3 \tau^1$ and ν^3. This observation already completes the task of proving that two-fold degeneracies must exist, since any linear combination of these two terms will be proportional to ρ^0. Hence, all eigenvalues of must appear twice. We check whether the two reflections σ_v and $C_2\sigma_v$ give any additional constraints. For σ_v we find

$$\sigma_v \rightarrow \begin{bmatrix} & & \tau^1 & \\ & \tau^1 & & \\ \tau^1 & & & \\ & & & \tau^1 \end{bmatrix} \equiv \rho^1 \nu^3 \tau^1, \tag{A.34}$$

and we may use the expression for C_2 to derive the action of the other reflection. We find no further symmetry constraints on the energy levels at M'.

Breaking the translations leads to the symmetry group C_{2v}, which does not have any $2D$ irreducible representation and therefore cannot protect degeneracies. Ignoring the constraints coming from the translation above, one observes that more terms are allowed on the Hamiltonian which in general will lift the degeneracies.

A.3.4   Mean-field momentum functions

In the same way as for the triangular lattice in Section A.2.1 we present the explicit orbital momentum fucntions which are used to decompose the nearest neighbor or next-nearest neighbor interactions. In Section 9.2.3 the basic structure of a mean field theory for both K-point and M-point order on the honeycomb lattice was discussed. Here we give explicit expressions for orbital momentum functions $\lambda_{ij}^{(n,\mathcal{I}_r)}(\vec{k})$ corresponding to $\Gamma_{ij}^{(1)}(\vec{k}-\vec{k}')$ and $\Gamma_{ij}^{(2)}(\vec{k}-\vec{k}')$.

The decomposition of the nearest neighbor interaction function $\Gamma_{ij}^{(1)}(\vec{k}-\vec{k}')$ consists of two irreducible representations. The first, A_1, is $1D$ and the second, E_2, $2D$. The orbital momentum functions are given by

$$
\begin{aligned}
\lambda_{AB}^{(1,A_1)}(\vec{k}) &= \frac{1}{\sqrt{3}}(1 + e^{-ik_1} + e^{ik_2}) \\
\vec{\lambda}_{AB}^{(1,E_2)}(\vec{k}) &= \frac{1}{\sqrt{2}}\left[\begin{array}{c} \frac{1}{\sqrt{3}}(-2 + e^{-ik_1} + e^{ik_2}) \\ e^{-ik_1} - e^{ik_2} \end{array} \right].
\end{aligned}
\tag{A.35}
$$

Note that we would have $\lambda_{BA}^{(1,A_1)} = \lambda_{AB}^{(1,A_1)*}$ and the formula for the decomposition is given in Eq. (9.52).

The Bravais lattice of the honeycomb lattice is a triangular lattice and we can therefore directly infer the orbital momentum functions which decompose the next-nearest neighbor function $\Gamma_{ij}^{(2)}(\vec{k}-\vec{k}')$ from the triangular lattice case. Note that we can write $\lambda_{AA}^{(n,\mathcal{I}_r)} = \lambda_{BB}^{(n,\mathcal{I}_r)} = \lambda^{(n,\mathcal{I}_r)}$. The orbital momentum functions read explicitly

$$
\begin{aligned}
\lambda^{(2,A_1)}(\vec{k}) &= \frac{1}{\sqrt{3}}(\cos k_1 + \cos k_2 + \cos k_3) \\
\vec{\lambda}^{(2,E_2)}(\vec{k}) &= \frac{1}{\sqrt{2}}\left[\begin{array}{c} \frac{1}{\sqrt{3}}(-2\cos k_1 + \cos k_2 + \cos k_3) \\ \cos k_2 - \cos k_3 \end{array} \right] \\
\lambda^{(2,B_1)}(\vec{k}) &= \frac{1}{\sqrt{3}}(\sin k_1 + \sin k_2 + \sin k_3) \\
\vec{\lambda}^{(2,E_1)}(\vec{k}) &= \frac{1}{\sqrt{2}}\left[\begin{array}{c} \frac{1}{\sqrt{3}}(-2\sin k_1 + \sin k_2 + \sin k_3) \\ \sin k_2 - \sin k_3 \end{array} \right],
\end{aligned}
\tag{A.36}
$$

i.e. there are the same four irreducible representations as in the triangular lattice nearest neighbor case.

A.4   Kagome lattice

The kagome lattice is another lattice with hexagonal symmetry, meaning that the Bravais lattice is triangular. However, the kagome lattice unit cell contains three inequivalent atoms, which are labeled by their sublattice index A, B and C. We choose the generators of lattice translations as

$$\vec{x}_1 = a \begin{bmatrix} 1 \\ \sqrt{3} \end{bmatrix}, \qquad \vec{x}_2 = a \begin{bmatrix} 1 \\ -\sqrt{3} \end{bmatrix}, \qquad (A.37)$$

where a is taken as the length of a bond, i.e. the distance between nearest neighbors. In terms of a these vectors are half of the triangular and honeycomb lattice vectors. Hence, the reciprocal lattice vectors are twice as large as was the case for the triangular lattice, and are given by

$$\vec{G}_1 = \frac{\pi}{a} \begin{bmatrix} 1 \\ 1/\sqrt{3} \end{bmatrix}, \qquad \vec{G}_2 = \frac{\pi}{a} \begin{bmatrix} 1 \\ -1/\sqrt{3} \end{bmatrix}. \qquad (A.38)$$

We take the origin to be the center of a hexagon of the kagome lattice and three vectors $\vec{l}_A$, $\vec{l}_B$ and $\vec{l}_C$ specifying the positions of the atoms in the unit cell with respect to the origin are given by

$$\vec{l}_A = \frac{a}{2} \begin{bmatrix} 1 \\ -\sqrt{3} \end{bmatrix}, \qquad \vec{l}_B = \frac{a}{2} \begin{bmatrix} 3 \\ -\sqrt{3} \end{bmatrix}, \qquad \vec{l}_C = a \begin{bmatrix} 1 \\ 0 \end{bmatrix}. \qquad (A.39)$$

Taking the A sublattice as a reference sublattice, we define the three nearest neighbor vectors connecting the sublattices as

$$\vec{\delta}_1 = \vec{l}_B - \vec{l}_A, \qquad \vec{\delta}_2 = \vec{l}_C - \vec{l}_B, \qquad \vec{\delta}_3 = \vec{l}_A - \vec{l}_C. \qquad (A.40)$$

In addition to these vectors we also define the vectors connecting next-nearest neighbors on the kagome lattice. They are given by

$$\vec{\delta}'_1 = \vec{l}_C - 2\vec{l}_A, \qquad \vec{\delta}'_2 = -2\vec{l}_C + \vec{l}_A, \qquad \vec{\delta}'_3 = \vec{l}_A + 2\vec{l}_C. \qquad (A.41)$$

The momentum dependent Hamiltonian of electrons hopping between nearest neighbors on the kagome lattice then takes the form

$$\mathcal{H}(\vec{k}) = -t \begin{bmatrix} 0 & 1 + T_1^* T_2^* & 1 + T_1^* \\ 1 + T_1 T_2 & 0 & 1 + T_2 \\ 1 + T_1 & 1 + T_2^* & 0 \end{bmatrix} \qquad (A.42)$$

with the familiar definition of T_i. It is not uncommon in the context of the kagome lattice to take into account hopping between next-nearest neighbors in the tight-binding

Hamiltonian. This removes the perfect flatness of the top band. The momentum dependent Hamiltonian matrix $\mathcal{H}'(\vec{k})$ corresponding to next-nearest neighbor hopping reads

$$\mathcal{H}'(\vec{k}) = -t' \begin{bmatrix} 0 & T_1^* + T_2^* & T_2 + T_1^* T_2^* \\ T_1 + T_2 & 0 & T_1^* + T_1 T_2 \\ T_2^* + T_1 T_2 & T_1 + T_1^* T_2^* & 0 \end{bmatrix}. \qquad \text{(A.43)}$$

In Section 9.4.2 we have intruced the matrix functions Λ_i which act on the sublattice degree of freedom and which are generalizations of the Pauli-matrices τ^i. They are 3×3 matrices and constitute the set of matrices spanning the space of Hermitian matrices, known as the Gell-Mann matices. Explicitly they read

$$\Lambda_{1a} = \begin{bmatrix} 0 & 1 & 0 \\ 1 & 0 & 0 \\ 0 & 0 & 0 \end{bmatrix}, \; \Lambda_{2a} = \begin{bmatrix} 0 & 0 & 0 \\ 0 & 0 & 1 \\ 0 & 1 & 0 \end{bmatrix}, \; \Lambda_{3a} = \begin{bmatrix} 0 & 0 & 1 \\ 0 & 0 & 0 \\ 1 & 0 & 0 \end{bmatrix}$$

$$\Lambda_{1b} = \begin{bmatrix} 0 & -i & 0 \\ i & 0 & 0 \\ 0 & 0 & 0 \end{bmatrix}, \; \Lambda_{2b} = \begin{bmatrix} 0 & 0 & 0 \\ 0 & 0 & -i \\ 0 & i & 0 \end{bmatrix}, \; \Lambda_{3b} = \begin{bmatrix} 0 & 0 & i \\ 0 & 0 & 0 \\ -i & 0 & 0 \end{bmatrix}$$

$$\Lambda_{1c} = \frac{1}{\sqrt{3}} \begin{bmatrix} 1 & 0 & 0 \\ 0 & 1 & 0 \\ 0 & 0 & -2 \end{bmatrix}, \; \Lambda_{2c} = \begin{bmatrix} 1 & 0 & 0 \\ 0 & -1 & 0 \\ 0 & 0 & 0 \end{bmatrix}. \qquad \text{(A.44)}$$

The first two sets, $\vec{\Lambda}_a$ and $\vec{\Lambda}_b$ correspond to bond ordered states as they connect different sublattices, while the third set $\vec{\Lambda}_c$ represents nontrivial charge order. Their symmetry properties are summarized and discussed in Section 9.4.2.

A.4.1   Low-energy theory and symmetry of Dirac matrices

The kagome lattice allows for two different types of low-energy description, depending on filling. As was mentioned in the main text (see Section 9.4.2), at filling $n = 1/3$ the spectrum is equivalent to that of the honeycomb lattice with conic degeneracies at the Dirac points $\vec{K}_\pm$. These isolated band touchings can be described by a Dirac theory fully analogous to the honeycomb lattice by projecting the linearly expanded Hamiltonian onto the eigenstates at $\vec{K}_\pm$, which we denote as $|+, j\rangle$ and $|-, j\rangle$ ($j = 1, 2$) for $\vec{K}_+$ and $\vec{K}_-$, respectively. Then, in the basis

$$\hat{\Phi}(\vec{q}) = \begin{bmatrix} \hat{\psi}_1(\vec{K}_+ + \vec{q}) \\ \hat{\psi}_2(\vec{K}_+ + \vec{q}) \\ \hat{\psi}_1(\vec{K}_- + \vec{q}) \\ \hat{\psi}_2(\vec{K}_- + \vec{q}) \end{bmatrix}. \qquad \text{(A.45)}$$

one can obtain the same low-energy Hamiltonian as the one corresponding to the honeycomb lattice Dirac points,

$$\mathcal{H}(\vec{q}) = \hbar v_F \nu^3 \vec{q} \cdot \vec{\tau}, \tag{A.46}$$

of course for a proper choice of $|\pm, j\rangle$. Here the set of Pauli matrices ν^i acts on the valley degree ($\pm$) of freedom and the τ^i matrices on the "sublattice" degree of freedom labeled by j. Note that $v_F = \sqrt{3}at/\hbar$.

We now proceed to derive the lattice symmetry transformation properties of the low-energy Dirac matrices. To this end, we first derive the action of the generators of the group C_{6v}''' on the spinor

$$\hat{\underline{\chi}} \equiv \begin{bmatrix} \hat{\chi}_{j1} \\ \hat{\chi}_{j2} \end{bmatrix} = \begin{bmatrix} \hat{\psi}_j(\vec{K}_+) \\ \hat{\psi}_j(\vec{K}_-) \end{bmatrix}, \tag{A.47}$$

and then project that action into the low-energy subspace. Following the standard recepy described in Section 9.1, it is straightforward to dedude that the translation operator $T(\vec{x}_1)$ acts as

$$T(\vec{x}_1) \quad \rightarrow \quad \begin{bmatrix} \omega & & & & & \\ & \omega & & & & \\ & & \omega & & & \\ & & & \omega^{-1} & & \\ & & & & \omega^{-1} & \\ & & & & & \omega^{-1} \end{bmatrix} \hat{\underline{\chi}}, \tag{A.48}$$

(again $\omega = e^{2\pi i/3}$) while the six-fold rotation C_6 acts as

$$C_6 \quad \rightarrow \quad \begin{bmatrix} & & & & & 1 \\ & & & \omega^{-1} & & \\ & & & & \omega & \\ & & 1 & & & \\ \omega & & & & & \\ & \omega^{-1} & & & & \end{bmatrix} \hat{\underline{\chi}}, \tag{A.49}$$

note that this is diagonal in valley space as the six-fold rotation exchanges $\vec{K}_\pm$. The reflection σ_v acts as

$$\sigma_v \quad \rightarrow \quad \begin{bmatrix} & \omega^{-1} & & & & \\ \omega & & & & & \\ & & 1 & & & \\ & & & & \omega & \\ & & & \omega^{-1} & & \\ & & & & & 1 \end{bmatrix} \hat{\underline{\chi}}. \tag{A.50}$$

In order to evaluate the symmetry properties of the Dirac matrices $\nu^i \tau^j$ we need to project the 6×6 matrices given above into the low-energy subspace spanned by $|\pm, j\rangle$. If $U_\pm$ are the matrices that contain the eigenvectors of $\mathcal{H}(\vec{K}_\pm)$ in their column, we construct the matrix $U = \text{Diag}(U_+, U_-)$ and evaluate $U^\dagger V U$, where V is a matrix of equation (A.51) and (A.53). Reading off the low-energy blocks from $U^\dagger V U$ yields for the translation

$$T(\vec{x}_1) \quad \rightarrow \quad \begin{bmatrix} \omega & & & \\ & \omega & & \\ & & \omega^{-1} & \\ & & & \omega^{-1} \end{bmatrix} \hat{\Phi}, \tag{A.51}$$

while the six-fold rotation C_6 takes the form

$$C_6 \quad \rightarrow \quad \begin{bmatrix} & & 1 & \\ & & & \omega^{-1} \\ \omega & & & \\ & 1 & & \end{bmatrix} \hat{\Phi}, \tag{A.52}$$

note that this is off-diagonal in valley space as the six-fold rotation exchanges $\vec{K}_\pm$. The reflection σ_v acts as

$$\sigma_v \quad \rightarrow \quad \tau^1 \hat{\chi}. \tag{A.53}$$

Time-reversal only exchanges $\vec{K}_+ \leftrightarrow \vec{K}_-$ and is thus easily seen to be represented in the low-energy subspace as

$$\mathcal{T} \quad \rightarrow \quad \mathcal{K} \nu^1 \hat{\Phi}, \tag{A.54}$$

where $\mathcal{K}$ denotes complex conjugation.

This representation is very similar to and for some operations coincides with the representation of the extended point group derived for the honeucomb lattice. This is not all that surprising since the lattices are closely related. A consequence of the similarity of the representations is that we find the transformation properties of the Dirac matrices precisely coincide with those of honeycomb lattice in the chiral representation. These were summarized in Table A.1 and we refer the reader to the second of the two rows. The chiral representation is applicable here since we have chosen the eigenstates $|\pm, j\rangle$ accordingly. This concludes the discussion of the transformation properties of Dirac matrices in case of the kagome lattice.

LATTICE FERMIONS IN MAGNETIC FIELDS

B.1 Magnetic translation algebra on the lattice

In this appendix we present some details of lattice fermions models in a magnetic field. We specify the lattice sites of the square lattice by $\vec{n} = (n_x, n_y) \in \mathbb{Z}^2$. The Hamiltonian for the triangular lattice in a square geometry is given by

$$\hat{H} = \hat{T}_x + \hat{T}_y + \hat{T}_{x+y} + \text{hc}, \tag{B.1}$$

where the translation operators $\hat{T}_i$ are given by

$$\hat{T}_i = \sum_{\vec{n}} \hat{\psi}^\dagger(\vec{n} + \vec{u}_i) e^{i\theta^i(\vec{n})} \hat{\psi}(\vec{n}). \tag{B.2}$$

The presence of the compact lattice vector potential $\theta^i(\vec{n})$ represents the magnetic field. In lattice gauge theory these (exponentiated) objects are sometimes referred to as link variables, i.e. $U_{ij} = e^{ia_{ij}}$. We choose to work with the representation $\theta^i(\vec{n})$, which is related to the continuum vector potential $\vec{A}$ as

$$\theta^i(\vec{n}) = \frac{e}{\hbar} \int_{\vec{n}}^{\vec{n}+\vec{u}_i} \vec{A} \cdot d\vec{l}. \tag{B.3}$$

One may observe the identification $a_{\vec{n}+\vec{u}_i,\vec{n}} = \theta^i(\vec{n})$. Note that we write $\vec{u}_i$ to indicate a unit vector in the i-direction. The lattice field strength for a square plaquette is give by

$$\nabla_{\vec{n}} \times \theta = \theta^x(\vec{n}) + \theta^y(\vec{n} + \vec{u}_x) - \theta^x(\vec{n} + \vec{u}_y) - \theta^y(\vec{n}) = 2\pi\phi. \qquad \text{(B.4)}$$

Calculating the field strength for the elementary triangles allows for an expression of $\theta^{x+y}(\vec{n})$ in terms of $\theta^x(\vec{n})$ and $\theta^y(\vec{n})$,

$$
\begin{aligned}
\pi\phi &= \theta^x(\vec{n}) + \theta^y(\vec{n} + \vec{u}_x) - \theta^{x+y}(\vec{n}) \\
&= \theta^{x+y}(\vec{n}) - \theta^x(\vec{n} + \vec{u}_y) - \theta^y(\vec{n}),
\end{aligned} \qquad \text{(B.5)}
$$

from which one immediately obtains

$$
\begin{aligned}
\theta^{x+y}(\vec{n}) &= \theta^x(\vec{n}) + \theta^y(\vec{n} + \vec{u}_x) - \pi\phi \\
&= \theta^x(\vec{n} + \vec{u}_y) + \theta^y(\vec{n}) + \pi\phi
\end{aligned} \qquad \text{(B.6)}
$$

It is a straightforward matter to show that $\hat{T}_x$ and $\hat{T}_y$ do not commute, but in fact satisfy

$$\hat{T}_y\hat{T}_x = e^{i2\pi\phi}\hat{T}_x\hat{T}_y. \qquad \text{(B.7)}$$

The is the lattice analog of the noncommutative nature of translation operators in the continuum which is discussed in Chapter 1. Neither $\hat{T}_x$ nor $\hat{T}_y$ commute with the Hamiltonian and we wish to find translation operators that do commute with the Hamiltonian, generally given by

$$
\begin{aligned}
\overline{T}_x &= \sum_{\vec{n}} \hat{\psi}^\dagger(\vec{n} + \vec{u}_x)e^{i\chi^x(\vec{n})}\hat{\psi}(\vec{n}) \\
\overline{T}_y &= \sum_{\vec{n}} \hat{\psi}^\dagger(\vec{n} + \vec{u}_y)e^{i\chi^y(\vec{n})}\hat{\psi}(\vec{n}).
\end{aligned} \qquad \text{(B.8)}
$$

By explicitly demanding that the following commutators vanish

$$[\overline{T}_x, \hat{T}_x] = [\overline{T}_x, \hat{T}_y] = [\overline{T}_x, \hat{T}_{x+y}] = 0, \qquad \text{(B.9)}$$

one obtains expressions for $\chi^i(\vec{n})$ as

$$
\begin{aligned}
\chi^x(\vec{n}) &= \theta^x(\vec{n}) + 2\pi\phi n_y \\
\chi^y(\vec{n}) &= \theta^y(\vec{n}) - 2\pi\phi n_x.
\end{aligned} \qquad \text{(B.10)}
$$

Even though these translation operators commute with the Hamiltonian, the do not commute between themselves,

$$[\overline{T}_x, \overline{T}_y] \neq 0. \tag{B.11}$$

One finds that instead they obey (in the Landau gauge, see below)

$$\overline{T}_x \overline{T}_y = e^{i2\pi\phi} \overline{T}_y \overline{T}_x. \tag{B.12}$$

If the flux ϕ is rational and given by p/q, p and q being relatively prime, then one finds

$$\overline{T}_x^q \overline{T}_y = e^{i2q\pi\phi} \overline{T}_y \overline{T}_x^q = \overline{T}_y \overline{T}_x^q. \tag{B.13}$$

(note that the asymmetry of $\overline{T}_x^q$ and $\overline{T}_x$ in this expression is due to the gauge choice). Hence, the operators $\overline{T}_x^q$ and $\overline{T}_x$ commute between themselves and the Hamiltonian and can acquire quantum numbers under the Hamiltonian.

B.2 Diagonalization of the Hamiltonian

In order to diagonalize the Hamiltonian we first need to specify a gauge. Two gauge choices will be discussed here, the Landau gauge, often the gauge of choice in the continuum, and the symmetric gauge. The Landau gauge, in the continuum and its lattice equivalent, is written as

$$\vec{A} = Bx\vec{u}_y, \quad \theta^x(\vec{n}) = 0, \ \theta^y(\vec{n}) = 2\pi\phi n_x, \tag{B.14}$$

whereas the symmetric gauge takes the form

$$\vec{A} = \frac{B}{2}(x\vec{u}_y - y\vec{u}_x), \quad \theta^x(\vec{n}) = -\pi\phi n_y, \ \theta^y(\vec{n}) = \pi\phi n_x \tag{B.15}$$

We treat the Landau gauge first. Fourier transforming yields

$$\hat{\psi}(\vec{p}) = \frac{1}{\sqrt{N_x N_y}} \sum_{\vec{n}} e^{-i(p_x n_x + p_y n_y)} \hat{\psi}(\vec{n}). \tag{B.16}$$

where N_i is the number of lattice sites in the i direction and $\vec{p}$ is the lattice momentum. The momentum is defined as $N_i p_i \in [0, 2\pi, 4\pi, \ldots, N_i 2\pi)$. The Hamiltonian in the Landau gauge takes the form

$$\hat{H} = -t \sum_{\vec{n},\vec{n}'} \hat{\psi}^\dagger(\vec{n}') \mathcal{M}_{\vec{n}'\vec{n}} \hat{\psi}(\vec{n}) + \text{hc} \tag{B.17}$$

with the matrix $\mathcal{M}_{\vec{n}'\vec{n}}$ defined as

$$\mathcal{M}_{\vec{n}'\vec{n}} = \delta_{\vec{n}',\vec{n}+\vec{u}_x} + \delta_{\vec{n}',\vec{n}+\vec{u}_y}e^{i2\pi\phi n_x} + \delta_{\vec{n}',\vec{n}+\vec{u}_x+\vec{u}_y}e^{i2\pi\phi(n_x+1/2)} \tag{B.18}$$

which becomes in momentum space

$$\hat{H} = -t\sum_{\vec{p},\vec{p}'}\hat{\psi}^\dagger(\vec{p}')\mathcal{M}_{\vec{p}'\vec{p}}\hat{\psi}(\vec{p}) + \text{hc} \tag{B.19}$$

with the momentum space matrix $\mathcal{M}_{\vec{p}'\vec{p}}$ defined as

$$\mathcal{M}_{\vec{p}'\vec{p}} = e^{-ip_x}\delta_{\vec{p}',\vec{p}} + (e^{-ip_y} + e^{i\pi\phi}e^{-i(p_x+p_y)})\delta_{p'_x,p_x+2\pi\phi}\delta_{p'_y,p_y}. \tag{B.20}$$

It is clear the Fourier transforming does not diagonalize the Hamitonian, as different momentum sectors are still coupled due to $\delta_{p'_x,p_x+2\pi\phi}$. Remembering that $\phi = p/q$ we can remedy this by defining $(k_x + 2\pi\phi j, k_y) = (p_x, p_y)$ with $j = 0, \ldots, q-1$ and at the same time make $\hat{\psi}(k_x + 2\pi\phi j, k_y) \equiv \hat{\psi}_j(k_x, k_y) = \hat{\psi}_j(\vec{k})$. This amounts to making the Brillouin zone q times smaller in the x direction, while making the real space unit cell q times larger. We note is passing that this only works if and only if p and q are relatively prime, as only in this case the prescription $(k_x + 2\pi\phi j, k_y) = (p_x, p_y)$ allows to access the full range $0 \le p_x < 2\pi$. The $\mathcal{M}$ matrix is rewritten as

$$\mathcal{M}^{j'j}_{\vec{k}'\vec{k}} = \mathcal{M}^{j'j}\delta_{\vec{k}',\vec{k}}$$
$$\mathcal{M}^{j'j} = e^{-i(k_x+2\pi\phi j)}\delta_{j',j} + (e^{-ik_y} + e^{i\pi\phi(1-2j)}e^{-i(k_x+k_y)})\delta_{j',j+1} \tag{B.21}$$

with Hamiltonian

$$\hat{H} = -t\sum_{\vec{k},j,j'}\hat{\psi}^\dagger_{j'}(\vec{k})\mathcal{M}^{j'j}\hat{\psi}_j(\vec{k}) + \text{hc} \equiv -t\sum_{\vec{k},j,j'}\hat{\psi}^\dagger_{j'}(\vec{k})\mathcal{H}^{j'j}(\vec{k})\hat{\psi}_j(\vec{k}) \tag{B.22}$$

At this point we particularize to the situation $\phi = 1/2$, which is the relevant case for the Chern insulator model discussed in this thesis. We have values $j = 0, 1$ and it is a simple matter to show that in this basis one has

$$\mathcal{H}(\vec{k}) = -2t\cos k_x \tau^3 - 2t\cos k_y \tau^1 + 2t\cos(k_x + k_y)\tau^2 \tag{B.23}$$

In general, the magnetic Brillouin zone is restricted to $0 \le k_x < 2\pi/q$ as a consequence of the folding expressed in $(k_x + 2\pi\phi j, k_y) = (p_x, p_y)$, meaning that the reciprocal lattice vector in the x direction is $\vec{G}_1 = (2\pi/q, 0)$. The example of $\phi = 1/2$ shows that the Hamiltonian as written in B.23 does *not* satisfy $\mathcal{H}(\vec{k} + \vec{G}_1) = \mathcal{H}(\vec{k})$.

This is easy to understand by looking at how the field operators respond to a shift by $\vec{G}_1$ in momentum space.

$$
\begin{aligned}
\hat{\psi}_j(\vec{k} + \vec{G}_1) &= \hat{\psi}(k_x + 2\pi/q + 2\pi\phi j, k_y) \\
&= \hat{\psi}(k_x + 2\pi(pj+1)/q, k_y) \\
&= \hat{\psi}(k_x + 2\pi\phi j', k_y)
\end{aligned}
\tag{B.24}
$$

where j' and j are related by $(pj+1) \bmod q = pj' \bmod q$, or $p(j'-j)-1 = 0 \bmod q$. An example is illustrative and we take $\phi = p/q = 3/5$. It may be verified that $j = 0$ is mapped to $j = 2$, $j = 1$ to $j = 3$, $j = 2$ to $j = 4$, $j = 3$ to $j = 0$ and $j = 4$ to $j = 1$. Collecting the $\hat{\psi}_j(\vec{k})$ in the vector operator $\hat{\Psi}(\vec{k})$, we have the general relation

$$
\hat{\Psi}(\vec{k} + \vec{G}_1) = U^\dagger \hat{\Psi}(\vec{k}).
\tag{B.25}
$$

The matrix $U^\dagger$ effectively operates as a translation operator of the index j by an amount j_Δ given by the solution of $pj_\Delta - 1 = 0 \bmod q$. Note that periodic boundary conditions apply. The eigenvalues of a translation operator are given by $e^{i2\pi j_\Delta l/q}$, with $l \in [0, 1, \ldots, q-1]$. If V is the matrix that diagonalizes $U^\dagger$ such that $V^\dagger U^\dagger V = D$ with D a diagonal matrix with the eigenvalues on the diagonal, then we have the relation

$$
\hat{\Phi}(\vec{k} + \vec{G}_1) = D\hat{\Phi}(\vec{k})
\tag{B.26}
$$

where $\hat{\Phi}(\vec{k}) = V^\dagger \hat{\Psi}(\vec{k})$, which is the first part of the gauge transformation on the state operators. The second part is achieved by defining a new matrix $D(\vec{k}) = \mathrm{Diag}(d_1, \ldots, d_q)$, with $d_l = e^{ik_x l}$. We observe that $D(\vec{G}_1) = D$, which we use to define $D^\dagger(\vec{k})\hat{\Phi}(\vec{k})$, which is invariant under $\vec{k} \to \vec{k} + \vec{G}_1$. Hence, we obtain a Hamiltonian obeying $\tilde{\mathcal{H}}(\vec{k} + \vec{G}_1) = \tilde{\mathcal{H}}(\vec{k})$ by defining

$$
\tilde{\mathcal{H}}(\vec{k}) = D^\dagger(\vec{k})V^\dagger \mathcal{H}(\vec{k})VD(\vec{k})
\tag{B.27}
$$

For the particular case of $\phi = 1/2$ this amounts to

$$
V = e^{-i\pi\tau^2/4}, \qquad D(\vec{k}) = \begin{bmatrix} 1 & \\ & e^{ik_x} \end{bmatrix},
\tag{B.28}
$$

which yields $V^\dagger \tau^1 V = \tau^3$, $V^\dagger \tau^2 V = \tau^2$ and $V^\dagger \tau^3 V = -\tau^1$. It is straightforward to use these relations to obtain the transformed Hamiltonian.

We proceed to discuss the case of the symmetric gauge in a similar fashion. Again we write the Hamiltonian using the matrix $\mathcal{M}$ and obtain

$$
\mathcal{M}_{\vec{n}'\vec{n}} = \delta_{\vec{n}',\vec{n}+\vec{u}_x} e^{-i\pi\phi n_y} + \delta_{\vec{n}',\vec{n}+\vec{u}_y} e^{i\pi\phi n_x} + \delta_{\vec{n}',\vec{n}+\vec{u}_x+\vec{u}_y} e^{i\pi\phi(n_x - n_y)}
\tag{B.29}
$$

Using the same Fourier transform as before one derives in momentum space

$$\hat{H} = -t \sum_{\vec{p},\vec{p}'} \hat{\psi}^\dagger(\vec{p}') \mathcal{M}_{\vec{p}'\vec{p}} \hat{\psi}(\vec{p}) + \text{hc} \tag{B.30}$$

with the momentum space matrix $\mathcal{M}_{\vec{p}'\vec{p}}$ defined as

$$\mathcal{M}_{\vec{p}'\vec{p}} = e^{-ip_x} \delta_{p'_x,p_x} \delta_{p'_y,p_y-\pi\phi} + e^{-ip_y} \delta_{p'_x,p_x+\pi\phi} \delta_{p'_y,p_y}$$
$$+ e^{-i(p_x+p_y)} \delta_{p'_x,p_x+\pi\phi} \delta_{p'_y,p_y-\pi\phi}. \tag{B.31}$$

Since we still have $\phi = p/q$ we are forced to fold the Brillouin zone according to the rule $(k_x + \pi\phi j_x, k_y + \pi\phi j_y) = (p_x, p_y)$, which amounts to a magentic Brillouin zone given by $0 \leq k_x < \pi/q$ and $0 \leq k_y < \pi/q$. Substituting the definition of these new momenta into the matrix of equation (B.2), we derive

$$\mathcal{M}^{j'j}_{\vec{k}'\vec{k}} = \mathcal{M}^{j'j} \delta_{\vec{k}'\vec{k}} = \delta_{\vec{k}'\vec{k}} \left(e^{-ik_x} e^{-i\pi\phi j_x} \delta_{j'_x,j_x} \delta_{j'_y,j_y-1} + \right.$$
$$\left. e^{-ik_y} e^{-i\pi\phi j_y} \delta_{j'_x,j_x+1} \delta_{j'_y,j_y} + e^{-i(k_x+k_y)} e^{-i\pi\phi(j_x+j_y)} \delta_{j'_x,j_x+1} \delta_{j'_y,j_y-1} \right), \tag{B.32}$$

where we have written j to denote the double index (j_x, j_y). The label j takes values in $j \in [0, 1, \ldots, 2q \times 2q - 1)$, which means that we have considerably increased the dimensionality of the of the state operator $\hat{\Psi}(\vec{k}) = \hat{\psi}_j(\vec{k})$ as compared to the Landau gauge.

Appendix C

Basic elements of group theory

The purpose of this appendix is to collect and summarize all the basic elements of group theory required to follow and understand the symmetry analysis presented in the main text. The following brief overview is therefore far from exhaustive, but it serves to introduce notation and the main concepts, in particular the extended point groups.

The group of all symmetry operations leaving a given Bravais lattice invariant is the space group S. It consists of all translations T, an Abelian subgroup of S, and the point group G. The point group can be viewed as the factor group of the space group, i.e. $G = S/T$. Throughout this work we denote general point group elements by R, meaning that $R \in G$. Translations over a lattice vector $\vec{x}$ [see equation (**??**)] are written as $T(\vec{x})$. The translation subgroup T is generated by two elements, which are $T(\vec{x}_1)$ and $T(\vec{x}_2)$ corresponding to the two lattice vectors $\vec{x}_1$ and $\vec{x}_2$. The point group G, which for our purposes is always C_{nv} with n generally beig either 4 or 6, is generated by two elements. These are the n-fold rotation C_n and the reflection σ_v. The relfection σ_v is always taken as the operations which reflects in the x-axis, i.e. $(x, y) \rightarrow (x, -y)$. Any element $R \in G$ can then be written as $R = C_n^{m_1} \sigma_v^{m_2}$. Consequently, the space group S is generated by lements $T(\vec{x}_2)^{m_4} T(\vec{x}_1)^{m_3} C_6^{m_2} \sigma_v^{m_1}$. Note that point group operations and translations do not commute, but instead satisfy $T(\vec{x})R = RT(R\vec{x})$.

In the main text we exclusively talk about the point groups C_{nv}. For spinless particles in $2D$ these groups are exactly equivalent to D_n, which are groups generated

by the n-fold rotation C_n and a non-commuting two-fold rotation C_2' around the x-axis. Hence, C_2' takes the place of σ_v, leaving all algebraic relations invariant. Below we comment on the distinction between C_{nv} and D_6 in the presence of the electron spin.

C.1   Translational symmetry breaking and "extended" point groups

The central theme of this work is interaction-induced translational symmetry breaking. In particular we have classified translational symmetry broken site, bond and flux ordered states based on lattice symmetries. Translational symmetry breaking removes a subset of translations from the full group of translations T, leading to reduced group of invariant translations which we denote as $\widetilde{T}$. Having estabslished this new group of invariant translations (which is smaller than T), we can take the space group and again calculate the point by $\widetilde{G} = S/\widetilde{T}$. The point group $\widetilde{G}$ is larger than G, as it contains elements of T no longer part of $\widetilde{T}$. In particular, if $t_1 \equiv T(\vec{x}_1)$ is no longer part of $\widetilde{T}$, it belongs to the extended point group $\widetilde{G}$.

Both for the case of the square and the hexagonal Bravais lattice we consider translational symmetry breaking such that $\widetilde{T}$ is generated by $T(2\vec{x}_1)$ and $T(2\vec{x}_2)$. This means that $T(\vec{x}_1) = t_1$, $T(\vec{x}_2) = t_2$ and $T(\vec{x}_1 + \vec{x}_2) = t_3$ are added to the point group. To illustrate this more clearly, let us take the hexagonal group C_{6v} as an example. This group has 12 elements, but the group C_{6v}''' (three primes indicate three broken elementary translations), which also contains $t_{1,2,3}$, contains 48 elements, i.e. $48 = 12 + 3 \times 12$. Algebraic properties of these elements can be worked out using $T(\vec{x})R = RT(R\vec{x})$ and the fact that $t_i t_j = |\epsilon_{ijk}| t_k$. In particular, the conjugacy classes of the group C_{6v}''' can be calculated and the character table can be obtained in the standard way. As the point group C_{6v} is a proper subgroup of C_{6v}''' all irreducible representations of C_{6v} will also appear as irreducible representations of C_{6v}''', in addition to new irreducible representations originating from the nontrivial translations. The character tables of the groups C_{6v}''' (hexagonal) and C_{4v}''' (square) are given in Table C.6 and Table C.7, respectively. They can the used in the standard way to decompose any representation into irreducible representations.

A distinct extended point group is obtained if we anticipate translational symmetry breaking of a hexagonal lattice which triples the unit cell. In that case the translations $T(\vec{x}_1) = t_1$, $T(\vec{x}_1 + \vec{x}_2) = t_2$ (redefining the t_i) are added to the point group, leading to the group C_{6v}''. The procedure for obtaining the character table is exactly the same, however one should be careful to implement the correct algebraic relations between these t_1 and t_2. Specifically, they are each others inverse. The

Point group C_{2v}			I	C_2	σ_v	σ_v'
$x^2 + y^2$, z^2	z	A_1	1	1	1	1
xy	L_z	A_2	1	1	-1	-1
xz	R_y, x	B_1	1	-1	1	-1
yz	R_x, y	B_2	1	-1	-1	1

Table C.1: Character table of the point group C_{2v}.

character table of C_{6v}'' is given in Table C.5.

C.2   The point groups C_{4v} and C_{6v}

In the main text we discuss square and hexagonal lattice systems. The square lattice systems have symmetry group C_{4v}, while the hexagonal lattices have point group C_{6v}. We have already mentioned that each of these groups can be generated by two elements. In case of C_{4v} these are C_4 and σ_v. All other point group operations can be written in terms of these generators as follows

$$C_2 = C_4^2, \quad C_4^{-1} = C_4^3,$$
$$\sigma_{v1} = \sigma_v, \quad \sigma_{v2} = C_2\sigma_v \quad \sigma_{d1} = C_4\sigma_v, \quad \sigma_{d2} = C_4^{-1}\sigma_v. \tag{C.1}$$

These operations are graphically shown on the left side of Fig. C.1.

In case of C_{6v} the generators of the group are C_6 and σ_v. The other point group operations can be written in terms of them as

$$C_3 = C_6^2, \quad C_2 = C_6^3, \quad C_3^{-1} = C_6^4, \quad C_6^{-1} = C_6^5,$$
$$\sigma_{v1} = \sigma_v, \quad \sigma_{v2} = C_3\sigma_v \quad \sigma_{v3} = C_3^{-1}\sigma_v,$$
$$\sigma_{d1} = C_6\sigma_v, \quad \sigma_{d2} = C_2\sigma_v \quad \sigma_{d3} = C_6^{-1}\sigma_v. \tag{C.2}$$

These operations are shown in Fig. C.1 as well, on the right side.

We note again that if we exchange σ_v and C_2', i.e. a rotation of π around the x-axis instead of a reflection, but keep the algebraic structure of group elements defined in (C.1) and (C.2) then we obtain the (dihedral) groups D_4 and D_6. The irreduble representations of C_{4v} and C_{6v} are listed in the character tables of Table C.1, C.1, C.3, and C.4.

Point group C_{4v}			I	C_2	$2C_4$	$2\sigma_v$	$2\sigma_d$
$x^2 + y^2, z^2$	z	A_1	1	1	1	1	1
	L_z	A_2	1	1	1	-1	-1
$x^2 - y^2$		B_1	1	1	-1	1	-1
xy		B_2	1	1	-1	-1	1
(xz, yz)	$\begin{matrix}(x,y) \\ (L_x, L_y)\end{matrix} \Big\}$	E	2	-2	0	0	0

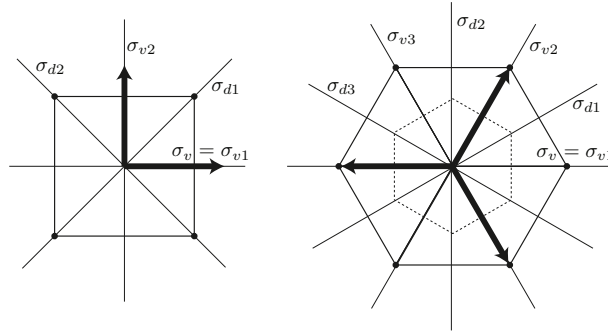**Table C.2:** Character table of the point group C_{4v}.

Figure C.1: Graphical representation of the point group symmetries of $2D$ square lattices (left) and hexagonal lattices (right). The reflections are given in terms of the generators $C_{4,6}$ and σ_v in the text of the present appendix.

C.2.1 M-point representation of hexagonal symmetry operations

In Section 9.4.1 we have introduced a particular representation of the hexagonal symmetry groups which proved very helpful in deriving condensate functions transforming as irreducible representations. Here we come back to this representations and provide some additional details, such as commutation relations for various elements.

The representation is defined by the actions of the rotations, reflections, and translations on the the linearly independent functions $\cos(\vec{Q}_\mu \cdot \vec{x})$, where $\vec{Q}_\mu$ ($\mu = 1, 2, 3$) are the three M-point vectors. The are collected in the 3-dimensional vector $\vec{\xi} = \xi_\mu(\vec{x}) = \cos(\vec{Q}_\mu \cdot \vec{x})$. As was shown in Section 9.4.1, we can obtain a representation of the lattice symmetry group by considering the effect of all lattice operations on the vector $\vec{\xi}$. Taking the translations, the effect of which is given by $\xi_\mu(\vec{x} + \vec{x}_j)$, we find three matrices G_j ($j = 1, 2, 3$) corresponding to $\vec{x}_j$, such that

Point group C_{3v}			I	$2C_3$	$3\sigma_v$
$x^2 + y^2, z^2$	z	A_1	1	1	1
	L_z	A_2	1	1	−1
$\left.\begin{matrix}(xz, yz) \\ (x^2 - y^2, xy)\end{matrix}\right\}$	$\left.\begin{matrix}(x, y) \\ (L_x, L_y)\end{matrix}\right\}$	E	2	−1	0

Table C.3: Character table of the point group C_{3v}.

Point group C_{6v}			I	C_2	$2C_3$	$2C_6$	$3\sigma_d$	$3\sigma_v$
$x^2 + y^2, z^2$	z	A_1	1	1	1	1	1	1
	L_z	A_2	1	1	1	1	−1	−1
		B_1	1	−1	1	−1	−1	1
		B_2	1	−1	1	−1	1	−1
(xz, yz)	$\left.\begin{matrix}(x, y) \\ (L_x, L_y)\end{matrix}\right\}$	E_1	2	−2	−1	1	0	0
$(x^2 - y^2, xy)$		E_2	2	2	−1	−1	0	0

Table C.4: Character table of the point group C_{6v}.

$\xi_\mu(\vec{x} + \vec{x}_j) = [G_j]_{\mu\nu}\xi_\nu(\vec{x})$. Hence, for a given translation the effect on $\vec{\xi}$ is given by G_j, i.e. $G_j\vec{\xi}$. The three matrices take the form

$$G_1 = \begin{bmatrix} -1 & & \\ & -1 & \\ & & 1 \end{bmatrix}, \; G_2 = \begin{bmatrix} 1 & & \\ & -1 & \\ & & -1 \end{bmatrix}, \; G_3 = G_1 G_2. \qquad \text{(C.3)}$$

Not surprisingly, all the G_j commute, square to one, and multiplying two of them gives the third. This follows from the M-point vectors, which have the same properties under addition. Another way of understanding this is to say that M-point order implies a quadrupled real space unit cell, meaning that an even number of elementary translations must always leave the system invariant.

Regarding the point group operations, we only need the actions of the generators C_6 and σ_v on the vector ξ. In the main text we defined the matrix X to correspond to the permutation of ξ_μ as a consequence of C_6, i.e.

$$\vec{\xi}(C_6\vec{x}) = X\vec{\xi}(\vec{x}), \quad X = \begin{bmatrix} 0 & 0 & 1 \\ 1 & 0 & 0 \\ 0 & 1 & 0 \end{bmatrix} \qquad \text{(C.4)}$$

Note that X has the property $X^3 = 1$ and thus $X^{-1} = X^2$. In addition the relation $X^{-1} = X^T$ holds, where X^T is the transpose. For the reflection σ_v we had defined an element Y such that

$$\vec{\xi}(\sigma_v \vec{x}) = Y\vec{\xi}(\vec{x}), \quad Y = \begin{bmatrix} 0 & 0 & 1 \\ 0 & 1 & 0 \\ 1 & 0 & 0 \end{bmatrix} \tag{C.5}$$

With the explicit matrix expression at hand it is a simple matter to show that $(XY)^2 = 1$, from which all algebraic relations between X and Y follow.

We now proceed to list some helpful algebraic commutation properties of the G_j and X. It is a simple matter to derive or check that

$$G_2 X = X G_1, \quad G_1 X^{-1} = X^{-1} G_2$$
$$G_1 X = X G_3, \quad G_3 X^{-1} = X^{-1} G_1$$
$$G_3 X = X G_2, \quad G_2 X^{-1} = X^{-1} G_3. \tag{C.6}$$

In the same way we have for the G_j and Y

$$G_2 Y = Y G_1$$
$$G_1 Y = Y G_2$$
$$G_3 Y = Y G_3. \tag{C.7}$$

We close by mentioning that the representation of C_{6v} in terms of X and Y is reducible and the decomposition is given by $A_1 \oplus E_2$. However, the elements G_j, X and Y generate a representation of C_{6v}''', which is irreducible and equal to F_1.

C.3 Symmetry properties with spin

Chapter 10 deals with spinful condensates or triplet condensates. The description of these condensates requires taking into account the point (or space) group respresenations acting on the spinor degree of freedom. In terms of equation (9.6) of the main text, one needs to consider the matrix U_R° acting on the spinor degree af freedom. It is a matrix belonging to $SU(2)$.

As was already mentioned before, for spinless particles the groups C_{nv} and D_n may be considered identical, as indeed both send $(x, y) \rightarrow (x, -y)$ under the reflection (C_{nv}) in the $x - z$ plane or the twofold rotation about the x-axis (D_n). In the spinful case, there is a difference however, since reflections and rotations act in different ways. The transformation properties for the n-fold rotation about the z-axis are

Conjugacy class	$\mathcal{C}_1''$	$\mathcal{C}_2''$	$\mathcal{C}_3''$	$\mathcal{C}_4''$	$\mathcal{C}_5''$	$\mathcal{C}_6''$	$\mathcal{C}_7''$	$\mathcal{C}_8''$	$\mathcal{C}_9''$
Representative	I	t_1	C_2	C_3	$t_1 C_3$	C_6	σ_v	$t_1 \sigma_v$	σ_d
A_1	1	1	1	1	1	1	1	1	1
A_2	1	1	1	1	1	1	-1	-1	-1
B_1	1	1	-1	1	1	-1	1	1	-1
B_2	1	1	-1	1	1	-1	-1	-1	1
E_1	2	2	-2	-1	-1	1	0	0	0
E_2	2	2	2	-1	-1	-1	0	0	0
E_1'	2	-1	0	2	-1	0	2	-1	0
E_2'	2	-1	0	2	-1	0	-2	1	0
G'	4	-2	0	-2	1	0	0	0	0

Table C.5: Character table of the point group C_{6v}''. Translations t_1 and t_2 correspond to $T(\vec{x}_1)$ and $T(\vec{x}_2)$, respectively. The irreducible representations that arise as a consequence of the added translations are E_1' (2D), E_2' (2D) and G' (4D). The conjugacy classes consist of the elements: $\mathcal{C}_1'' = \{I\}$, $\mathcal{C}_2'' = \{t_1, t_2\}$, $\mathcal{C}_3'' = \{C_2, t_i C_2\}$, $\mathcal{C}_4'' = \{C_3, C_3^{-1}\}$, $\mathcal{C}_5'' = \{t_i C_3, t_i C_3^{-1}\}$, $\mathcal{C}_6'' = \{t_i C_6, t_i C_6^{-1}, C_6, C_6^{-1}\}$, $\mathcal{C}_7'' = \{3\sigma_v\}$, $\mathcal{C}_8'' = \{3t_1\sigma_v, 3t_2\sigma_v\}$, $\mathcal{C}_9'' = \{3\sigma_d, 3t_i\sigma_d\}$.

straightforward to deduce, using the standard formula for $SU(2)$ rotations. A rotation about an axis $\hat{n}$ by an angle θ is given by

$$U = e^{-i\theta \hat{n}\cdot\vec{\sigma}/2} = \cos\frac{\theta}{2} - i\sin\frac{\theta}{2}\,\hat{n}\cdot\vec{\sigma} \tag{C.8}$$

Applying this formula to the n-fold rotations (where we take $n = 4, 6$ for definiteness), which are rotations about the z-axis, the rotation matrix becomes $e^{-i\pi\sigma^3/n}$ and the Pauli matrices transform as

$$C_n : \qquad \sigma^3 \to \sigma^3; \qquad \sigma^{\pm} \to e^{\pm i2\pi/n}\sigma^{\pm} \tag{C.9}$$

This is true for both C_{nv} and D_6. The distinction between the two groups comes from the reflections (C_{nv}) or the two-fold rotations (D_6). For the group D_n the two-fold rotation is also simple to write down. A rotation of π about the x-axis is given by $-i\sigma^1$ and thus we have

$$C_2' : \qquad \sigma^{2,3} \to -\sigma^{2,3}; \qquad \sigma^1 \to \sigma^1 \tag{C.10}$$

For the reflection on the other we need to take into account that a magnetic moment like spin can be thought of as generated by a small current loop. A spin pointing in

the x-direction may be thought of as a current loop in the $z - y$ plane and hence a reflection in the $x - z$ plane changes the current direction. The spin will be rotated by π. One observes that the only direction that does not change is a spin pointing in the y-direction. The transformation properties follow:

$$\sigma_v : \qquad \sigma^{1,3} \rightarrow -\sigma^{1,3}; \qquad \sigma^2 \rightarrow \sigma^2 \qquad\qquad \text{(C.11)}$$

We therefore observe that the transformation properties of the reflections and two-fold rotations differ and therefore define distinct point groups.

Another way of understanding the difference between C_{6v} is to view both C_{6v} and D_6 as subgroups of O_h, i.e. the group of all symmetries of the cube. It is known that all elements of O_h may be written as a product of a proper rotation and the inversion operation. Rotations rotate pseusovectors such as angular momentum and the electron spin, however, the inversion operation does nothing to a pseudovector. Therefore, in order to find out what member of $SU(2)$ corresponds to σ_v and C_2', one needs to find out what proper rotation make up these elements. In the first case it is a rotation about the x-axis and in the second case it is a rotation about the y-axis.

We stress here again that while details do depend on this difference in the spinful case the main conclusions reached in this work do not depend on whether the symmetry group is C_{6v} or D_6.

C.3.1 Spinful M-point representation of hexagonal symmetry operations

An important concept introduced in Chapter 10 is global rotation equivalence. For spinful condensates point group operations and translations may need to be combined with a global spin rotation in order to make them good symmetries. We have only treated spinful condensates constructed from M-point vectors in hexagonal systems and the connection between elements of C_{6v}''' and global $U(2)$ rotations (not $SU(2)$) is established via the 3×3 matrices G_j, X and Y (see Section C.2.1) acting on $\vec{\xi}$. This connection is explicitly expressed in equation (10.5) of the main text.

The mapping from the 3×3 representation, i.e. matrices which can be interpreted as rotation matrices of $O(3)$, to the space $U(2)$ preserves the algebraic structure and defines another representation, with the electron spin wavefunctions as basis functions. It is straighforward to associate a $U(2)$ matrix to an $O(3)$ rotation matrix, by determining the rotation axis and angle. For instance, the translation element G_1 corresponds to a rotation about the z-axis by π. Hence, the associated $U(2)$ matrix is

Conj. class	$\mathcal{C}_1'''$	$\mathcal{C}_2'''$	$\mathcal{C}_3'''$	$\mathcal{C}_4'''$	$\mathcal{C}_5'''$	$\mathcal{C}_6'''$	$\mathcal{C}_7'''$	$\mathcal{C}_8'''$	$\mathcal{C}_9'''$	$\mathcal{C}_{10}'''$
Repres.		t_1	C_2	$t_1 C_2$	C_3	C_6	σ_v	$t_1 \sigma_v$	σ_d	$t_1 \sigma_{d1}$
A_1	1	1	1	1	1	1	1	1	1	1
A_2	1	1	1	1	1	1	-1	-1	-1	-1
B_1	1	1	-1	-1	1	-1	1	1	-1	-1
B_2	1	1	-1	-1	1	-1	-1	-1	1	1
E_1	2	2	-2	-2	-1	1	0	0	0	0
E_2	2	2	2	2	-1	-1	0	0	0	0
F_1	3	-1	3	-1	0	0	1	-1	1	-1
F_2	3	-1	3	-1	0	0	-1	1	-1	1
F_3	3	-1	-3	1	0	0	1	-1	-1	1
F_4	3	-1	-3	1	0	0	-1	1	1	-1

Table C.6: The point group C_{6v}'''. Translations t_1 and t_2 correspond to $T(\vec{x}_1)$ and $T(\vec{x}_2)$, respectively. $t_3 = T(\vec{x}_1 + \vec{x}_2)$. The irreducible representations that arise as a consequence of the added translations are F_1, F_2, F_3 and F_4, all three-dimensional. The conjugacy classes consist of the elements: $\mathcal{C}_1''' = \{I\}$, $\mathcal{C}_2''' = \{t_1, t_2, t_3\}$, $\mathcal{C}_3''' = \{C_2\}$, $\mathcal{C}_4''' = \{t_iC_2\}$, $\mathcal{C}_5''' = \{t_iC_3, t_iC_3^{-1}, C_3, C_3^{-1}\}$, $\mathcal{C}_6''' = \{t_iC_6, t_iC_6^{-1}, C_6, C_6^{-1}\}$, $\mathcal{C}_7''' = \{3\sigma_v, t_1\sigma_{v2}, t_2\sigma_{v3}, t_3\sigma_{v1}\}$, $\mathcal{C}_8''' = \{t_1\sigma_v, t_2\sigma_v, t_2\sigma_{v2}, t_3\sigma_{v2}, t_1\sigma_{v3}, t_3\sigma_{v3}\}$, $\mathcal{C}_9''' = \{3\sigma_d, t_2\sigma_{d1}, t_3\sigma_{d2}, t_1\sigma_{v3}\}$, $\mathcal{C}_{10}''' = \{t_1\sigma_{d1}, t_3\sigma_{d1}, t_1\sigma_{d2}, t_2\sigma_{d2}, t_2\sigma_{d3}, t_3\sigma_{d3}\}$.

$-i\sigma^3$. We simply find for all translations.

$$
\begin{aligned}
G_1 &\rightarrow e^{-i\pi\sigma^3/2} = -i\sigma^3 \\
G_2 &\rightarrow e^{-i\pi\sigma^1/2} = -i\sigma^1 \\
G_3 &\rightarrow e^{-i\pi\sigma^2/2} = -i\sigma^2.
\end{aligned}
\tag{C.12}
$$

The matrix X, interpreted as rotation matrix, corresponds to a rotation by $2\pi/3$ about the axis $\hat{n} = (1, 1, 1)/\sqrt{3}$. We can decompose it into two separate rotations about the z and y-axes (Euler rotations) and obtain the $SU(2)$ matrices

$$
\begin{aligned}
X &\rightarrow e^{-i\pi\sigma^2/4} e^{-i\pi\sigma^3/4} \\
X^T &\rightarrow e^{i\pi\sigma^3/4} e^{i\pi\sigma^2/4}.
\end{aligned}
\tag{C.13}
$$

Note that these are elements of $SU(2)$ since X and X^T are proper rotations. This is different for Y, which has determinant -1. Therefore $-Y$ is a proper rotation which

can be identified with an element of $SU(2)$. One finds that

$$-Y \quad \rightarrow \quad e^{i\pi\sigma^2/4}e^{-i\pi\sigma^3/2} = -ie^{i\pi\sigma^2/4}\sigma^3, \tag{C.14}$$

which completes the mapping of G_j, X and Y onto $U(2)$ matrices. This mapping is at the heart of analyzing symmetry properties of spinful condensates. In particular, the appearance of an extra minus sign for Y is what causes some reflections to constitute good symmetries in the presence of spin, as explained in Chapter 10.

| Conjugacy class | $\mathcal{C}_1'''$ | $\mathcal{C}_2'''$ | $\mathcal{C}_3'''$ | $\mathcal{C}_4'''$ | $\mathcal{C}_5'''$ | $\mathcal{C}_6'''$ | $\mathcal{C}_7'''$ | $\mathcal{C}_8'''$ | $\mathcal{C}_9'''$ | $\mathcal{C}_{10}'''$ | $\mathcal{C}_{11}'''$ | $\mathcal{C}_{12}'''$ | $\mathcal{C}_{13}'''$ | $\mathcal{C}_{14}'''$ |
Representative	I	t_1	t_3	C_2	t_1C_2	t_3C_2	C_4	t_1C_4	σ_v	$t_3\sigma_v$	$t_1\sigma_v$	$t_2\sigma_v$	σ_{d1}	$t_1\sigma_{d1}$
A_1	1	1	1	1	1	1	1	1	1	1	1	1	1	1
A_2	1	1	1	1	1	1	1	1	-1	-1	-1	-1	-1	-1
B_1	1	1	1	1	1	1	-1	-1	1	1	1	1	-1	-1
B_2	1	1	1	1	1	1	-1	-1	-1	-1	-1	-1	1	1
E_1	2	2	2	-2	-2	-2	0	0	0	0	0	0	0	0
A_1'	1	-1	1	1	-1	1	1	-1	1	-1	-1	1	1	-1
A_2'	1	-1	1	1	-1	1	1	-1	-1	1	1	-1	-1	1
B_1'	1	-1	1	1	-1	1	-1	1	1	-1	-1	1	-1	1
B_2'	1	-1	1	1	-1	1	-1	1	-1	1	1	-1	1	-1
E_1'	2	-2	2	-2	2	-2	0	0	0	0	0	0	0	0
E_2	2	0	-2	2	0	-2	0	0	-2	0	0	2	0	0
E_3	2	0	-2	2	0	-2	0	0	2	0	0	-2	0	0
E_4	2	0	-2	-2	0	2	0	0	0	2	-2	0	0	0
E_5	2	0	-2	-2	0	2	0	0	0	-2	2	0	0	0

Table C.7: Character table of the point group C_{6v}'''. Translations t_1 and t_2 correspond to $T(\vec{x}_1)$ and $T(\vec{x}_2)$, respectively. $t_3 = T(\vec{x}_1 + \vec{x}_2)$. The conjugacy classes consist of the elements: $\mathcal{C}_1''' = \{I\}$, $\mathcal{C}_2''' = \{t_1, t_2\}$, $\mathcal{C}_3''' = \{t_3\}$, $\mathcal{C}_4''' = \{C_2\}$, $\mathcal{C}_5''' = \{t_1C_2, t_2C_2\}$, $\mathcal{C}_6''' = \{t_3C_2\}$, $\mathcal{C}_7''' = \{C_4, C_4^{-1}, t_3C_4, t_3C_4^{-1}\}$, $\mathcal{C}_8''' = \{t_1C_4, t_1C_4^{-1}, t_2C_4, t_2C_4^{-1}\}$, $\mathcal{C}_9''' = \{\sigma_{v1}, \sigma_{v2}\}$, $\mathcal{C}_{10}''' = \{t_3\sigma_{v1}, t_3\sigma_{v2}\}$, $\mathcal{C}_{11}''' = \{t_1\sigma_{v1}, t_2\sigma_{v2}\}$, $\mathcal{C}_{12}''' = \{t_2\sigma_{v1}, t_1\sigma_{v2}\}$, $\mathcal{C}_{13}''' = \{\sigma_{d1}, \sigma_{d2}, t_3\sigma_{d1}, t_3\sigma_{d2}\}$ and $\mathcal{C}_{14}''' = \{t_1\sigma_{d1}, t_1\sigma_{d2}, t_2\sigma_{d1}, t_2\sigma_{d2}\}$.

BIBLIOGRAPHY

[1] C. L. Kane and E. J. Mele, Phys Rev Lett **95**, 146802 (2005).

[2] L. Fu and C. L. Kane, Phys Rev B **74**, 195312 (2006).

[3] L. Fu, C. L. Kane, and E. J. Mele, Phys Rev Lett **98**, 106803 (2007).

[4] J. E. Moore and L. Balents, Phys Rev B **75**, 121306 (2007).

[5] R. Roy, Phys Rev B **79**, 195321 (2009).

[6] B. A. Bernevig, T. L. Hughes, and S.-C. Zhang, Science **314**, 1757 (2006).

[7] M. Koenig, S. Wiedmann, C. Bruene, A. Roth, H. Buhmann, L. W. Molenkamp, X.-L. Qi, and S.-C. Zhang, Science **318**, 766 (2007).

[8] D. Hsieh, D. Qian, L. Wray, Y. Xia, Y. S. Hor, R. J. Cava, and M. Z. Hasan, Nature **452**, 970 (2008).

[9] Y. Xia, L. Wray, D. Qian, D. Hsieh, A. Pal, H. Lin, A. Bansil, D. Grauer, Y. S. Hor, R. J. Cava, and M. Z. Hasan, arXiv (2008).

[10] D. C. Tsui, H. L. Stormer, and A. C. Gossard, Phys Rev Lett **48**, 1559 (1982).

[11] X.-G. Wen, Adv Phys **44**, 405 (1995).

[12] M. Z. Hasan and C. L. Kane, Rev Mod Phys **82**, 3045 (2010).

[13] S. M. Girvin, A. H. MacDonald, and P. M. Platzman, Phys Rev Lett **54**, 581 (1985).

[14] F. D. M. Haldane, Phys Rev Lett **55**, 2095 (1985).

[15] T. Neupert, L. Santos, S. Ryu, C. Chamon, and C. Mudry, Phys Rev B **86**, 035125 (2012).

[16] D. Thouless, M. Kohmoto, M. Nightingale, and M. den Nijs, Phys Rev Lett **49**, 405 (1982).

[17] S.-C. Zhang, Int J Mod Phys B **6**, 25 (1992).

[18] G. E. Volovik, *The Universe in a Helium Droplet* (Oxford University Press, USA, 2009).

[19] W. P. Su, J. R. Schrieffer, and A. J. Heeger, Phys Rev Lett **42**, 1698 (1979).

[20] N. Furukawa, *Geometry, Topology and Physics* (Taylor and Francis, New York, 2003 (2nd edition)).

[21] A. P. Schnyder, S. Ryu, A. Furusaki, and A. W. W. Ludwig, Phys Rev B **78**, 195125 (2008).

[22] S. Ryu, A. P. Schnyder, A. Furusaki, and A. W. W. Ludwig, New J Phys **12**, 065010 (2010).

[23] C. L. Kane and E. J. Mele, Phys Rev Lett **95**, 226801 (2005).

[24] H. B. Nielsen and M. Ninomiya, Phys Lett B **130**, 389 (1983).

[25] K. Wilson, Rev Mod Phys **47**, 773 (1975).

[26] A. C. Hewson, *The Kondo Problem to Heavy Fermions* (Cambridge University Press, Cambridge, England, 1993).

[27] E. Dagotto, T. Hotta, and A. Moreo, Phys Rep **344**, 1 (2001).

[28] E. Dagotto, *Nanoscale Phase Separation and Colossal Magnetoresistance* (Springer, Berlin, 2002).

[29] R. Shindou and N. Nagaosa, Phys Rev Lett **87**, 116801 (2001).

[30] I. Martin and C. D. Batista, Phys Rev Lett **101**, 156402 (2008).

[31] Y. Akagi and Y. Motome, J Phys Soc Jpn **79**, 083711 (2010).

[32] S. Kumar and J. van den Brink, Phys Rev Lett **105**, 216405 (2010).

[33] G.-W. Chern, Phys Rev Lett **105**, 226403 (2010).

[34] Y. Motome and N. Furukawa, Phys Rev Lett **104**, 106407 (2010).

[35] M. Udagawa and R. Moessner, Phys Rev Lett **111**, 036602 (2013).

[36] M. Udagawa, H. Ishizuka, and Y. Motome, Phys Rev Lett **108**, (2012).

[37] R. Flint and T. Senthil, Phys Rev B **87**, 125147 (2013).

[38] H. J. Schulz, Phys Rev Lett **65**, 2462 (1990).

[39] Z. Y. Weng, C. Ting, and T. Lee, Phys Rev B **43**, 3790 (1991).

[40] T. Li, Epl-Europhys Lett **97**, 37001 (2012).

[41] J. Vergés, V. Martin-Mayor, and L. Brey, Phys Rev Lett **88**, 136401 (2002).

[42] S. Yunoki, A. Moreo, and E. Dagotto, Phys Rev Lett **81**, 5612 (1998).

[43] S. Kumar and P. Majumdar, Phys Rev Lett **92**, 126602 (2004).

[44] S. Kumar and P. Majumdar, Phys Rev Lett **96**, 016602 (2006).

[45] S. Kumar and P. Majumdar, Eur Phys J B **50**, 571 (2006).

[46] Z. Y. Meng, T. C. Lang, S. Wessel, F. F. Assaad, and A. Muramatsu, Nature **464**, 847 (2010).

[47] F. Wang, Phys Rev B **82**, 024419 (2010).

[48] Y.-M. Lu and Y. Ran, Phys Rev B **84**, 024420 (2011).

[49] A. Vaezi and X.-G. Wen, arXiv (2010).

[50] Y. Yafet and C. Kittel, Phys Rev **87**, 290 (1952).

[51] C. Castelnovo, R. Moessner, and S. L. Sondhi, Nature **451**, 42 (2008).

[52] J. S. Gardner, M. J. P. Gingras, and J. E. Greedan, Rev Mod Phys **82**, 53 (2010).

[53] Z. Nussinov and G. Ortiz, P Natl Acad Sci Usa **106**, 16944 (2009).

[54] B. Uchoa, T. G. Rappoport, and A. H. Castro Neto, Phys Rev Lett **106**, 016801 (2011).

[55] A. M. Black-Schaffer, Phys Rev B **81**, 205416 (2010).

[56] A. M. Black-Schaffer, Phys Rev B **82**, 073409 (2010).

[57] M. Daghofer, N. Zheng, and A. Moreo, Phys Rev B **82**, 121405 (2010).

[58] O. Smirnova, M. Azuma, N. Kumada, Y. Kusano, M. Matsuda, Y. Shimakawa, T. Takei, Y. Yonesaki, and N. Kinomura, J. Am. Chem. Soc. **131**, 8313 (2009).

[59] S. Okubo, F. Elmasry, W. Zhang, M. Fujisawa, T. Sakurai, H. Ohta, M. Azuma, O. A. Sumirnova, and N. Kumada, J. Phys.: Conf. Ser. **200**, 022042 (2010).

[60] R. Ganesh, D. N. Sheng, Y.-J. Kim, and A. Paramekanti, Phys Rev B **83**, 144414 (2011).

[61] A. Mulder, R. Ganesh, L. Capriotti, and A. Paramekanti, Phys Rev B **81**, 214419 (2010).

[62] H. C. Kandpal and J. van den Brink, Phys Rev B **83**, 140412 (2011).

[63] J. Bréger, M. Jiang, N. Dupré, Y. S. Meng, Y. Shao-Horn, G. Ceder, and C. P. Grey, Journal of Solid State Chemistry **178**, 2575 (2005).

[64] R. Yu, S. Yunoki, S. Dong, and E. Dagotto, Phys Rev B **80**, 125115 (2009).

[65] A. Mishra, M. Ma, F.-C. Zhang, S. Guertler, L.-H. Tang, and S. Wan, Phys Rev Lett **93**, 207201 (2004).

[66] M. Biskup, L. Chayes, and Z. Nussinov, Commun Math Phys **255**, 253 (2005).

[67] Z. Nussinov, M. Biskup, L. Chayes, and J. van den Brink, Europhys Lett **67**, 990 (2004).

[68] F. Trousselet, A. M. Oleś, and P. Horsch, Epl-Europhys Lett **91**, 40005 (2010).

[69] S. Liang, M. Daghofer, S. Dong, C. Şen, and E. Dagotto, Phys Rev B **84**, 024408 (2011).

[70] J. Riera, K. Hallberg, and E. Dagotto, Phys Rev Lett **79**, 713 (1997).

[71] N. Elstner, R. Singh, and A. Young, Phys Rev Lett **71**, 1629 (1993).

[72] R. Roy, Phys Rev B **79**, 195322 (2009).

[73] D. Hsieh, Y. Xia, D. Qian, L. Wray, J. H. Dil, F. Meier, J. Osterwalder, L. Patthey, J. G. Checkelsky, N. P. Ong, A. V. Fedorov, H. Lin, A. Bansil, D. Grauer, Y. S. Hor, R. J. Cava, and M. Z. Hasan, Nature **460**, 1101 (2009).

[74] Y. Xia, D. Qian, D. Hsieh, L. Wray, A. Pal, H. Lin, A. Bansil, D. Grauer, Y. S. Hor, R. J. Cava, and M. Z. Hasan, Nat Phys **5**, 398 (2009).

[75] K. von Klitzing, G. Dorda, and M. Pepper, Phys Rev Lett **45**, 494 (1980).

[76] F. D. M. Haldane, Phys Rev Lett **61**, 2015 (1988).

[77] C.-X. Liu, X.-L. Qi, X. Dai, Z. Fang, and S.-C. Zhang, Phys Rev Lett **101**, 146802 (2008).

[78] Y. Taguchi, Y. Oohara, H. Yoshizawa, N. Nagaosa, and Y. Tokura, Science **291**, 2573 (2001).

[79] Y. Machida, S. Nakatsuji, Y. Maeno, T. Tayama, T. Sakakibara, and S. Onoda, Phys Rev Lett **98**, 057203 (2007).

[80] H. Takatsu, S. Yonezawa, S. Fujimoto, and Y. Maeno, Phys Rev Lett **105**, 137201 (2010).

[81] K. K. Gomes, W. Mar, W. Ko, F. Guinea, and H. C. Manoharan, Nature **483**, 306 (2012).

[82] X.-L. Qi, Y.-S. Wu, and S.-C. Zhang, Phys Rev B **74**, 085308 (2006).

[83] H. Zhang, C. Lazo, S. Blügel, S. Heinze, and Y. Mokrousov, Phys Rev Lett **108**, 056802 (2012).

[84] S. Raghu, X.-L. Qi, C. Honerkamp, and S.-C. Zhang, Phys Rev Lett **100**, 156401 (2008).

[85] K. Ohgushi, S. Murakami, and N. Nagaosa, Phys Rev B **62**, R6065 (2000).

[86] K. Sun, H. Yao, E. S. Fradkin, and S. A. Kivelson, Phys Rev Lett **103**, 046811 (2009).

[87] K. Sun, Z.-C. Gu, H. Katsura, and S. Das Sarma, Phys Rev Lett **106**, 236803 (2011).

[88] S. Uebelacker and C. Honerkamp, Phys Rev B **84**, 205122 (2011).

[89] P. Schobinger-Papamantellos, J. Rodríguez-Carvajal, and K. H. J. Buschow, Journal of Magnetism and Magnetic Materials **310**, 63 (2007).

[90] L. D. C. Jaubert, M. Haque, and R. Moessner, Phys Rev Lett **107**, 177202 (2011).

[91] L. D. C. Jaubert, S. Piatecki, M. Haque, and R. Moessner, Phys Rev B **85**, 054425 (2012).

[92] I. Affleck and J. B. Marston, Phys Rev B **37**, 3774 (1988).

[93] J. Lorenzana, G. Seibold, C. Ortix, and M. Grilli, Phys Rev Lett **101**, 186402 (2008).

[94] M. Yamanaka, W. Koshibae, and S. Maekawa, Phys Rev Lett **81**, 5604 (1998).

[95] D. Agterberg and S. Yunoki, Phys Rev B **62**, 13816 (2000).

[96] H. Aliaga, B. Normand, K. Hallberg, M. Avignon, and B. Alascio, Phys Rev B **64**, 024422 (2001).

[97] X. Chen, S. Dong, and J. M. Liu, Phys Rev B **81**, 064420 (2010).

[98] A. H. Castro Neto, F. Guinea, N. M. R. Peres, K. S. Novoselov, and A. K. Geim, Rev Mod Phys **81**, 109 (2009).

[99] Y. Hatsugai, T. Fukui, and H. Aoki, Phys Rev B **74**, 205414 (2006).

[100] Y. Kato, I. Martin, and C. D. Batista, Phys Rev Lett **105**, 266405 (2010).

[101] M. Onoda and N. Nagaosa, J Phys Soc Jpn **71**, 19 (2002).

[102] S. Ryu, C. Mudry, C.-Y. Hou, and C. Chamon, Phys Rev B **80**, (2009).

[103] R. W. Jackiw, Phys Rev D **29**, 2375 (1984).

[104] D. N. Sheng, Z.-C. Gu, K. Sun, and L. Sheng, Nat Commun **2**, 389 (2011).

[105] N. Regnault and B. A. Bernevig, Phys. Rev. X **1**, 021014 (2011).

[106] J. W. F. Venderbos, M. Daghofer, and J. van den Brink, Phys Rev Lett **107**, 116401 (2011).

[107] J. W. F. Venderbos, S. Kourtis, J. van den Brink, and M. Daghofer, Phys Rev Lett **108**, 126405 (2012).

[108] T. Neupert, L. Santos, C. Chamon, and C. Mudry, Phys Rev Lett **106**, (2011).

[109] R. A. Muniz, A. Rahmani, and I. Martin, arXiv (2011).

[110] J. W. F. Venderbos, M. Daghofer, J. van den Brink, and S. Kumar, Phys Rev Lett **109**, 166405 (2012).

[111] X.-L. Qi and S.-C. Zhang, Rev Mod Phys **83**, 1057 (2011).

[112] C. Bruene, C. X. Liu, E. G. Novik, E. M. Hankiewicz, H. Buhmann, Y. L. Chen, X.-L. Qi, Z. X. Shen, S.-C. Zhang, and L. W. Molenkamp, Phys Rev Lett **106**, 126803 (2011).

[113] E. Tang, J.-W. Mei, and X.-G. Wen, Phys Rev Lett **106**, 236802 (2011).

[114] R. B. Laughlin, Phys Rev Lett **50**, 1395 (1983).

[115] X.-L. Qi, Phys Rev Lett **107**, 126803 (2011).

[116] Y.-L. Wu, N. Regnault, and B. A. Bernevig, Phys Rev B **86**, 085129 (2012).

[117] S. Das Sarma, M. H. Freedman, and C. Nayak, Phys Rev Lett **94**, 166802 (2005).

[118] Y. Tokura and N. Nagaosa, Science **288**, 462 (2000).

[119] Z. Fang, K. Terakura, and N. Nagaosa, New J Phys **7**, 66 (2005).

[120] G. Jackeli and G. Khaliullin, Phys Rev Lett **102**, 017205 (2009).

[121] D. Pesin and L. Balents, Nat Phys **6**, 376 (2010).

[122] J. van den Brink, G. Khaliullin, and D. Khomskii, Phys Rev Lett **83**, 5118 (1999).

[123] T. Hotta, M. Moraghebi, A. Feiguin, A. Moreo, S. Yunoki, and E. Dagotto, Phys Rev Lett **90**, 247203 (2003).

[124] H. Pen, J. van den Brink, D. Khomskii, and G. Sawatzky, Phys Rev Lett **78**, 1323 (1997).

[125] W. Koshibae and S. Maekawa, Phys Rev Lett **91**, 257003 (2003).

[126] D. J. Thouless, Phys Rev B **40**, 12034 (1989).

[127] B. A. Bernevig and S.-C. Zhang, Phys Rev Lett **96**, 106802 (2006).

[128] H. Zhang, C.-X. Liu, X.-L. Qi, X. Dai, Z. Fang, and S.-C. Zhang, Nat Phys **5**, 438 (2009).

[129] C. Nayak, S. H. Simon, A. Stern, M. H. Freedman, and S. Das Sarma, Rev Mod Phys **80**, 1083 (2008).

[130] X. Hu, M. Kargarian, and G. A. Fiete, Phys Rev B **84**, 155116 (2011).

[131] Y.-F. Wang, Z.-C. Gu, C.-D. Gong, and D. N. Sheng, Phys Rev Lett **107**, 146803 (2011).

[132] S. Nishimoto, M. Nakamura, A. O'Brien, and P. Fulde, Phys Rev Lett **104**, 196401 (2010).

[133] P. Matl, N. Ong, Y. Yan, Y. Li, D. Studebaker, T. Baum, and G. Doubinina, Phys Rev B **57**, 10248 (1998).

[134] W. A. Harrison, *Electronic Structure and Properties of Solids* (W.H. Freeman, San Francisco, 1980).

[135] J. C. Slater and G. F. Koster, Phys Rev **94**, 1498 (1954).

[136] B. Normand and A. M. Oles, Phys Rev B **78**, (2008).

[137] T. Nomura and K. Yamada, J Phys Soc Jpn **69**, 1856 (2000).

[138] F. Wilczek, Phys Rev Lett **49**, 957 (1982).

[139] F. D. M. Haldane, Phys Rev Lett **67**, 937 (1991).

[140] Y.-L. Wu, B. A. Bernevig, and N. Regnault, Phys Rev B **85**, 075116 (2012).

[141] S. Kourtis, J. W. F. Venderbos, and M. Daghofer, Phys Rev B **86**, 235118 (2012).

[142] S. A. Parameswaran, R. Roy, and S. L. Sondhi, Phys Rev B **85**, 241308 (2012).

[143] B. A. Bernevig and N. Regnault, Phys Rev B **85**, 075128 (2012).

[144] M. O. Goerbig, Eur Phys J B **85**, 15 (2012).

[145] R. Roy, arXiv (2012).

[146] Y. Hatsugai and M. Kohmoto, Phys Rev B **42**, 8282 (1990).

[147] B. A. Bernevig and T. L. Hughes, *Topological Insulators and Topological Superconductors* (Princeton University Press, Princeton and Oxford, 2013).

[148] T. Fukui, Y. Hatsugai, and H. Suzuki, J Phys Soc Jpn **74**, 1674 (2005).

[149] E. J. Bergholtz and Z. Liu, arXiv (2013).

[150] S. A. Parameswaran, R. Roy, and S. L. Sondhi, arXiv (2013).

[151] W. Metzner, M. Salmhofer, C. Honerkamp, V. Meden, and K. Schoenhammer, arXiv (2011).

[152] C. Platt, W. Hanke, and R. Thomale, arXiv (2013).

[153] E. Dagotto, Rev Mod Phys **66**, 763 (1994).

[154] G. R. Stewart, Rev Mod Phys **83**, 1589 (2011).

[155] S.-W. Cheong and M. V. Mostovoy, Nat Mater **6**, 13 (2007).

[156] R. Ramesh and N. A. Spaldin, Nat Mater **6**, 21 (2007).

[157] K. F. Wang, J. M. Liu, and Z. F. Ren, Adv Phys **58**, 321 (2009).

[158] H. Y. Hwang, Y. Iwasa, M. Kawasaki, B. Keimer, N. Nagaosa, and Y. Tokura, Nat Mater **11**, 103 (2012).

[159] R. Nandkishore, L. S. Levitov, and A. V. Chubukov, Nat Phys **8**, 158 (2012).

[160] R. Nandkishore, G.-W. Chern, and A. V. Chubukov, Phys Rev Lett **108**, 227204 (2012).

[161] R. Nandkishore and A. V. Chubukov, Phys Rev B **86**, 115426 (2012).

[162] G.-W. Chern, R. M. Fernandes, R. Nandkishore, and A. V. Chubukov, Phys Rev B **86**, 115443 (2012).

[163] G.-W. Chern and C. D. Batista, Phys Rev Lett **109**, 156801 (2012).

[164] M. L. Kiesel, C. Platt, and R. Thomale, Phys Rev Lett **110**, 126405 (2013).

[165] A. V. Maharaj, R. Thomale, and S. Raghu, Phys Rev B **88**, 205121 (2013).

[166] C. Nayak, Phys Rev B **62**, 4880 (2000).

[167] C. Weeks and M. Franz, Phys Rev B **81**, 085105 (2010).

[168] A. G. Grushin, E. V. Castro, A. Cortijo, F. de Juan, M. A. H. Vozmediano, and B. Valenzuela, Phys Rev B **87**, 085136 (2013).

[169] J. Wen, A. Rueegg, C. C. J. Wang, and G. A. Fiete, Phys Rev B **82**, 075125 (2010).

[170] Q. Liu, H. Yao, and T. Ma, Phys Rev B **82**, 045102 (2010).

[171] Y. Zhang, Y. Ran, and A. Vishwanath, Phys Rev B **79**, 245331 (2009).

[172] C. Fang, M. J. Gilbert, and B. A. Bernevig, Phys Rev B **86**, 115112 (2012).

[173] X. Wan, A. M. Turner, A. Vishwanath, and S. Y. Savrasov, Phys Rev B **83**, 205101 (2011).

[174] A. A. Burkov, M. D. Hook, and L. Balents, Phys Rev B **84**, 235126 (2011).

[175] A. A. Burkov and L. Balents, Phys Rev Lett **107**, 127205 (2011).

[176] C. Fang, M. J. Gilbert, X. Dai, and B. A. Bernevig, Phys Rev Lett **108**, 266802 (2012).

[177] F. D. M. Haldane, Phys Rev Lett **93**, 206602 (2004).

[178] J.-M. Hou, Phys Rev Lett **111**, 130403 (2013).

[179] M. A. H. Vozmediano, M. I. Katsnelson, and F. Guinea, Phys Rep **496**, 109 (2010).

[180] S. Gopalakrishnan, P. Ghaemi, and S. Ryu, Phys Rev B **86**, 081403 (2012).

[181] C. Fang, M. J. Gilbert, and B. A. Bernevig, Phys Rev B **88**, 085406 (2013).

[182] K. Sun and E. S. Fradkin, Phys Rev B **78**, 245122 (2008).

[183] T. L. Hughes, E. Prodan, and B. A. Bernevig, Phys Rev B **83**, 245132 (2011).

[184] L. Fu and C. L. Kane, Phys Rev B **76**, 045302 (2007).

[185] E. V. Castro, A. G. Grushin, B. Valenzuela, M. A. H. Vozmediano, A. Cortijo, and F. de Juan, Phys Rev Lett **107**, 106402 (2011).

[186] M. Serbyn and P. A. Lee, Phys Rev B **87**, 174424 (2013).

[187] X.-G. Wen, F. Wilczek, and A. Zee, Phys Rev B **39**, 11413 (1989).

[188] S. Chakravarty, R. Laughlin, D. Morr, and C. Nayak, Phys Rev B **63**, 094503 (2001).

[189] G. Kotliar, Phys Rev B **37**, 3664 (1988).

[190] P. Kotetes and G. Varelogiannis, Epl-Europhys Lett **84**, 37012 (2008).

[191] C.-H. Hsu, S. Raghu, and S. Chakravarty, Phys Rev B **84**, 155111 (2011).

[192] W. Cho, R. Thomale, S. Raghu, and S. A. Kivelson, Phys Rev B **88**, 064505 (2013).

[193] C. Chamon, C.-Y. Hou, R. W. Jackiw, C. Mudry, S.-Y. Pi, and A. Schnyder, Phys Rev Lett **100**, 110405 (2008).

[194] B. Seradjeh, C. Weeks, and M. Franz, Phys Rev B **77**, (2008).

[195] B. Seradjeh and M. Franz, Phys Rev Lett **101**, (2008).

[196] K. S. Novoselov, A. K. Geim, A. V. Morozov, D. Jiang, Y. Zhang, S. V. Dubonos, I. V. Grigorieva, and A. A. Firsov, Science **306**, 666 (2004).

[197] C.-Y. Hou, C. Chamon, and C. Mudry, Phys Rev Lett **98**, (2007).

[198] A. Cortijo, A. G. Grushin, and M. A. H. Vozmediano, Phys Rev B **82**, 195438 (2010).

[199] G. W. Semenoff, Phys Rev Lett **53**, 2449 (1984).

[200] C. W. J. Beenakker, Rev Mod Phys **80**, 1337 (2008).

[201] K. Asano and C. Hotta, Phys Rev B **83**, 245125 (2011).

[202] J. L. Manes, F. Guinea, and M. A. H. Vozmediano, Phys Rev B **75**, (2007).

[203] N. M. R. Peres, Rev Mod Phys **82**, 2673 (2010).

[204] J. L. Manes, Phys Rev B **76**, 045430 (2007).

[205] D. M. Basko, Phys Rev B **78**, 125418 (2008).

[206] V. P. Gusynin, S. G. Sharapov, and J. P. Carbotte, Int J Mod Phys B **21**, 4611 (2007).

[207] H. M. Guo and M. Franz, Phys Rev B **80**, 113102 (2009).

[208] L. Messio, C. Lhuillier, and G. Misguich, Phys Rev B **83**, 184401 (2011).

[209] G.-W. Chern, A. Rahmani, I. Martin, and C. D. Batista, arXiv (2012).

[210] H. Ishizuka and Y. Motome, Phys Rev B **87**, 081105 (2013).

[211] M. Daghofer and M. Hohenadler, arXiv (2013).

Samenvatting

Voor een groot aantal vaste stoffen geldt dat hun eigenschappen slechts kunnen worden begrepen door de (soms sterke) wisselwerking tussen de elektronen in die vaste stof in beschouwing te nemen. Wisselwerkingen ofwel interacties tussen de elektronen, voortvloeiend uit de repulsieve Coulomb-kracht, zijn namelijk verantwoordelijk voor een grote verscheidenheid aan fysische verschijnselen en materiaaleigeschappen. Men kan denken aan Mott-isolatie, diverse vormen van magnetisme, orbitaalordening, ferro-elektriciteit en supergeleiding. In dit proefschrift bestuderen we interacties tussen elektronen op verschillende manieren en kijken we specifiek naar het karakter van de elektronische grondtoestand.

In het eerste deel van dit proefschrift bestuderen we de wisselwerking tussen gelokaliseerde elektronen en anderzijds elektronen die door het kristalrooster kunnen bewegen. Gelokaliseerde elektronen behoren toe aan een specifiek atoom in het kristalrooster en vormen (gelokaliseerde) spin momenten. Een dergelijke wisselwerking zorgt er in het algemeen voor dat de gelokaliseerde spin momenten de neiging hebben allemaal in dezelfde richting te wijzen, dat wil zeggen een "ferromagnetische" toestand te realiseren. De interactie tussen de gelokaliseerde spin momenten zelf daarentegen, is van "anti-ferromagnetische" aard en heeft daarom de neiging om deze spin momenten in tegenovergestelde richting te laten wijzen. Het systeem kan niet tegelijk aan beide neigingen toegeven omdat ze met elkaar in strijd zijn. Afhankelijk van de materiaal-specifieke relatieve grootte van die twee met elkaar strijdige interacties vindt het systeem een middenweg. Een dergelijk compromis kan leiden tot nieuwe en interessante magnetische en elektronische toestanden. Voor zowel ferromagnetische en anti-ferromagnetische toestanden kunnen we altijd een as vinden waarlangs we alle spins kunnen leggen. Dat soort toestanden heten "collineair": alle spins liggen op één lijn. Toestanden waarvoor dat niet geldt, maar waarvoor alle spins in één vlak liggen heten "coplanair" (coplanar). Dan zijn er nog toestanden waarvoor ook dat laatste niet geldt, en die worden doorgaans aangeduid met de term "niet-coplanair" (non-coplanar). Zulke toestanden zijn zeldzaam, maar kunnen juist ontstaan als gevolg van met elkaar strijdige interacties.

In de hoofdstukken twee tot en met vier laten we zien hoe nieuwe interessante magnetische toestanden worden gevormd als compromis tussen met elkaar strijdende interacties. Een belangrijke factor bij het vinden van een dergelijk compromis blijkt de structuur van het kristalrooster te zijn. Als het kristalrooster "gefrustreerd" is geeft dat vaak aanleiding tot niet-coplanaire toestanden. De magnetische energie van een verzameling spins op een rooster wordt meestal uitgedrukt als som over de energie van naburige paren spins. Een gefrustreerd rooster is een rooster waarvoor geldt dat de magnetische energie niet voor elk paar naburige spins minimaal kan zijn. Hoofdstuk drie bespreekt de spin-elektron interactie voor een hexagonaal grafeen-rooster, ook wel kippengaasrooster genoemd, en dat is een voorbeeld van een rooster dat juist niet gefrustreerd is. Hoofdstuk vier behandelt vervolgens het gefrustreerde schaakbordrooster (in het Engels "checkerboard"). Niet alleen is dit een voorbeeld van een gefrustreerd rooster, het heeft ook de eigenschap dat de magnetische interactie tussen de spins geen unieke toestand selecteert die de laagste energie heeft. Er bestaat een hele verzameling magnetische toestanden die de totale magnetische energie minimaliseren. Elektronen die met de gelokaliseerde spins wisselwerken veranderen dat en kiezen een speciale toestand als unieke grondtoestand.

Waarom zijn deze bijzondere magnetische toestanden die onstaan door de wisselwerking van gelokaliseerde spins en niet-gelokaliseerde elektronen interessant? De reden is de volgende: als de spins niet allemaal in een vlak liggen (een niet-coplanaire toestand) en de elektronen door deze magnetische toestand bewegen, dan lijkt het voor hen net alsof ze door een echt magneetveld bewegen. Van elektronen in een magneetveld weten we dat dit leidt tot de speciale Landau-kwantisatie van de energieën en het Quantum Hall Effect. Het Quantum Hall Effect kan ook optreden zonder magneetveld in het geval elektronen met spins wisselwerken die een magneetveld nabootsen. Die eigenschap maakt van de materialen waarin dit verschijnsel voorkomt topologische isolatoren. Topologische isolatoren zijn elektrisch isolerende materialen die speciale geleidende randtoestanden hebben.

In het tweede deel van dit proefschrift gaan we een stap verder en kijken we naar mogelijkheden om niet alleen het Quantum Hall Effect zonder magneetveld na te bootsen in magnetische materialen, maar het Fractionele Quantum Hall Effect. Het Fractionele Quantum Hall Effect in een twee-dimensionaal elektrongas ontstaat als gevolg van de sterke interactie tussen elektronen in het laagste "Landau-level", de volkomen vlakke elektronenband die onstaat als gevolg van het magneetveld. Nu we weten dat een dergelijke elektronenband ook kan ontstaan zonder magneetveld, rijst de vraag of de mogelijkheid bestaat dat effectieve interacties tussen elekotronen in die band tot een Fractioneel Quantum Hall Effect kunnen leiden. Op die vraag wordt in de hoofstukken vijf tot en met zes ingegaan en we tonen aan dat die mogelijkheid inderdaad bestaat.

In het derde deel van dit proefschrift kiezen we een ander perspectief om het effect

van elektron correlaties te onderzoeken. Het vetrekpunt is de vrije bandenstructuur van het materiaal, die afhangt van het kristalrooster. De dichtheid van electronen bepaalt het Fermi-oppervlak en we stellen de vraag hoe interacties de bandenstructuur dicht bij dat Fermi-oppervlak veranderen. We gaan ervan uit dat de interacties tussen elektronen aanleiding geven tot elektronische ordening die beschreven kan worden met dichtheidsgolven. Dat kunnen ladingsdichtheidsgolven, spindichtheidsgolven, maar ook paardichtheidsgolven of fluxdichtheidsgolven zijn. Al deze dichtheidsgolven klassificeren we op grond van de roostersymmetrieën die zij behouden of breken. Vervolgens laten we voor zowel roosters met dezelfde symmetrie als een vierkant rooster, als roosters met dezelfde symmetrie als een driehoeksrooster zien dat de symmetrie van een dichtheidsgolf al heel veel vertelt over de elektronische eigenschappen van de dichtheidsgolf. In het bijzonder leert de symmetrie van de dichtheidsgolf ons veel over het topologische karakter van de bandenstructuur die bij de dichtheidsgolf hoort. Daarmee kunnen we een licht laten schijnen op de manier waarop, en onder welke omstandigheden, interacties tussen elektronen topologische toestanden der materie induceren.

Curriculum Vitae

Op 31 januari 1984 werd ik geboren te Kleve, Duitsland, waarna ik mijn jeugd doorbracht in Stokkum, Gelderland. Ik behaalde mijn VWO diploma in 2002 aan het St. Ludgercollege te Doetinchem en schreef mij in voor de studies economie en rechten in Rotterdam. Daar ontdekte ik dat mijn passie meer lag bij de studie der natuur en ik zette mijn universitaire loopbaan daarom voort aan de universiteit Leiden, waar ik in 2003 begon als eerstejaars student natuurkunde. In 2006 behaalde ik het Bachalor diploma in de natuurkunde cum laude, na een onderzoeksstage in de groep van Professor Edgar Groenen. Al vanaf mijn eerste jaar in Leiden ben ik lid geweest van de opleidingscommissie.

In datzelfde jaar startte ik de Masteropleiding natuurkunde in Leiden. In 2007 eindigde het lidmaatschap van de opleidingscommissie en tussen 2007 en 2008 had ik als student-lid zitting in het bestuur van de faculteit Wiskunde en Natuurwetenschappen in Leiden. Het afsluitende masteronderzoek in de theoretische natuurkunde verrichte ik in de onderzoeksgroep van Professor Carlo Beenakker. Het Masterdiploma theoretische natuurkunde behaalde ik in 2009 cum laude.

Meteen aansluitend begon ik aan het promotie-onderzoek in de groep van Professor Jeroen van den Brink. De eerste maanden daarvan werkte ik in Leiden, waar ik het werkcollege voor het mastervak Quantum Theory begeleidde. In 2010 verhuisde ik naar Dresden om mijn onderzoek aan het IFW Dresden voort te zetten, waar Jeroen van den Brink directeur van het instituut voor theoretische vaste-stof fysica geworden was. Ik het kader van mijn promotie onderzoek heb ik meerdere internationale conferenties en zomerscholen bezocht en mijn onderzoek daar gepresenteerd.

Naast mijn academische werk heb ik mij steeds zeer geïnteresseerd voor sport en heb ik verschillende sporten actief en met groot plezier beoefend.

Na mijn promotie zal ik mijn wetenschappelijke werk voortzetten in de onderzoeksgroep van Professor Liang Fu aan het Massachusetts Institute of Technology in Boston.

LIST OF PUBLICATIONS

Published papers

- S. Kourtis, J.W.F. Venderbos, and M. Daghofer, "Fractional Chern insulator on a triangular lattice of strongly correlated t_{2g} electrons". Physical Review B **86**, 235118 (2012). (*Chapter 7 of this thesis*)

- J.W.F. Venderbos, M. Daghofer, J. van den Brink and S. Kumar, "Switchable Quantum Anomalous Hall state in a strongly frustrated lattice magnet". Physical Review Letters **109**, 166405 (2012). (*Chapter 4 of this thesis*)

- J.W.F. Venderbos, S. Kourtis, J. van den Brink and M. Daghofer, "Fractional quantum-Hall liquid spontaneously generated by strongly correlated t_{2g} electrons". Physical Review Letters **108**, 126405, (2012). (*Chapter 6 of this thesis*)

- Ruijuan Xiao, F. Tasnadi, K. Koepernik, J.W.F. Venderbos, M. Richter, and M. Taut "Density functional investigation of rhombohedral stacks of graphene: Topological surface states, nonlinear dielectric response, and bulk limit". Physical Review B **84**, 165404 (2011).

- J.W.F. Venderbos, M. Daghofer and J. van den Brink, "Narrowing of topological bands due to electronic orbital degrees of freedom". Physical Review Letters **107**, 116401 (2011). (*Chapter 5 of this thesis*)

- J.W.F. Venderbos, M. Daghofer, J. van den Brink and S. Kumar, "Macroscopic degeneracy and emergent frustration in a honeycomb lattice magnet". Physical Review Letters **107** 076405 (2011). (*Chapter 3 of this thesis*)

- C.W.J. Beenakker, J.W.F. Venderbos, and M.P van Exter, "Two-photon speckle a Probe for Multi-dimensional Entanglement". Physical Review Letters **102**, 193601 (2009).

Preprints to appear

- C. Ortix, J.W.F. Venderbos, R. Hayn and J. van den Brink, "Absence of helical surface states in bulk semimetals with broken inversion symmetry", arXiv:cond-mat/1307.2698, submitted to Physical Review Letters (2013)

- M. Manzardo, J.W.F. Venderbos, J. van den Brink, and C. Ortix, "Engineering a topological Mott insulating phase in a Dirac-semimetal superlattice", to appear (2013).

- J.W.F. Venderbos, "Lattice symmetry classification of general density waves in two dimensions", to be published. (*see chapter 8, 9 and 10 of this thesis*)

- J.W.F. Venderbos, "Topological semimetallic and insulating states from spin density wave formation in hexagonal lattices", to be published. (*see chapter 10 of this thesis*)

Acknowledgements

Stellingen

behorende bij het proefschrift

Integer and Fractional Quantum Hall effects in Lattice Magnets

1. Meetkundige frustratie van interacties vloeit niet uitsluitend voort uit de structuur van een kristalrooster, maar kan ook ontstaan als gevolg van een competitieve wisselwerking tussen enerzijds gelokaliseerde magnetische momenten en anderzijds bewegende elektronen in een kristalrooster dat niet gefrustreerd is.

   dit proefschrift, hoofdstuk 4

2. Met elkaar wisselwerkende gelokaliseerde magnetische momenten en bewegende elektronen in een driehoekig kristalrooster, beschreven met een effectief Kondo-rooster model, kunnen leiden tot een elektronische grondtoestand die equivalent is met de "Quantum Hall"-toestand. In het geval de bewegende elektronen zich in verschillende orbitalen bevinden, kan hun bandenstructuur de Quantum Hall Landau levels zodanig nabootsen, dat effectieve interacties binnen een dergelijke band een "Fractional Quantum Hall"-toestand induceren.

   dit proefschrift, hoofdstuk 5, 6 en 7

3. Dichtheidsgolven van verschillende aard, zoals ladings-, paar- of fluxdichtheidsgolven, zijn condensaten van deeltjes en gaten die geïnduceerd worden door wisselwerking tussen elektronen. Door alle mogelijke dichtheidsgolven te classificeren op basis van de symmetrieën van het kristalrooster kan men sterke uitspraken doen over de eigenschappen van de elektronische grondtoestand, in het bijzonder het "gemiddelde veld"-spectrum van deze dichtheidsgolven, zonder verdere vergelijkingen op te lossen.

   dit proefschrift, hoofdstuk 9

4. Symmetrische spindichtheidsgolven op roosters met hexagonale symmetrie kunnen worden verkregen uit de symmetrische ladingsdichtheidsgolven. De elektronische eigenschappen van deze spindichtheidsgolven hangen niet af van de specifieke structuur van het rooster, maar slechts van de transformatie-eigenschappen onder de roostersymmetriegroep.

dit proefschrift, hoofdstuk 10

5. De voorspelling van chirale spintoestanden op roosters met hexagonale symmetrie is zeer interessant en het wordt hoog tijd voor een experimentele bevestiging daarvan.

6. De ontdekking van topologische toestanden van materie en in het bijzonder de topologische isolatoren illustreert hoe vaste stoffen dikwijls de laboratoria zijn waar concepten uit de hoge-energie fysica kunnen worden geobserveerd en getest.

Hasan & Kane, Rev. Mod. Phys. 82, 3045 (2010); Qi & Zhang, Rev. Mod. Phys. 83, 1057 (2011)

7. Het heeft de belangstelling voor topologische isolatoren behoorlijk geholpen dat er niet lang na hun ontdekking materialen als zodanig geïdentificeerd zijn in het experiment.

8. Het kan heel gunstig zijn om als theoretisch natuurkundige voor te lopen op het experiment, maar de vraag is hoe ver.

9. "Iets kan zijn verzonnen en daardoor juist bestaan. Dat soms iets niet verzonnen is, neemt men zomaar aan."

Herman Finkers, uit "Na de pauze"

10. Geld wordt niet verdiend of verloren, maar slechts verplaatst, van de ene illusie naar de andere.

Jörn Venderbos

Leiden, maart 2014